

Design of a Mobile Robotic Platform with Variable Footprint

by

Alexander N. Wilhelm

A thesis
presented to the University of Waterloo
in fulfillment of the
thesis requirement for the degree of
Master of Applied Science
in
Mechanical Engineering

Waterloo, Ontario, Canada, 2007

©A. N. Wilhelm, 2007

I hereby declare that I am the sole author of this thesis. This is a true copy of the thesis, including any required final revisions, as accepted by my examiners.

I understand that my thesis may be made electronically available to the public.

Alexander N. Wilhelm

Abstract

This thesis presents an in-depth investigation to determine the most suitable mobile base design for a powerful and dynamic robotic manipulator. It details the design process of such a mobile platform for use in an indoor human environment that is to carry a two-arm upper-body humanoid manipulator system. Through systematic dynamics analysis, it was determined that a variable footprint holonomic wheeled mobile platform is the design of choice for such an application. Determining functional requirements and evaluating design options is performed for the platform's general configuration, geometry, locomotion system, suspension, and propulsion, with a particularly in-depth evaluation of the problem of overcoming small steps. Other aspects such as processing, sensing and the power system are dealt with sufficiently to ensure the feasibility of the overall proposed design. The control of the platform is limited to that necessary to determine the appropriate mechanical components. Simulations are performed to investigate design problems and verify performance. A basic CAD model of the system is included for better design visualization.

The research carried out in this thesis was performed in cooperation with the German Aerospace Center (*Deutsches Zentrum für Luft- und Raumfahrt*)'s Robotics and Mechatronics Institute (DLR RM). The DLR RM is currently utilizing the findings of this research to finish the development of the platform with a target completion date of May 2008.

Acknowledgements

It started with the desire to combine the research depth of a Canadian Master's degree with an exciting opportunity for robotics development in Germany. Three people at Waterloo were willing to subscribe to this unorthodox undertaking. When I could not decide, all three became my supervisors; I would like to thank Chris Clark, Jan Huissoon, and William Melek for each contributing their advice and expertise.

On the other side of the Atlantic, the support of the German Aerospace Center's Robotics and Mechatronics Institute, who made this project possible, needs to be acknowledged. Specifically, I would like to thank Norbert Sporer for giving me this opportunity, as well as the other researchers and staff at the institute who made my eight month stay a very enjoyable and informative one. In particular, my thanks go to Matthias Fuchs and Werner Friedl for their guidance and assistance with starting and working on a design that they have now continued. I am grateful for being given the chance to help define this project and look forward to seeing it come to fruition in the near future.

My appreciation also goes out to my friends Andreas and Bernard who helped me think through some problems that had others baffled; you certainly helped me crack the puzzle.

Last but not least, I would like to thank my parents and my girlfriend Emily for their love and support irregardless of whether I was in Waterloo, Munich or Toronto.

Table of Contents

Abstract	iii
Acknowledgements	iv
Table of Contents	v
List of Figures	viii
List of Tables.....	xix
Chapter 1 Introduction.....	1
1.1 Motivation	1
1.2 Background	1
1.3 Literature Review	5
1.4 Design Goals	19
1.5 Thesis Contribution	32
1.6 Thesis Organization.....	32
Chapter 2 Evaluation of Configurations.....	33
2.1 Options	33
2.2 Evaluation Criteria.....	34
2.3 Evaluated Configurations	38
2.4 Evaluation Results.....	46
2.5 Chosen Configuration.....	46
Chapter 3 Variable Footprint Mechanism	47
3.1 Concept.....	47
3.2 Optimization of Selected Configuration.....	54
3.3 Mechanism Kinetics	56
3.4 Drive Selection	91
3.5 VFM – Conclusions.....	94
Chapter 4 Stability.....	95
4.1 Stability Measure.....	95
4.2 Analysis	99
Chapter 5 Step Passing Behaviour	108
5.1 Background	108
5.2 Simple Theory	108
5.3 Experimental System Characterization	111

5.4 Step Passing Behaviour Experiment	121
5.5 Advanced Theory	123
5.6 Simulation	127
5.7 Applications to Platform Design	132
5.8 Conclusions	138
Chapter 6 Suspension	139
6.1 Problem Definition and Goals	139
6.2 Background	139
6.3 Review of Options	140
6.4 Tire Only	142
6.5 Passive Spring & Damper	148
6.6 Suspension: Conclusion	157
Chapter 7 Locomotion System	158
7.1 Footprint Geometry	159
7.2 Mobility	159
7.3 Kinematics & Dynamics	160
7.4 Selection of Wheel Type	160
Chapter 8 Drive System Kinetics	161
8.1 Co-operating Manipulators Model Derivation	161
8.2 Kinematics	167
8.3 Dynamics	175
8.4 Control	178
8.5 Simulation	180
8.6 Conclusion	204
Chapter 9 Component Volume, Mass, Energy and Power Analysis	205
9.1 Sensing Components	205
9.2 Processing Components	208
9.3 Power Requirements	209
9.4 Energy Storage	210
9.5 Mass Estimate	211
9.6 Volume Estimate	211
9.7 Base Geometry	213
Chapter 10 Proposed Design	219

Appendix A Existing Mobile Robots and Manipulators	227
Appendix B Multi-body Dynamic Modelling in Modelica/Dymola	230
Limitations of Model.....	230
Appendix C Disturbance Forces due to Upper Body Dynamics	231
Appendix D Tire Model	232
Appendix E Propulsion System Calculations.....	233
Tire Properties affecting Propulsion.....	233
Requirements at the Wheel.....	233
Requirements for the Drivetrain.....	236
Appendix F Configuration Evaluation Matrix.....	240

List of Figures

Figure 1.1: Justin on its table mount shown in different configurations [2].	2
Figure 1.2: Lightweight Robot III.	2
Figure 1.3: The torso's workspace [2], units are in (mm).	3
Figure 1.4: DLR Robotler mobile manipulator with previous generation light-weight arm.	4
Figure 1.5: Mori et al. add another joint (a to b on L) to change the platform footprint (R)[20].	7
Figure 1.6: Wada et al.'s caster drive mechanism [24].	8
Figure 1.7: A pair of Omniwheel universal wheels from Kornylak Corporation [].	9
Figure 1.8: West and Asada's ball wheel mechanism [33].	9
Figure 1.9: Continuous Alternating Wheel by Byun et al.	10
Figure 1.10: Workpartner robot [38].	11
Figure 1.11: T3 platform with wheels on prismatic joints [40].	11
Figure 1.12: Octal Wheel robot [41].	11
Figure 1.13: The Walk'n roll robot [42].	11
Figure 1.14: Chugo et al's rocker-bogie platform climbing a step [43].	11
Figure 1.15: NASA Robonaut Centuar concept [44].	12
Figure 1.16: Wada et al.'s variable footprint mechanism in a) narrow, b) isotropic and c) wide configuration [45].	12
Figure 1.17: Variable wheel arrangement mechanism of OMR-SOW [46].	13
Figure 1.18: Nomad's transforming chassis in the compact (T-L) and deployed (T-R) with the steps of deployment (B) [].	13
Figure 1.19: HELIOUS-VI tracked robot [49].	14
Figure 1.20: Azimut tracked robot [50].	14
Figure 1.21: HERMES, a statically stable humanoid [51].	14
Figure 1.22: Nomadic XR4000 platform with PUMA 560 manipulator [16].	14
Figure 1.23: The NASA Robonaut mounted on the Segway RMP with custom 'training wheels' [55].	16
Figure 1.24: Hitachi's dynamic balancing two-wheeled robot with side-ways tilt joint [60].	16
Figure 1.25: Ballbot with kickstands deployed (L) and balancing on the single wheel (R) [61].	17
Figure 1.26: The Honda Asimo can walk up stairs [63].	17
Figure 1.27: The IMR-Type 1 wheeled robot is capable of static and dynamic balance [67].	18
Figure 1.28: initial 'wish list' for Mobile Platform.	21

Figure 1.29: 50% and 95% human mid-section beside Justin, values in (m).....	28
Figure 1.30: QFD ‘House of Quality’ Matrix.....	31
Figure 2.1: Different potential approaches to mobility.	34
Figure 2.2: Difference between maximum and minimum footprint radius decreases as the number of contact points increases.	39
Figure 2.3: Platform reach: (L to R) dynamic two-wheeled balance, shift of centre of mass by platform tilt, shift of contact point by leg extension.....	41
Figure 2.4: Hybrid balance strategies.	42
Figure 2.5: Concept A4: leg retracted, dynamic balance (top left), leg extended, torso upright (top right), leg extended, torso horizontal (bottom).....	43
Figure 2.6: Concept A3: torso upright (left), platform by itself (top right), with torso horizontal (bottom right).	44
Figure 2.7: Concept C3: legs retracted and torso upright (top, front legs extended with torso and arms extended horizontally (bottom).	45
Figure 3.1: C2 side view showing design parameters	51
Figure 3.2: Integrated slider moment relative to parallel offset distance u (m) and offset angle ζ (rad) with horizontal offset $a = 0$ m. The moment becomes zero at $\zeta = 90^\circ$ when the offset is horizontal as in C2b.....	52
Figure 3.3: Integrated slider moment relative to horizontal offset a (m) and parallel offset angle ζ (rad) with $u = 0.1$ m. For all angles, the moment reaches a minimum at $a = 0$, with the absolute minimum of zero for $\zeta = 90^\circ$	52
Figure 3.4: Integrated slider moment relative to horizontal offset a (m) and parallel offset distance u (m) with $\zeta = 0^\circ$ (upright). The moment is lowest at $a = 0$, no horizontal offset, and the smallest value of parallel offset, $u = 0.05$ m.....	52
Figure 3.5: Summed upper and middle leg forces (N), taken along leg towards base for different parameter combinations; $\zeta = 90^\circ$, no horizontal offset ($a = 0$ m) is lowest.	53
Figure 3.6: Three options for wheel placement in the VFM: (a) a single lower leg joint requires the wheel to be offset somewhere below or to the outside of the joint; (b) by splitting the leg, the lower leg joint can be located on either side of the wheel, eliminating the horizontal and vertical offset, but this makes the wheel unit quite wide; (c) a compromise is reached by splitting the leg joint <i>and</i> offsetting the wheel vertically so that the width of the wheel unit can be kept smaller.	55
Figure 3.7: Variable definition for kinematic analysis.....	56

Figure 3.8: Leg angle is a non-linear function of leg extension distance (leg length $l = 0.4$ m).....	58
Figure 3.9: Vertical slider position relative to extension distance and angle (leg length $l = 0.4$ m)....	58
Figure 3.10: Vertical slider velocity and acceleration for a constant leg extension velocity of 1 m/s (no extension acceleration, leg length $l=0.4$ m).	58
Figure 3.11: Leg angle velocity and acceleration for constant leg extension velocity (no extension acceleration, leg length $l = 0.4$ m).....	59
Figure 3.12: Free-body diagram of simplified static and dynamic analysis.	60
Figure 3.13: Horizontal forces at V and B due to horizontal wheel offset b in static equilibrium.	62
Figure 3.14: Horizontal force into base at L and out of base at D , static equilibrium condition, for different horizontal wheel offsets (b). Legend as in Figure 3.13.	63
Figure 3.15: the horizontal force at the outer slider (B_x) at various configurations and accelerations.	64
Figure 3.16: B_x integrated over leg extension to show linear dependence on horizontal offset b and vertical offset d with acceleration of 2 m/s^2	65
Figure 3.17: Horizontal force at the bottom outer leg joint (V_x) for various configurations and accelerations.....	65
Figure 3.18: Normal force N at tire (L is left and R is right) for various configurations and accelerations.....	66
Figure 3.19: N_L and N_R (left and right) integrated over x to show linear relationship to b and d , acceleration of 2 m/s^2	67
Figure 3.20: The ground friction factor necessary for given acceleration depends on the wheel offset b , the vertical offset d and the leg extension x	67
Figure 3.21: Horizontal force at right (front) side slider/top inner leg joint with acceleration and varying configurations.	68
Figure 3.22: Vertical force in slider (at L) due to acceleration; upwards on forward (right) side, downwards on left (rear). If not counteracted, slider will retract/extend.....	69
Figure 3.23: Torque to hold leg at 2 m/s^2 with and without leg masses of 1 kg/leg for varying actuation positions	70
Figure 3.24: Dymola model. Green arrows show forces at various points; system currently at rest...	72
Figure 3.25: Case 1ref, torso vertical & arms down - forces on leg 2 (opposite acceleration direction). Steady-state values of simulated forces shown are similar to the simplified dynamic analysis in 3.3.3, for instance P_x is 1065 N versus 1017 N in the simplified analysis.	74

Figure 3.26: Case 1ref - torque at joint T to hold legs in position; the steady state value for leg 4 of 3.7 Nm corresponds reasonably with the value of 4.4 Nm found during the simplified dynamic analysis. 75

Figure 3.27: Case 1a - torque to hold leg position. Torque for the two pairs of legs is the same; the pair opposite the acceleration/underneath the extended arms increases during acceleration at 2 s. 75

Figure 3.28: Case 1b - torque to hold leg position. The torque in leg 2, which is directly underneath the extended arms/opposite the acceleration, increases over twice as much as the torque for the pair of legs in case 1a. 75

Figure 3.29: Case 1c – torque to hold leg position. The shorter leg extension almost quadruples the torque in case 1c as compared to case 1b. 76

Figure 3.30: Case 1d - torque to hold leg position, legs extended. The horizontal torso with a 3 kg load requires a torque slightly above case 1b with the torso vertical and 15 kg load..... 76

Figure 3.31: Case 1a - the effect of acceleration on the suspension as indicated by the body pitch angle—up to 1.4° tilt—and the suspension force in a front and rear wheel, which shows that the front wheel actually loses contact shortly after acceleration begins before regaining contact around 2.5 s. 77

Figure 3.32: Case 1a - Forces on leg 1 (under and to the side of the torso, away from acceleration direction)—same as leg 2. 77

Figure 3.33: Case 1b - forces on leg 2 (under arms, away from acceleration direction). Forces are almost twice as high as for leg 1 in case 1a. 78

Figure 3.34: Case 1c – forces on leg 2 (under extended arm, away from acceleration direction). 78

Figure 3.35: Case 2a - platform angular position, velocity and acceleration. Acceleration at 3.4 rad/s² from 2 s up to 2.8 rad/s. 80

Figure 3.36: Case 2a – forces on leg 1 (to side of torso). Increased leg forces during rotational acceleration from 2 to 2.8 s, notably vertically at the lower base joint *D*, the lower leg joint *V*, and the wheel normal *N*, as well as laterally at the centre leg joint *T* and lower base joint *D*. 80

Figure 3.37: Case 2a - forces on leg 2 (in front of torso). Increased forces primarily due to rotational velocity, which reaches a maximum at 2.8s. 81

Figure 3.38: Case 2a - torque to hold leg position with legs extended..... 81

Figure 3.39: Case 2b - torque to hold leg position with legs retracted; the acceleration induced torque from 2 to 2.8 s now exceeds the velocity induced torque thereafter, and both are higher than in case 2a. 82

Figure 3.40: Case 2b - angular velocity and acceleration of platform.	82
Figure 3.41: Case 2b - snapshot of configuration. Torso is rotated 45° so that extended arms roughly line up with two legs.	83
Figure 3.42: Case 2b – forces on leg 2 (under arm). Sideways V_y and D_y forces increase significantly during the higher acceleration of case 2b with the legs retracted; they drop off when acceleration ends.	83
Figure 3.43: Case 2b – forces on leg 1 (to side of arm, in front of torso). Again, V_y and D_y forces increase significantly during acceleration.	84
Figure 3.44: Simple model of platform (top view) for estimating the point at which combined linear and angular acceleration effects are greatest.	85
Figure 3.45: Force between outside leg and base for varying leg extension h and centre of rotation location d_p , $m_b = 60$, $m_{leg} = 5$, $c = h/2$, $v = 1.6\text{m/s}$. The force increases with decreasing leg extension; the maximum for each extension varies but lies towards the outside of the platform.	86
Figure 3.46: Case 3a, legs extended, arms horizontal – forces on leg 1 (outside leg, facing same way as torso).	87
Figure 3.47: Case 3b, legs retracted, arms down – forces on leg 1 (outside leg, facing same way as torso). The combined rotational and linear acceleration is much smaller than in 3a.	88
Figure 3.48: Case 3a, legs extended, arms horizontal - velocity and acceleration.	88
Figure 3.49: Case 3b, legs retracted, arms down - velocity and acceleration.	88
Figure 3.50: Case 3a, legs extended, arms horizontal - torque to hold leg position.	89
Figure 3.51: Case 3b, legs retracted, arms down - torque to maintain leg position. The torque peaks and levels out higher than case 3a.	89
Figure 3.52: Power for constant velocity extension of 1 m/s at body acceleration of 2 m/s with 15 kg load and leg mass of 1 kg.	92
Figure 4.1: Top view of platform showing stability parameters.	95
Figure 4.2: platform configuration showing centre of mass locations for stability analysis.	96
Figure 4.3: Torso and arms vertical, stability as a function of leg-extension angle at three different payloads.	100
Figure 4.4: Stability with payload of 3kg and varying vertical torso rotation (θ_{torso}), torso and arms horizontal, no acceleration, legs extended at 70°	101
Figure 4.5: Stability for varying payload and vertical torso rotation with torso and arms horizontal, no acceleration, legs extended at 70°	101

Figure 4.6: Stability for varying payload and vertical torso rotation with torso vertical, arm horizontal, no acceleration, legs retracted to 15°	102
Figure 4.7: Stability for varying payload and vertical torso rotation, torso vertical, arms horizontal, no acceleration, legs extended to 70°	102
Figure 4.8: Stability for varying leg extension and load, torso vertical, arm horizontal and extended over wide side ($\theta_{torso} = 90^\circ$), no acceleration.	103
Figure 4.9: Same as above but leg extension expressed in metres.	103
Figure 4.10: Stability for varying payload and vertical torso rotation, torso vertical, arms horizontal, acceleration at 2 m/s ² in the x-direction (0°), legs retracted to 15°	104
Figure 4.11: Stability for varying payload and vertical torso rotation, torso vertical, arms horizontal, acceleration at 2 m/s ² in the x-direction (0°), legs extended to 70°	105
Figure 4.12: Stability for varying payload and vertical torso rotation, torso and arms horizontal, acceleration at 2 m/s ² in the x-direction (0°), legs extended to 70°	105
Figure 4.13: Stability for varying payload and vertical torso rotation, torso vertical, arms horizontal, acceleration at 2 m/s ² in the y-direction (90°), legs extended to 70°	106
Figure 4.14: Stability for varying payload and vertical torso rotation, torso and arms horizontal, acceleration at 2 m/s ² in the y-direction (90°), legs extended to 70°	106
Figure 5.1: Rigid system model showing similarities to a slider-crank.	109
Figure 5.2: Static torque relationship for non-dimensionalized parameters.	111
Figure 5.3: Front view of drive unit in test stand with belt drive to left of and bevel gear above tire.	113
Figure 5.4: test stand with drive unit.	115
Figure 5.5: static force balance used to calculate wheel/ground friction factor.	116
Figure 5.6: Aluminium angle piece fixed in test stand to simulate a step edge.	118
Figure 5.7: Top view of skid marks and slight damage of floor under heaviest load; note large width of indentation and low depth due to wider contact area. Lower ruler scale in cm.	119
Figure 5.8: Side view of skid marks and slight damage of floor under heaviest load; note large width of indentation and low depth due to wider contact area. Ruler in cm.	120
Figure 5.9: Top view of indentation of floor under lightest load; note narrow width of indentation and high depth due to wider contact area. Lower ruler scale in cm.	120
Figure 5.10: Close-up of short-pile commercial carpet test surface.	121
Figure 5.11: experimental cart, side view with short wheelbase.	122
Figure 5.12: Improved system model with spring-damper wheel.	123

Figure 5.13: Energy for 16 mm step height, comparing rigid and elastic tire. The sub-figure on the right is an enlargement of the start of the step climb using the same units as the main figure. .	129
Figure 5.14: Radial (c) and vertical (d) spring compression, 16 mm step height, torque step from 0.73 to 3.91 Nm at 3 s, tire lifts off ground at 3.07 s.	129
Figure 5.15: Forces at front wheel resolved into vertical components for both spring-damper and rigid model, 16 mm step height. Torque step from 0.73 to 3.91 Nm at 3 s for elastic wheel, 0.73 to 4.63 Nm for rigid wheel. Elastic wheel reaches top of step at 3.66 s, rigid wheel at 3.86 s.	130
Figure 5.16: ND static torque compared to simulation results showing effect of different ND spring constants, where $K = k_c b/mg$ and all other ND groups are held at experimental conditions. K=146 is experimental setup.	131
Figure 5.17: The factor by which front-wheel drive torque is larger than all-wheel drive torque is shown here for different wheelbase lengths, wheel radius = 0.1 m.	133
Figure 5.18: Maximum platform tilt angle α for a step height of 3 cm.	134
Figure 5.19: Rear wheel set at the step corner; the tilt α causes higher loading at the rear.	135
Figure 5.20: Torque for surmounting step with all wheels driven, $r = 0.1$ m, $k_c = 62000$	136
Figure 5.21: ND static torque compared to simulation results for different situations. K for $b/r = 6.16$ is 30, for $b/r = 11.6$ is 56.	137
Figure 6.1: Suspension options.	141
Figure 6.2: Quarter-car model.	143
Figure 6.3: frequency response under maximum load for different damping constants at a spring constant of 120 kN (left) and for different spring constants at a tire damping constant of 250 Ns/m (right).	144
Figure 6.4: The damping c required for critical damping depends on the spring constant k and the system mass m , which are shown here for potential tires and payloads.	144
Figure 6.5 Second torso joint acceleration used to generate an example of a severe disturbance due to the upper-body.	145
Figure 6.6: Second torso joint angle and velocity used to generate upper-body disturbance.	146
Figure 6.7: pitch angle of base for torso disturbance (raising 3 kg from horizontal torso & arm position to vertical torso, horizontal arm) for different tire spring constants, constant damping at 200 Ns/m. Legs extended to 70° , torso facing narrow side.	146
Figure 6.8: angular acceleration due to torso disturbance as described above for different tire spring constants.	146

Figure 6.9: vertical position of top of base during torso disturbance as described above for different tire spring constants.....	147
Figure 6.10: vertical acceleration of top of base during torso disturbance as described above for different tire spring constants.....	147
Figure 6.11: Spring constant necessary to give the indicated suspension travel under maximum load (800N).....	148
Figure 6.12: Quarter-car model with added spring-damper element in addition to tire.....	149
Figure 6.13: Frequency response of quarter car with spring constant of 40 kN/m, showing effect of varying damping ratio from 0.64 to 1 at minimum load (left) and 1 to 1.57 at maximum load (right), tire spring constant is 150 kN/m, tire damping constant is 250 Ns/m.....	150
Figure 6.14: Frequency response of quarter car model for different suspension spring constants, critically damped for full load over four tires (as in Table 6.4), full load applied, tire 150 kN/m, 250 Ns/m.....	150
Figure 6.15: Frequency response at different loading, spring constant is 40 kN/m, damping constant is 2344 Ns/m (critically damped for maximum load over four wheels, 34.35 kg).....	151
Figure 6.16: Right (top) and left (bottom) suspension travel for torso disturbance (raising 3 kg from torso & arm in horizontally extended position to vertical torso, horizontal arm) for different spring constants, critically damped for maximum load over four wheels. Legs extended to 70°, torso facing narrow side.....	152
Figure 6.17: Base pitch angle for different spring constants during torso disturbance as above.....	152
Figure 6.18: Angular acceleration for different spring constants, torso disturbance as above.....	153
Figure 6.19: Vertical position of top of base for different spring constants, torso disturbance as above.....	153
Figure 6.20: vertical acceleration of base for different spring constants, torso disturbance as described above.....	153
Figure 6.21: Vertical base position and acceleration during torso disturbance at two different leg extensions with tire only (tire spring constant of 150 kN/m and tire damping constant of 250 Ns/m) and passive spring-damper suspension (spring constant of 40 kN/m, damping constant of 2344 Ns/m).....	154
Figure 6.22: Angular base position and acceleration during torso disturbance comparing tire only and passive spring-damper suspension at two different leg lengths as described above.....	155
Figure 6.23: horizontal position of base during torso disturbance comparing tire only to passive spring-damper suspension at two different leg lengths as described above.....	155

Figure 7.1: Wheel type footprint geometry.....	159
Figure 8.1: Top view of platform showing drive kinematic parameters, where the ‘cooperating manipulator’ is highlighted in orange.	161
Figure 8.2: One leg of the platform as a manipulator with end-effector at base centre.....	162
Figure 8.3: Drive rotational speed for different velocity angle (λ) and steering angle (φ) combinations at maximum x-velocity of 1.6. Peak is at 153 rpm.	169
Figure 8.4: Steering angle for steady-state pure angular motion is such that the wheel is perpendicular to a line radial to the base centre.....	170
Figure 8.5: Plot of (36) with $\dot{x}=1.6$, $h=0.308$ m: increasing the base rotational velocity ($\dot{\theta}$) increases drive speed ($\dot{\rho}$) and shifts the steering angle (φ) at which the drive speed reaches a maximum away from zero.	171
Figure 8.6: Required steering axis rotation speed to achieve x-velocity of 1.6 m/s for different steering angles (φ) and casters offsets (b).	172
Figure 8.7: Steering speed for angular velocity only at $h = 0.308$, $\dot{\theta} = 1.6/0.308$, for different caster lengths, b , and at different steering positions, φ	173
Figure 8.8: Maximum steering velocity as defined by the maximum linear velocity of 1.6 m/s in relation to the caster length b and the effective leg extension h	174
Figure 8.9: x-y path in global co-ordinates with reference numbers to motion described in Table 8.3.	182
Figure 8.10: x, y, θ velocity and acceleration trajectories (in the global frame).	183
Figure 8.11: Global x-position for different caster lengths (cm) showing the portion of the test trajectory where the base travels along the y-axis.	184
Figure 8.12: Global x-position for different caster lengths (cm), showing the last portion of the test trajectory where the base should return to origin.....	184
Figure 8.13: Platform decelerating in x-direction, then immediately accelerating in y-direction; final image at 7 s with 8 frames back to about 6.3 s. The path of base is shown in blue, where some deviation is apparent in the return motion (the lower path line) from the starting path that it should return on. Caster length of 0.02 cm.	185
Figure 8.14: Global x-velocity during caster reversal for different caster lengths (cm).	186
Figure 8.15: Global angular velocity ($\dot{\theta}$) during caster reversal (desired velocity is zero).....	186
Figure 8.16: Wheel 3 steering angle (φ) during caster reversal for different caster lengths (cm).	187
Figure 8.17: Wheel 3 steering velocity ($\dot{\varphi}$) during caster reversal, different caster lengths (cm).	187

Figure 8.18: Wheel 3 driving velocity ($\dot{\rho}$) during wheel reversal. different caster lengths (cm).	187
Figure 8.19: Wheel 3 steering torque at caster reversal for different caster lengths (cm).....	188
Figure 8.20: Wheel 3 drive torque at caster reversal for different caster lengths (cm).	188
Figure 8.21: Wheel 3 steering joint power during caster reversal, different caster lengths (cm).....	188
Figure 8.22: Wheel 3 drive joint power during caster reversal for different caster lengths (cm).....	189
Figure 8.23: Global x velocity during curve for different caster lengths (cm).....	189
Figure 8.24: Platform motion during curve acceleration. Final image at 10 s with 7 frames back to about 8.7 s. Path of base centre in blue.	190
Figure 8.25: Wheel 3 steering velocity during curve for different caster lengths (cm).....	190
Figure 8.26: Wheel 3 drive power during curve - close-up of negative maximum at 9.11 s.	191
Figure 8.27: Wheel 3 steering torque during curve for different caster lengths (cm).	191
Figure 8.28: Wheel 3 steering joint power during curve for different caster lengths (cm).	191
Figure 8.29: Platform during combined linear and angular velocity phase showing path of base and motion history at 0.1 s intervals, caster of 2 cm, $h = 0.578$ m.....	192
Figure 8.30: Global x velocity during combined linear and angular velocity.	193
Figure 8.31: Wheel 3 steering angle during combined linear and angular velocity.	193
Figure 8.32: Wheel 3 steering velocity during combined linear and angular velocity.	193
Figure 8.33: Wheel 3 steering joint torque during combined linear and angular velocity.	194
Figure 8.34: Wheel 3 steering joint power during combined linear and angular velocity.	194
Figure 8.35: Top, front and side view of wheel unit configuration showing vertical and horizontal offset necessary for lower leg joint to clear caster wheel envelope. Caster arm in green with 2 cm caster. Values in (m).....	195
Figure 8.36: Platform during linear deceleration with constant angular velocity at 13.4 s; freeze frames at ~ 0.1 intervals back to 13.0 s. Path of wheel 2 steering axis in blue. 2 cm caster length, $h = 0.578$ m.....	198
Figure 8.37: Velocity, torque and power for drive joints of all wheels with caster length of 2.0 cm, $h = 0.578$ m, no payload.	199
Figure 8.38: Velocity, torque and power for steering joints of all wheels with caster length of 2.0 cm, $h = 0.578$ m, no payload.	200
Figure 8.39: Wheel 3 drive torque and power (joint velocity is nearly identical), comparing no payload to maximum payload with acceleration, $h = 0.578$ m, caster of 2.0 cm.	201
Figure 8.40: Wheel 3 drive joint velocity, torque and power, comparing the smallest wheel base ($h = 0.308$ m) to the largest ($h = 0.578$ m) at a payload of 15 kg. Caster length of 2.0 cm.....	202

Figure 8.41: Wheel 3 steering joint velocity, torque and power, comparing the smallest wheel base ($h = 0.308$ m) to the largest ($h = 0.578$ m) at a payload of 15 kg. Caster length of 2.0 cm	203
Figure 8.42: Change in angular velocity and acceleration with smaller wheelbase.	204
Figure 8.43: The small wheelbase results in large wheel slip.....	204
Figure 9.1: Potential laser scanner coverage with a) 3 and b) 4 Hokuyo units.....	207
Figure 9.2: Base proper footprint dimensions.....	212
Figure 9.3: Comparison of heights of system and 95% male.	214
Figure 9.4: Chosen base shape and footprint in retracted as well as extended configuration compared to a human cross section and standard door sizes.	217
Figure 9.5: clearance (mm) when travelling over the edge of a 15° ramp with a 2 cm sill.	218
Figure 10.1: Torso upright and facing the narrow side with the legs retracted for best manoeuvrability through narrow spaces.	221
Figure 10.2: Torso upright and facing the wide side with the legs retracted.	222
Figure 10.3: Top view of system with legs retracted.	223
Figure 10.4: Two legs extended with torso over narrow side; configuration for best reach.....	224
Figure 10.5: Two legs extended and torso over wide side reaching down to the ground.	225
Figure 10.6: Top view of two legs extended and torso over wide side.....	225
Figure 10.7: Side view of base with cover removed; battery place-holders in green, computer place- holders in brown.	226

List of Tables

Table 1.1: Lightweight Robot III specifications.....	3
Table 1.2: Segway Robotic Mobility Platform specifications.....	16
Table 1.3: Requirements for a hypothetical universal service robot	20
Table 1.4: Goal prioritization	22
Table 1.5: Technical requirement summary, ordered by importance score.	25
Table 1.6: Width and breadth from anthropometric data[] and Justin’s specifications.....	28
Table 2.1: Description of criteria for configuration evaluation.....	35
Table 3.1: Variable footprint mechanism design options.....	48
Table 3.2: Horizontal extension distance (x in cm) for different leg lengths and extension angles	57
Table 3.3: Simulation parameters.....	71
Table 3.4: Linear acceleration simulation cases.....	73
Table 3.5: angular acceleration simulation cases	79
Table 3.6: Centripetal forces, $m_b=45 + 50 + 3$, $m_{leg} = 5$, $c = h/2$, $v = 1.6$	86
Table 3.7: Centripetal forces, $m_b=45 + 50 + 15$, $m_{leg} = 5$, $c = h/2$, $v = 1.6$	86
Table 3.8: Combined linear and angular acceleration simulation cases.....	87
Table 3.9: Maximum forces for simulated cases. Forces are resolved in the base; positive x is away from base, positive z is down	90
Table 4.1: Simplified Arm & Torso geometry	97
Table 4.2: Stability values for different configurations.....	107
Table 5.1: Wheel specifications.	112
Table 5.2: Drive unit specifications.....	114
Table 5.3: Coefficients for relationship between input reference voltage and wheel output torque at different wheel speeds.	115
Table 5.4: drive wheel friction on different surfaces - experimental results.....	117
Table 5.5: Friction factors from literature.	119
Table 5.6: Experimental cart specifications.	122
Table 5.7: Experimental and simulation results.	130
Table 5.8: Cart parameters to represent upper-body and base as designed.....	133
Table 5.9: Friction factor required to support torque for climbing selected step heights.....	138
Table 6.1: Comparison of suspension options.....	141
Table 6.2: Different tire spring and damping constants from literature.	142

Table 6.3: Maximum and Minimum angular and vertical base acceleration do to torso disturbance for different tire spring constants, damping 200 Ns/m.	147
Table 6.4: Suspension travel at maximum load for different spring constants.	148
Table 6.5: Maximum and minimum angular and vertical acceleration do torso disturbance with passive spring-damper suspension and varying spring constants.	151
Table 6.6: Maximum and minimum angular and linear base acceleration do to torso disturbance for tire only and passive spring-damper suspension at leg extensions of 50° and 70°.	156
Table 6.7: candidate wheel properties.	157
Table 7.1: Summary of attributes of the different wheel types.	158
Table 8.1: D-H parameters for leg ‘manipulator’	163
Table 8.2: Simulation parameters	180
Table 8.3: Test trajectory description	181
Table 8.4: Maximum velocities, torques and power for drive and steering joints, absolute values at different payload and leg extensions, caster length of 2 cm.	197
Table 9.1: Potential laser scanner with volume, mass and power specifications [110].	206
Table 9.2: Potential computer configuration with volume, mass and power specifications.	208
Table 9.3: System peak and average power requirements.	209
Table 9.4: Specifications of potential battery, Ultralife UBI-2590 [113].	210
Table 9.5: Energy supply to meet requirements and its mass.	210
Table 9.6: Volume of base proper remaining after electronics and energy storage.	213
Table 9.7: The merits of different base shapes, with figures indicating wheel positions.	215
Table 9.8: Footprint dimensions related to a square footprint of the same perimeter.	216
Table 10.1: Specifications of system as proposed.	220

Chapter 1

Introduction

1.1 Motivation

In general, the motivation in combining robotic manipulators with mobile platforms is to create a system with a much larger workspace, thereby improving the manipulator's flexibility in terms of both potential applications and where they can be performed. Locomotion coupled with manipulation allows the robot to perform new tasks that require transportation of objects and manipulation during locomotion, such as sweeping or wiping an area [1]. It also can increase end-effector performance through increased acceleration, velocity and force. In service robotics, mobility makes robots much more useful in performing tasks in an environment where interaction with humans is required. More general background can be found in the literature review, section 1.3.

A mobile platform to carry the existing upper-body humanoid, known as Justin (see 1.2.1), is the primary need of the German Aerospace Center (*Deutsches Zentrum für Luft- und Raumfahrt*)'s Robotics and Mechatronics Institute (DLR RM). This will allow the expansion of research and experimentation into the challenging new areas that mobility brings such as mobile manipulation and navigation. A recent extensive literature review (section 1.3) revealed that no existing mobile platform adequately meets the needs of the DLR RM. Developing a custom system allows for harmonization with Justin such that its functionality and strengths are not hindered. Furthermore, the design should serve as a demonstration of DLR RM technology. Thus, it should be tailored to complement the existing strengths in lightweight design, highly dynamic response and the ability to adapt to the environment using force sensing, torque control and programmable impedance/stiffness. Therefore, this thesis tackles the problem of designing a custom mobile platform that gives Justin the desired mobility with the least performance restrictions.

1.2 Background

1.2.1 Existing Manipulation System

In May of 2006, the DLR RM first presented Justin, a humanoid two-arm system capable of dexterous manipulation. Mounted on a table, it consists of a torso, two arms with dexterous hands, and a head housing a vision system. It has 43 degrees-of-freedom (DoF) [2]. The total mass of the upper body system without any payload is 50 kg. Figure 1.1 shows Justin in different kinematic configurations.

1.2.1.1 Arms & Hands

The robotic arm design first existed as an independent 7 DoF manipulator known as the *DLR Lightweight Robot III*, which arguably has the best force-to-weight ratio for a robot of its size – it can lift its own weight [3]. Some dynamic specifications of the arm are given in Table 1.1. The hands

have 13 DoF and weigh 1.8 kg each [4]. This weight must be considered as part of the arm payload. Each of the four fingers can exert 30 N perpendicular to its surface at the fingertip.

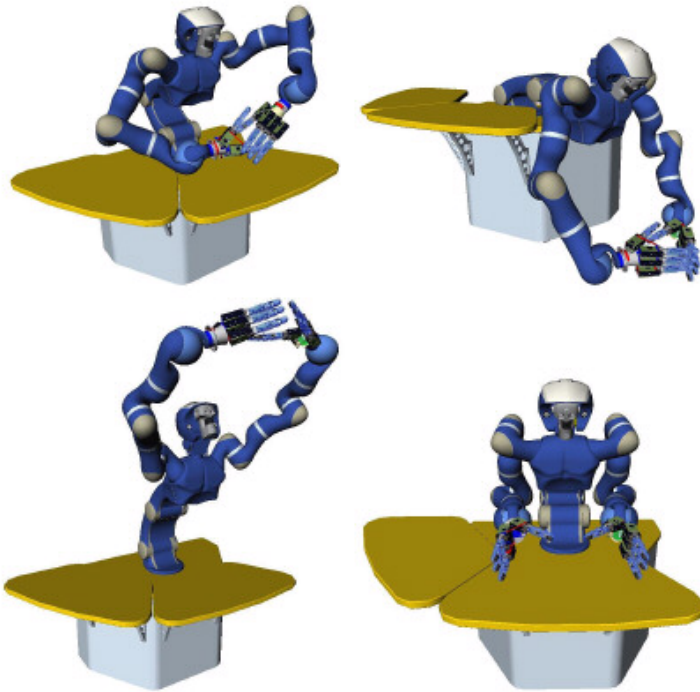


Figure 1.1: Justin on its table mount shown in different configurations [2].



Figure 1.2: Lightweight Robot III

Table 1.1: Lightweight Robot III specifications

Mass	14 kg
Payload	15 kg, 7 kg at peak velocity
Joint speed	120 – 180 deg/s
Overall length	1226 mm
Typical power use	100 W
Control modes	position, torque, impedance

1.2.1.2 Torso

The torso has 3 DoF: one vertical rotation axis that can rotate $+200/-140^\circ$ and two actuated pitch axes. The first pitch axis can rotate $\pm 90^\circ$ from upright. The second pitch axis has a maximum rotation of 135° . Its minimum rotation is dependent on the first pitch axis such that the minimum angle is the maximum of 0° and the negative of the first pitch axis angle. The upper body is on a fourth axis parallel to axes 2 and 3 is passively linked in such a way that the chest always remains perpendicular to the base of the torso. This configuration allows for a ‘squat’ position with a lower centre of gravity and an extended position where the reach of the arms is about 2 m with the torso mounted on a 60cm platform (Figure 1.3). Definitive operating velocity limits have not yet been determined, but are estimated at about 100 deg/s. The current maximum operation range is around 50 deg/s [5]. The torso utilizes similar actuation and control strategies as the arm [2].

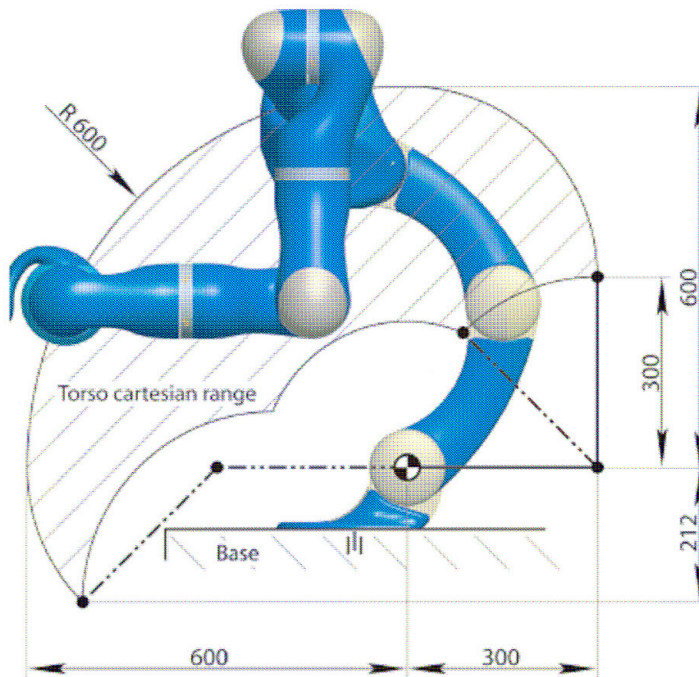


Figure 1.3: The torso's workspace [2], units are in (mm).

1.2.1.3 Pan/Tilt Head with Vision System

The DLR existing 3D imaging unit, which combines a laser-range scanner, a laser-strip profiler, and a stereo camera, is mounted on a pan-tilt unit. It provides a field of view well suited for manipulation in front of and towards the base of Justin, with overlapping ranges from the three sensors between 50 and 2000 mm. This is extended by the panning and tilting of the head unit. As designed, the unit weighs 2.5 kg.

1.2.2 Previous Mobile Manipulator

In 2004, the DLR RM presented a mobile manipulator [6] consisting of a single previous generation DLR LWR-II arm and a vision system mounted on an omnidirectional mobile platform with a footprint of 56×63 cm. It uses four steered and driven wheels with 6" tires. The platform was developed by the Technical University of Munich and uses the same locomotion system as the robot ROMAN [7]. Although no mass data is available, a rough estimate by the author suggests a mass of over 100 kg.



Figure 1.4: DLR Robutler mobile manipulator with previous generation light-weight arm.

1.3 Literature Review

There have been numerous efforts to increase the workspace of a robotic manipulator by placing it on a mobile base, ranging from simple single-arm manipulators on statically stable wheeled bases to fully legged humanoid robots. Reviewing previous designs and their evaluations will help to determine the best design for Justin. Platform concepts are categorized into static stability, dynamic stability, and hybrid stability in sections 1.3.1, 1.3.2, and 1.3.3 below. A review of stability measures for mobile manipulators follows in section 1.3.4. Also, a summary of past and present robots is provided in Appendix A.

1.3.1 Statically Stable Platforms

A platform that is statically stable requires no control or force input to remain stable and stationary. Statically stable bases can be equipped with a variety of wheels or tracks for propulsion and as points of support. Four or more ‘legs’ mimicking human or animal appendages can also be used, whereby at least three must be touching the ground at all times to ensure static stability. A total of six legs is commonly used. A base with more than three points of support is hyperstatic and requires some form of suspension if all points are to maintain ground contact over uneven terrain [8].

1.3.1.1 Locomotion

Three measures are used to quantify a robot’s locomotion ability: the degree of mobility, the degree of steerability, and the degree of manoeuvrability [9]. The platform’s number of independent motion constraints determines the degree of mobility. For a planar workspace with 3 degrees of freedom (DoF), the degree of mobility is

$$\delta_m = 3 - \text{rank}[C_1(\beta_s)]$$

where C_1 is a matrix formed from the constraint equations for all the wheels, such as rolling and sliding constraints, and β_s represents the variable steering angles. It has dimension of the number of differentiable degrees of freedom, that is the number of degrees that can be directly manipulated without first requiring time for re-orientation. Similarly, the degree of steerability is determined by the number of independently controllable steering parameters,

$$\delta_s = \text{rank}[C_{1s}(\beta_s)] \quad (1.1)$$

where C_{1s} is a matrix formed from the steering constraint equations. Together, they form the degree of manoeuvrability:

$$\delta_M = \delta_m + \delta_s \quad (1.2)$$

A mobile robot can be omnidirectional, which means that it can move in any direction regardless of the robot’s orientation – it has a manoeuvrability of $\delta_M = 3$. It may however need to take time to reorient its wheels in order to deal with non-continuous path curvature. If the robot is holonomic, its constraints rely only on position, not derivatives of position. A non-holonomic robot has constraints that rely on derivatives that cannot be integrated to form a position constraint. Thus an omnidirectional holonomic robot can move in any direction at any time. Holonomic omni-

directionality allows the most efficient trajectories to be executed and offers the most flexibility with respect to end-effector position during motion.

An additional criteria for an omnidirectional platform is its degree of isotropy: a fully isotropic platform can move in any direction at equal velocity regardless of platform configuration; a platform that is non-isotropic loses some of the advantages of holonomic omnidirectionality up to the extreme case where the possible velocity in one or more directions is zero and the platform is no longer holonomic. Thus isotropy is considered a desirable quality [10].

1.3.1.1.1 Fixed Standard Wheels

Fixed standard wheels have only 1 DoF. Sideways velocity is not permitted, which is a non-holonomic constraint. This has the advantage that the wheel counters lateral forces passively, but it restricts mobility. In order to achieve 3 DoF in the plane, fixed wheels can either be combined with steered standard wheels to achieve car-like motion, or in a differential drive configuration, with two standard wheels that are located coaxially. The differential robot steers by applying a different velocity to each wheel to cause body rotation. While both achieve a manoeuvrability value of two, the differential drive achieves this with a mobility of two versus a mobility of only one for the combination of a fixed wheel with a steered wheel, making the differential drive the more common choice for mobile robotics. If the wheel axis goes through the vertical centerline of the robot, the robot can turn on the spot by driving the wheels in opposite directions.

1.3.1.1.2 Steered Standard Wheels

Compared to the fixed standard wheel, a steered standard wheel has an additional degree of freedom in the form of a vertical axis of rotation that intersects the horizontal axis. This allows the wheel to be oriented without changing its position on the ground. If a platform is created with steerable wheels and no fixed wheels, it is omnidirectional (but not holonomic), as shown by Bétourné and Campion [11]; a two-wheeled robot always has a mobility of one, a three-wheeled robot where the wheel centers are not aligned has a mobility of one during compatible wheel configurations. Only two wheels are kinematically necessary; if additional steerable wheels are used, the platform becomes redundant and co-ordination is needed to ensure the wheels are all aligned with one centre of rotation. A singular configuration occurs when the wheel axes coincide. Bétourné and Campion also look at the dynamics of such a platform when the constraints are not perfectly satisfied by modeling the ground-tire interaction friction forces and torques [12]. Alexander and Maddocks look at the kinematics of standard wheeled platforms in general and present a quasi-static model that includes slip occurring due to alignment error [13].

1.3.1.1.3 Differentially Steered Dual Standard Wheels

Bétourné and Fournier propose two differentially driven wheels close together rotating around a single axis in order to avoid the high scrubbing friction of steering a stationary standard wheel. They find such a wheel to be kinematically equivalent to a standard wheel with the same geometry [14].

Borenstein uses an instrumented compliant linkage between two sets of dual standard steered wheels to reduce odometry error due to slippage that always occurs in real-world conditions [15].

1.3.1.1.4 Synchronized Steered Wheels

By linking three or more steered wheels such that they are always parallel to one another, only one motor each is needed for steering and driving. However, the platform orientation cannot be changed unless an additional actuator is used to rotate it relative to the wheels [8].

1.3.1.1.5 Free Castor Wheels

Essentially a steered standard wheel without actuation that has a horizontally offset steering access, free caster wheels are used as passive supports. Theoretically, castor wheels do not add any constraints. However, they do cause disturbances when they rotate around their vertical axis, particularly when the direction of travel is reversed.

1.3.1.1.6 Powered Caster Wheels

In a powered caster, the vertical steering axis and the horizontal drive axis are actuated. Creating a holonomic omnidirectional platform with powered castors is possible, such as the Nomad XR4000 [16], but, because of the extra degrees of freedom that create an over-constrained condition, it requires precise control coordination [17] and the wheel contact point is subject to high scrubbing forces during steering [18]. Holmberg and Khatib claim that powered casters are an effective way to create a holonomic vehicle because they allow the use of standard pneumatic tires with their associated suspension and traction properties. Such tires have a continuous well-defined contact point path and thus no vibrations, as well as good step climbing capability [16].

Mori et al. propose a caster wheel which they use in their omnidirectional ODV9 platform that is actively driven and steered by only one motor; a brake unlocks the steering axis to switch between modes [19]. Mori et al. also look at the response of the steering axis when the wheel climbs a small step and the potential of adding another vertical axis rotational joint in the caster to facilitate changing the width of the platform as shown in Figure 1.5 [20].

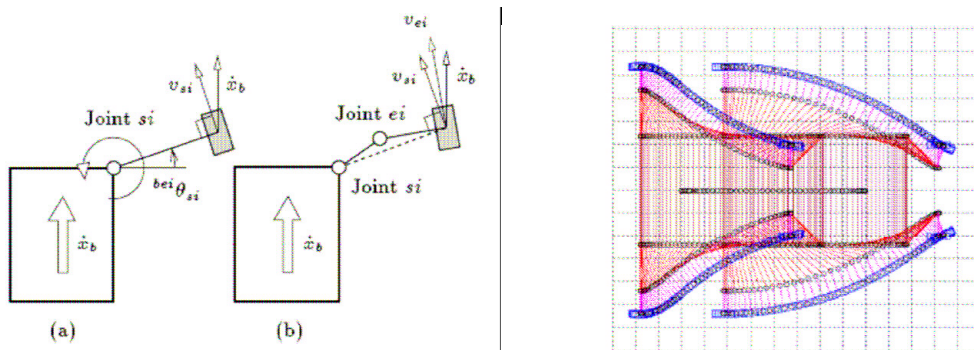


Figure 1.5: Mori et al. add another joint (a to b on L) to change the platform footprint (R)[20].

Lee et al. develop a control system for their three-wheeled powered-caster platform that has two modes, one for omnidirectional motion, the other for improved stability. In the latter mode, one caster arm is aligned *towards* the direction of motion, thus increasing the footprint of the platform [21].

1.3.1.1.7 Split Offset Caster Wheels

A split-offset caster has a caster offset like a normal caster but instead of one wheel at its end there are two wheels separated by an offset distance. This is supposed to greatly reduce scrubbing of the tire during turning because the two wheels on the same axis some distance apart roll rather than scrub during steering [22]. Jung and Kim look at three different ways and the conditions that need to be fulfilled to augment the mobility of a mobile platform with $\delta_m=2$ through the addition of another joint to create an omnidirectional vehicle; they find the split-offset caster to be best [23].

Wada et al.'s dual-wheel caster drive uses two parallel differentially driven wheels mounted on a driven rotational stage that acts as the caster arm (Figure 1.6). They go on to propose a design where the caster wheels are mechanically synchronized such that drive and steering are decoupled and require only one motor each, which they use together with an independent motor to orient the top of the base to create a holonomic omnidirectional 'synchro-caster drive' platform [24]. While this reduces the number of actuators and control complexity required, the mechanical linkage is quite complex and voluminous. Han et al. develop a platform using the same wheel concept, requiring only two wheel units by placing a passive caster at the steering axis to provide additional support [25]. Yamada et al. find a dynamic model for a platform employing two sets of offset casters and run a prototype with resolved acceleration control [26].

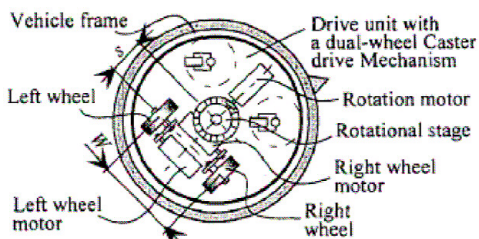


Figure 2: Vehicle with a dual-wheel caster mechanism

Figure 1.6: Wada et al.'s caster drive mechanism [24].

Yu et al. have a very similar two-wheeled caster design called the Active Offset Split Caster (ASOC) [22]. They find that by actuating each wheel separately, no additional motor is needed to control the steering axis. Spenko et al. add a passive horizontal rotational joint in the offset to allow both wheels to maintain ground contact on uneven terrain [18]. They find the ASOC design to have reduced torque and power requirements for steering compared to a conventional powered caster, with a larger reduction for a larger distance between wheels and for more elastic tire material, which is more likely to roll rather than scrub in the ASOC. Unlike Yu et al., Spenko et al. do consider not just rolling friction but also still some scrubbing with the ASOC when it rotates.

1.3.1.1.8 Omnidirectional Wheels

Omnidirectional wheels allow motion in any direction, and can independently control their heading, speed and orientation, allowing for a fully holonomic platform. They can be classified into two types; 'universal wheels' which use rollers mounted at an angle inside a larger wheel (Figure 1.7), and ball wheels, which use a spherical ball constrained by some sort of mechanism.



Figure 1.7: A pair of Omniwheel universal wheels from Kornylak Corporation [27].

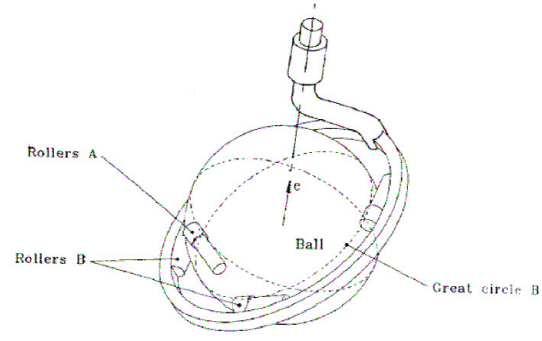


Figure 1.8: West and Asada's ball wheel mechanism [33].

The ‘universal wheel’ exists in several variations that depend on the size and orientation of the rollers. The ‘classical’ universal wheel has rollers perpendicular to the wheel axis; three of these in a triangle pattern provide holonomic omnidirectional motion. Such a wheel suffers from vibration introduced when successive rollers contact the ground [8] and is sensitive to debris or small floor imperfections [18]. Putting two classical universal wheels side-by-side improves ground contact smoothness but creates horizontal vibration as the contact point switches from one wheel to the other [28]. The Swedish or Mecanum wheel has the rollers at a 45° angle compared to the classic universal wheel, providing for smoother ground contact but creating lateral forces and vibrations, which is why such wheels are usually used in opposing pairs [28]. Asama et al. have developed a mechanism to drive a platform with four Swedish wheels using three actuators in a decoupled manner [29], however the mechanism, which uses several differentials, appears quite bulky.

In their review of wheel types, Ferriere et al. decide universal wheels are better than offset caster wheels because only three motors are required, whereas with caster wheels, at least one must be actuated for steering as well to avoid singularities (for a minimum of 4 actuators). As drawbacks of universal wheels, they mention the load capacity, the low bump height that can be surmounted, which is a function of roller rather than wheel diameter, and the vibrations that occur due to the gaps between rollers. [28].

The ball wheel has limited traction due to its small ground contact area [8], but it does not have the very limited obstacle height restriction and limited load capacity of the universal wheel roller. It is usually driven in an inverse mouse ball fashion to provide full motion control, but other drives have been tried. Ferriere et al. developed a ball wheel driven using a universal wheel and supported by two or three ball bearings, which allows slip-free control of the wheel with reduced vibration, however the mechanism is bulky [30, 31, 32]. West and Asada use a ring with rollers as shown in Figure 1.8 to create a driven and a free direction for the ball wheel [33].

Lee states that previous ball wheel approaches that have one constrained and one unconstrained direction of motion, relying on three cooperating wheel units to achieve 3 DoF motion, are not robust on irregular ground where some units may lose contact. They develop a system that drives the ball wheel using redundant standard wheel actuators. These change their contact pressure on a polymeric ball wheel based on a weighted torque optimization method. A prototype wheel unit with 30.5 cm radius is capable of surmounting 10 cm steps, a 0.33 ratio [34].

Many other people have created improved or novel omnidirectional wheels. Pin uses two truncated spheres, each with two rotational axes, essentially approximating a ball wheel but with better drivability and smoother operation than a universal wheel [35]. The mechanism has a fairly large footprint due to the pair of semi-spheres needed for each unit. Diegel et al. improve the Swedish wheel by allowing the rollers to be locked and their angle changed, thus reducing the high drag losses in both straight and diagonal operation [36]. Byun et al. use alternating inner and outer rollers (Figure 1.9) to create a rolling surface without any gaps for their continuous alternating wheel (CAW) [37].

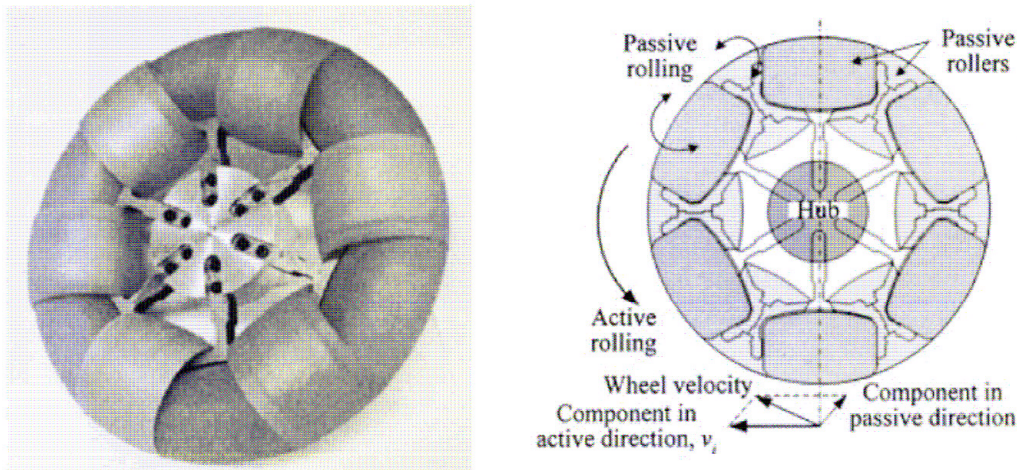


Figure 1.9: Continuous Alternating Wheel by Byun et al.

Existing unconstrained wheel types all suffer from increased complexity, generally have limited ground clearance and reduced suspension options, plus their unconstrained nature means they cannot be used to passively offset forces during cornering or manipulator movement [8].

1.3.1.1.9 Wheel-Leg Hybrids

Some groups have looked at a hybrid of wheels and legs with one or more active DoFs in an effort to combine the efficiency and speed of rolling with the flexibility of walking. The Workpartner [38, 39] is a centaur-like vehicle with four wheels mounted at the end of four legs, each with three DoF (Figure 1.10). The vehicle can operate in a rolling, walking and combination mode.

The T-3 uses six actively steered and powered wheels on vertical prismatic legs, allowing it to move omnidirectionally and adjust its posture in concert with force-feedback (Figure 1.11) [40].

The “Octal Wheel,” with eight wheels in pairs can climb steps by rotating one wheel up relative to the other using an actuated arm that pivots between the centre of the two wheels (Figure 1.12) [41].



Figure 1.10: Workpartner robot [38].

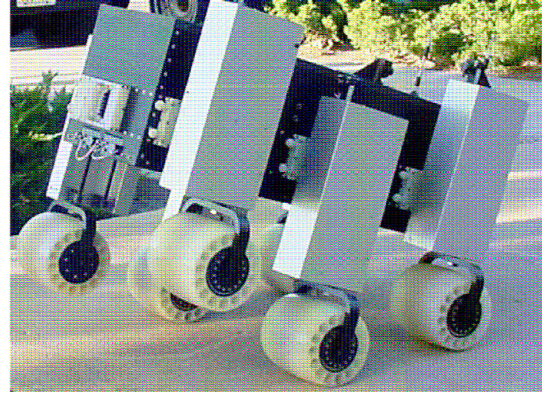


Figure 1.11: T3 platform with wheels on prismatic joints [40].



Figure 1.12: Octal Wheel robot [41].

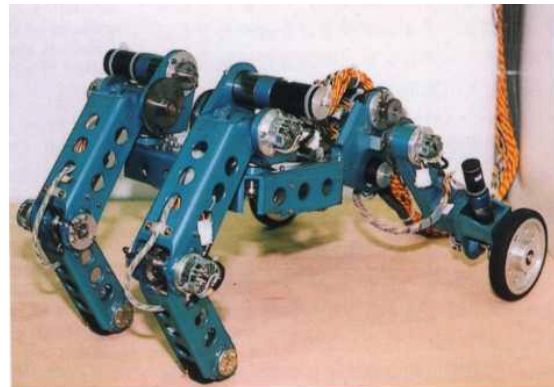


Figure 1.13: The Walk'n roll robot [42].

The “Walk’n roll” robot has two front legs with three joints and one lockable passive wheel each and two rear legs with one joint and one actively driven wheel each [42]. It is capable of operating in wheeled mode, a hybrid mode, and a stair climbing mode. Chugo et al. develop an omnidirectional robot with seven universal wheels and a passive rocker-bogie suspension that can climb steps up to 150 mm, although it must align the bogie with the step to do so (Figure 1.14) [43].

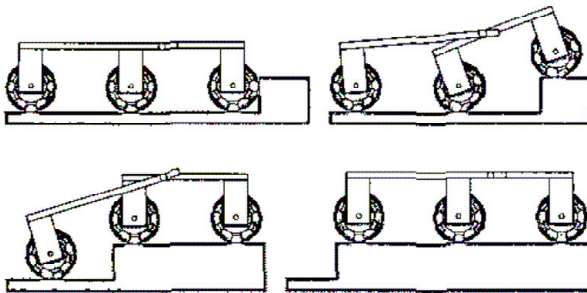


Figure 1.14: Chugo et al’s rocker-bogie platform climbing a step [43].

A centaur robot proposed for the NASA Robonaut uses a 3 DoF waist to move its upper body and thus shift the centre of gravity of the four-legged, four-wheeled vehicle, allowing one wheel to be lifted while the other three maintain static balance. Each leg has 1 rotational DoF on a common axis to provide active suspension and each wheel is actively steered [44].

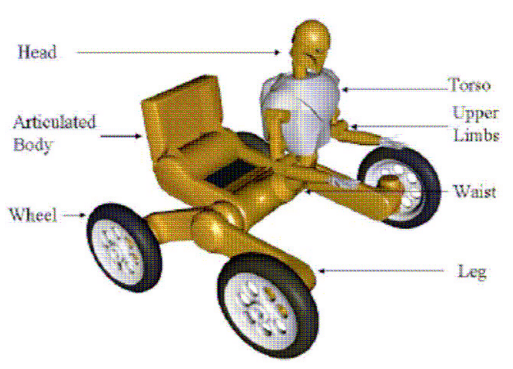


Figure 1.15: NASA Robonaut Centuar concept [44].

Another benefit of mounting wheels on legs that has not been greatly explored is the potential to increase the footprint and the static stability by extending the legs outward from the centre of mass. Finding that stability and manoeuvrability are conflicting requirements, Wada et al. use four omnidirectional ‘ball wheels’ at the end of a cross-shaped mechanism (Figure 1.16) to create a powered wheelchair platform with variable footprint geometry [45]. In addition to improving the static stability, the variable footprint allows a reduction in width for passing through narrow doorways. Furthermore, it causes a change in gear ratio because of the mechanism’s behaviour as a continuously variable transmission (CVT). The footprint is changed using the extra degree of freedom available in the drive wheels.

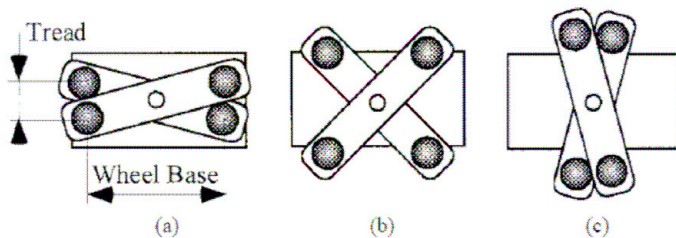


Figure 1.16: Wada et al.’s variable footprint mechanism in a) narrow, b) isotropic and c) wide configuration [45].

Song and Byon have a similar idea, creating a platform with ‘steerable omnidirectional wheels’ (OMR-SOW), that use the ‘continuous alternating wheel’ mentioned earlier connected to a steering arm mechanism (Figure 1.17). It also acts as a continuously variable transmission [46].

A variable footprint is implemented to improve compactness during transportation on the Nomad rover developed at CMU, which uses two pairs of four-bar linkages to not only move the wheels outward but also to provide for steering during part of the linkage travel (Figure 1.18) [47].

These hybrid approaches, though very different in nature, show some of the possible advantages to combining wheeled propulsion with an additional ‘leg’.

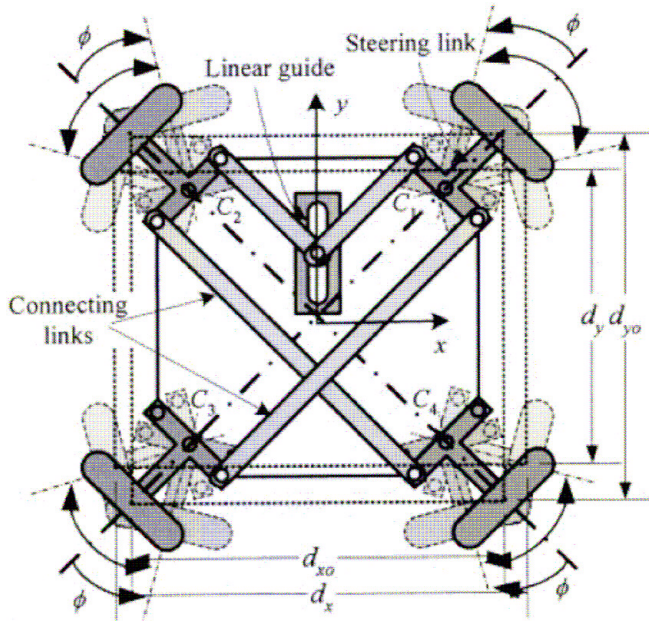


Figure 1.17: Variable wheel arrangement mechanism of OMR-SOW [46].

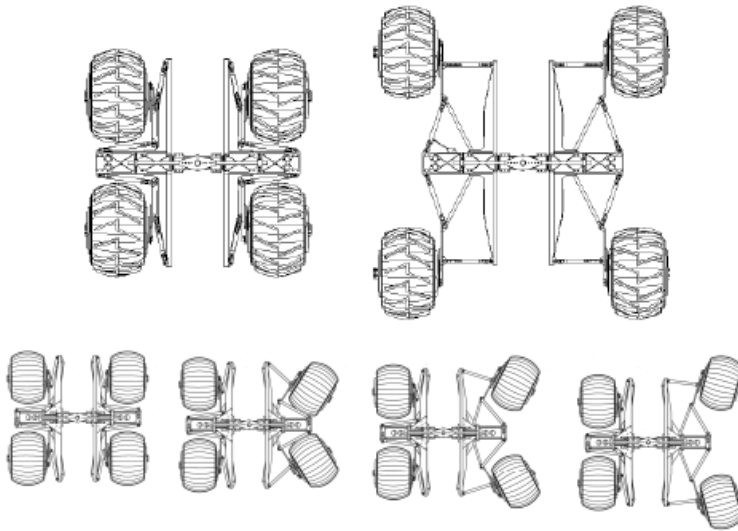


Figure 1.18: Nomad's transforming chassis in the compact (T-L) and deployed (T-R) with the steps of deployment (B) [48].

1.3.1.1.10 Tracks

Tracks can be used instead of wheels. They provide better grip but also have higher resistance and can cause damage to the terrain. Helios-VI (Figure 1.19) is a tracked vehicle that can ascend and descend stairs [49]. It maintains balance while on an incline by dynamically shifting the load it is carrying. Azimut (Figure 1.20), with 12 DoF in its legs, can even go up circular staircases [50].



Figure 1.19: HELIOUS-VI tracked robot [49]



Figure 1.20: Azimut tracked robot [50]

1.3.1.2 Statically Stable Mobile Manipulators and Humanoids

The simplest platform to implement, static stability requires a base that is some combination of a large footprint, a heavy mass, and a low centre of mass. Hermes (Figure 1.21) is such a system created from commercially available parts with a base mass of 200 kg [51]. Older projects combined commercial manipulators with commercial bases, such as the use of a Nomad XR4000 platform with a PUMA 560 manipulator (Figure 1.22) [16].



Figure 1.21: HERMES, a statically stable humanoid [51].



Figure 1.22: Nomadic XR4000 platform with PUMA 560 manipulator [16].

1.3.2 Dynamically Stabilized Platforms

Dynamically stabilized platforms can take different forms: two wheel dynamic, single ball dynamic, two-legged (biped), multi-legged, or some kind of hybrid. All dynamic platforms use motion and acceleration to move the centre of mass and counteract overturning forces. Thus, the top of the platform and any mounted manipulator is disturbed.

1.3.2.1 Locomotion

1.3.2.1.1 Two-wheel

Two-wheel dynamic balance acts by stabilizing what is essentially an inverted pendulum in one plane; in the other plane, orthogonal to the ground, the platform is statically stable. Turning is accomplished through differential drive steering. This form of balance has been popularized by the Segway, which is now also available as the Segway RMP or robotic mobility platform (Table 1.2, Figure 1.23) [52] and is being used at numerous US institutions [53]. Brooks remarks upon the following benefits of such a dynamically stable platform: the weight can be put up high, a small footprint is possible, it can tilt forward, and it is resistant to perturbations [54]. Other groups [55, 56] have found the following issues with the RMP:

- Potential for catastrophic failure
- Platform tilts up to 45°; the mounted manipulator and its sensors must be able to deal with this tilt, which can be problematic for the end-effector
- Balance system reacts negatively to contact with fixed objects
- Higher power use than static base
- Proprietary design

Other groups have also created mobile robots using two-wheel dynamic balance, such as the robot JOE and the Toyota Work Partner robot [57, 58]. Thibodeau et al., developers of the uBot, show how control of the posture of the whole body by tilting at the wheels can aid in applying force to the environment by using its mass and traction with the ground. These benefits are shown to increase with centre of mass height and decrease with increasing mass [59]. Hitachi has created a two-wheel dynamic balance humanoid with an additional rotational active degree of freedom perpendicular to the drive axis (Figure 1.24) to allow the robot to tilt sideways, for instance to lean into turns [60].



Figure 1.23: The NASA Robonaut mounted on the Segway RMP with custom ‘training wheels’ [55].



Figure 1.24: Hitachi’s dynamic balancing two-wheeled robot with side-ways tilt joint [60].

Table 1.2: Segway Robotic Mobility Platform specifications.

Model	Segway RMP 200
Mass	64 kg
Drive Motors	4 Nm peak torque, 1.65 rated torque
Geartrain	24:1
Maximum Acceleration	1.96 m/s
Maximum Payload	45 kg
Maximum Tilt Angle	45°
Cost (2006)	US\$ 18,000

1.3.2.1.2 Single-wheel

The ‘Ballbot’ developed at CMU [61] uses only a single powered spherical wheel that must be dynamically balanced in all directions (Figure 1.25). It is holonomic and has a very small footprint. Nakajima et al. take a slightly different approach with a single wheel that is ‘rugby ball’ shaped; tilting sideways makes the robot steer [62].

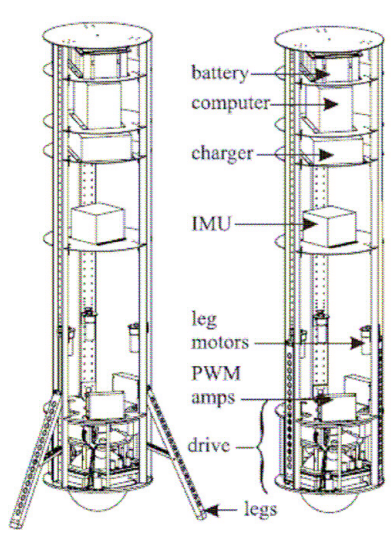


Figure 1.25: Ballbot with kickstands deployed (L) and balancing on the single wheel (R) [61].

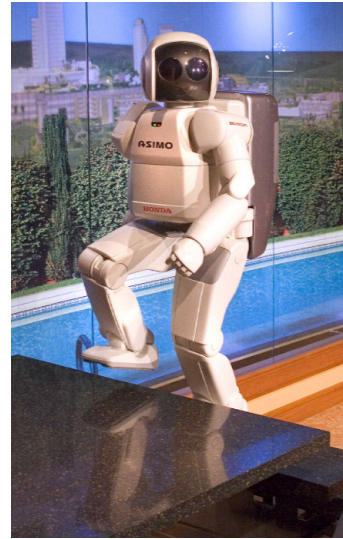


Figure 1.26: The Honda Asimo can walk up stairs [63].

1.3.2.1.3 Legged

Dynamic legged platforms typically have a biped configuration and attempt to mimic human walking. They are highly complex but are well suited to human environments. Some have been demonstrated to be able to go up and down stairs (Figure 1.26) and over uneven terrain [63, 64]. Nevertheless, the state of the art is still far away from the flexibility of human walking. Top speeds of 6 km/h have been reached [63], but energy usage is high. Some consider a bipedal walking robot unnecessarily complex, heavy and power intensive due to the large number of DoFs and associated actuators [65].

Approaches that mimic natural walking and capture some of the energy in a footstep for the next step have not yet been implemented in a full humanoid form. McNeill Alexander investigated the mechanical cost of transport, defined as $(energy\ cost)/(body\ weight \times distance\ travelled)$, which is about 0.05 for human walking at 1.3 m/s. The Cornell biped, which mimics the pendulum motion of human walking and is actuated only at the ankles, achieves 0.055. The Honda Asimo with fully motorized controlled joints has an estimated cost of 1.6 [66].

1.3.3 Static/Dynamic Hybrid Platforms

An option for stability that has not been explored very much is using a hybrid of static and dynamic balance, where one or the other is applied depending on the situation. In static mode, no energy is required to balance the platform and the system is fairly rigid. When static stability can no longer be guaranteed, the system begins to balance actively. This is exhibited in the IMR-Type1, which drives statically balanced on flat ground, but uses dynamic balance to climb stairs (Figure 1.27) [67]. An earlier, simpler but similar robot was developed by Matsumoto et al. [68]. Matsumoto et al. also created a biped with wheeled legs that had four modes: 4-wheeled, 2-wheeled, and stair negotiation [69]. Steeves et al. simulated an unmanned ground vehicle design that could drive with four wheels, jump, flip, employ a bouncing gait, and travel as an inverted pendulum [70].



Figure 1.27: The IMR-Type 1 wheeled robot is capable of static and dynamic balance [67].

1.3.4 Stability Measures

Abo-Shanab and Sepehri have devised a method to model the dynamic stability of mobile manipulators that includes tire friction, sliding, rotating over one axle, and bouncing. They apply it in a two-link planar manipulator simulation [71, 72]. Garcia et al. proposed a stability measure that includes the dynamic effects due to the platform and manipulator inertia and motion. The measure is meant for use with statically stable walking robots and is called Normalized Dynamic Energy Stability Margin [73]. Korayem and Ghariblu extend the definition of dynamic load carrying capacity (DLCC) to mobile manipulators. They find the position out of the union of all positions from which the base and manipulator can follow a desired trajectory where the manipulator can carry the maximum load. [74].

A stability measure popular in the control of biped robots is Zero Moment Point (ZMP), detailed for instance by Sugano et al. [75]. They use ZMP analysis to define a measure of stability that considers the manipulator as a system of particles and the ground as a flat horizontal surface. If the zero moment point – the point on the ground where the sum of gravity, inertial force and external moments are zero – is within a certain region, the system is stable.

Papadopoulus and Rey devise the Force-Angle stability measure, which calculates the force at the centre of mass and its angle to all potential tipping axes. The minimum angle then determines the measure. It requires knowledge of the location of the ground contact points relative to the centre of mass, the external forces and moments, and linear and angular accelerations [76]. The same authors go on to propose an automatic tip-over prevention scheme that restores balance in the case of static instability by returning the manipulator to the home position and moving the base appropriately [77].

1.4 Design Goals

1.4.1 Goals

The goal of a service robot is to be able to work effectively in a human environment, be it at home, in the office, or in industry. A robot that has the same abilities as humans will be well suited for working in such an environment. It is envisioned that such a robot should be able to do anything humans can do and more—service robots should be able to handle objects and move around in an unconstrained environment in much the same way as people [2]. Unfortunately, many of the basic functionalities expected of these robots are beyond the reach of current technology, and more realistic goals must be set. Thus, as a starting point, the requirements of a hypothetical ‘Universal Service Robot’ are detailed in Table 1.3.

Using a structure that mimics humans is likely to be a good approach for achieving these abilities, however, it is not necessarily the most effective approach. The human body can be used as inspiration for designing a human-friendly robot, but should not be a constraint on its design. Other solutions can be just as or even more effective at reaching the goal. For instance, feet, though well suited for walking, are not as efficient a transportation device on reasonably flat surfaces as wheels, which can roll. In terms of the mobile platform, this means it should ‘fit’ into human spaces and be able to navigate them effectively, but does not necessarily need to function the same way as a human.

The main objective of this research is to create an optimized platform for the DLR RM upper-body humanoid Justin, creating a system for research and experiments in mobile manipulation. In order to effectively accomplish the objective of this research within the desired timeline, it was decided to limit the environment to be indoors without stairs, although there may be ramps and small steps such as those on door sills. Beyond its primary role as a research platform, the system is roughly targeted for service in a home and office environment. The initial more realistic goal ‘wish-list’ for the platform is shown in Figure 1.28. These are then prioritized in section 1.4.2 and translated to measurable engineering targets in section 1.4.4.

Table 1.3: Requirements for a hypothetical universal service robot

<p><u>The Universal Service Robot</u></p> <p><i>can do anything humans can do and more</i></p> <p>GEOMETRY</p> <ul style="list-style-type: none"> ● maximum dimensions no larger than human <p>KINEMATICS</p> <ul style="list-style-type: none"> ● can traverse <ul style="list-style-type: none"> ○ rough terrain ○ puddles ○ stairs ○ ramps ○ carpet ○ gaps, e.g. elevator entrance ● can operate in confined spaces ● can move holonomically and omnidirectionally with isotropic force, speed and accel ● has better workspace <ul style="list-style-type: none"> ○ can reach everything human can reach, plus full rotation <p>DYNAMICS</p> <ul style="list-style-type: none"> ● can lift and move own weight/at least weight of human <ul style="list-style-type: none"> ○ is faster than human 	<p>CONTROL</p> <ul style="list-style-type: none"> ● is more precise <ul style="list-style-type: none"> ○ can do fine assembly <p>NAVIGATION AND PLANNING</p> <ul style="list-style-type: none"> ● never loses orientation ● immune to distraction from <ul style="list-style-type: none"> ○ noise ○ bright light ○ crowds <p>ENDURANCE</p> <ul style="list-style-type: none"> ● can automatically refuel/recharge in minutes ● continuous runtime possible <p>INTERACTION</p> <ul style="list-style-type: none"> ● protects humans <ul style="list-style-type: none"> ○ does not crush or contain them ● protects itself <ul style="list-style-type: none"> ○ knows its limits ○ does what its told <p>RESISTANCE TO ENVIRONMENT</p> <ul style="list-style-type: none"> ● better than human <ul style="list-style-type: none"> ○ waterproof ○ chemical resistant ○ UV resistant ● resistant to injury from falls, impact with objects
--	---



Figure 1.28: initial 'wish list' for Mobile Platform

1.4.2 Safety

Safety is considered to be a criteria that must be fulfilled to a level appropriate for the system's application irregardless of other priorities. Operating in a human environment, the platform should avoid injury to humans, itself, and its surroundings, in that order. It is necessary to design all aspects such that the desired level of safety is reached and increased safety levels desired in the future are achievable; at this stage, since the platform will be a research prototype used solely under expert supervision, the safety requirements are not as critical as for a hypothetical consumer application.

1.4.3 Priorities

The goals expressed above were categorized and prioritized into three groups as shown in Table 1.4. They are discussed in more detail below.

Table 1.4: Goal prioritization

Priority	Goal	Weighting
High	<ul style="list-style-type: none">• High Mobility• High Stability• Payload Carrying Capability	9
Medium	<ul style="list-style-type: none">• Dexterity in the Workspace• Powerful	3
Low	<ul style="list-style-type: none">• High Precision• Fast• Long Runtime• Low Complexity• Durable• Easy Repair/Upgrade	1

1.4.3.1 Mobility

Ideally, the mobile manipulator should be able to traverse any terrain a human can. The more of the environment it can reach, the more useful it is. For the home/office robot, the indoor environment can include tight areas such as around desks, tables, tight passages through doors and corridors, different floor surfaces ranging from thick carpet to slippery tile and disturbances such as door sills, moving and stationary obstacles, and areas that require a large reach, such as countertops or high shelves. Also, the robot should recognize where it cannot go, such as down stairs or through spaces that are too narrow. The mobile manipulator must be able to perform tasks that interact with the environment and the object it is carrying *while moving*. That is, the system must be able to move the manipulator

and base simultaneously in a controlled manner. Rather than just point-to-point motion, this requires the implementation of a controlled trajectory with minimal restrictions on position and velocity.

1.4.3.2 Stability

Of equal importance to high mobility is high stability. A system that becomes unstable:

- Cannot complete its task
- May lose or damage its payload
- May cause damage to itself
- May cause damage to its surroundings
- May result in injury of nearby humans

As is apparent, the consequences of a loss of stability are quite severe.

Justin has a high payload capacity, high dynamics, and a fairly high mass, as detailed in 1.2.1. Hence, maintaining stability can be a challenge. For instance, the static moment created at Justin's base when fully extended horizontally while holding a 3 kg load is 411 Nm. If the torso and arm decelerate at maximum torque into this configuration from the maximum velocity, the moment increases to over 1800 Nm (with the base rigidly attached to the ground). More scenarios are explored in Appendix C.

While it would be nice for the base to be stable while carrying the maximum load over the entire workspace, this may not be realistic in real situations. Consider moving a 15 kg mass (a conservative amount based on estimates of the torso's abilities) from about chin height to 1.5 m in front of you – this sounds difficult, and indeed is beyond your reach. Even at maximum human reach, to be safe, such a movement should only be made with a maximum of 8 kg and then only infrequently (based on NIOSH Recommended Weight Limit formula [78]). Designing for stability of the maximum load over the entire workspace will lead to a system oversized for most tasks, especially in a human environment where such lifting at large extensions should not occur. Realistic targets that sacrifice some peak load performance in order to provide better overall performance need to be chosen.

1.4.3.3 Payload Carrying Capability

Payload capacity should not be unduly restricted in order to improve stability.

1.4.3.4 Dexterity in the Workspace

The base should restrict the joint workspace of Justin (Figure 1.3) as little as possible in order to maintain its versatility.

1.4.3.5 Powerful

To perform tasks effectively, the system must have sufficient power to accelerate and move the anticipated payload over the expected terrain in a reasonable amount of time. Again, some

compromise must be made between achieving maximum performance under worst-case conditions and over-dimensioning for average conditions. The platform base load is the mass of Justin (50 kg), on top of which comes the payload—up to 26.4 kg—and the mass of the platform itself.

1.4.3.6 Fast

The mobile manipulator should be able to move at typical human velocities. At least a walking pace needs to be achievable. Speeds much above this could be considered dangerous and threatening by humans, whereas a slower top speed would decrease the robot utility in that tasks cannot be performed in a reasonable amount of time. It should be able to reach full walking speed quickly in a similar time span to that of a human; roughly 0.5-1 s.

1.4.3.7 Long Runtime

Ideally, the base should be able to function for an entire working day without or with only brief interruption so that productivity is not hindered by platform downtime. This would mean a runtime of eight hours, or four hours with a recharge time of less than one hour, or perhaps a way to swap energy supplies. Since this is a low priority, shorter runtimes are acceptable if necessary to meet other goals.

1.4.3.8 Low Complexity

Given two options that achieve the higher priorities equally well, the one with lower complexity is preferable, since this will reduce design time, cost and sources of potential problems. Furthermore, less complexity means fewer actuators, which reduces system mass and power use.

1.4.3.9 Precision

The robot should have good positioning ability that increases in precision towards the manipulator tip, since this is where most interactions will occur. However, because of the redundancy of the system, imprecision in one part can be compensated for by another. Thus, if the base positioning capability is imprecise, the manipulator can account for it if its position is well known and as long as its workspace boundary is not reached in the process. This makes platform precision a low priority.

1.4.4 Determining Requirements Using Quality Function Deployment

Quality Function Deployment (QFD) is a method in making decisions for product development that helps determine and relate the key design characteristics [79]. It is designed to translate customer needs—in this case potential platform users at the DLR—into engineering requirements. The most commonly used tool of QFD is the ‘House of Quality’ matrix, and it is used here to plan the overall platform requirements. Figure 1.30 has customer needs on the left related to engineering requirements at the top with corresponding measurable specifications below. The top triangle shows interrelation between engineering requirements. Using the weightings of the customer needs times the scoring in the center of the matrix, each engineering requirement is given an importance rank, which helps guide further development. For instance, ‘ground DoF type’ is related highly to ‘High Mobility’, scoring a 9 in that row, moderately to ‘Low Complexity’, scoring a 3, and somewhat to ‘Fast’, scoring a 1 in that

row. The weighting of ‘High Mobility’, ‘Low Complexity’ and ‘Fast’ are 9, 1, and 1 respectively. Thus the total score for ‘ground DoF type’ is $9 \times 9 + 3 \times 1 + 1 \times 1 = 85$. The top five measurable requirements are identified as:

1. Footprint size, maximum direction; Footprint size, minimum direction; Footprint area
4. System mass
5. Payload before tip-over with full extension

The requirements are discussed below in the order they appear in the ‘House of Quality’ matrix (Figure 1.30). A summary of the requirements in order of importance is given in Table 1.5.

Table 1.5: Technical requirement summary, ordered by importance score.

Requirement	Score	Rank
Footprint size, maximum dimension	135	1
Footprint area	135	1
Footprint size, minimum dimension	135	1
System mass	128	4
Maximum extended payload before tip-over	108	5
Ground DoF type	85	6
Turning radius	81	7
maximum bump height	64	8
Acceleration	58	9
Maximum payload	55	10
Maximum slope	45	11
Forward velocity	37	12
Angular velocity	37	12
Maximum power draw	37	12
Runtime	30	15
Number of actuators	28	16
Average power draw	27	17
Difference in reach with Justin un/mounted	27	17
Trajectory error	10	19
Position error	9	20
Energy storage density	9	20

1.4.4.1 Acceleration

Score: 58 Rank: 9

The acceleration is primarily a measure of the platform power. No data on typical human acceleration could be found to use as a basis, so it was assumed that the robot should be able to reach peak speed in less than one second from a standing start. This means the base should be able to accelerate itself, Justin and any payload at least at 1.6 m/s^2 , with a target of 2 m/s^2 . The faster the acceleration is, the quicker the platform can reach places, increasing its mobility. The amount of time spent accelerating is likely to be a small fraction of the total trajectory, however. Faster acceleration also reduces the safety of the platform because it gives humans around the robot less time to react and increases inertial forces. Naturally, a higher system mass makes the acceleration harder to achieve. A higher acceleration will increase the power draw and thus reduce the runtime.

1.4.4.2 Forward & Angular Velocity

Score: 37 Rank: 12

Given the goal of achieving a walking pace, this translates into a forward velocity of up to 1.6 m/s (about 6 km/h), which is a brisk walking speed. Much higher speeds become unsafe in an indoor human environment, as it increases the likelihood of collisions. Another consideration for a ‘fast’ and mobile platform is its angular velocity; particularly in indoor environments, much time is spent turning to avoid obstacles. The system should be able to turn-around 180° in under one second, which translates to 0.5 rev/s or $\pi \text{ rad/s}$. Angular velocity is related to the footprint size and the location of the drive units on the footprint, since this will determine the effective turning radius. Maintaining a fast speed will somewhat increase the energy use due to increased resistance losses, and will make it more difficult to maintain a precise trajectory.

1.4.4.3 Ground Degrees of Freedom Type

Score: 85 Rank: 6

While it is clear that to have full mobility in a plane, three degrees of freedom are required, the way these are achieved has an impact on the mobility. The best mobility and speed is achieved if the platform is holonomic, that is it can change the direction of acceleration instantaneously to any other direction. Slightly less versatile is omnidirectionality, which allows acceleration in any direction but not instantaneously, and last in mobility performance are systems that can only accelerate in a limited range of directions because of nonholonomic constraints. In terms of complexity this order is generally reversed.

1.4.4.4 Runtime

Score: 30 Rank: 15

& Energy Storage Density

Score: 9 Rank: 20

The running time depends on the (average) amount of power required and the amount of energy available from storage. Fast movement with a heavy payload and much acceleration will reduce the runtime. A system with more actuators will have a somewhat lower runtime because the power losses are greater for several actuators as opposed to one large actuator. Given the same mass and volume available for energy storage, the higher the energy storage density, the longer the runtime can be, or alternatively, the lighter the platform and the smaller its footprint can be given the same runtime.

1.4.4.5 Difference in Reach with Justin Mounted/Unmounted Score: 27 Rank: 17

One criteria for dexterity in the workspace is determining how much the base interferes with the workspace of Justin in a stationary setting; looking at the difference in reach area is a measure of this. It is related to the footprint size, as a small footprint will restrict the workspace at ground level less.

1.4.4.6 Maximum Extended Payload Before Tip-over Score: 108 Rank: 5

One way to determine the platform's stability is to see how much load it can handle with the upper body in its fully extended position before the system tips over. Since a tip-over could be quite dangerous to bystanders and cause damage to the system and the environment, this criteria is also a measure for safety.

Given Justin's large reach combined with its high payload capacity, it is unreasonable to design the base to be able to handle the maximum payload of both arms, or 26.4 kg, with the torso and arms fully extended horizontally (a distance of about 1.5 m); doing so would create a system, likely heavy and bulky, that would be engineered for an infrequent and usually avoidable situation. Much like a human, the system will simply need to be closer to heavy objects in order to lift them. It is believed that at maximum extension, 3 kg is a sufficient payload requirement, one that exceeds human abilities and thus should suffice for objects in the human environment that may need to be reached at a distance. For the torso positioned vertically upright and the arm extended horizontally—a configuration likely to be more common, for instance for picking an object from a shelf or cupboard—a payload of 15 kg, which is about the mass of a case of twenty full 0.5 L glass bottles, should be supported.

1.4.4.7 Maximum Payload Score: 55 Rank: 10

In its most stable configuration, the base should be able to handle Justin's maximum payload of 26.4 kg. However, again, it would result in an over-dimensioned system to require maximum acceleration be achieved at this payload; instead, 15 kg will be the payload for stable acceleration and deceleration considerations. A higher payload will result in a larger power draw and higher system mass, or, conversely, the platform will have to weigh less in order to maintain the same peak system mass and power draw.

1.4.4.8 Footprint – Maximum Dimension Score: 135 Rank: 1

Footprint – Minimum Dimension Score: 135 Rank: 1

Footprint – Area Score: 135 Rank: 1

The QFD analysis shows the footprint characteristics – area, minimum & maximum size – to be among the most important factors, being important for mobility, workspace, stability and safety. However, the relationship between these different priorities and the footprint measures is of conflicting 'direction'; in terms of mobility, a small footprint allows travel and rotation in confined and cluttered spaces, and similarly, the dexterity of the manipulator is not overly restricted. In terms of safety, a smaller footprint is less likely to collide with environment. On the other hand, for

stability, the larger the footprint, the further the centre of mass can move before it causes the system to tip-over.

The ideal goal for operating in a human environment would be to have a footprint no larger than a human's—the dimensions of a mid-section of a typical human are shown in Figure 1.29 and Table 1.6. It should be noted that humans have the capability to extend their stance by changing their leg position, though their footprint is always limited to the width of the person's foot in one direction. Humans thus must align themselves accordingly when lifting heavy objects. Also shown in the table are relevant dimensions of Justin, which has a notably larger elbow–elbow distance but otherwise is more compact than the average human.

Table 1.6: Width and breadth from anthropometric data[80] and Justin's specifications

		50% Male	95% Male	Justin
		(m)	(m)	(m)
Width	Hip	0.35	0.41	0.23 (torso width)
	Elbow-Elbow	0.42	0.51	0.606
Breadth	Chest	0.24	0.28	0.24 (∅ of torso base)

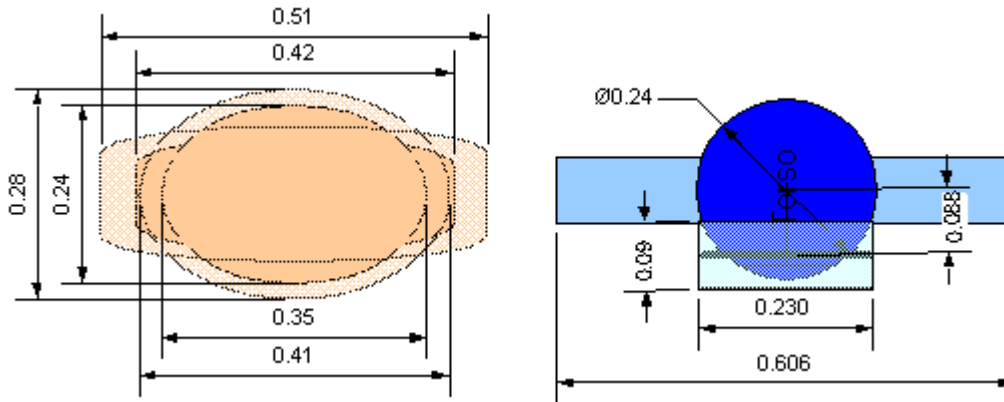


Figure 1.29: 50% and 95% human mid-section beside Justin, values in (m).

1.4.4.9 Turning Radius

Score: 81 Rank: 7

Highly related to the platform mobility is how little space it needs to turn, since this will determine the size of confined spaces it can operate in without restrictions on its motion.

1.4.4.10 Maximum Bump Height

Score: 64 Rank: 8

Although an indoor environment generally has a flat floor, there are small steps such as those found at door sills, which are usually no more than 3 cm in height. The platform needs to have the power to overcome these steps in order to ensure its mobility in the environment; as later analysis will show,

small steps actually pose high power demands on wheeled vehicles. How the platform handles the disturbance forces of bumps and small steps will also affect the precision of the end-effectors and in extreme cases the stability of the system. Though not apparent in this measure, the maximum bump height will also be a factor in the base geometry in terms of ground clearance and the selection of tire size and type.

1.4.4.11 Maximum Slope **Score: 45 Rank: 11**

In order to navigate wheelchair- and loading ramps that can occur in a typical indoor office or industrial environment, the system should be able to travel up a ramp of 4.8° with an acceleration of 0.5m/s^2 without stability problems. A drop-off in peak acceleration is deemed acceptable here, again so as to not over-design to this infrequent situation.

1.4.4.12 Trajectory Error **Score: 10 Rank: 19**

In order to perform tasks that interact with the environment while moving, the platform must be able to track a path at the desired velocity, otherwise the precision of the task will suffer. Because such tasks are unlikely to require high precision or can be performed by making the manipulator compliant, the low importance of this requirement is appropriate.

1.4.4.13 Position Error **Score 9 Rank: 20**

The error in position is the obvious measure for the platform's precision. It is related to the trajectory error with the difference that it is not concerned with the speed along the path, only the position.

1.4.4.14 Number of Actuators **Score: 28 Rank: 16**

The number of actuators gives some idea of the complexity of the system. Every actuator has an associated mechanism, involving moving parts and associated supports that make the system complex, but will also serve some purpose to improve mobility or stability. Each actuator must also be controlled and supplied with power.

1.4.4.15 Average Power Draw **Score: 27 Rank: 17**

Maximum Power Draw **Score: 37 Rank: 12**

The power draw together with the available energy storage is what determines the runtime. The power draw is increased by the desired acceleration and velocity, which are in turn factors in 'fast' and 'powerful'.

1.4.4.16 Mass **Score: 128 Rank: 4**

As is apparent from the QFD analysis, the mass of the platform is one of the most important measures as it is an underlying factor in many goals and is tied to several other criteria as well. In most cases, a higher mass is a negative characteristic. Only for stability is increased mass a benefit, and then only if it is low to the ground. Of course, stability is deemed very important, so a suitable alternative to

ensure stability must be found and/or an appropriate compromise made. In terms of the negative effects of a higher mass and associated higher inertia:

- Higher acceleration load
 - Slower acceleration
 - or
 - Higher power draw & energy use, leading to shorter runtime/more energy storage
 - or
 - Reduced payload capacity
- Higher momentum
 - Increased impact forces reduce the safety of the platform

1.5 Thesis Contribution

Making the existing upper-body humanoid Justin mobile poses a significant challenge that differs from previous mobile manipulators due to the combination of its large mass, high payload capacity, large workspace and high-speed dynamics. No existing mobile platform can support Justin and meet the requirements outlined in section 1.4.4. This thesis presents the design of a mobile platform for a powerful, highly dynamic upper-body humanoid with a targeted use as a general purpose indoor service robot that will meet the needs of the DLR RM. It can also serve as a model for other mobile robot designs that require the transportation of a large variable payload high off the ground that wish to avoid the high energy use and undesired motion of dynamically balanced systems while nonetheless achieving excellent mobility and stability. In solving this design problem, this work makes the following notable contributions:

- reconcile conflicting mobility and stability criteria while maintaining low mass
 - achieved using a variable footprint as introduced in section 2.3.5, a new application as applied to a mobile manipulator.
 - change in footprint is performed using a novel mechanism described in Chapter 3.
- In depth investigation of climbing small steps such as door sills in Chapter 5
 - found to be a significant torque and power requirement
 - experimentation shows importance of tire elasticity
 - new easy-to-use dynamic model that includes elasticity presented
 - model application to this and other designs allows for improved actuator and tire selection
- Expansion of research for mobile robot drive power requirements, stability, suspension requirements and drive kinetics modeling

1.6 Thesis Organization

The remainder of this thesis is organized as follows: In Chapter 2, different design configurations are evaluated, which leads to the selection of a statically stable platform with variable footprint. The configuration of and details about the mechanism used to create a variable footprint are presented in Chapter 3. The resulting stability of the design is investigated in Chapter 4. Chapter 5 looks at the problem of climbing small steps with elastic tires, which is relevant to the design of the drive system. The need for a suspension for the platform is addressed in Chapter 6. Configuration choices are made for the drive system in Chapter 7, and its kinetics are modeled and simulated in Chapter 8, where the caster length is also chosen. Chapter 9 looks at the component mass and component volume, energy and power requirements. Finally, Chapter 10 concludes the thesis by presenting a CAD mock-up and specifications of the preliminary design.

Chapter 2

Evaluation of Configurations

Apostolopoulos points out that: “A design phase that is practically unexplored and often neglected is that of *configuration* during which locomotion concepts are synthesized and evaluated and a decision regarding which concept to carry into full design is made... What is not widely realized is that configuration is the foundation to design and to successful mobile robot development” [48]. This analysis will attempt to give the configuration design phase its due, focusing on the specifics of an indoor mobile platform for Justin.

2.1 Options

As discussed in the literature review, there are a number of methods to provide mobility for a robotic system; they are summarized in Figure 2.1. Given the requirements laid out in 1.3, two of these options can immediately be dismissed as unsuitable or unnecessary for the intended application of the platform. Tracks, while well suited for difficult outdoor terrain, can damage interior flooring, as the tread undergoes sliding motion when the vehicle is turning. They have a higher resistance to movement than wheels because of sliding and of the tread structure, which also takes up a large volume and ground footprint. Similarly, legs are unnecessary for the indoor environment without stairs. While surmounting steps would be a benefit, the current state-of-the-art in legged propulsion is not only to a certain extent proprietary technology, but cannot compete when it comes to the efficiency and speed of other options. The cost of transport $c_{transport}$ is given as

$$c_{transport} = \frac{c_{energy}}{mg \times d} \quad (2.1)$$

where the energy cost, c_{energy} , is the mechanical work performed [13], which for wheeled platforms can be defined as

$$c_{energy} = \frac{\mu_{roll} mg}{r} \times d \quad (2.2)$$

where μ_{roll} is the rolling resistance, mg is the weight of the platform, r is the wheel radius and d is the distance travelled. Substituting (2.2) into (2.1),

$$c_{transport} = \frac{\mu_{roll}}{r} . \quad (2.3)$$

Thus the cost of transport is a function of rolling resistance, which is typically < 0.005 m for indoor environments (see Appendix E), and the radius. For a tire of radius 0.1 m, the cost of transport is up to 0.05, the same as human walking [13]. Developing legs that exceed the state-of-the-art and meet the requirements, particularly with respect to safety, stability and run time, was deemed to be beyond the goals and the scope of this work. Thus, the platform will have wheels; options that remain are the type of balance (static, dynamic or hybrid), the type of wheel, and their configuration.

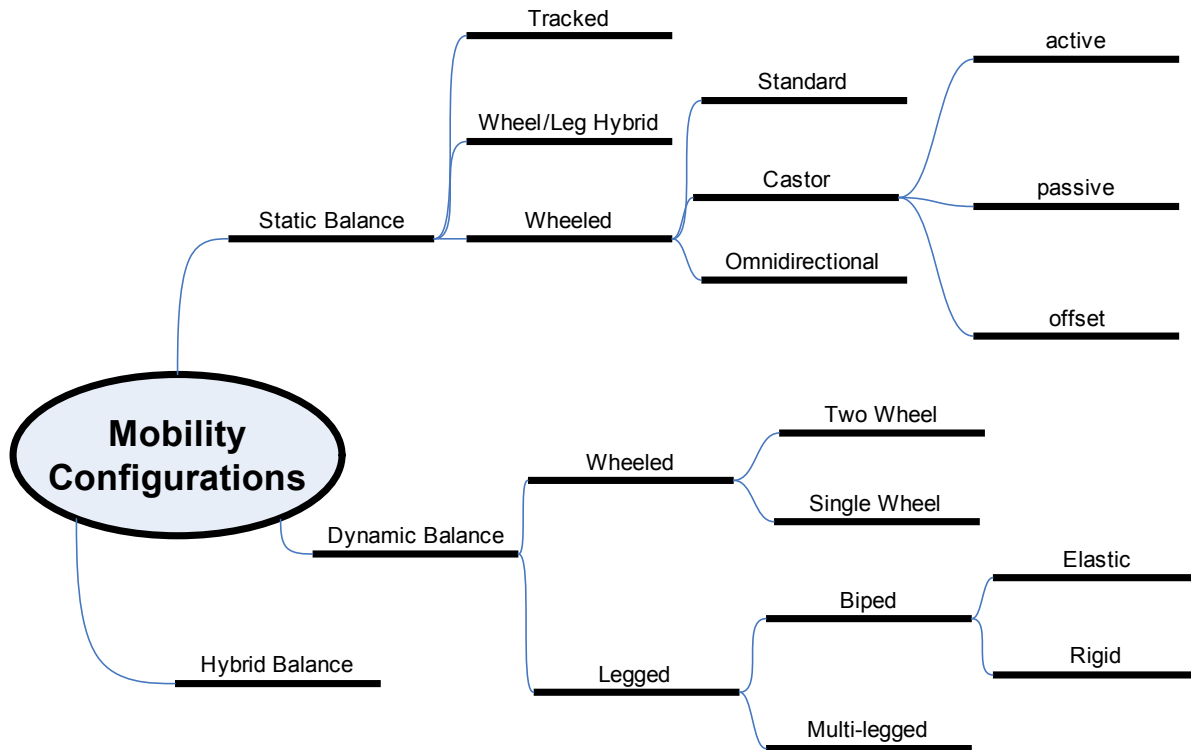


Figure 2.1: Different potential approaches to mobility.

2.2 Evaluation Criteria

Different configuration options will be investigated with respect to their ability to meet the goals for the platform. The important goals relevant to this design level, that is, the selection of the platform's basic configuration, are formulated as Mobility, Stability, Complexity, and Power & Energy. The goal of 'Fast' will be met during the actuator selection stage. 'Dexterity in the Workspace' will be addressed by the base geometry design. 'Long Runtime' is covered under some extent under the heading 'Energy', which considers the demand for energy, but will also be an issue when the energy storage system, which satisfies the supply of energy, is investigated. The goals are weighted relative to the prioritization determined in section 1.4.4. The criteria for evaluating each configuration's ability to meet the goals are listed in Table 2.1.

Each criterion for each evaluated configuration is given a rank relative to the best value, which scores one, down to the worst, which scores zero. This ranking is then multiplied by the sub-category's weighting and all of the rankings in that category are summed to give a category rank for that configuration between zero and one, one being a perfect score for all criteria. The category rank is in turn multiplied by the category weight to give the category score at the end of the evaluation table, where category scores are highlighted in red if they are below half of the maximum score. The final score then consists of the sum of the weighted category scores, and an overall rank is given to the configurations based on this score.

Table 2.1: Description of criteria for configuration evaluation.

CRITERIA	SUB-CATEGORY	DESCRIPTION
Geometry	Height, Width, Breadth	maximum and minimum dimensions at ankle height
	CM Height	height of the centre of mass above ground level
	Wheel Radius	nominal wheel radius
	Actuator Mass	mass of the actuators is estimated at 2 kg each
	Actuator Volume	each actuator is estimated to require a volume of 2 L
	Fixed Mass	mass of the base without the actuators
	Total Mass	mass of the base with actuators
	Support distance required to balance 15 kg horizontally extended	<p>The necessary horizontal distance h from the centre of the base to the support point to create a static moment balance between the base mass and the moment of the extended arm and torso with 15 kg load is</p> $h = \frac{m_u l_u}{m_b + m_u}$ <p>where m_b is the base mass including the part of the torso that does not tilt, m_u is the tilted upper-body mass and l_u is the horizontal distance from the base centre to upper body centre of mass.</p>
Mobility weight: 9 (30% of total weight)	Minimum Footprint Area	The smallest footprint (at ankle height) that the configuration can take up with all flexible components retracted; the smaller this is, the more easily the system can move through cluttered spaces and thus the larger its workspace.
	Turning Footprint	The circular area swept by the widest part of the platform (in its minimum footprint configuration) represents the amount of floor space the platform needs in order to turn on the spot.
	Holonomic/Omni/Steered	A platform with the ability to move in a holonomic manner was given three, in an omnidirectional manner two, and a simply steered manner one point.
	Reach at 3 kg Load	The longest distance that Justin could extend beyond the edge of the platform while carrying 3 kg at its end stably; this is lower for large platforms, but also those that must lean to balance, since the lean is opposite the direction of extension.

Stability weight: 10 (33% of total weight)	Minimum distance from centre of mass to tip edge in most stable configuration	The smallest horizontal distance from the centre of mass to the edge of the support polygon in the platform's most stable configuration (variable footprint enlarged) with the torso vertical represents how much of a safety margin exists before tip-over towards the platform's weakest side, such as between two wheels. This ensures a design that is focused only on one direction of potential tip-over is not overly favoured.
	Maximum distance from centre of mass to tip edge in most stable configuration	As in the above except that here the distance is measured to the 'strongest' point, for instance from the centre of mass to the wheel that is furthest from it.
	Maximum Footprint Area	The area of the polygon enclosed by the platform's support points (variable footprint fully extended). The larger this area, the safer the static stability of the platform. This stands in direct opposition to the Minimum Footprint Area criteria in the mobility category, where a smaller value is better.
	Minimum Horizontal Tip-over Force	The smallest amount of force that needs to be applied to the platform at a height of 60 cm from the ground in order to make it tip over; for static platforms, a function of platform fixed mass, actuator mass, and minimum distance to tip edge.
	Maximum Horizontal Tip-over Force	Same as above but the force required is in the most stable direction (maximum distance to tip edge).

Complexity weight: 6 (20% of total weight)	Number of actuators plus number of degrees of freedom	Each degree of freedom requires components that are many times more complex than a rigid connection; if the degree is actuated, the complexity is increased not just by the actuator itself but by the necessary control and support components. Thus actuated DoFs are valued worse than un-actuated ones by counting the actuator and its DoF.
	Control System	The platform is given a qualitative score between 3 (high) and 1 (low) to represent the expected complexity of the control system.
	Mechanical Design	The platform is given a qualitative score between 3 (high) and 1 (low) to represent the expected complexity of the mechanical design.
	Emergency Stop	The platform is given a qualitative score between 3 (high) and 1 (low) to represent the expected complexity of an emergency stop mechanism, which needs to attempt to maintain stability in the case of a system power failure. This penalizes dynamic platforms that cannot stand on their own without such a mechanism.
	Approximate Available Volume	This value is 30% of the estimated total volume minus the estimated volume for drive systems and drive energy storage. It represents the volume estimated to be available to implement the platform electronics, sensors and other base components. The smaller this space, the more complex the design will need to be in order to fit all the components.
Power & Energy weight: 3 (10% of total weight)	Power to Accelerate at 1 m/s ²	The power is derived from the kinetic energy (see below) assuming constant acceleration to top speed in $t = 0.8$ s; $Power = K.E. / t$ (not ranked).
	Kinetic Energy at 1m/s	Kinetic energy depends on the total mass m , $K.E. = 1/2mv^2$ and is determined for a velocity, v , of 1.6 m/s. Thus mass is repeated as a criteria in this category.
	Energy Storage Volume	Assuming a runtime of two hours of acceleration at 50% efficiency and an energy storage density of 2000 L/Whr, the energy storage volume $V_{Storage}$ is estimated as $V_{Storage} = 2hrs \times \frac{Power}{50\%} \times 2000 L/Whr$
	Power to Balance Sudden Addition of 15 kg Mass	Qualitative estimate of the power required to keep the platform balanced upon a sudden addition of mass to one side; between 3 (high) and 1 (low, no power).

2.3 Evaluated Configurations

As mentioned in 2.1, not all configuration options are considered. Before performing a detailed analysis, a wide variety of configuration styles were first evaluated subjectively for their expected performance in the categories of mobility, stability, precision, energy, mass and complexity. Those that showed promise were then expanded into numerous sub-configurations based on the following classification:

1. Number of ground-contact points
2. Type of wheels (ball, standard, steered, castor)
3. Propulsion degrees of freedom
4. Steering degrees of freedom
5. Number of additional degrees of freedom and type (for platform reconfiguration)

The evaluation results for the configurations that underwent detailed analysis are shown in Appendix F.

2.3.1 Number of Contact Points

The larger the number of ground-contact support points, the smaller the difference between the best and the worst tip-over point, and thus, the better the balance overall. This can be expressed by the ratio of smallest (fp_{min}) to largest (fp_{max}) footprint radius,

$$\frac{fp_{min}}{fp_{max}} = \cos\left(\frac{360^\circ}{n_{contact}} / 2\right)$$

where $n_{contact}$ is the number of contact points all an equal distance in radius from the centre-of-mass (CM) and distributed equally around, as shown in Figure 2.2. For instance, using the minimum of three points for static balance, with angles between them of 120° , the worst-case tip-over point (half-way between two contact points) only gives a support distance that is half the best-case point, whereas four equally distributed contact points give a worst-case distance 0.707 of the best-case and six gives a ratio of 0.87. Since this is a cosinusoidal function, the marginal benefit of more legs decreases as the number of legs increase. In addition, complexity increases with more contact points, as does mass and energy use, because multiple components are generally less efficient than one single comparable component. For instance, two wheels, although they can be sized for a smaller load than one wheel, will each have a set of bearings and bearing losses that together will sum to more than a larger single wheel's bearing mass and losses. Thus the number of contact points in the detailed evaluation is limited to four.

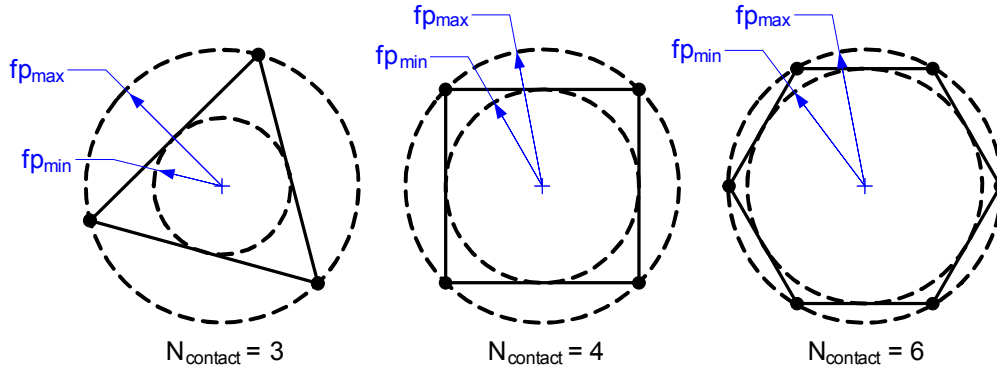


Figure 2.2: Difference between maximum and minimum footprint radius decreases as the number of contact points increases.

2.3.2 Type of Wheels & Their Degrees of Freedom

As described in 1.3.1.1, different locomotion types have different benefits. Because of their inability to surmount small steps, universal wheels are not considered. Because of the large amount of space and complexity required to implement a driven ball wheel, it is only considered in a single-wheel configuration. To at least be able to turn on the spot, the only possible configuration using fixed standard wheels is as a differential drive. For optimum traction, it is desired to have all-wheel drive. Thus free casters or free ball wheels are not considered. For the purposes of selecting a configuration, steered standard wheels are essentially interchangeable with powered caster wheels or split-offset caster wheels and are not evaluated separately. The type of wheel determines the number of degrees of freedom in propulsion and steering.

2.3.3 Additional Degrees of Freedom

In addition to the wheels, actuated degrees of freedom to allow repositioning of the contact points are considered. Essentially, this puts the wheels on ‘legs’ that can be extended and retracted to change the footprint size. One configuration also tilts the body position relative to the contact points by employing a joint in a horizontal axis. Several different potential joint combinations were investigated and the most promising considered in the detailed evaluation.

2.3.4 Baseline: Non-Reconfigurable Static Platform

In order to evaluate the merits of dynamic balance and reconfigurable platforms, several simple static platforms are included in the evaluation. For a statically stable footprint with three contact points and a width of 0.4 m, to achieve marginal stability with a horizontally extended Justin and 15 kg load, the base alone would need to weigh 146 kg. Accelerating the 201 kg system, ignoring for the moment that it would likely tip over, requires about 80% more power than with a 57 kg base. As an alternative to the heavy base, a larger, lighter static base could be used, but the base footprint would need to be 0.78 m wide to statically support the above mentioned load with a base mass of 57 kg.

2.3.5 Approaches for Reconciling Goals for High Stability and High Mobility

Methods for achieving high stability and high mobility are often found to be in conflict. Several ideas to solve this dilemma are considered here and evaluated in different configurations in Appendix F; they can be divided into three categories:

1. Dynamic wheeled balance
2. Centre of mass shift by actuated platform movement
3. Actuated support point shift

Let us evaluate the merits of these three categories by looking at their effect on the ‘reach’ criteria as shown in Figure 2.3:

1) Dynamic balance must, in the steady state condition, maintain the centre of mass directly above the wheel axis. This means that it must lean back if the manipulator moves forward, reducing the reach of manipulator, l to the distance a :

$$a = l - x_t \quad (2.4)$$

$$x_t = h \sin \theta_1 \quad (2.5)$$

where θ is determined such that that the horizontal distance from the torso to the centre of mass x_{CM} puts the centre of mass over the wheel axis. Because the centre of mass is below the extended torso, the distance in reach that is lost due to the tilt, x_b , is larger than the distance the centre of mass is moved. The higher the centre of mass, the smaller this difference is.

The height of the manipulator also decreases by

$$y = h \cos \theta . \quad (2.6)$$

A dynamic base can handle movements of the centre of mass location and disturbance forces as long as they do not exceed the platform’s ability to produce a counteracting force through wheel acceleration. This category is represented in evaluation configuration 2.4 (Appendix F).

2) In the concept of centre of mass shift by actuated platform movement, a small statically stable footprint of width $2x_b$ is augmented by having the body tilt in order to shift the centre of mass. The system is stable as long as the CM is kept inside the area vertically above the two wheel axes, which means that the body does not need to tilt as much as in case 1), where stability is restricted to being on a line directly above the single axis. Because the tilt angle is smaller, $\theta_2 < \theta_1$, the reach b is larger,

$$b = l - x_t - x_b \quad (2.7)$$

$$x_t = h \sin \theta_2 \quad (2.8)$$

and the change in height, defined as in case 1), is not as large. However, the footprint is larger by $2x_b - 2r$, where r is the wheel radius of 1). Of course the larger the footprint, the less tilting is required, up to a point where it becomes unnecessary entirely and the case degenerates into the simple statically stable platform.

For this concept, an extra actuator that must accelerate the entire upper-body mass is necessary. Since this category provides poorer reach at static conditions than the following category and doesn’t

provide for the synergy between the drive actuation and the dynamic balance of the previous category, it is not evaluated further except as an addition to concept 1) in evaluation 2.7.

Similarly, internally shifting a mass to change the centre of mass is not as effective because only a limited mass can be moved through a limited range and an additional actuator is required.

3) In the third case, rather than changing the location of the centre of mass, the tip axis is moved by moving out the ground contact point, which is done without affecting the height of the platform. The reach is reduced to c by the distance the tip axis is moved, which is equivalent to the distance the centre of mass was moved back in cases 1) and 2),

$$c = l - x_b \tag{2.9}$$

$$x_b = x_{CM} \tag{2.10}$$

Thus the reach is reduced more for the dynamic and tilt concepts than for this case where the contact point is changed. In case 3), the height of the centre of mass is inconsequential for static stability. It should also be noted that the reduction in reach could be considered zero if the contact point extension mechanism does not interfere with the workspace, such as if it were to extend under a table. Case three is represented in evaluations 3.2, 3.3, 4.2, and 4.3. Evaluations 3.2 and 4.2 use a method of moving the contact point that only requires one actuator. Evaluations 3.3 and 4.3 have an extra actuator per leg to facilitate hybrid balance as described below in 2.3.5.1.

It should be noted that in reality the reach reduction due to a tilt with Justin is even greater than the simplified analysis shown here, as the torso kinematics restrict the rotation of the first joint to only 90° ; this was ignored to give a balanced theoretical comparison here.

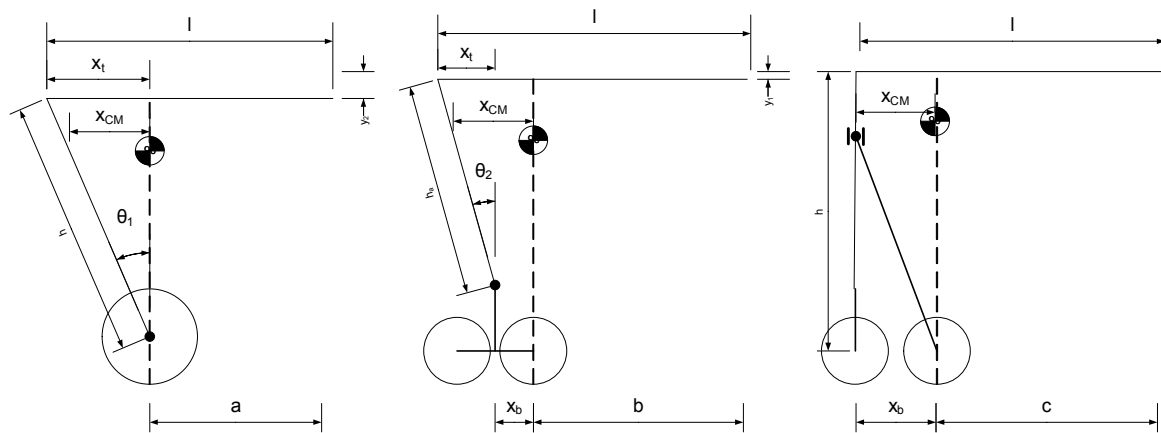


Figure 2.3: Platform reach: (L to R) dynamic two-wheeled balance, shift of centre of mass by platform tilt, shift of contact point by leg extension.

2.3.5.1 Hybrid Balance

One approach to attempt to reduce the drawbacks of two-wheeled dynamic balance is to expand on the ‘kickstand’ device concept used by other researchers [55, 56] and make it useable during normal operation. This means giving the platform some form of omnidirectional wheel that can stay down

during motion. By making the length of the support leg variable, it should be possible to operate with the wheel off the ground (or at least with it offering no vertical resistance) as a dynamic balance platform, with the wheel on the ground and leg extension fixed as a static balance platform, or in combination, with dynamic balance kicking in as an emergency backup should the load become too much for the support leg in its current position.

Two possible hybrid balance strategies are depicted in Figure 2.4. In the top strategy, if the platform starts to tip, causing the drive wheel to lose ground contact, the leg can be extended out to bring the centre of mass back over the stable region. In the lower strategy, which works even if the leg is at its maximum extension and the platform begins to tip, the support leg is retracted until the drive wheel regains ground contact, at which point it must accelerate the platform in the direction of tip to create a counter-acting force. Both strategies require a leg with an actuated rotary and prismatic joint, which must hold the significant load of the upper body in the horizontally extended position. Excluding dynamic forces, the leg rotary joint would roughly require a torque of 300 Nm.

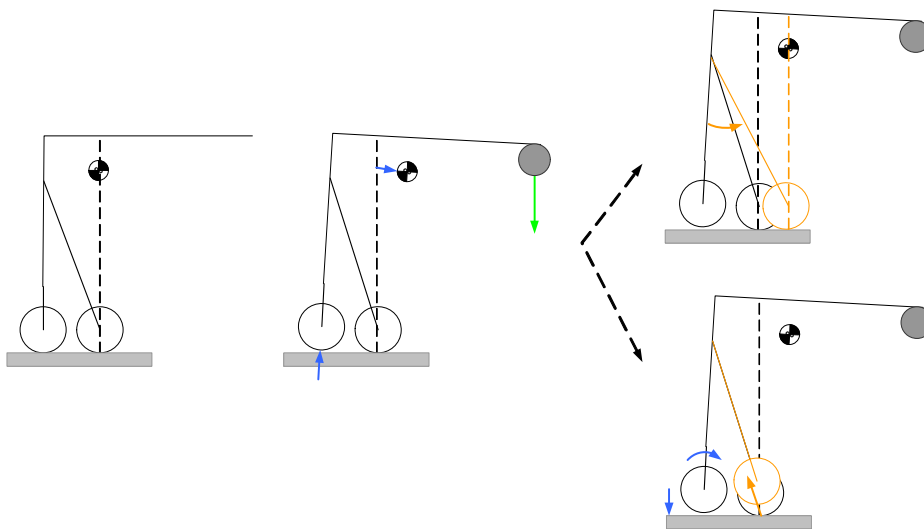


Figure 2.4: Hybrid balance strategies.

2.3.6 Concepts

2.3.6.1 Concept A4 (Evaluation Configuration 2.6)

The concept is similar to the Segway RMP, with a differential drive that can dynamically balance (Figure 2.5). In addition, it has a prismatic support leg with a ball wheel, allowing for hybrid balance as described above. Only two drive actuators are needed, plus two actuators for the leg, one for extension and one for the angle. With the leg retracted, the platform is very compact, measuring only as wide as the tire diameter.

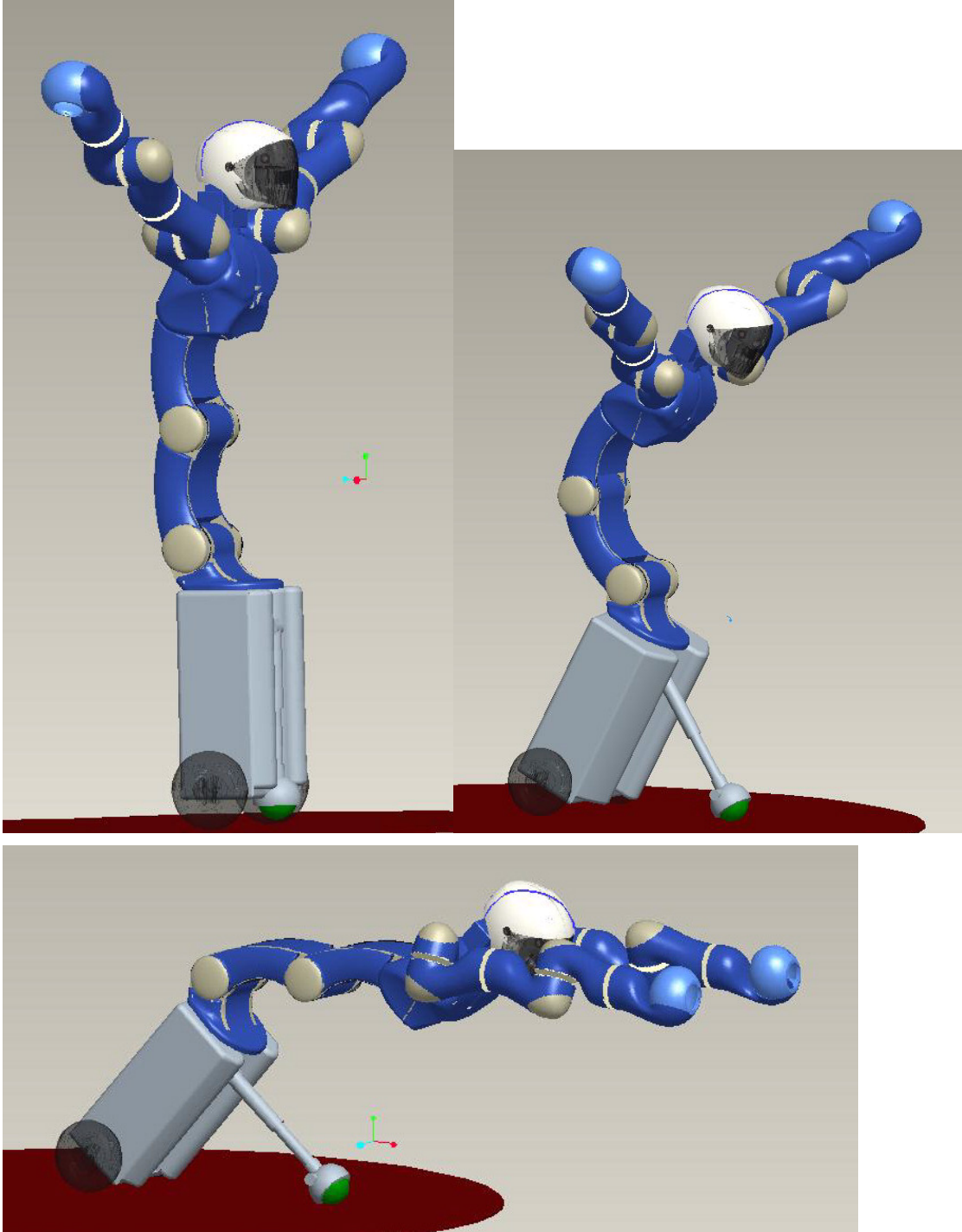


Figure 2.5: Concept A4: leg retracted, dynamic balance (top left), leg extended, torso upright (top right), leg extended, torso horizontal (bottom).

2.3.6.2 Concept A3 (Evaluation Configuration 2.7)

Similar to concept A4, this concept adds a rotational joint perpendicular to the wheel axis to allow the platform to tilt sideways as well (Figure 2.6). Thus in addition to the hybrid balance with the wheel axis and the support leg, it can balance as in case 2) in the sideways direction. In order to keep the ball wheel within its operating range, the body-end of the support leg is tied to the sideways tilt joint such that it rotates opposite with it and remains perpendicular to the ground. Three actuators are needed in addition to the two drive actuators, one for leg extension, one for leg angle, and one for the sideways tilt.

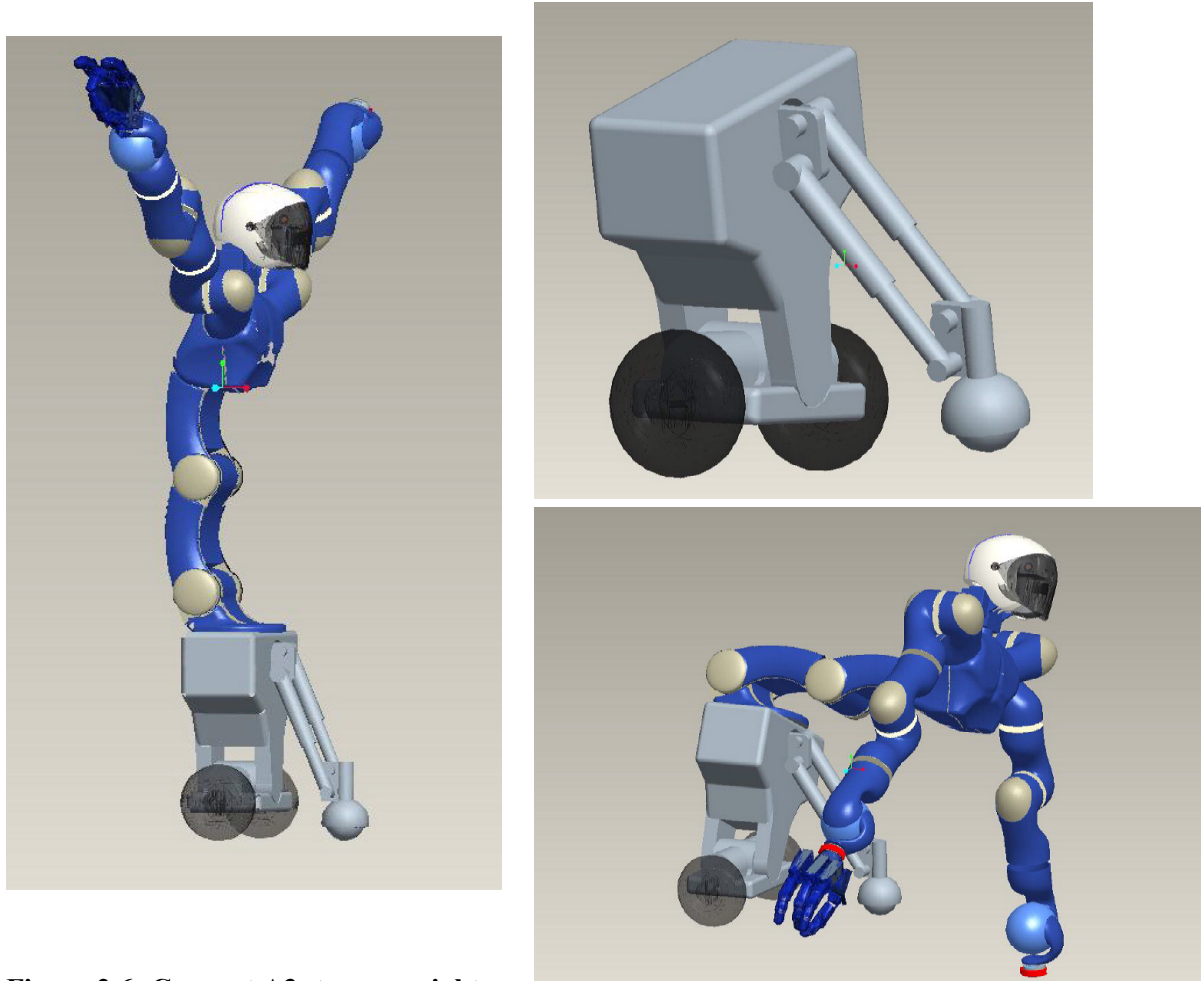


Figure 2.6: Concept A3: torso upright (left), platform by itself (top right), with torso horizontal (bottom right).

2.3.6.3 Concept C3 (Evaluation Configuration 3.2)

Concept C3 shown in Figure 2.7 uses a mechanism to change the wheel contact position that only requires one actuator, doesn't affect platform height or tilt, and its actuator doesn't need to carry the load of the upper-body (details in 3.3).

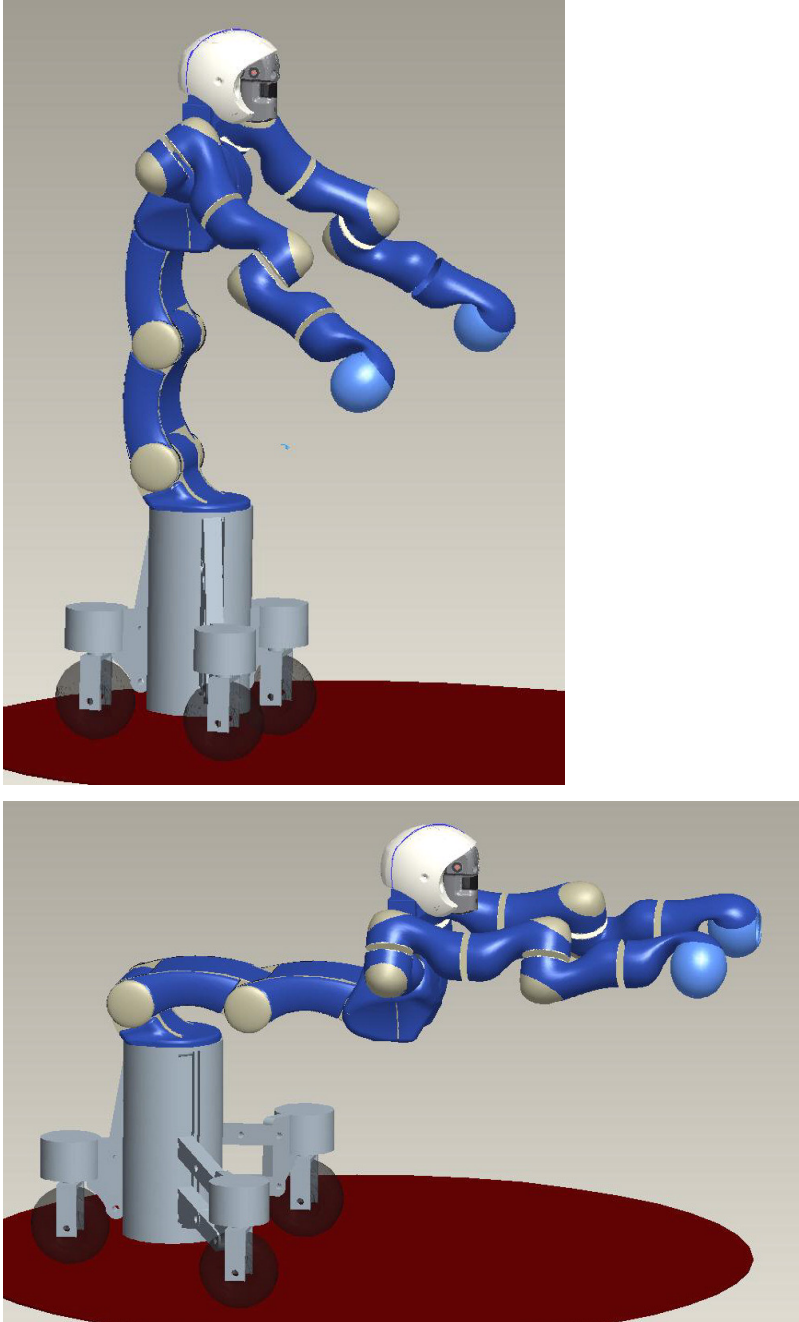


Figure 2.7: Concept C3: legs retracted and torso upright (top, front legs extended with torso and arms extended horizontally (bottom)).

2.4 Evaluation Results

In the evaluation matrix (Appendix F), certain key configurations are repeated with parameters varied or optimized within the range of

- height: 0.4 – 0.6 m
- width: 0.2 – 0.5 m
- breadth: 0.2 – 0.5 m
- CM height: 0.3 – 0.5 m
- base mass: 50 – 100 kg

The final and category scores for the different configurations in Appendix F allow one to make several general observations:

- A single ball wheel is inherently unstable in all directions, requiring extensive dynamic balance control. Although it has an advantage in being very mobile, this does not prevent the ball wheel configurations (1.2a, 1.2b) from scoring most poorly.
- Dynamic balance using a two-wheeled platform (configuration 2.4) such as the Segway RMP actually scores quite poorly due to its inherent instability in one direction. Its relatively low complexity is not enough to keep it from scoring just above the ball wheel designs at the bottom of the ranking. Adding some form of support leg to this design (configurations 2.5-2.7) improves the stability score, though this is offset by the increased complexity—two of these designs score higher than a simple statically stable base of the same footprint size (configuration 3.1a), but actually lower than a larger statically stable base (configuration 3.1b).
- A four-wheeled configuration is superior to a three-wheeled one due to the increased stability as discussed in 2.3.1.
- Adding actuation to allow change of the contact point positions offers superior mobility and stability, giving these configurations (3.2, 3.3, 4.2, 4.3) the best ranking despite their complexity being greater than that of the simple static platforms. The configurations where only one actuator is used for contact point extension (configurations 3.2, 4.2) are less complex and thus rank higher. Though the benefits of the hybrid balance (configurations 3.3, 4.3) are not fully reflected in the evaluation, neither are the drawbacks, such as the much greater actuator power required.

2.5 Chosen Configuration

The highest scoring configuration is a four-wheeled platform with a variable footprint, similar to concept C3 above but with one extra wheel. This extra support point increases the stability score by 22%. Although the complexity score worsens, the four-wheeled configuration still scores 5% better than the comparable three-wheeled configuration. Thus the four-wheeled variable footprint design is chosen for further development.

Chapter 3

Variable Footprint Mechanism

3.1 Concept

The previous section showed that a system with a variable footprint best meets the design requirements. This section describes the design of the mechanism used to change the footprint.

3.1.1 Goals

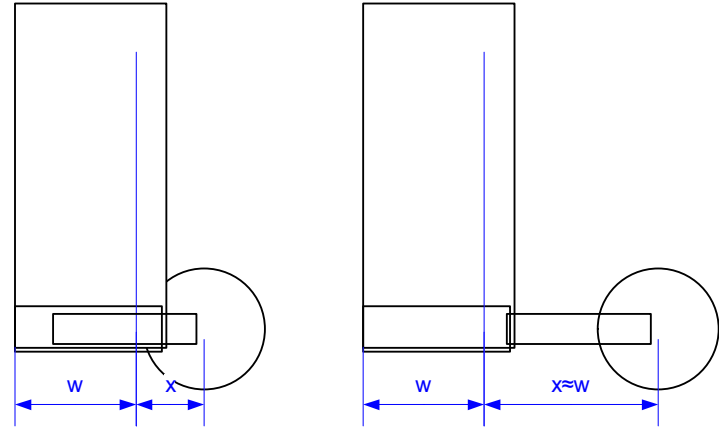
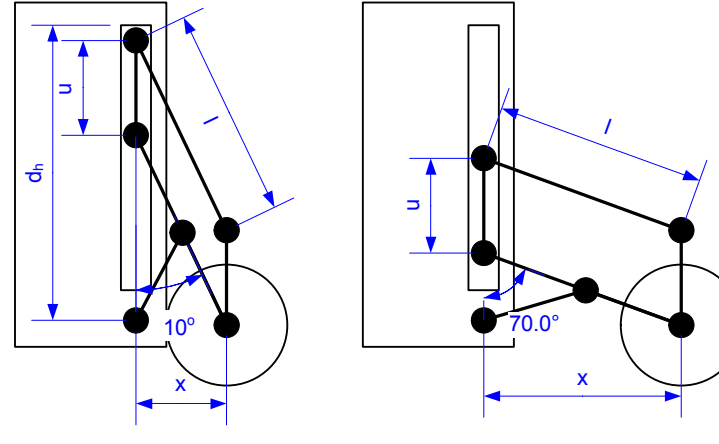
Based on the evaluation criteria in section 1.4.4, the best variable footprint mechanism (VFM) should have, compared to a platform without the mechanism:

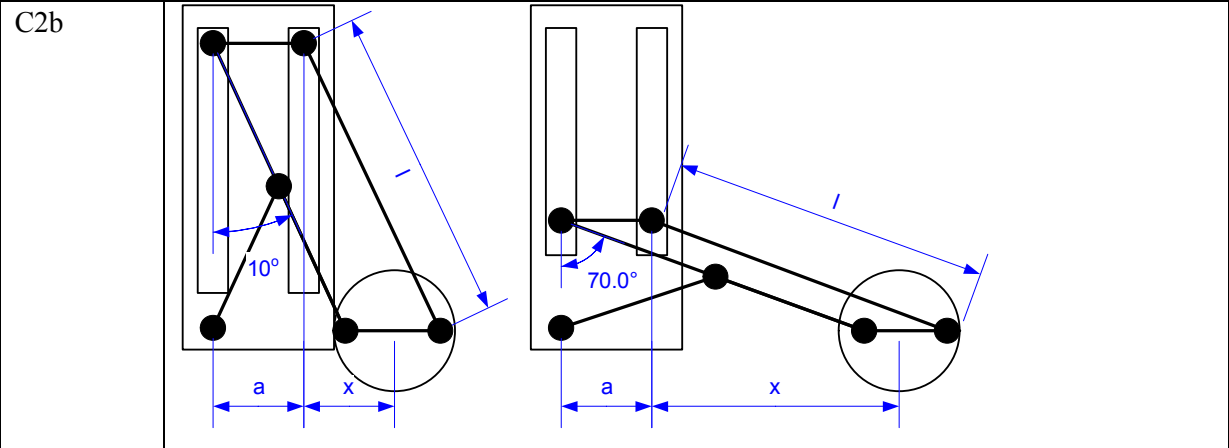
1. **Largest change in footprint size** – in order to combine the best mobility with the best stability of the platform.
2. **Smallest increase in base weight** – because increasing the weight of the base has a negative effect on safety and increases the power requirements.
3. **Smallest increase in volume** – due to the increased complexity of fitting more components into a limited space.
4. **Lowest power consumption** – power consumption is one of the evaluation criteria to be minimized.
5. **Smallest effect on steering** – to avoid increasing the complexity of the control system and the mechanical design. Since the position of the wheels will change, an effect on steering cannot be avoided, but it is helpful if the steering axis remains vertical so that steering angles remain consistent and no unwanted caster develops.
6. **No change to the height of the base or its posture** – While in some situations, it may be beneficial to change the height of the platform, the upper body cannot easily compensate in all directions for such changes if they are unwanted. This also complements the 4th goal, since changing the platform's height requires extra energy.

3.1.2 Configurations

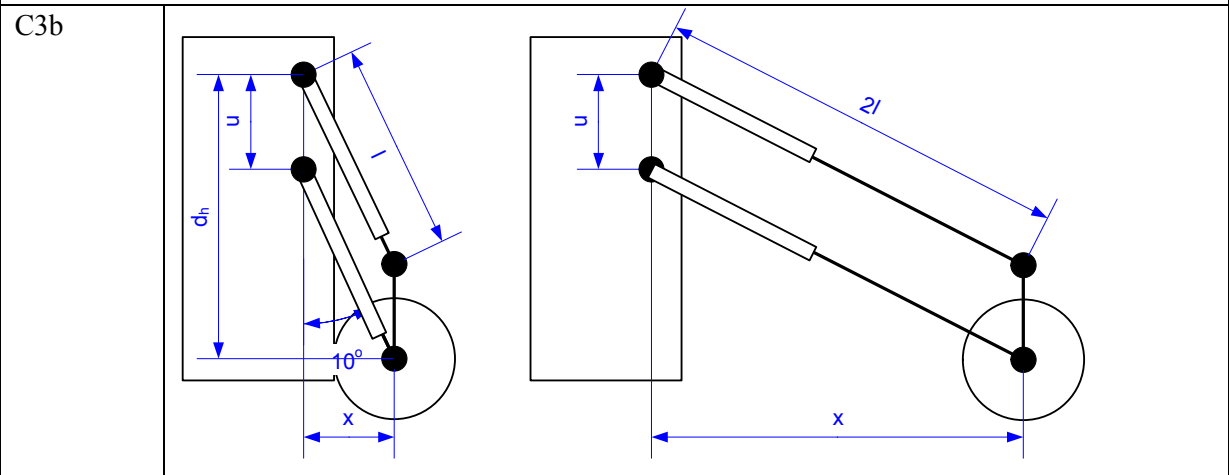
A number of different configurations were evaluated based on the goals listed above; they are depicted and described in Table 3.1.

Table 3.1: Variable footprint mechanism design options

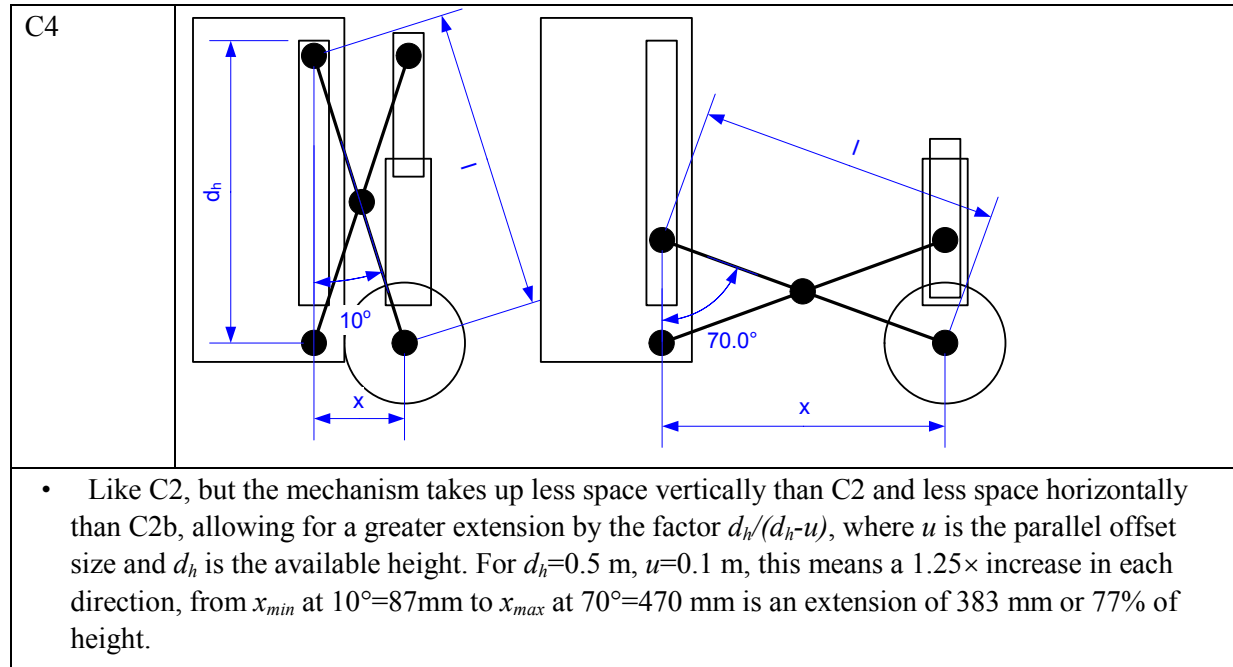
<p>Horizontal prismatic</p>	
<ul style="list-style-type: none"> • Simple; requires only one prismatic actuator per wheel. • Prismatic must carry high moment and lateral force when extended (acts like a cantilevered beam). • Theoretically, extension is limited to the width of platform, assuming prismatic can double its length. For a width of 480 mm (95% human shoulder width), the extension distance is 96% of the height of a 500 mm high platform. In practice, an actuator with this amount of extension and load capacity is not known to exist; actuators are typically 10-20 cm longer than their stroke, meaning practical extension is in the range of 330 mm or 66% of height, and high side loads require a large actuator or additional guides. 	
<p>C2</p>	
<ul style="list-style-type: none"> • Load of platform carried through lower members; no energy required to maintain position and only friction needs to be overcome to change position (ignoring dynamics) • Parallel legs keep steering axis vertical at all times • Extension distance is limited to maximum height of platform minus the space needed for the parallel offset (u) and by approach of singularity at 0° and at 90° leg angle (high lateral forces); for the range from 10° to 70°, extension is 61% of height assuming 20% of height is taken up by the offset and mechanism structure. 	



- Like C2 except parallel offset a is horizontal; improves extension distance but increases width of base.



- Prismatic and rotational joint controlled to maintain height and level of platform (though tilting could be enabled if desired)
- Load carried through leg – must support load in prismatic and rotary joint when changing footprint
- Parallel legs keep steering axis vertical at all times
- Leg extension is limited to $x_l = \sqrt{(2(d_h - u))^2 - d_h^2}$, where it is assumed the prismatic can double its length.
- For an un-extended leg of 0.5 m (maximum leg length of 1 m), extension is $\Delta x = x_{\max} - x_{\min} = d_h (\tan 60^\circ - \tan 10^\circ) = 778 \text{ mm}$ or 156% of height



3.1.2.1 Option: Horizontal Prismatic

While a horizontal prismatic design is attractive due to its simplicity, there is no known prismatic actuator with a comparable extension distance to the other options with which this could be practically implemented. Actuators of sufficient moment load-carrying capacity are large and bulky with poor body length to extension ratios.

3.1.2.2 Option: C3b

Despite C3b's attractive extension capabilities which would allow a footprint more than twice as large as the other options, its load distribution is very poor; the lower leg prismatic must work against a large fraction (depending on the weight distribution between the wheels) of the mass of the platform that could be 500 N or more, and the rotational joint at the top of the leg must counteract a moment that increases as the extension increases and is equal to the vertical wheel loading times the extension distance, which could reach over 400 Nm. To maintain a constant 1 m/s horizontal extension, the leg prismatic must move at up to 0.87 m/s, creating a peak power requirement of roughly 400 W, and the rotational joint must move at up to $420^\circ/\text{s}$ for a peak power requirement of almost 3 kW. These requirements make C3b an unattractive option.

3.1.2.3 Option C2:

C2 has a variety of different sub-configurations that were explored by parametric analysis. As shown in Figure 3.1, u is the parallel offset between legs and a is the horizontal distance of the wheel axis to the lower outside leg joint. By varying angle ζ , the parallel offset can be changed from vertical at 0° through to horizontal at 90° .

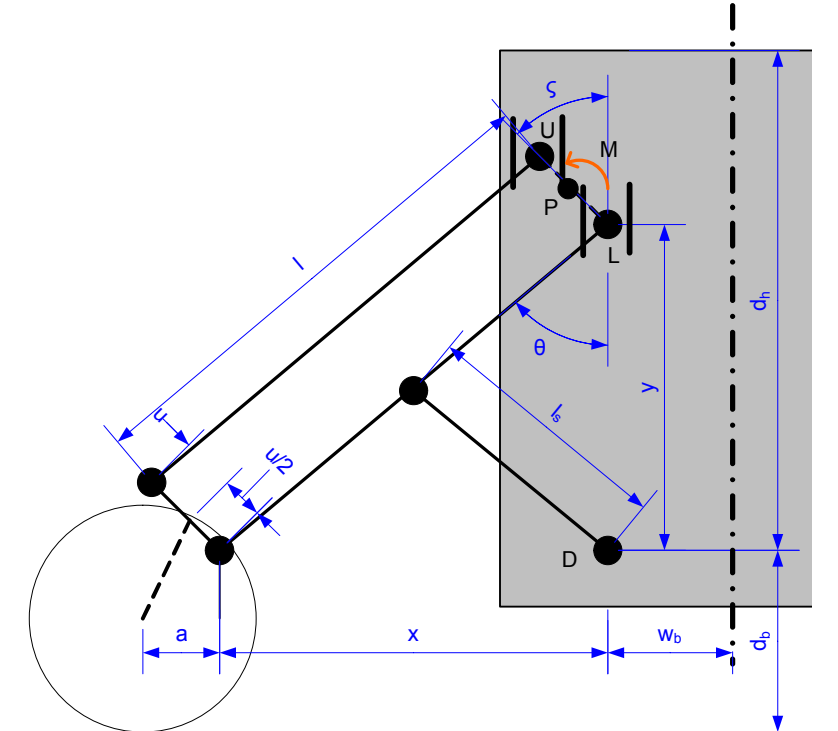


Figure 3.1: C2 side view showing design parameters

The optimum parameter choice is determined using a simple static analysis, similar to that shown later in section 3.3.2. The given parameters do not affect the horizontal and vertical force transmitted to the base at D and P . They do affect the force distribution in the legs which in turn causes a moment at the slider, M , which exists in the model because slider forces are transferred through the single point P rather than being distributed along the slider as they would be in reality. Since the forces and moments vary depending on the leg position, the parameters are best compared by integrating from the minimum to the maximum leg extension distance. Looking at the absolute of the integrated value for the moment at the slider in Figure 3.2 to Figure 3.4, it becomes apparent that when $\zeta = 90^\circ$, that is, when the parallel offset is horizontal as in 2b, the moment becomes independent of u and x . If a is then also $= 0$ (directly below the lower leg joint), there is no moment at all. Not only does this reduce the stress on the slider, this also minimizes the forces in the legs (no force goes towards moment), making this configuration advantageous. Figure 3.5 compares the sum of the leg forces for various configurations. Of course, horizontal disturbance and dynamic forces will likely introduce a moment, but zero static moment makes for the smallest moment overall.

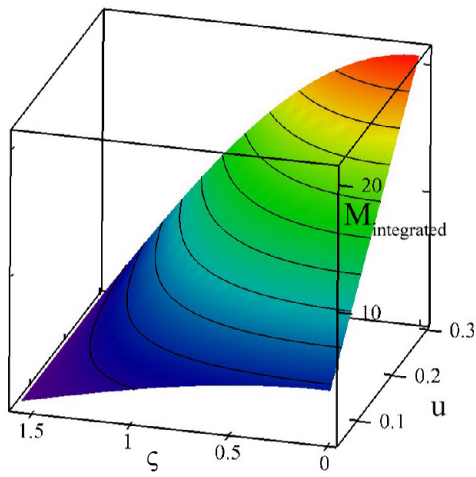


Figure 3.2: Integrated slider moment relative to parallel offset distance u (m) and offset angle ζ (rad) with horizontal offset $a = 0$ m. The moment becomes zero at $\zeta = 90^\circ$ when the offset is horizontal as in C2b.

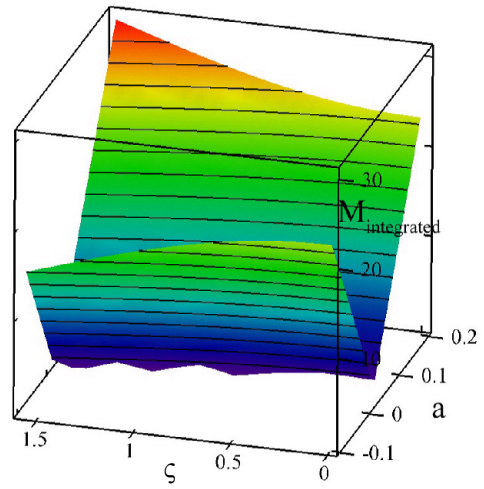


Figure 3.3: Integrated slider moment relative to horizontal offset a (m) and parallel offset angle ζ (rad) with $u = 0.1$ m. For all angles, the moment reaches a minimum at $a = 0$, with the absolute minimum of zero for $\zeta = 90^\circ$.

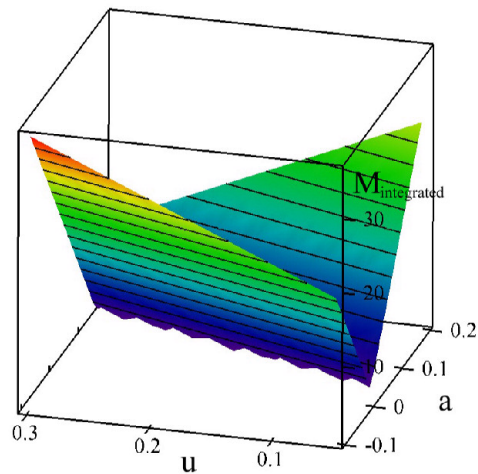


Figure 3.4: Integrated slider moment relative to horizontal offset a (m) and parallel offset distance u (m) with $\zeta = 0^\circ$ (upright). The moment is lowest at $a = 0$, no horizontal offset, and the smallest value of parallel offset, $u = 0.05$ m.

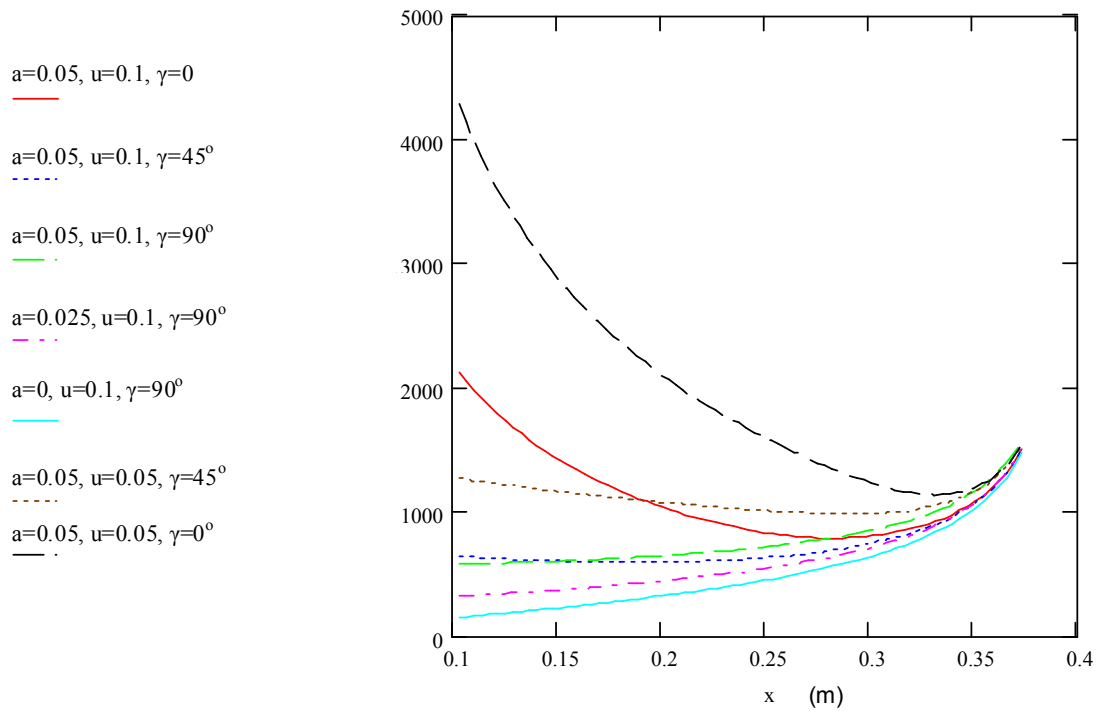


Figure 3.5: Summed upper and middle leg forces (N), taken along leg towards base for different parameter combinations; $\zeta = 90^\circ$, no horizontal offset ($a = 0$ m) is lowest.

3.1.2.4 Option C4

Option C4 has very similar behaviour to option C2 in the $\zeta = 90^\circ$ position. Both configurations have the same extension distance.

Comparing the pros and cons of option C2 with $\zeta = 90^\circ$ versus option C4:

- C2: Parallel mechanism with horizontal offset
 - Normally no force in upper leg
 - Requires more base width
- C4: Scissor mechanism
 - No upper leg; normally no force in part of leg above wheel past the centre joint
 - High part of platform extends outward with leg

The drawback of the linear guide over the wheel extending outwards with leg extension is minor, as a height of 60 cm fits under most tables. However, it would infringe upon Justin's workspace. To reduce this, the linear guide can be made to telescope, such that at full extension it would only extend upwards about 40 cm. Thus, the drawbacks of C4 are reduced; the drawback of C2, the increased width, cannot be removed. C4 is chosen as the optimum VFM.

3.2 Optimization of Selected Configuration

There are several options for executing the chosen configuration with corresponding trade-offs in terms of space requirements and optimal force distribution in the linkages. The primary concern common to all options is the limit of the extension angle of the leg; the closer this angle is allowed to come to the singular positions at 0° and 90° , the more severe the kinematic and kinetic issues, which tend to be proportional to the tangent of this angle.

The challenge in designing the leg mechanism is how to best leave room for the drive wheel. In the case of a caster wheel, which is offset from the vertical steering axis, the width of the envelope required for it to be able to rotate is the wheel diameter plus twice the caster offset distance. This means that the lower leg joint must be offset from the wheel centre as in Figure 3.6 a), either vertically as shown in cyan, horizontally as shown in green or somewhere in-between, introducing unwanted torques as discussed previously. Alternately, if the lower leg joint is to be attached coincident with the wheel axis, it must be offset significantly to either side, as shown in Figure 3.6 b). In order to allow the maximum leg length and consequently the largest extension distance, the joint should be as low as possible. However, putting the joint at or below the level of the wheel's horizontal axis means that the leg mechanism must be wider than the wheel diameter of 20 cm plus twice the caster offset, which could conflict with other components and the desired footprint size. Considering that the leg and wheel attachments are likely to add a few centimeters on either side, with a caster of 2 cm, this means a caster envelope width of 24 cm and a wheel unit width of around 30cm.

With a maximum height to the top of the base of 63 cm (see section 9.7.1) and a nominal ground clearance of 8 cm, the base itself is 55cm high. Assuming that at least 4 cm each at top and bottom are needed for structural components of the base and the leg slider, and leaving 2 cm for suspension travel, the maximum available space for the mechanism to move vertically is 45 cm if the lower leg joint at the wheel is mounted coincident with the wheel axle and offset to either side along the axis to be outside of the wheel & caster rotation envelope.

If the lower leg joint is placed above the wheel in order to keep the leg as narrow as possible, a loss in height consisting of the wheel radius, 10 cm, plus about 4 cm for mechanism and structural components, 2 cm for suspension travel and 4 cm for structural components at the top, leaves only 35 cm for the mechanism to move vertically.

In order to place the lower joint such that it does not protrude horizontally past the wheel envelope as shown in Figure 3.6 c), it needs to be at a height of 8.7 cm above the drive axle in its highest suspension travel. Subtracting 8.7 cm and another 2 cm for suspension travel from the bottom and 4 cm for structural components from the top, this leaves 40.3 cm.

Technically, the slider only needs to be long enough to accommodate the leg in its minimum angle position. This means the maximum leg length can be determined by equation 6.1:

$$l = \frac{y_{\max}}{\cos \theta_{\min}} \quad (3.1)$$

For a minimum angle of 10° , this gives a leg length of 40.9 cm, and for 15° , 41.9 cm. To allow a little bit of leeway, a leg length of 40 cm is chosen. The final arrangement with the chosen caster length (section 8.5.2.4) can be seen in Figure 8.35.

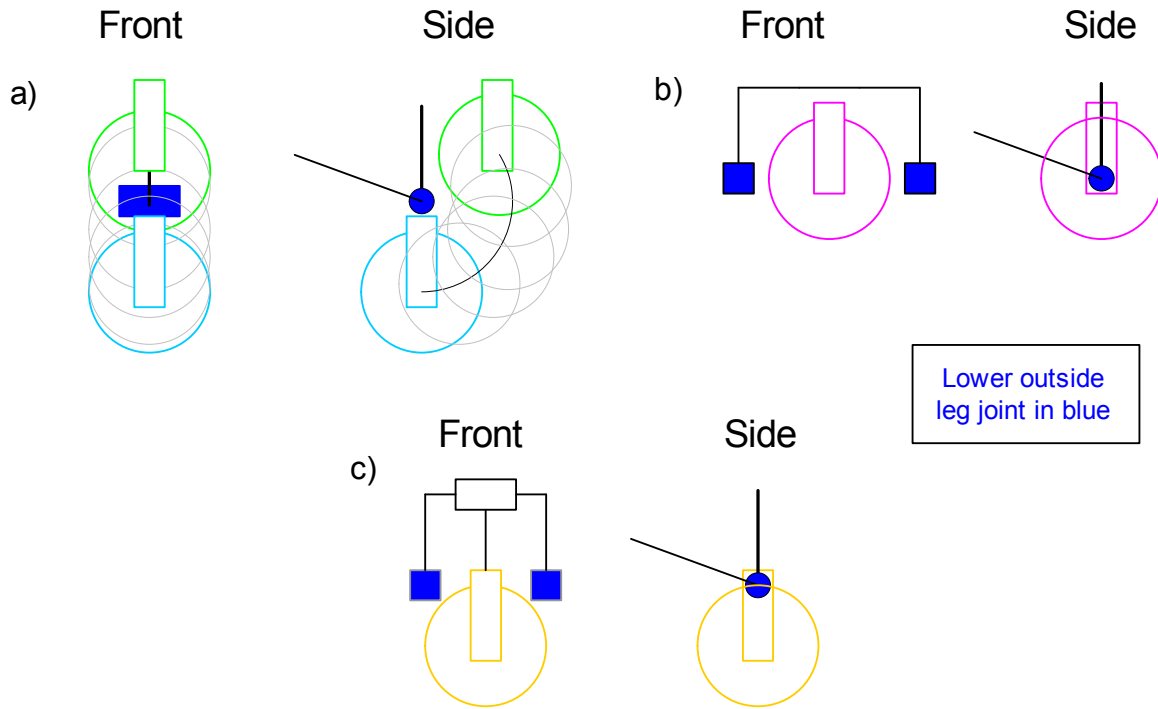


Figure 3.6: Three options for wheel placement in the VFM: (a) a single lower leg joint requires the wheel to be offset somewhere below or to the outside of the joint; (b) by splitting the leg, the lower leg joint can be located on either side of the wheel, eliminating the horizontal and vertical offset, but this makes the wheel unit quite wide; (c) a compromise is reached by splitting the leg joint *and* offsetting the wheel vertically so that the width of the wheel unit can be kept smaller.

3.3 Mechanism Kinetics

3.3.1 Kinematics

The VFM is a mechanism with 1 DoF consisting of two links and six joints, four rotational and two prismatic, that together constrain its motion to the x-direction while maintaining parallel sides. Kinematic parameters are shown in Figure 3.7.

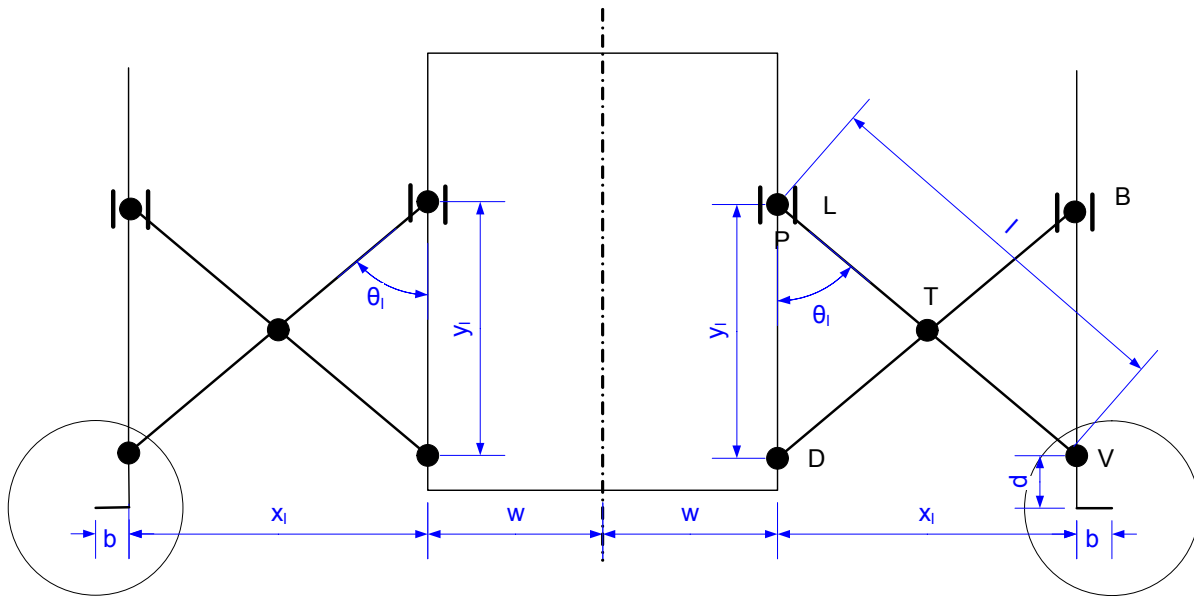


Figure 3.7: Variable definition for kinematic analysis.

The horizontal leg extension x and the vertical guide travel y depend on the leg length l and the leg angle θ (Figure 3.8) as shown in (3.2) and (3.3),

$$x = l \sin \theta \quad (3.2)$$

$$y = l \cos \theta. \quad (3.3)$$

Thus, the relationship between the leg extension distance and the vertical travel distance is non-linear (Figure 3.9),

$$y = \sqrt{l^2 - x^2} = x \tan \theta. \quad (3.4)$$

Differentiating gives the vertical speed,

$$\dot{y} = \frac{-x\dot{x}}{\sqrt{l^2 - x^2}} \quad (3.5)$$

or, using (3.3),

$$\dot{y} = -l\dot{\theta} \sin \theta \quad (3.6)$$

where the angular velocity is

$$\dot{\theta} = \frac{\dot{x}}{l \cos \theta} = \frac{\dot{x}}{y}. \quad (3.7)$$

Thus the vertical velocity can also be expressed in terms of the horizontal velocity and the leg angle by substituting (3.7) into (3.6),

$$\dot{y} = \dot{x} \tan \theta \quad (3.8)$$

Since the relationship is tangential, the vertical speed for any horizontal speed increases towards infinity as the leg angle approaches 90° .

Vertical slider acceleration can be found by differentiating again,

$$\ddot{y} = \ddot{x} \tan \theta + \dot{x} \dot{\theta} \sec^2 \theta. \quad (3.9)$$

and angular acceleration is

$$\ddot{\theta} = \frac{\ddot{x}}{l \cos \theta} + \frac{\dot{\theta}^2 \sin \theta}{\cos \theta} = \frac{\ddot{x}}{y} + \frac{\left(\frac{\dot{x}}{y}\right)^2 x}{y} = \frac{\ddot{x}y^2 + \dot{x}^2 x}{y^3}. \quad (3.10)$$

These relationships are shown in Figure 3.10 and Figure 3.11. The horizontal wheel offset b basically acts to alter the effective leg extension distance; it represents both a fixed wheel offset and a potential variable offset due to a caster wheel.

For a leg length of $l = 0.4$ m, the leg extension is 69.5 mm at 10° , 104 mm at 15° , 376 mm at 70° and 394 mm at 80° , as evident in Figure 3.8. From 10 to 80° , this leads to an extension distance of 324.5 mm; from 15 to 70° , a 306 mm extension. Further examples are given in Table 3.2.

Table 3.2: Horizontal extension distance (x in cm) for different leg lengths and extension angles

		Leg Angle ($^\circ$)			
		10	15	10	15
		70	70	80	80
Leg Length (cm)	start angle	35	40	45	+1
	end angle	26.8	30.6	34.5	0.77
		23.8	27.2	30.6	0.68
		28.4	32.4	36.5	0.81
		25.4	29.0	32.7	0.73

The vertical slider velocity needed to maintain a horizontal velocity of 1 m/s increases from 0.18 m/s to 2.75 m/s at 70° and 5.67 m/s at 80° . The acceleration increases even more rapidly from -2.6 m/s^2 at 10° to -62 m/s^2 at 70° and -477 m/s^2 at 80° (Figure 3.10). Note that this is just for a horizontal velocity; horizontal acceleration will increase the vertical acceleration further.

If instead the leg is actuated through a rotational joint, the rotational speed $\dot{\theta}$ is of interest; it too varies depending on the angle and increases sharply towards the extended position if a constant horizontal velocity (\dot{x}) is to be maintained, reaching 7.3 rad/s at 70° and 14.4 rad/s at 80° . The effect for acceleration is similar but even more pronounced.

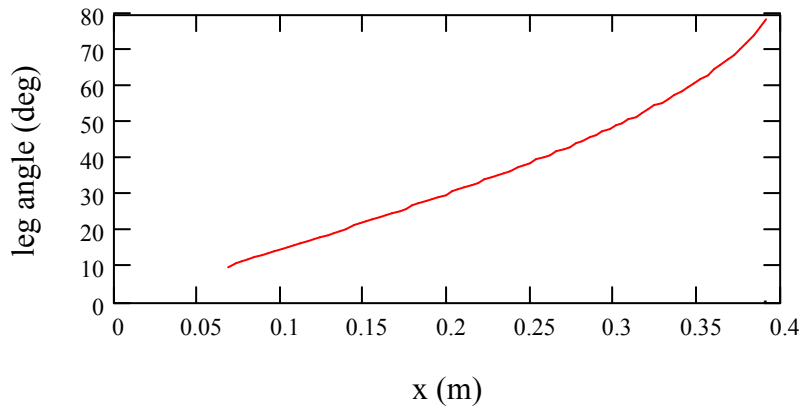


Figure 3.8: Leg angle is a non-linear function of leg extension distance (leg length $l = 0.4$ m).

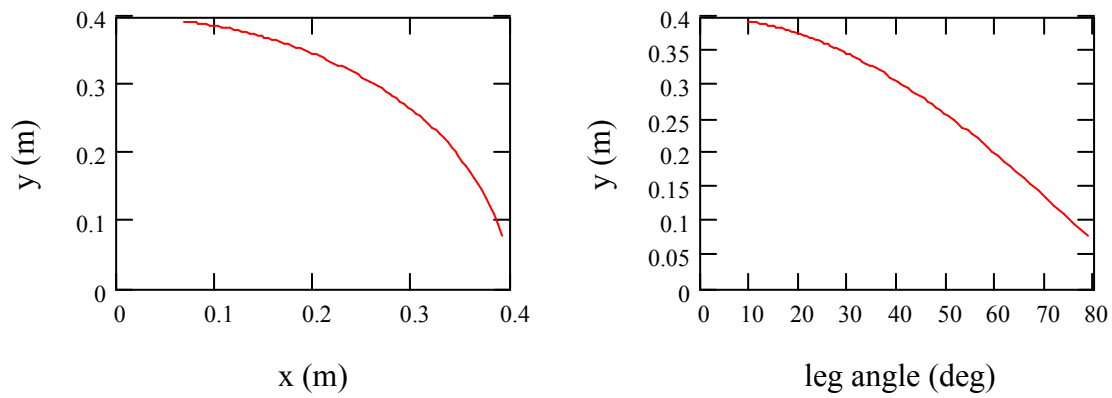


Figure 3.9: Vertical slider position relative to extension distance and angle (leg length $l = 0.4$ m).

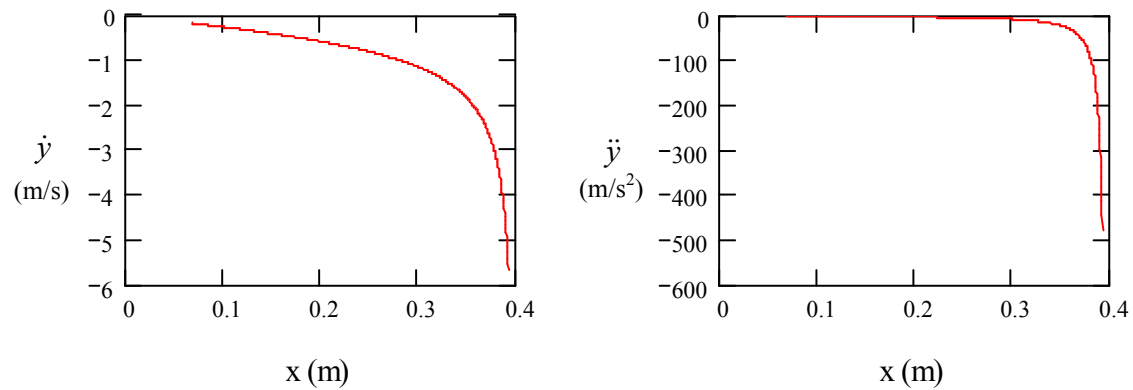


Figure 3.10: Vertical slider velocity and acceleration for a constant leg extension velocity of 1 m/s (no extension acceleration, leg length $l=0.4$ m).

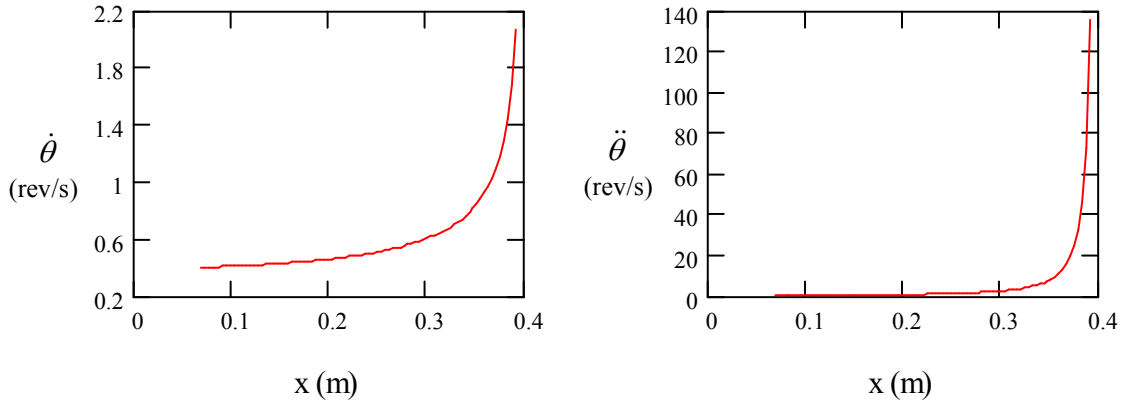


Figure 3.11: Leg angle velocity and acceleration for constant leg extension velocity (no extension acceleration, leg length $l = 0.4$ m).

3.3.2 Statics

For this initial analysis, the leg and wheel components are considered to be mass-less links; their mass is included in the system mass. The platform and upper body are modeled as one mass with a centre of gravity at c_b above the lower leg joint. Friction in the joints is ignored, as is wheel deflection. The free-body diagram in Figure 3.12 shows forces at the various connection points named in Figure 3.7, where force components are given the subscripts x for horizontal and y for vertical as well as L to indicate the left-hand side as shown in the figure.

Of particular interest are the forces on the two sliders at P and B—their horizontal components to determine the bearing load and resultant friction force in the slider, and the vertical component at P since this is one possible location to actuate the mechanism. Alternatively, the mechanism can be actuated at one of the rotary joints B, D, L or V, as suggested by the torque Γ . The analysis begins with actuation at the slider: P_y in place and Γ removed. The sliders are considered to have point contact with the rotational joint co-incident with the linear joint. Thus, reaction forces to the leg, L, are equal to forces on the body, P:

$$P_x = L_x \quad (3.11)$$

$$P_y = L_y. \quad (3.12)$$

Two links of length l with angle θ to the base vertical connect the wheel and wheel upright to the base. Because these ‘legs’ are pin jointed, no moment is carried through the joints, but the forces therein are not necessarily aligned with the leg, as they have three connection points. In x and y components, the forces in the leg link LV sum to:

$$-L_x + T_x + V_x = 0 \quad (3.13)$$

$$L_y + T_y + V_y = 0 \quad (3.14)$$

$$\left(V_x + L_x\right)\left(\frac{l}{2}\right)\cos\theta + \left(V_y - L_y\right)\left(\frac{l}{2}\right)\sin\theta = 0 \quad (3.15)$$

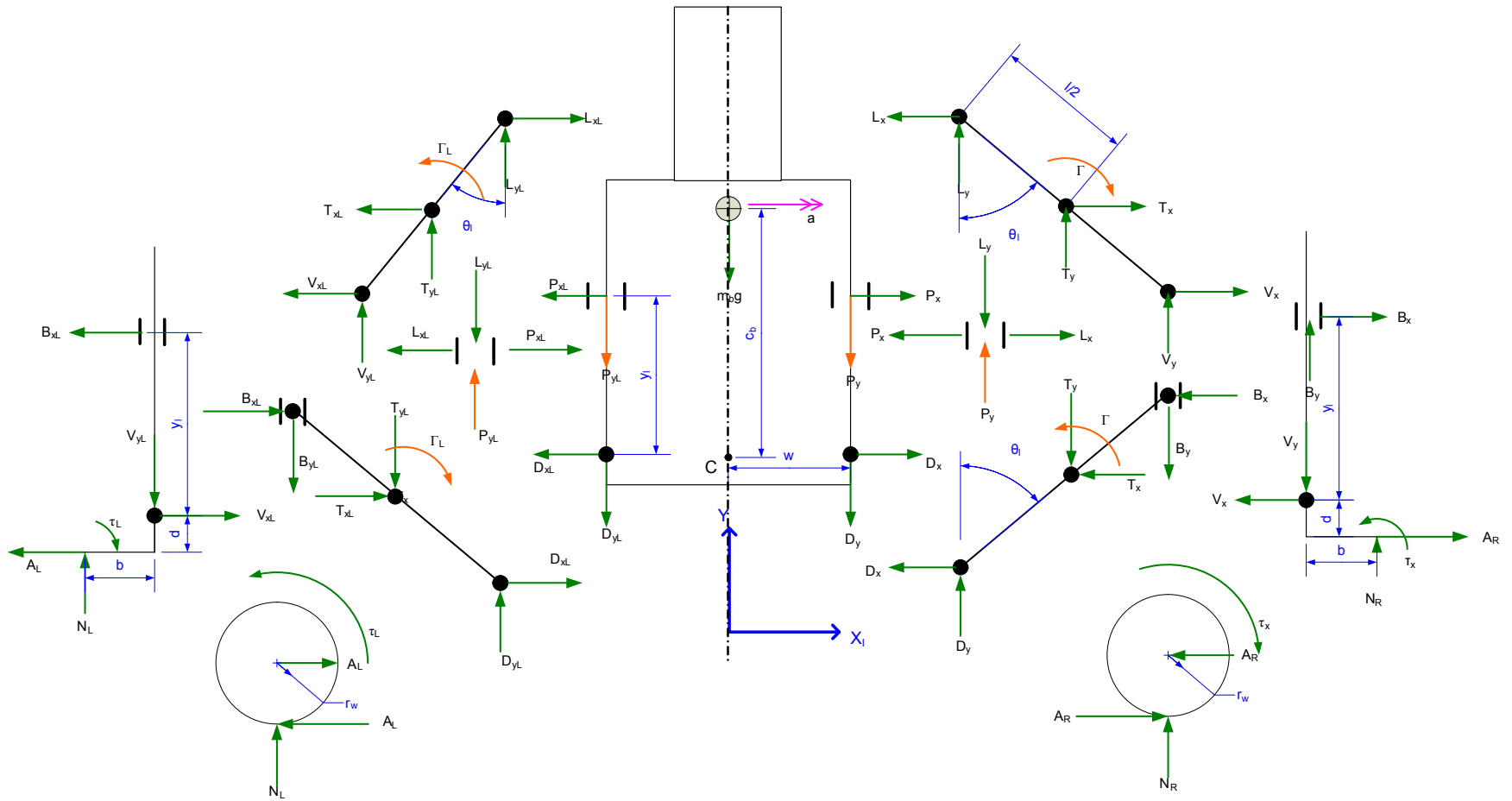


Figure 3.12: Free-body diagram of simplified static and dynamic analysis.

and in the leg link BD to:

$$-D_x - T_x - B_x = 0 \quad (3.16)$$

$$D_y - T_y - B_y = 0 \quad (3.17)$$

$$\left(-D_x + B_x\right)\left(\frac{l}{2}\right)\cos\theta - \left(D_y + B_y\right)\left(\frac{l}{2}\right)\sin\theta = 0. \quad (3.18)$$

The wheel upright has two design variables – the vertical and horizontal wheel offsets d and b respectively – and one operational variable, the vertical slider height y . Its forces sum to:

$$B_x - V_x + A_R = 0 \quad (3.19)$$

$$B_y - V_y + N_R = 0 \quad (3.20)$$

$$\tau_R + V_y b + V_x d - B_x(y + d) - B_y b = 0 \quad (3.21)$$

where τ_R is the applied torque of the drive motor. To remain static, the wheel of radius r_w must hold the moment

$$A_R r_w = \tau_R. \quad (3.22)$$

Finally, the base forces sum to:

$$P_x - P_{xL} + D_x - D_{xL} = 0 \quad (3.23)$$

$$-P_y - P_{yL} - D_y - D_{yL} - m_b g = 0 \quad (3.24)$$

$$\left(P_{yL} + D_{yL} - P_y - D_y\right)\left(\frac{b}{2}\right) - \left(D_{xL} + D_x\right)c_b + \left(P_x + P_{xL}\right)(y - c_b) = 0 \quad (3.25)$$

Similar force balances account for the left side of the system, resulting in $2 \times (3 \times 3 + 2 + 1) + 3 = 27$ equations and 30 unknowns. To solve the under-determined system, three unknowns must be chosen. Since the outside slider is freely sliding, assuming friction to be negligible, $B_y = 0$ and $B_{yL} = 0$. Lastly, the wheel torques are set to be equal,

$$\tau_R = -\tau_L \quad (3.26)$$

In the static condition shown with no acceleration, outside forces or applied torques,

$$\tau_L = \tau_R = 0. \quad (3.27)$$

Thus

$$A = A_L = 0. \quad (3.28)$$

Assuming the base and torso masses are centered, weight is distributed equally if all legs are extended an equal amount as shown in this 2D simplification, and the normal force is simply

$$N = N_L = \frac{1}{4} \left(m_b + m_{upper}\right) g. \quad (3.29)$$

This load is then carried through the lower part of the leg connecting the bottom of the wheel upright to the top of the base (VT). From there, it goes through the lower part of the other leg to the base (TD). Thus,

$$V_y = V_{yL} = -T_y = -T_{yL} = -D_y = -D_{yL} = N. \quad (3.30)$$

If there is a wheel offset, the horizontal force V_x in the bottom outside leg joint and the horizontal force at the top of outside leg joint are non-zero, equal in magnitude but opposite in direction, and depend also on the leg position,

$$V_x = B_x = B_{xL} = V_{xL} = \frac{1}{4} m_b g \frac{b}{y}. \quad (3.31)$$

Because b is small and y relatively large, the force is fairly small, reaching only 92 N at 80° with a system mass of 130 kg; some forces for different configurations are shown in Figure 3.13.

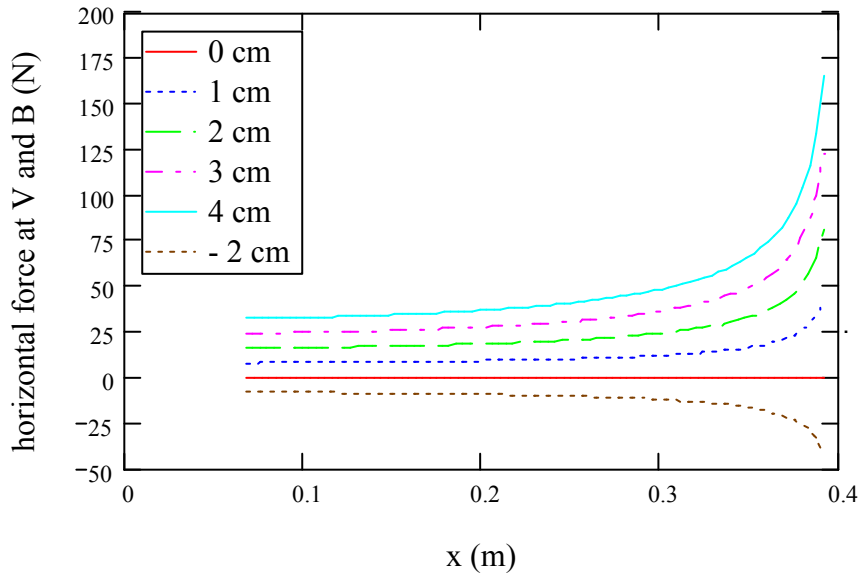


Figure 3.13: Horizontal forces at V and B due to horizontal wheel offset b in static equilibrium.

At the wheel intersection point T , the horizontal force consists of

$$T_x = T_{xL} = \frac{1}{4} m_b g \frac{x}{y} + \frac{1}{2} m_b g \frac{b}{y} \quad (3.32)$$

where the second term is relatively small due to b , but the first term gets very large as the leg angle increases because $x/y = \tan \theta$. The same forces relating to the tangent of the leg angle are transferred to the bottom inner leg joint at D and in opposite direction at the top inner leg joint at L/P , where they push into the base. Both see only half of the smaller force due to the wheel offset b compared to the point T —the effect is the same as extending the leg out by the additional amount b ,

$$-D_x = -D_{xL} = L_x = L_{xL} = \frac{1}{4} m_b g \frac{x}{y} + \frac{1}{4} m_b g \frac{b}{y}. \quad (3.33)$$

Thus, horizontal loading of the linear slider bearing at L/P increases sharply towards the higher range of leg extension (Figure 3.14), increasing to 875 N at 70° ($x = 0.374$ m) and 1808 N at 80° ($x = 0.394$ m) with no offset.

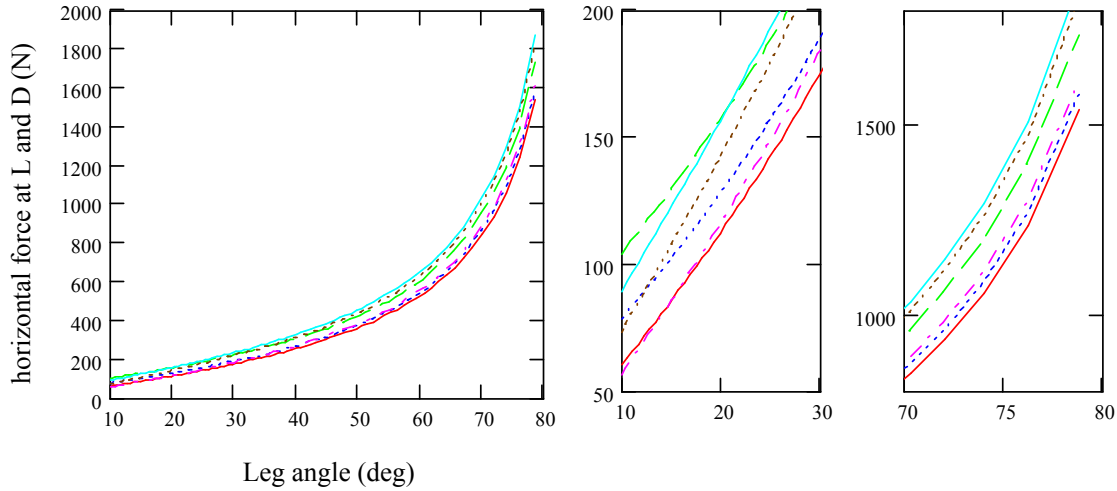


Figure 3.14: Horizontal force into base at L and out of base at D , static equilibrium condition, for different horizontal wheel offsets (b). Legend as in Figure 3.13.

Unlike the bottom inner leg joint, at the top inner leg joint on the slider at L , there is, in this situation, no vertical force,

$$P_y = P_{yL} = L_y = L_{yL} = 0 \quad (3.34)$$

This is a very important result, because it means that no actuation force is necessary to hold the system in a static state and the force needed to activate the leg mechanism does not need to work against the normal load. There will be static friction that opposes motion; typical rolling element linear bearings have coefficients of friction between 0.002 and 0.005. Using the later figure, the worst case frictional force in the static condition is 4.4 N at 70° ($x = 0.374$) and 9 N at 80° ($x = 0.394$) with no offset. When the leg mass is included in the analysis, it acts to pull the leg down and out with its gravitational force,

$$P_y = m_{leg} g . \quad (3.35)$$

The horizontal wheel offset is detrimental in that it introduces horizontal loading on the slider at B , which would otherwise be unloaded in the static condition, at the bottom outer leg joint at V , and adds to T , L and D , albeit in a relatively small way. If the offset is zero, loading on the upper portion of the wheel upright and the upper portion of the leg connected to it (VB , BT) are zero, which would appear to make these components unnecessary, however, they are essential for keeping the wheel upright and attached steering mechanism parallel to the base, counteracting the drive torque. With the wheel axle below the lower wheel upright leg joint, any horizontal force on the wheel will also produce a torque which a horizontal force in the upper joint must help counter. These members play a further role once dynamic forces are considered. Similarly, the vertical wheel offset d does not come into the static analysis, but will become a factor when sideways disturbance and acceleration forces are considered.

3.3.3 Dynamics

The static model presented above is extended to include the dynamic effects of linear platform acceleration by changing equation (3.23) to be

$$P_x - P_{xL} + D_x - D_{xL} = m_b a, \quad (3.36)$$

where a is the acceleration in the X-direction. The mass of the wheel and leg continue to be neglected. The force is provided by the external torque, which becomes

$$-\tau_L = \tau_R = \frac{1}{4} m_b a r_w. \quad (3.37)$$

This exerts a horizontal force at the centre of the tire,

$$-A_L = A_R = \frac{1}{4} m_b a, \quad (3.38)$$

which causes the top outer leg joint slider to have an increased horizontal load as seen in Figure 3.15,

$$B_x = \frac{1}{4} m_b a \frac{dh + r_w h - bc_b}{(b+h)y} + \frac{1}{4} m_b g \frac{b}{y} \quad (3.39)$$

$$B_{xL} = -\frac{1}{4} m_b a \frac{dh + r_w h - bc_b}{(b+h)y} + \frac{1}{4} m_b g \frac{b}{y}. \quad (3.40)$$

where

$$h = x + w \quad (3.41)$$

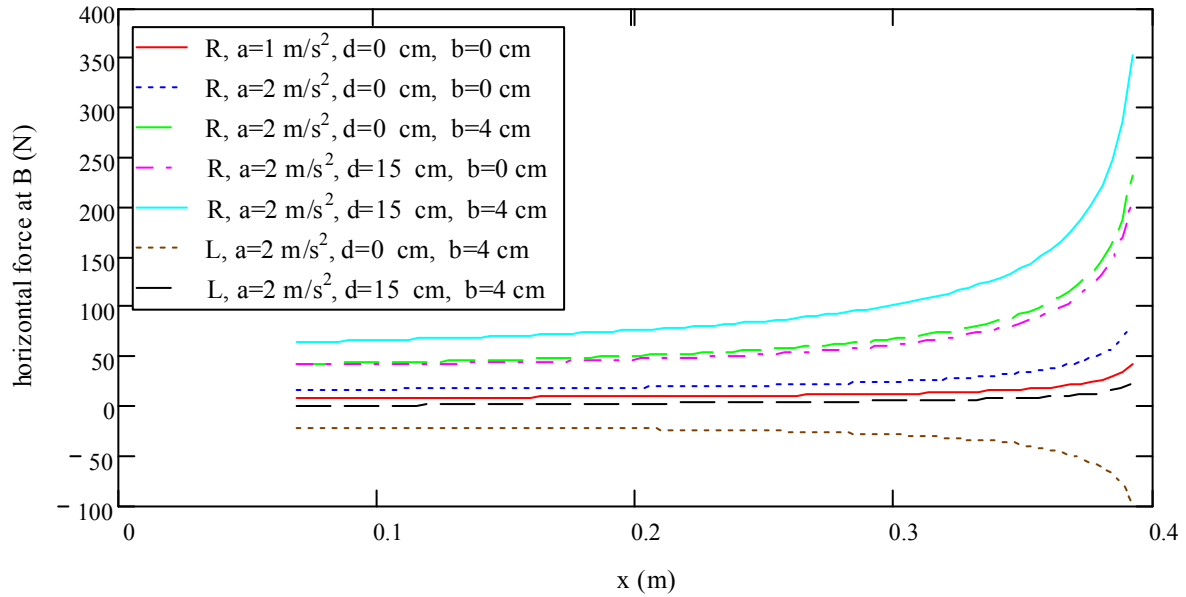


Figure 3.15: the horizontal force at the outer slider (B_x) at various configurations and accelerations.

Integrating B_x over x at $a = 2 \text{ m/s}^2$ to look at the overall effect of d and b on all parts of the system, we see that d and b are linearly related to B_x and that b has a much greater effect than d (Figure 3.16).

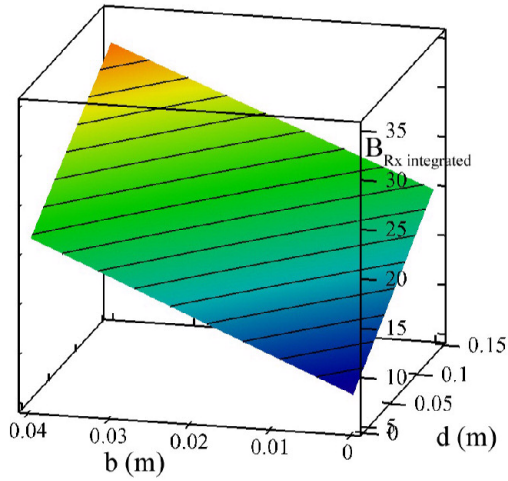


Figure 3.16: B_x integrated over leg extension to show linear dependence on horizontal offset b and vertical offset d with acceleration of 2 m/s^2 .

The horizontal force at V is also increased, as shown in Figure 3.17.

$$V_x = \frac{1}{4} m_b \left[a + a \frac{vh}{(b+h)y} + a \frac{r_w h - bc_b}{(b+h)y} - g \frac{b}{y} \right] \quad (3.42)$$

$$V_{xL} = \frac{1}{4} m_b \left[-a - a \frac{vh}{(b+h)y} - a \frac{r_w h - bc_b}{(b+h)y} + g \frac{b}{y} \right] \quad (3.43)$$

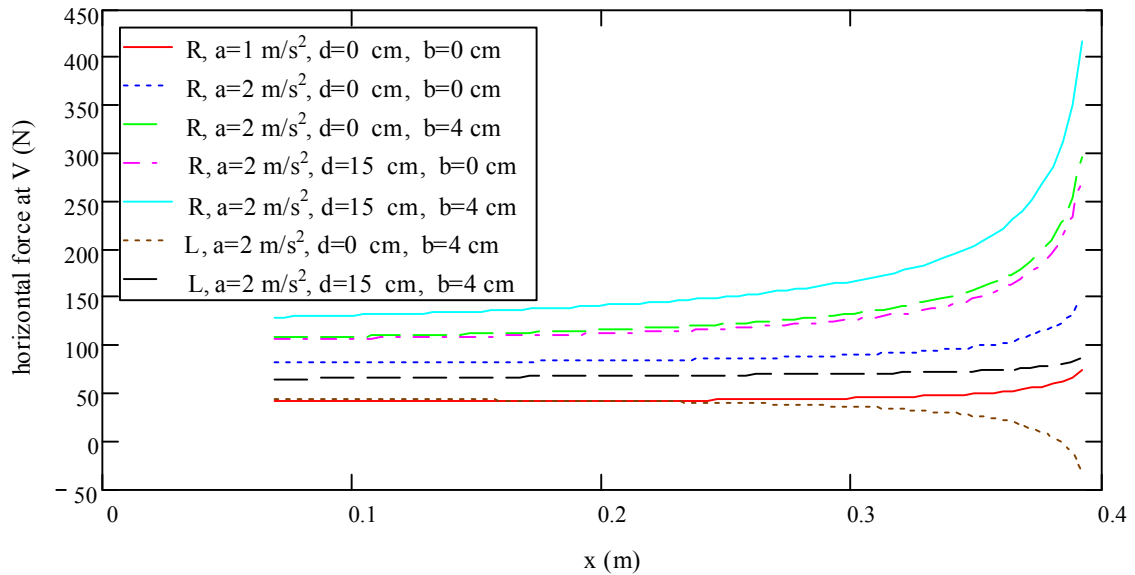


Figure 3.17: Horizontal force at the bottom outer leg joint (V_x) for various configurations and accelerations.

With the platform at its maximum acceleration, but the leg extension fixed, the weight shifts to the rear tire (the one opposite the direction of acceleration) by an amount that depends on the wheelbase at that moment – a smaller wheelbase (legs retracted) causes a larger weight shift (Figure 3.18). This effect on the normal forces is made slightly more pronounced by a vertical wheel offset (d). N_L and N_R are integrated in the same fashion as B_x ; Figure 3.19 shows the linear relationship to b and d .

$$N_R = \frac{1}{4} m_{sys} [g - aY] \quad (3.44)$$

$$N_L = \frac{1}{4} m_{sys} [g + aY] \quad (3.45)$$

where

$$Y = \frac{d + r_w + c_b}{b + h}, \quad (3.46)$$

which is the vertical distance to the CM over the horizontal distance to the wheel contact point.

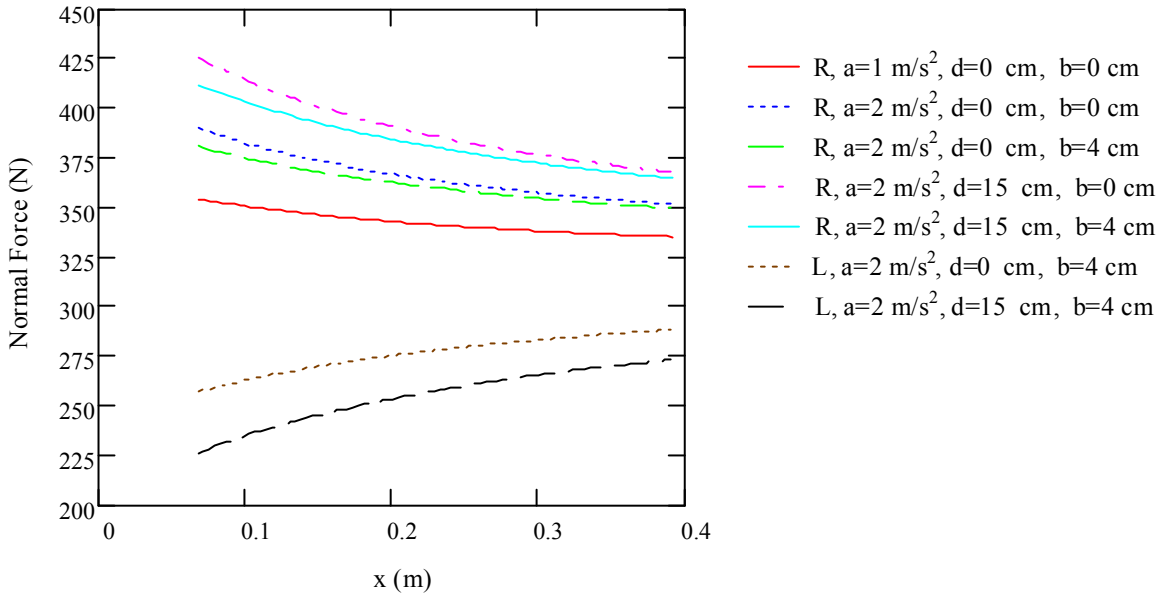


Figure 3.18: Normal force N at tire (L is left and R is right) for various configurations and accelerations.

This weight shift due to acceleration is also apparent at the inside lower leg joint D ,

$$D_y = -\frac{1}{4} m_{sys} \left[g - aY + a \frac{y}{x} \right] \quad (3.47)$$

$$D_y = -\frac{1}{4} m_{sys} \left[g + aY - a \frac{y}{x} \right]. \quad (3.48)$$

The ground friction for the left and right wheel, $\mu_{Lground}$ and $\mu_{Rground}$, that is necessary to allow an acceleration of the platform with a certain effective wheelbase and centre of mass height can be found as follows:

$$\mu_{Rground} = \frac{A_R}{N_R} = \frac{\frac{1}{4} m_{sys} a}{\frac{1}{4} m_{sys} [g - aY]} = \frac{a}{g - aY} = \frac{a}{g - aY} \quad (3.49)$$

$$\mu_{Lground} = \frac{a}{g + aY} \quad (3.50)$$

Thus at 2 m/s², the front (right) wheel needs a friction coefficient of up to 0.31 with $d = 0.15$ m and $b = 0.04$ m as seen in Figure 3.20.

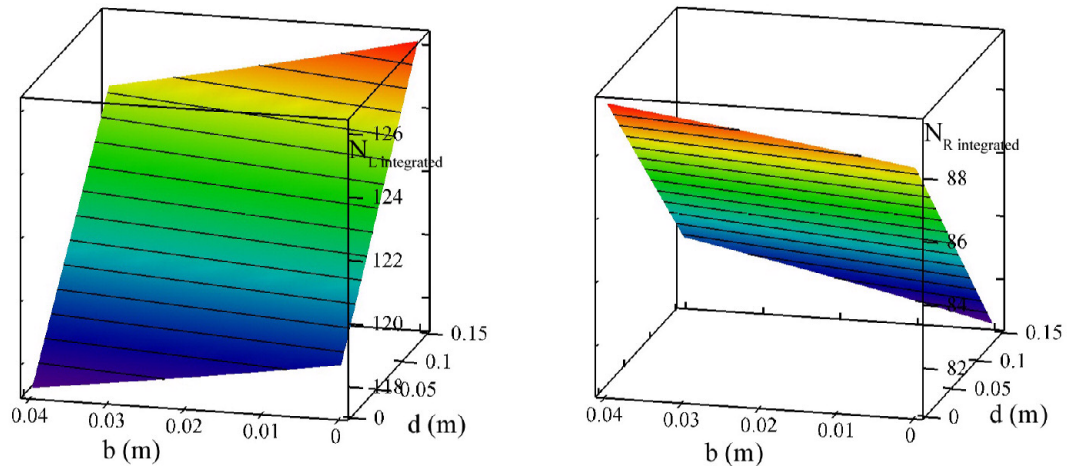


Figure 3.19: N_L and N_R (left and right) integrated over x to show linear relationship to b and d , acceleration of 2 m/s².

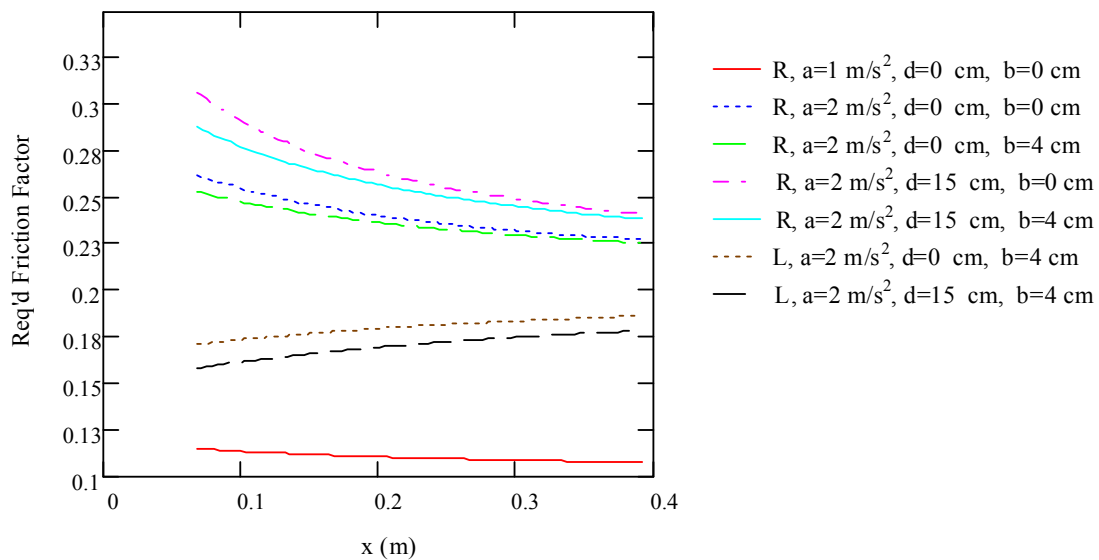


Figure 3.20: The ground friction factor necessary for given acceleration depends on the wheel offset b , the vertical offset d and the leg extension x .

The acceleration of the body mass causes a slight difference in horizontal forces between one side of the body and the other (L_x/P_x , D_x).

$$L_x = \frac{1}{4} m_b \left[g \frac{(b+x)}{y} - a \frac{w(d+r_w) - c_b(x+b)}{(b+h)y} \right] \quad (3.51)$$

$$L_{xL} = \frac{1}{4} m_b \left[g \frac{(b+x)}{y} + a \frac{w(d+r_w) - c_b(x+b)}{(b+h)y} \right] \quad (3.52)$$

$$D_x = \frac{1}{4} m_b \left[-g \frac{b+x}{y} - a - a \frac{w(d+r_w) - c_b(x+b)}{(b+h)y} \right] \quad (3.53)$$

$$D_{xL} = \frac{1}{4} m_b \left[g \frac{b+x}{y} + a + a \frac{w(d+r_w) - c_b(x+b)}{(b+h)y} \right] \quad (3.54)$$

At -2 m/s^2 , this increases the horizontal force inwards at L and outwards at D to a maximum of 2088 N at 80° and 1017 N at 70° , both with a 4 cm horizontal offset and no vertical offset (Figure 3.21). This rise in normal force on the slider of course affects the friction in the linear bearing, increasing it to a maximum of 10.4N and 5.1N respectively.

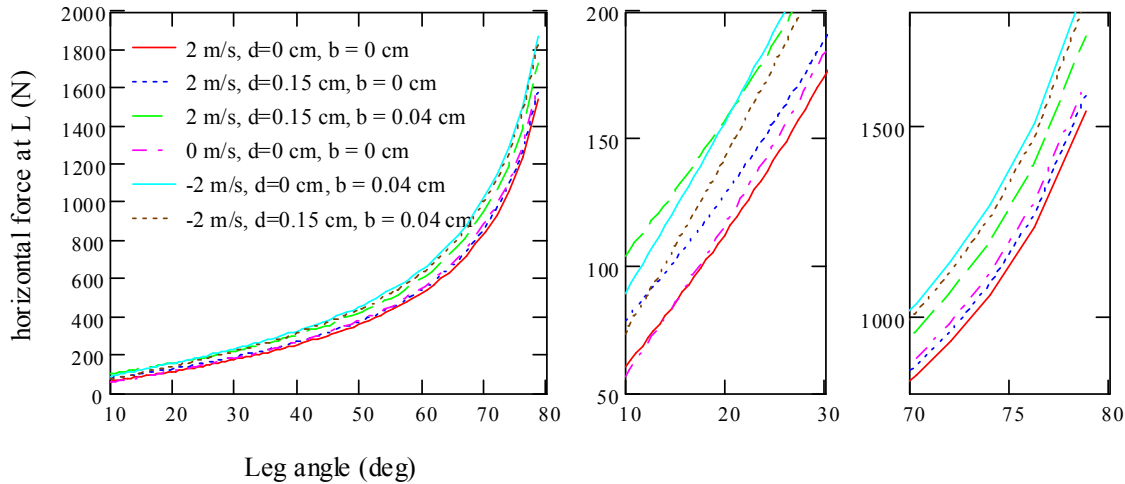


Figure 3.21: Horizontal force at right (front) side slider/top inner leg joint with acceleration and varying configurations.

In addition to the frictional force opposing any motion at the slider, the acceleration creates a significant vertical force of up to 369 N at 10° and 242 N at 15° at the body slider (L_y) that must be opposed by P_y if the leg is to be prevented from retracting on the side in the direction of motion (right) and extending on the opposite side (left). Note that extending opposite the acceleration direction would actually increase the platform's stability while the retraction occurs at the leg that experiences less normal load due to the acceleration. This force is unaffected by the wheel offsets (d and b).

$$L_y = -L_{Ly} = \frac{1}{4} m_b a \frac{y}{x} \quad (3.55)$$

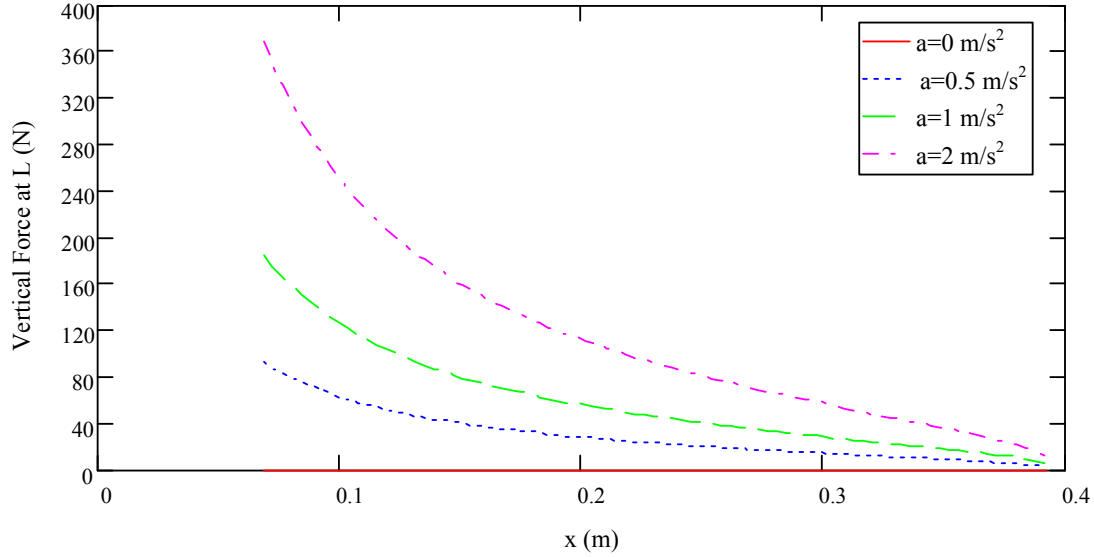


Figure 3.22: Vertical force in slider (at L) due to acceleration; upwards on forward (right) side, downwards on left (rear). If not counteracted, slider will retract/extend.

If the leg mass of each leg, m_b , is included in the analysis as a point mass at T , the vertical force that must be applied to the slider becomes

$$L_{,y} = \left(\frac{1}{4} m_b + m_l \right) a \frac{y}{x} + 2m_l g \quad (3.56)$$

$$L_{,yL} = - \left(\frac{1}{4} m_b + m_l \right) a \frac{y}{x} + 2m_l g, \quad (3.57)$$

which means that the weight of the legs must be opposed. The leg mass also adds to the acceleration load.

Instead of applying a force at the slider, a torque Γ could be applied at any of the rotational joints (L , T , B , D). The applied vertical slider force P_y is removed and thus L_y becomes zero. At the centre joint, this torque would be

$$\Gamma = \frac{1}{8} m_b a y = \frac{1}{8} m_b a l \cos(\theta). \quad (3.58)$$

At the top inner leg joint (L), bottom outer leg joint (V), the top outer leg joint (B) and the bottom inner leg joint (D), the torque to hold the VFM in position is

$$\Gamma = \frac{1}{4} m_b a y. \quad (3.59)$$

These all have the advantage that they vary with the cosine rather than the tangent of the leg angle and as such do not approach infinity towards zero leg angle (Figure 3.23), though this is offset by the speed of the joint not going to zero at zero leg angle (Figure 3.11). The torque is half as large at the centre as at the other joints, although the centre joint must move twice as fast as the other joints, making the power requirements the same. Including the leg mass makes the torque in the centre joint,

$$\Gamma = \frac{1}{8}m_b ay + \frac{1}{2}m_l ay + \frac{1}{2}m_l gx \quad (3.60)$$

$$\Gamma_L = \frac{1}{8}m_b ay + \frac{1}{2}m_l ay - \frac{1}{2}m_l gx \quad (3.61)$$

and in the other joints,

$$\Gamma = \frac{1}{4}m_b ay + m_l ay + m_l gx \quad (3.62)$$

$$\Gamma_L = \frac{1}{4}m_b ay + m_l ay - m_l gx \quad (3.63)\text{Å}$$

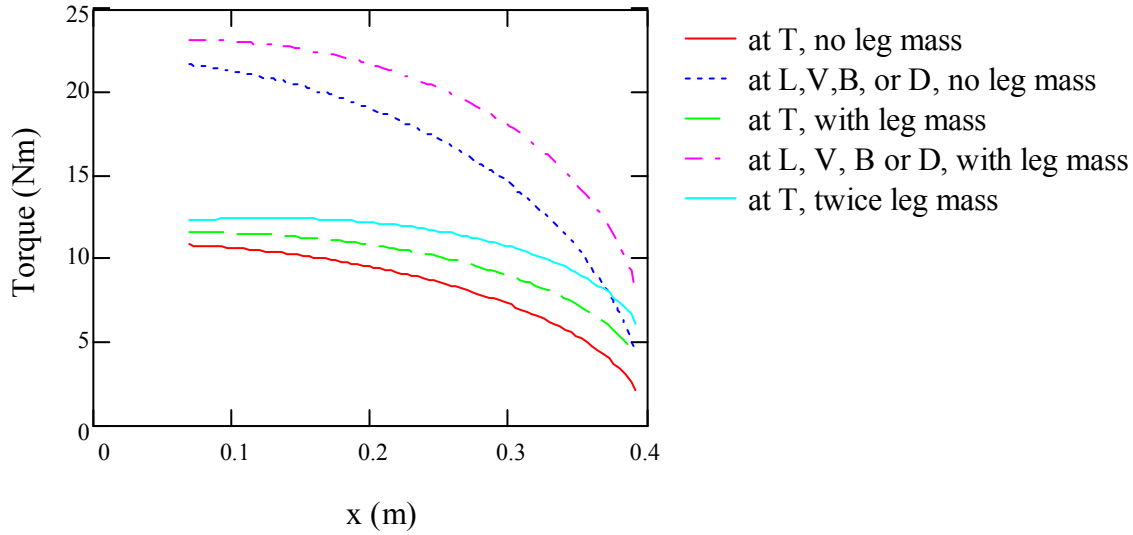


Figure 3.23: Torque to hold leg at 2 m/s² with and without leg masses of 1kg/leg for varying actuation positions

Including the mass of the legs and the wheel uprights separately from the body does not change the trend of the other results, nor does it affect the values very much if at all, generally resulting in a slight reduction. The difference in normal force for instance is about 1% less when the legs and wheel uprights are modeled with masses at their centres of 1 kg and 3 kg respectively. B_x stays the same, V_x and V_y are slightly reduced, L_x and L_y are reduced about 10% at peak, D_x and D_y about 14%.

The static and dynamic analyses show that it is beneficial to avoid a horizontal and vertical wheel offset, with the horizontal offset b having the much more significant effect. Horizontal forces at the base increase greatly past a 70° (0.374 m) leg extension, while vertical forces increase somewhat towards a smaller leg extension. Linear acceleration causes significant forces that will retract/extend the leg mechanism if they are not counteracted and also increases loading on the side of the platform away from the acceleration.

3.3.3.1 Leg Extension Limits

To limit VFM forces, velocities and accelerations, it is decided to limit the maximum leg extension angle to 70°. Limiting the minimum leg extension to 15° provides enough space for the leg components and the caster wheel in the retracted position with the wheel located under the lower outside leg joint, and also reduces some forces.

3.3.4 Simulation

A dynamic multi-body simulation was performed in the Dymola/Modelica environment using an accurate model of the upper body and a lower body set up as described in Table 8.2 and shown in Figure 3.24. This closely resembles the anticipated design.

Table 3.3: Simulation parameters

Component	Geometry	Mass	Inertia
Justin	Torso, arms & head as designed. Hands: CM 10 cm from end of hand	Torso: 49 kg Arms: 13 kg Head: 2.5 kg Hands: 1.8 kg Load: 3 – 15 kg	Torso, arms & head as designed. Hands: $I_{xx} = I_{yy} = I_{zz} = 0.001$ Load: $I_{xx} = I_{yy} = I_{zz} = 0.001$
Body	Height: 55 cm Radius: 0.2 m	45 kg	uniform cylinder
Ground Clearance	0.08 m		
Legs	Length: 0.4 m 0.04 m outer and 0.03 m inner diameter	1 kg each	hollow cylinder
Suspension	$k = 40000$ N/m, $c = 2344$ Ns/m		
Wheel Upright	Vertical offset: 0.087 m Horizontal offset: 0 m	2.5 kg	point mass
Wheels	Radius: 0.1 m Width: 0.05 m Caster: 0.02 m	0.5 kg	torus
TOTAL		115 kg plus load	

Unlike the previous simplified analysis, the simulation is three-dimensional and does not reduce the system to two wheels. It uses the proper design geometry where the legs are not directly opposite one-

another; simulation results for configurations that match the simplified analysis are similar, though the additional detail in the simulation model causes some difference that should give a more realistic result. For instance, the acceleration affects all bodies, and angular acceleration in the horizontal plane is possible due to the suspension, which allows a pitch angle. Furthermore, more complex scenarios can be investigated in 3D simulation. More details about the simulation environment including its limitations can be found in Appendix B.

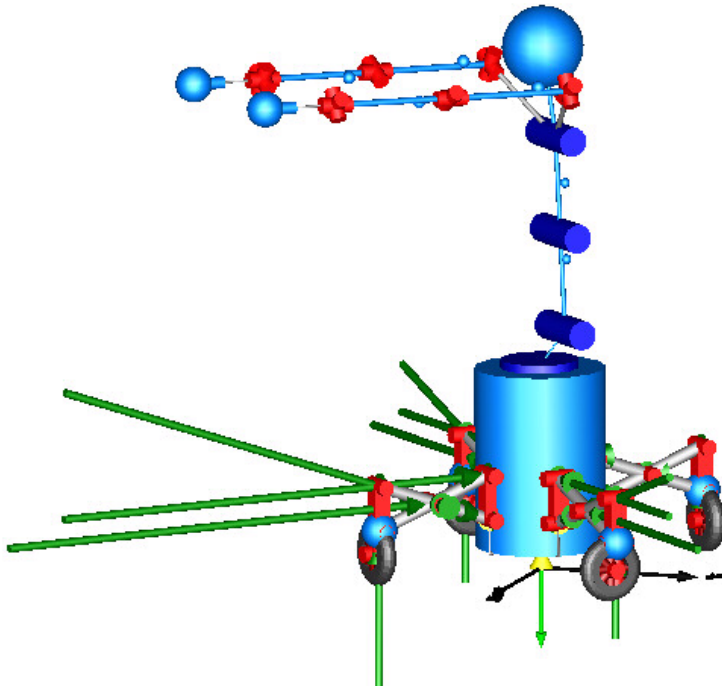


Figure 3.24: Dymola model. Green arrows show forces at various points; system currently at rest.

Forces at points described in the static and dynamic analyses in the previous sections are plotted and discussed for various conditions below. Forces are resolved in the leg frame, with direction x along the leg horizontally and positive towards the outside of the leg, y is horizontally perpendicular to the leg, and z is positive down. The legs are held in position by a torque at the leg centre (T). The wheels are velocity controlled. For the linear acceleration experiments, the wheels start aligned with the acceleration direction and have a trailing caster. Differences between simulations with caster and without caster are not large and seem to correspond to the change in wheelbase; the ‘no caster’ situation appears to lie in the middle of values from the caster oriented in and caster oriented out. For the angular acceleration experiments, the wheels start perpendicular to the base and are then oriented by the control system.

3.3.4.1 Linear Acceleration

Linear acceleration adds loading on the side opposite the direction of acceleration. Forces will be higher if that side already is loaded due to the upper-body position and load; this is explored in five cases, 1a through 1d, as detailed in Table 3.4.

The first case, 1ref, is set up to resemble the earlier simplified dynamic analysis as much as possible by attempting to put the centre of mass near the platform centre. The results are similar; for instance, in steady state, P_x is 1065 N versus 1017 N in the simplified analysis, the holding torque is 3.7 Nm versus 4.4 Nm.

Table 3.4: Linear acceleration simulation cases

Case	Movement	Leg Extension	Upper-Body Position	Payload	Figures
1ref	-2 m/s ² at 45 ° (in line with leg 2 & 4)	70°	Torso rotation: 0 (facing away from acceleration). Torso vertical, arms vertical down	15 kg	Figure 3.25 & Figure 3.26
1a	-2 m/s ² in x-direction at 2 s	70°	Torso rotation: 0 (facing away from acceleration). Torso vertical, arms horizontal (away from acceleration)	15 kg	Figure 3.27, Figure 3.31, Figure 3.32
1b	-2 m/s ² at 45 ° (in line with leg 2 & 4)	70°	Torso rotation: 45° (facing away from acceleration) Torso vertical, arms horizontal	15 kg	Figure 3.28, Figure 3.33
1c	-2 m/s ² at 45 ° (in line with leg 2 & 4)	36.9° (half-way)	Torso rotation: 45° (facing away from acceleration) Torso vertical, arms horizontal	3 kg	Figure 3.29, Figure 3.34
1d	-2 m/s ² at 45 ° (in line with leg 2 & 4)	70°	Torso rotation: 45° (facing away from acceleration) Torso horizontal , arms horizontal,	3 kg	Figure 3.30

Comparing case 1a to case 1b shows that linear acceleration in a direction along a leg puts a higher load on the opposing rear leg in case 1b than when acceleration is in a direction between two legs. This is expected since in the former case the high load on the side over which the torso is leaning is split evenly between legs 1 and 2, while with the later it rests primarily on leg 2, with lesser loading being split between legs 1 and 3. The legs facing the acceleration direction, 3 and 4 in the first case and leg 4 in the second case, have the lowest loading.

Notable in these results is the oscillation in force, which occurs due to the suspension and associated weight shift. This oscillation causes a higher peak force shortly after the acceleration begins before decaying to a steady state value caused by the suspension's damping. In particular, Figure 3.31 shows how in case 1a the acceleration causes a change in pitch angle with some

overshoot. During the overshoot, the leg facing the acceleration direction (leg 4) actually loses ground contact (the suspension force goes to zero).

In case 1c, the legs are retracted to their half-way position (37°), which is close to the minimum that still allows stable acceleration with a 3 kg load, the torso is in an upright position and the arms are held horizontal opposite to the acceleration direction. A simulation with legs at 30° was found to be unstable. This condition exhibits the highest holding torque, which agrees with theory in that torque should increase at smaller leg extensions, however it significantly exceeds the value predicted, particularly during early transient response at about 2.5 s. The forces in leg 2, the leg with the highest loading, on the other hand are smaller than in case 1b.

With the legs extended, it is also possible to accelerate a 3 kg load with the arms *and* torso horizontally extended. This requires a torque on leg 2 that is somewhat higher than case 1b, as shown in Figure 3.30.

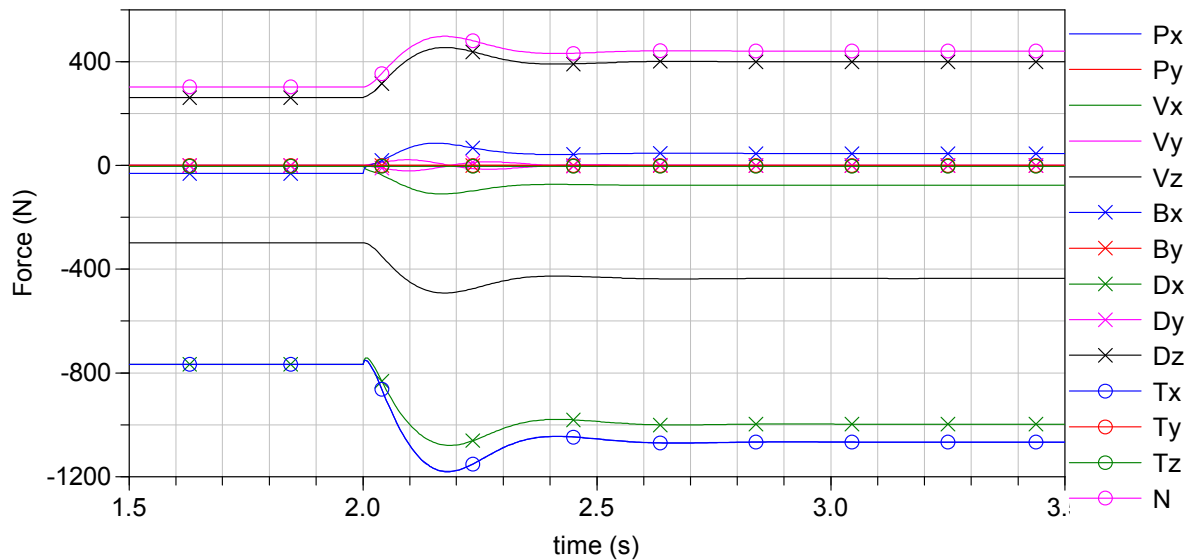


Figure 3.25: Case 1ref, torso vertical & arms down - forces on leg 2 (opposite acceleration direction). Steady-state values of simulated forces shown are similar to the simplified dynamic analysis in 3.3.3, for instance P_x is 1065 N versus 1017 N in the simplified analysis.

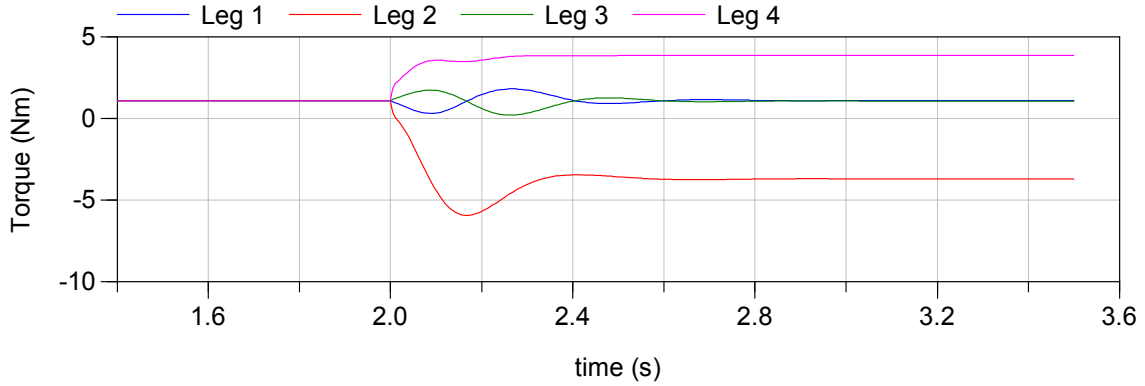


Figure 3.26: Case 1ref - torque at joint T to hold legs in position; the steady state value for leg 4 of 3.7 Nm corresponds reasonably with the value of 4.4 Nm found during the simplified dynamic analysis.

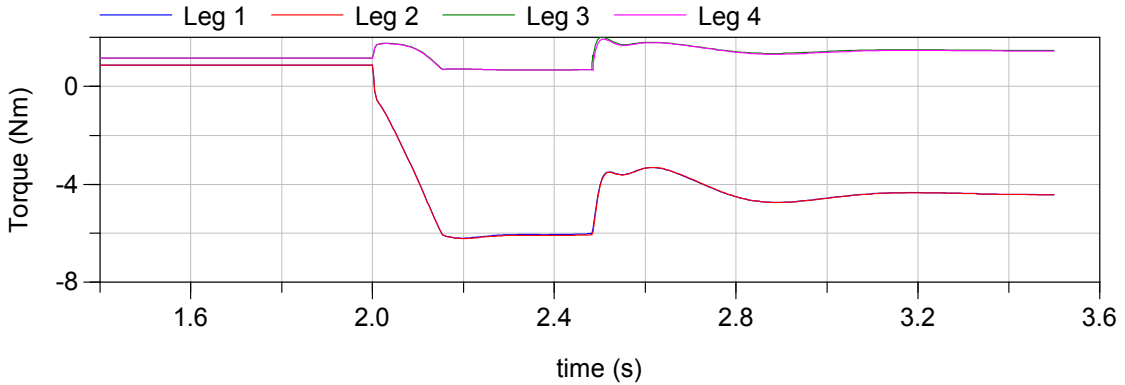


Figure 3.27: Case 1a - torque to hold leg position. Torque for the two pairs of legs is the same; the pair opposite the acceleration/underneath the extended arms increases during acceleration at 2 s.

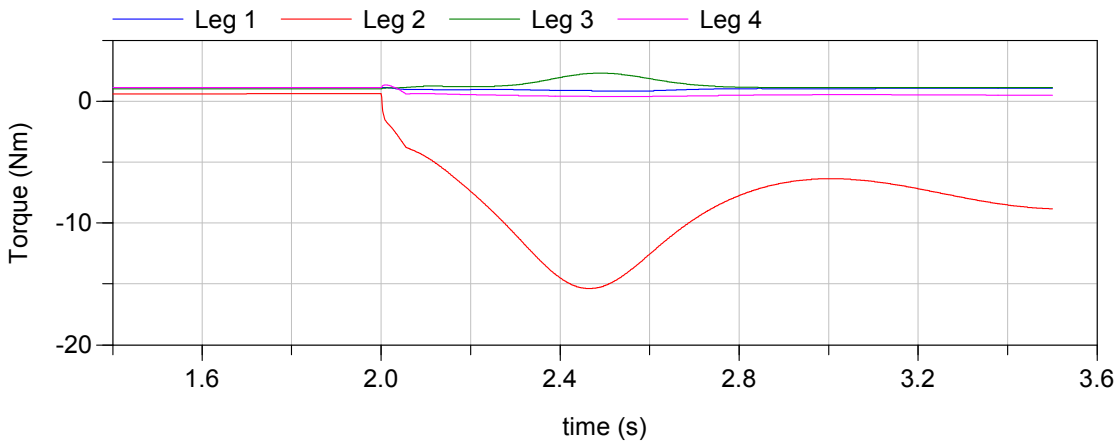


Figure 3.28: Case 1b - torque to hold leg position. The torque in leg 2, which is directly underneath the extended arms/opposite the acceleration, increases over twice as much as the torque for the pair of legs in case 1a.

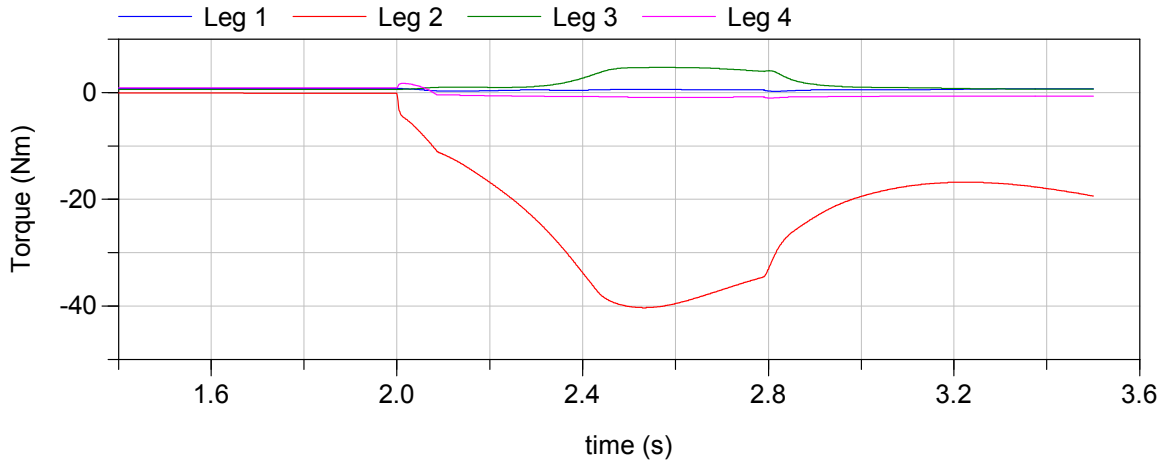


Figure 3.29: Case 1c – torque to hold leg position. The shorter leg extension almost quadruples the torque in case 1c as compared to case 1b.

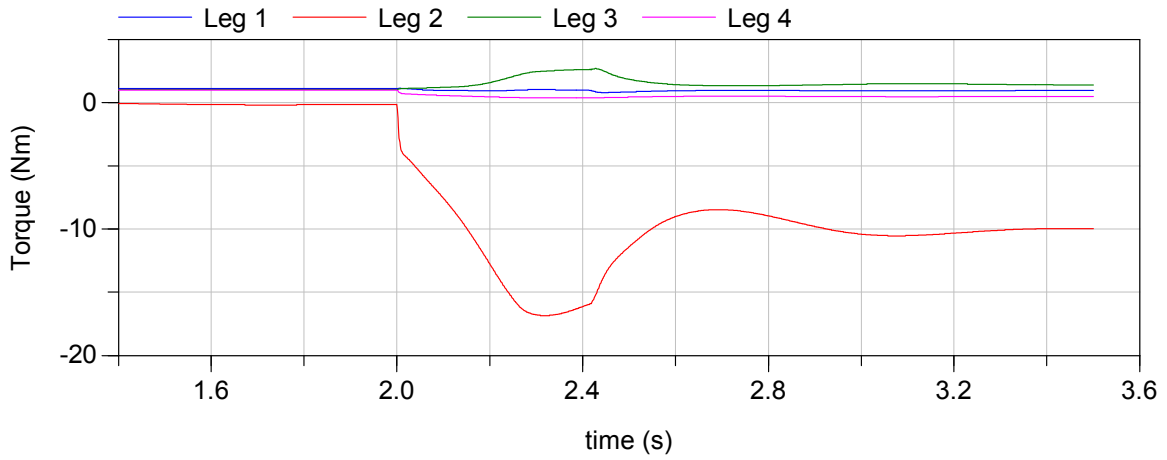


Figure 3.30: Case 1d - torque to hold leg position, legs extended. The horizontal torso with a 3 kg load requires a torque slightly above case 1b with the torso vertical and 15 kg load.

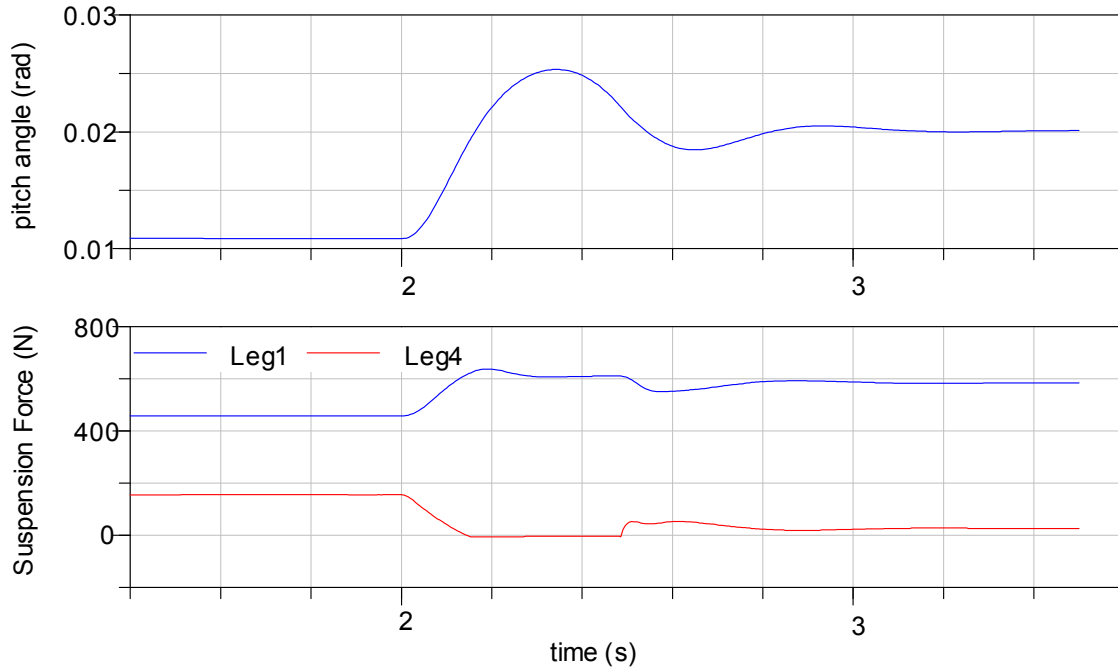


Figure 3.31: Case 1a - the effect of acceleration on the suspension as indicated by the body pitch angle—up to 1.4° tilt—and the suspension force in a front and rear wheel, which shows that the front wheel actually loses contact shortly after acceleration begins before regaining contact around 2.5 s.

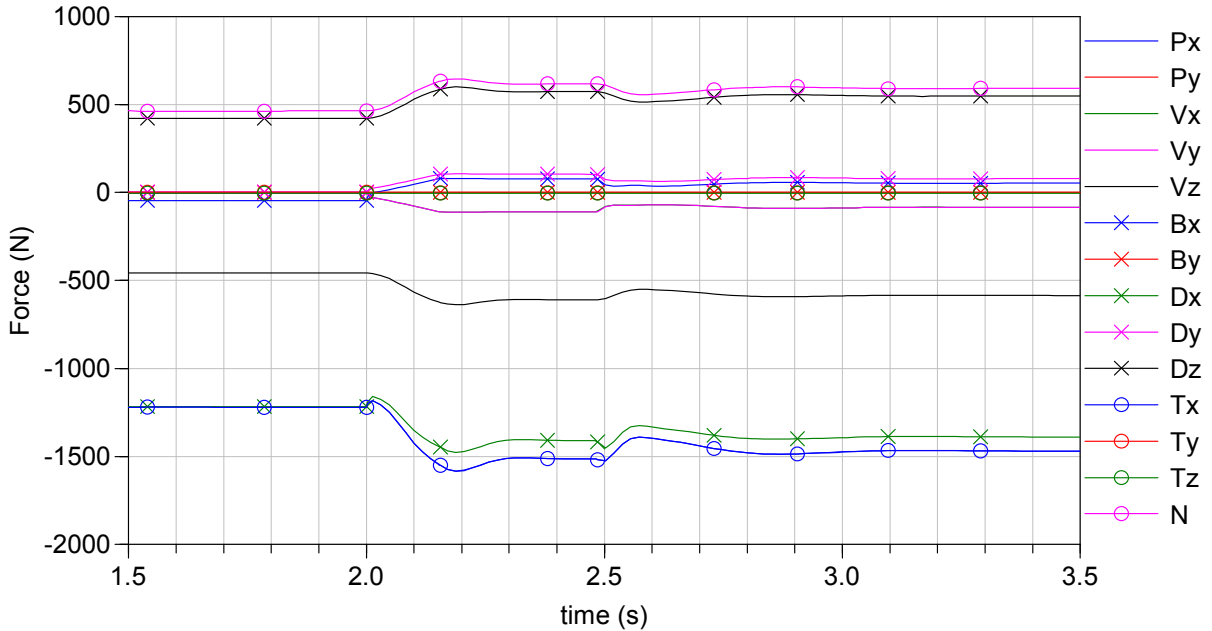


Figure 3.32: Case 1a - Forces on leg 1 (under and to the side of the torso, away from acceleration direction)—same as leg 2.

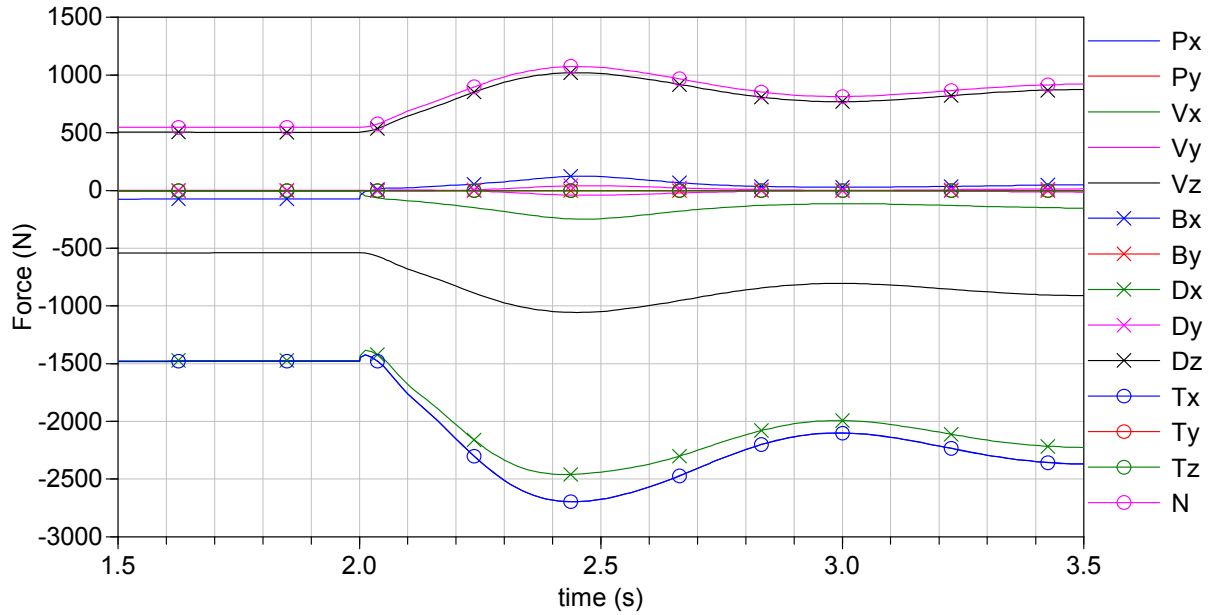


Figure 3.33: Case 1b - forces on leg 2 (under arms, away from acceleration direction). Forces are almost twice as high as for leg 1 in case 1a.

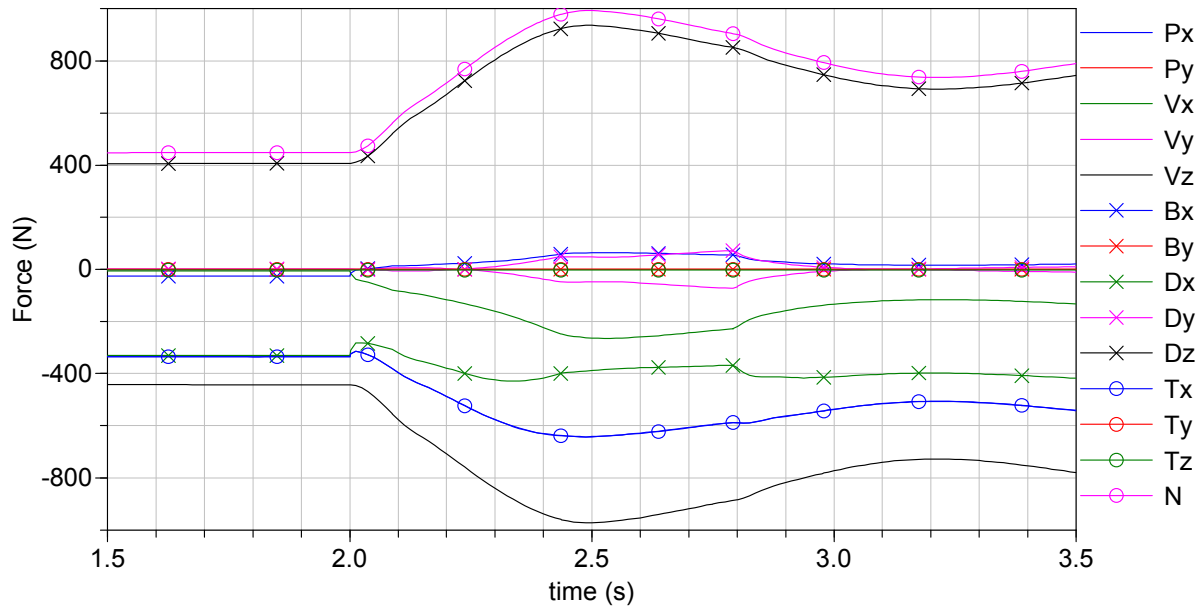


Figure 3.34: Case 1c – forces on leg 2 (under extended arm, away from acceleration direction).

3.3.4.2 Angular Acceleration and Velocity

The platform can rotate around its centre with a pure angular acceleration $\ddot{\theta}_b$ and velocity $\dot{\theta}_b$ (no linear movement) that is limited by the maximum drive wheel acceleration a_{max} and velocity v_{max} and the distance to the centre as determined by the footprint extension h . This is expressed in the following simple relations:

$$\dot{\theta}_b = \frac{v_{\max}}{h} \quad (3.64)$$

$$\ddot{\theta}_b = \frac{a_{\max}}{h} \quad (3.65)$$

Thus, angular acceleration and velocity reaches a maximum at the smallest leg extension. Due to the centripetal and coriolis effects, not only the angular acceleration but also the angular velocity has an effect on the forces in the VFM, and the highest forces are thus expected at maximum acceleration and velocity, where forces due to angular acceleration are expected to act tangentially and those due to angular velocity radially. Cases 2a and 2b explore angular acceleration and velocity with varying configurations as detailed in Table 3.5.

These cases clearly show the effect of acceleration between 2.0 and 2.8 s, which shows a different response than constant velocity after 2.8 s. Overall, the forces generated by velocity are much greater than those by acceleration. Case 2a, Leg 1, which is to the side of the horizontal arm & torso, has increased x- and z-forces primarily during the acceleration period, because this is when the tangential angular acceleration forces acting on the torso, which is at right angles to this leg, are transferred. Leg 2 on the other hand, which is radially in line with the torso, has increasing forces depending mainly on the angular velocity. In case 2b, with the larger acceleration, increases in the V_y and D_y forces, which are both perpendicular to the leg, appear during acceleration in leg 1 and leg 2. The holding torque for case 2b is substantially higher than in case 2a.

Table 3.5: angular acceleration simulation cases

Case	Movement	Leg Extension	Upper-Body Position	Payload	Figures
2a	Accelerate at 3.4 rad/s ² to 2.8 rad/s (max for this condition)	70°	Torso rotation: 0° Torso vertical, arm horizontal	3 kg	Figure 3.35 to Figure 3.38
2b	accelerate at 6.1 rad/s ² to 5.2 rad/s	15°	Torso rotation: 45° Torso vertical, arms to side, 30° down from horizontal	15 kg	Figure 3.41 to Figure 3.43

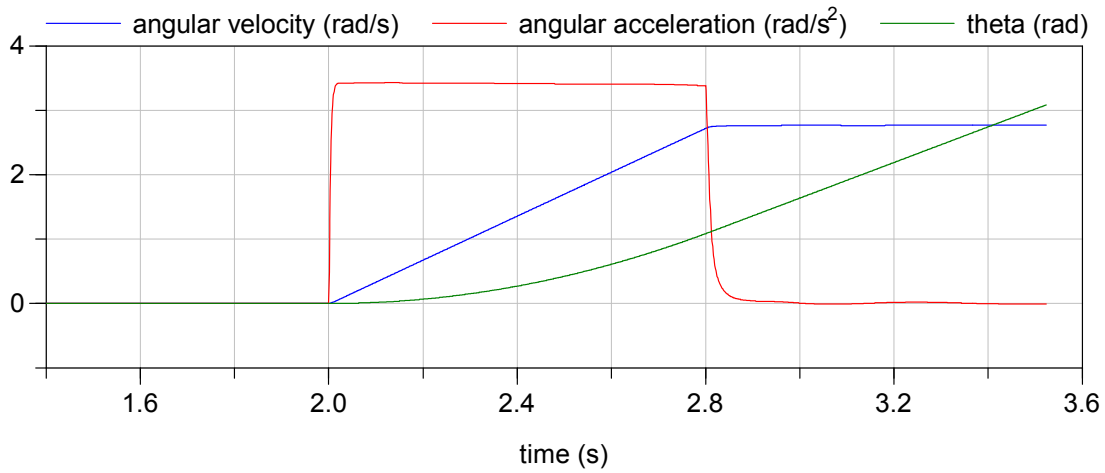


Figure 3.35: Case 2a - platform angular position, velocity and acceleration. Acceleration at 3.4 rad/s² from 2 s up to 2.8 rad/s.

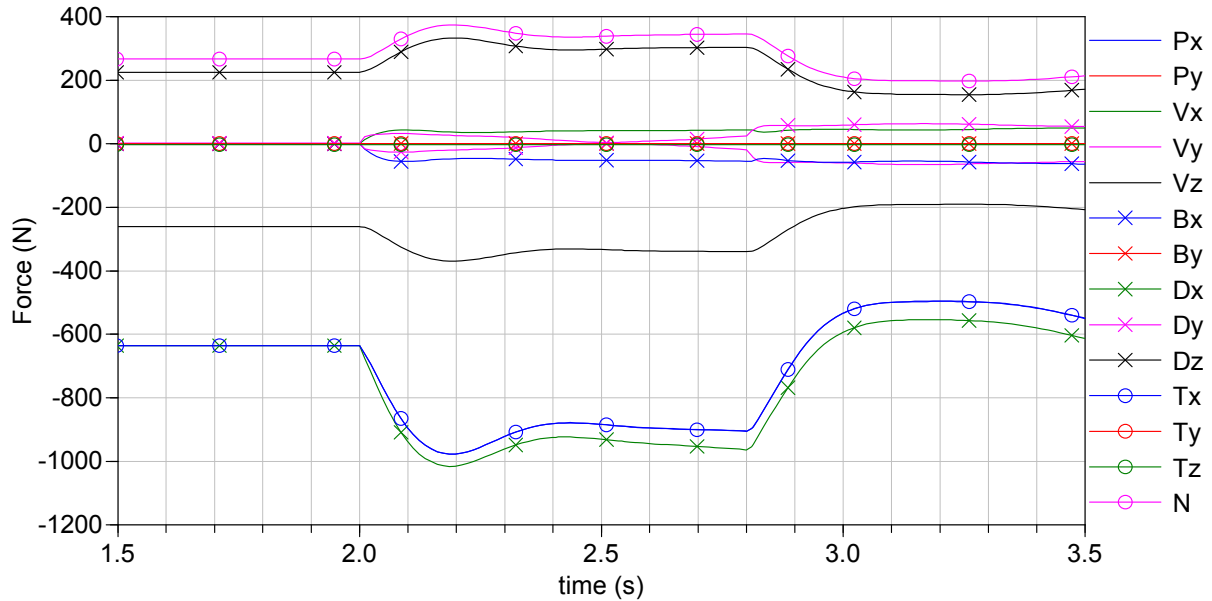


Figure 3.36: Case 2a – forces on leg 1 (to side of torso). Increased leg forces during rotational acceleration from 2 to 2.8 s, notably vertically at the lower base joint *D*, the lower leg joint *V*, and the wheel normal *N*, as well as laterally at the centre leg joint *T* and lower base joint *D*.

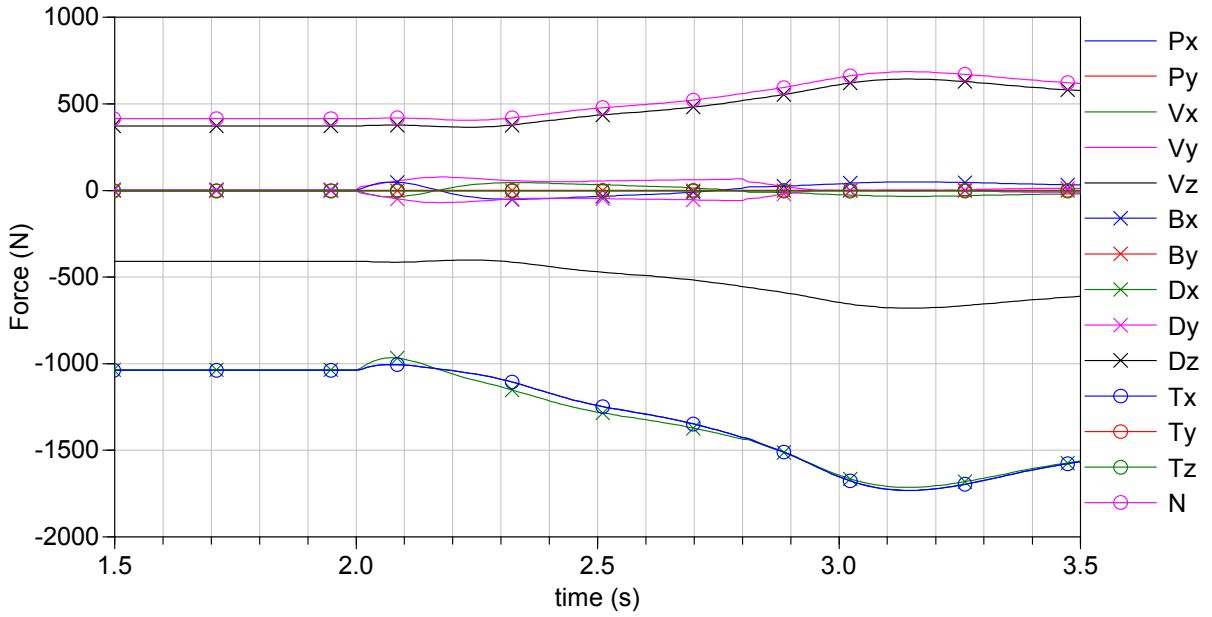


Figure 3.37: Case 2a - forces on leg 2 (in front of torso). Increased forces primarily due to rotational velocity, which reaches a maximum at 2.8s.

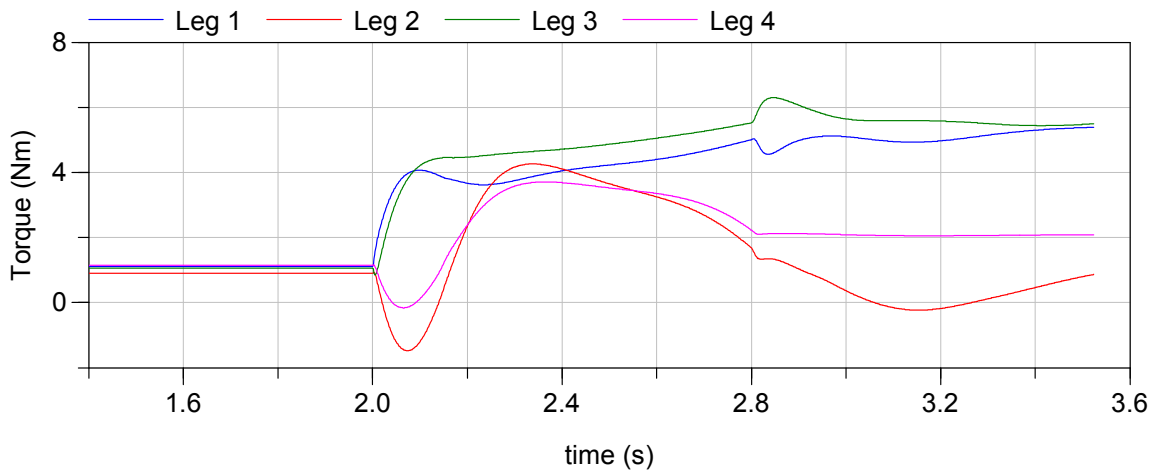


Figure 3.38: Case 2a - torque to hold leg position with legs extended.

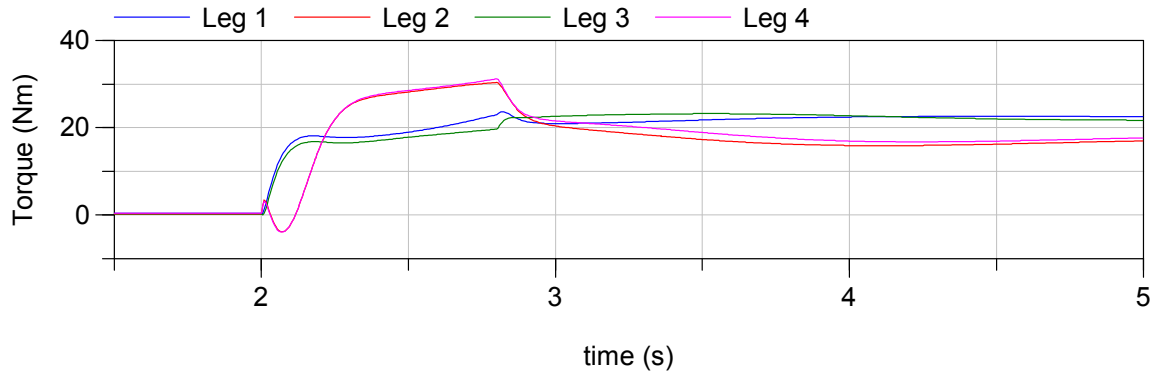


Figure 3.39: Case 2b - torque to hold leg position with legs retracted; the acceleration induced torque from 2 to 2.8 s now exceeds the velocity induced torque thereafter, and both are higher than in case 2a.

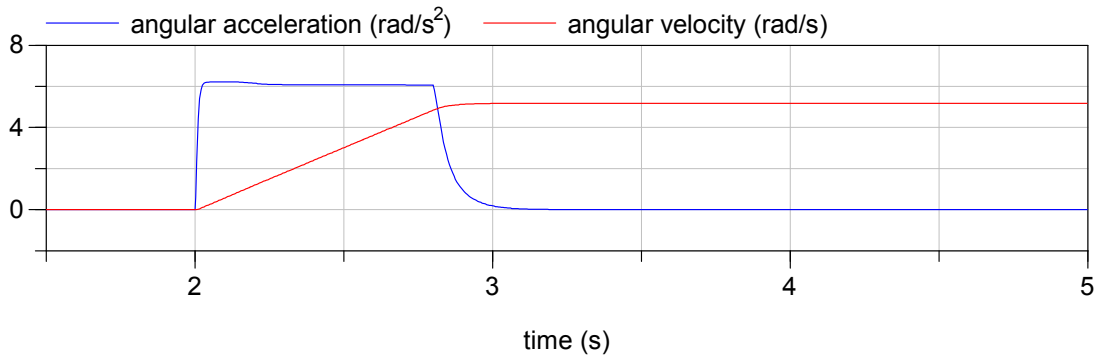


Figure 3.40: Case 2b - angular velocity and acceleration of platform.

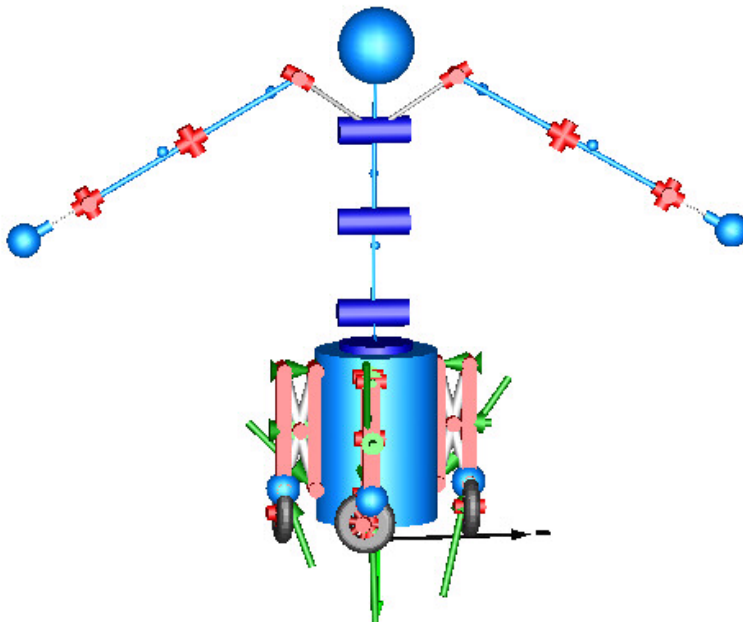


Figure 3.41: Case 2b - snapshot of configuration. Torso is rotated 45° so that extended arms roughly line up with two legs.

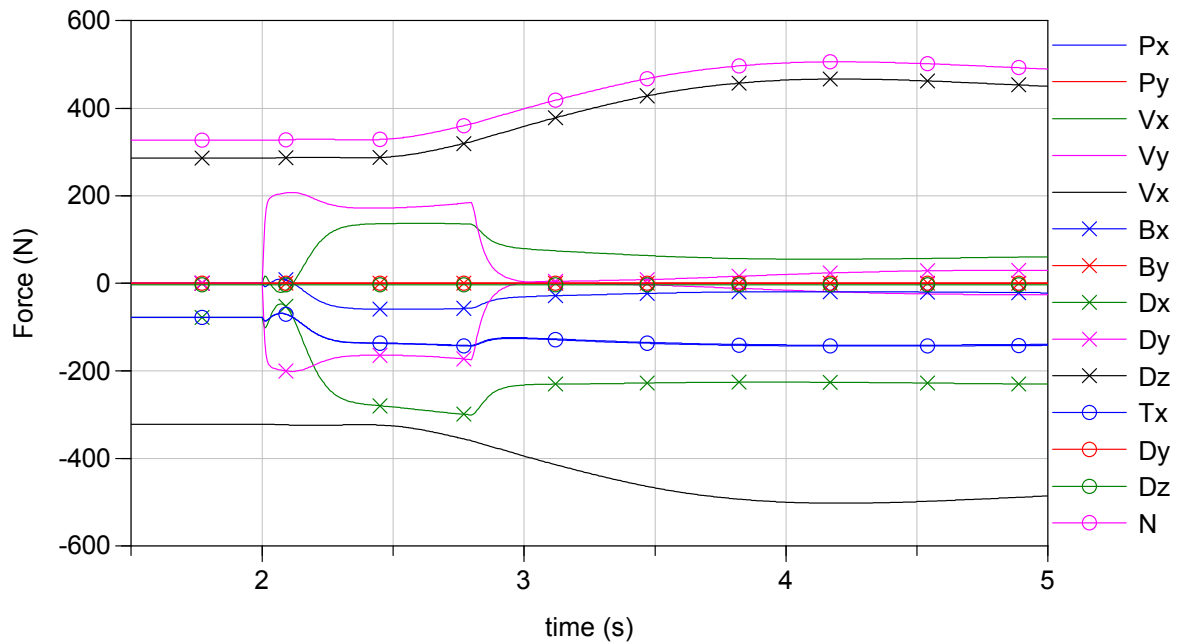


Figure 3.42: Case 2b – forces on leg 2 (under arm). Sideways V_y and D_y forces increase significantly during the higher acceleration of case 2b with the legs retracted; they drop off when acceleration ends.

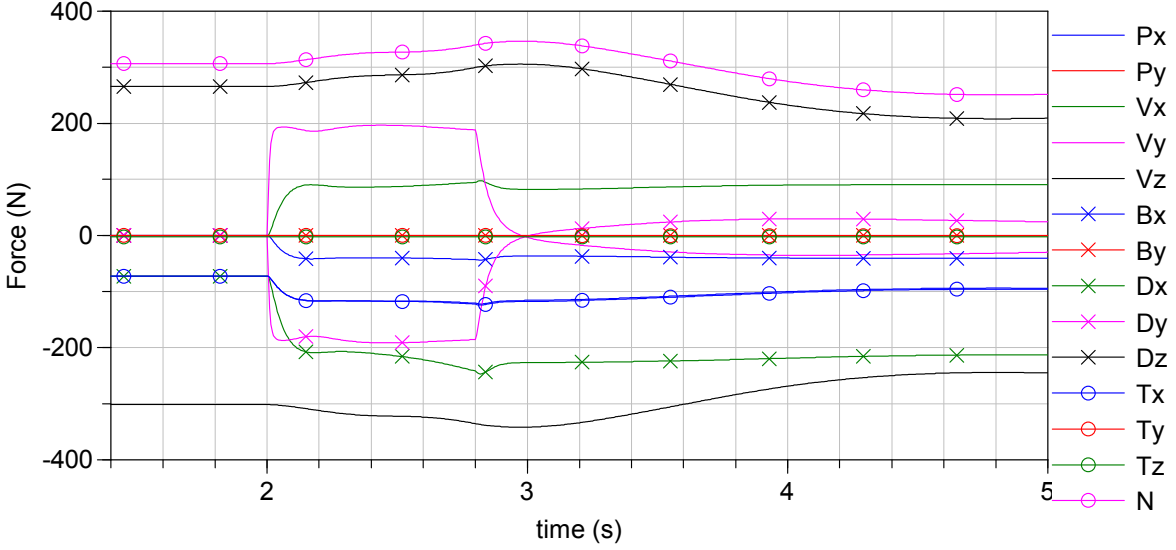


Figure 3.43: Case 2b – forces on leg 1 (to side of arm, in front of torso). Again, V_y and D_y forces increase significantly during acceleration.

3.3.4.3 Angular and Linear Acceleration and Velocity

While pure angular motion around the centre of the platform causes centripetal and coriolis forces, their effect is limited as the majority of the system mass lies close to the point of rotation. Since the platform is to be holonomic, it can rotate around any point in the ground plane inside or outside the platform footprint. In order to find the point where effects on the VFM should be greatest given the constraints of the drive wheel acceleration and velocities, the following simplified analysis was performed: the system consists of three bodies; the base and two legs with centre of masses located half-way out from the base. It rotates around a point located on the axis through the centre-of-masses. The angular acceleration and velocity are determined as follows:

$$\dot{\theta}_b = \frac{v_{\max}}{l} \quad (3.66)$$

$$\ddot{\theta}_b = \frac{a_{\max}}{l} \quad (3.67)$$

$$l = h + d_p \quad (3.68)$$

$$a_{\text{bradial}} = d_p \dot{\theta}_b^2 = \frac{d_p v_{\max}^2}{(h + d_p)^2} \quad (3.69)$$

$$a_{\text{leg radial}} = (d_p + h/2) \dot{\theta}_b^2 = \frac{(d_p + h/2) v_{\max}^2}{(h + d_p)^2} \quad (3.70)$$

where h is distance from the far moving wheel (traveling at $v_{\max}=1.6$ m/s) to the base and d_p is the distance from the base to the centre of rotation, which is along the radial direction away from the far moving wheel, as seen in Figure 3.44.

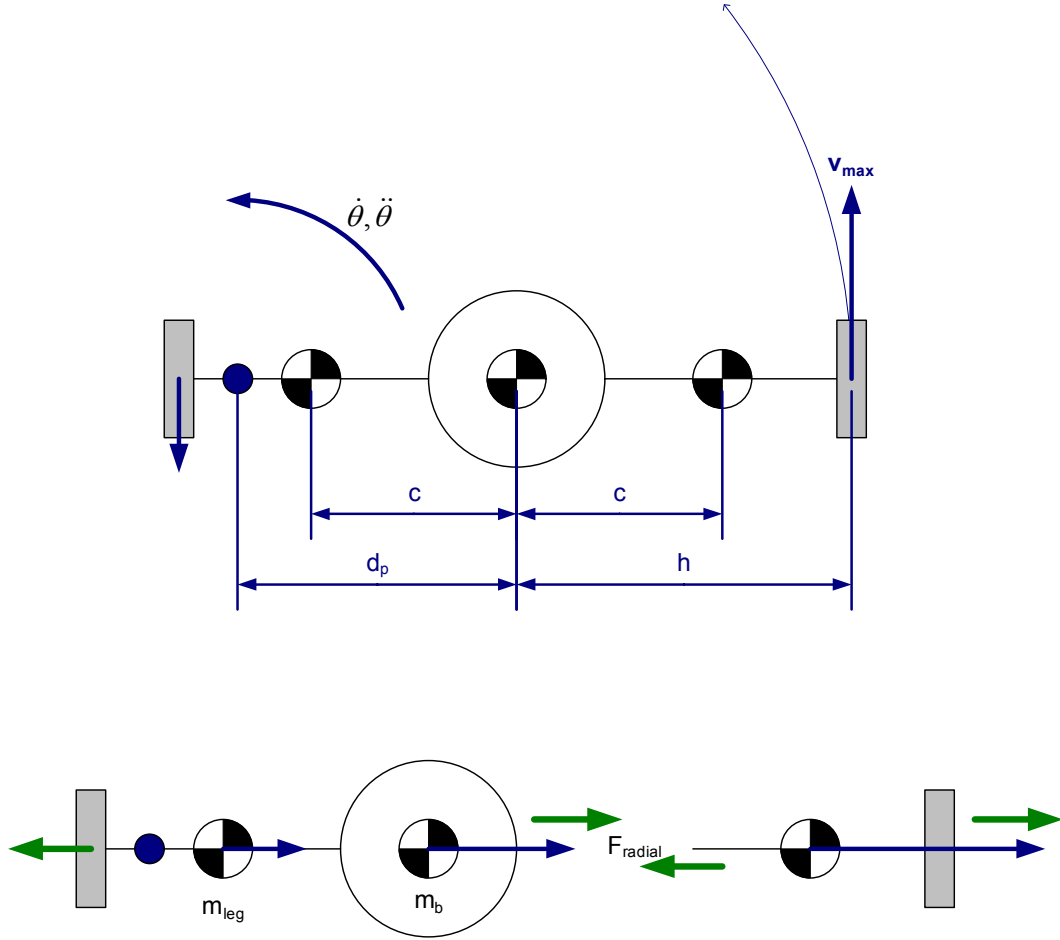


Figure 3.44: Simple model of platform (top view) for estimating the point at which combined linear and angular acceleration effects are greatest

The force between the outside leg and the base serves as a metric as high loading is expected here in this situation, and is determined as follows:

$$F_{radial} = m_b a_{b radial} + m_{leg} a_{leg radial} \quad (3.71)$$

$$F_{radial} = m_b \left(\frac{d_p v_{max}^2}{(h + d_p)^2} \right) + m_{leg} \left(\frac{(d_p + h/2) v_{max}^2}{(h + d_p)^2} \right) \quad (3.72)$$

$$F_{radial} = \frac{1}{2} \frac{v^2 (2m_b d_p + 2m_{leg} + m_{leg} h)}{(h + d_p)^2} \quad (3.73)$$

This force is then maximized over the range $d_p = 0 \dots h$ to find the worst-case centre of rotation; some results are shown in Table 3.6 and Table 3.7. The point of maximum force lies close to the far wheel (where $h = d_p$), but slightly on the inside towards the base, at a distance depending on the leg extension, as is evident in Figure 3.45. Further analysis of forces at the absolute maximum force centre of rotation is performed below using the more accurate system model in Dymola; simulation cases are listed in Table 3.8.

Table 3.6: Centripetal forces, $m_b=45 + 50 + 3$, $m_{leg} = 5$, $c = h/2$, $v = 1.6$

	h	d_p	F_{radial}
Maximum (Legs Retracted)	0.308 (min)	0.293	219
Legs Extended	0.578 (max)	0.550	117

Table 3.7: Centripetal forces, $m_b=45 + 50 + 15$, $m_{leg} = 5$, $c = h/2$, $v = 1.6$

	h	d_p	F_{radial}
Maximum (Legs Retracted)	0.308 (min)	0.295	244
Legs Extended	0.578 (max)	0.553	130

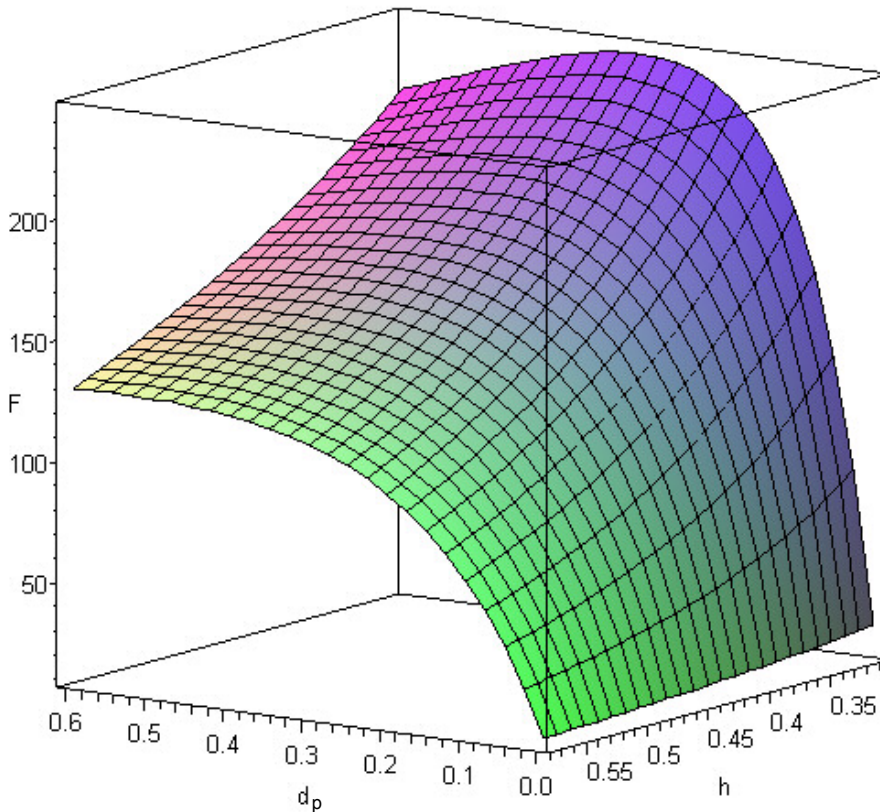


Figure 3.45: Force between outside leg and base for varying leg extension h and centre of rotation location d_p , $m_b = 60$, $m_{leg} = 5$, $c = h/2$, $v = 1.6\text{m/s}$. The force increases with decreasing leg extension; the maximum for each extension varies but lies towards the outside of the platform.

Table 3.8: Combined linear and angular acceleration simulation cases

Case	Movement	Leg Extension	Upper-Body Position	Payload	Figures
3a	As in Table 3.7, with outer wheel at 1.6 m/s; angular acceleration at 1.8 rad/s ² to 1.5 rad/s, linear acceleration at 0.75 m/s ²	70°	torso rotation: -45° (facing towards leg 1) torso vertical, arms horizontal	15 kg	Figure 3.46 to Figure 3.48
3b	As in table Table 3.7, with outer wheel at 1.6 m/s; angular acceleration at 3.3 rad/s ² to 2.7 rad/s, linear acceleration at 0.78 m/s ²	15°	torso rotation: -45° (facing towards leg 1) torso vertical, arms vertical down	15 kg	Figure 3.49 to Figure 3.47

As suggested by the preceding analysis, rotation around a point outside of the centre of the platform towards one of the wheels produces higher forces than rotation around the platform centre. Comparing case 3b to 2b shows this, as forces for the rotation around a point close to wheel 3 produce higher loading than rotation around the platform centre despite the more conservative torso position. Case 3a has the highest loads in the y-direction (sideways or horizontally perpendicular to the leg) at V_y and D_y . These occur past 2.8 s after angular acceleration has ended and the angular velocity has reached its peak.

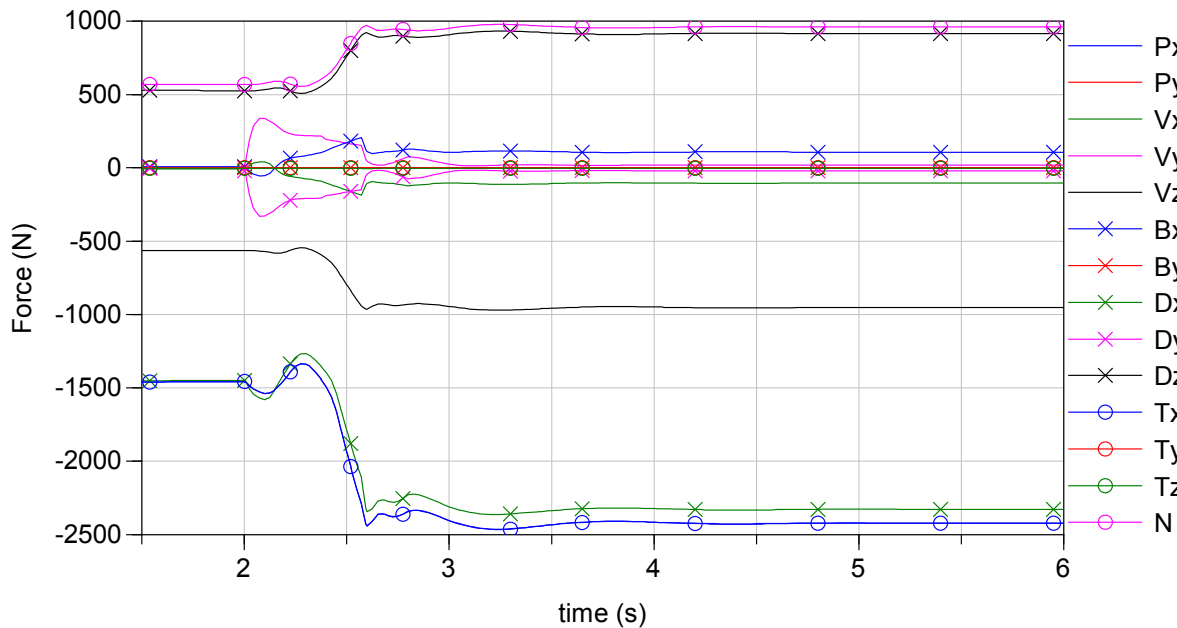


Figure 3.46: Case 3a, legs extended, arms horizontal – forces on leg 1 (outside leg, facing same way as torso).

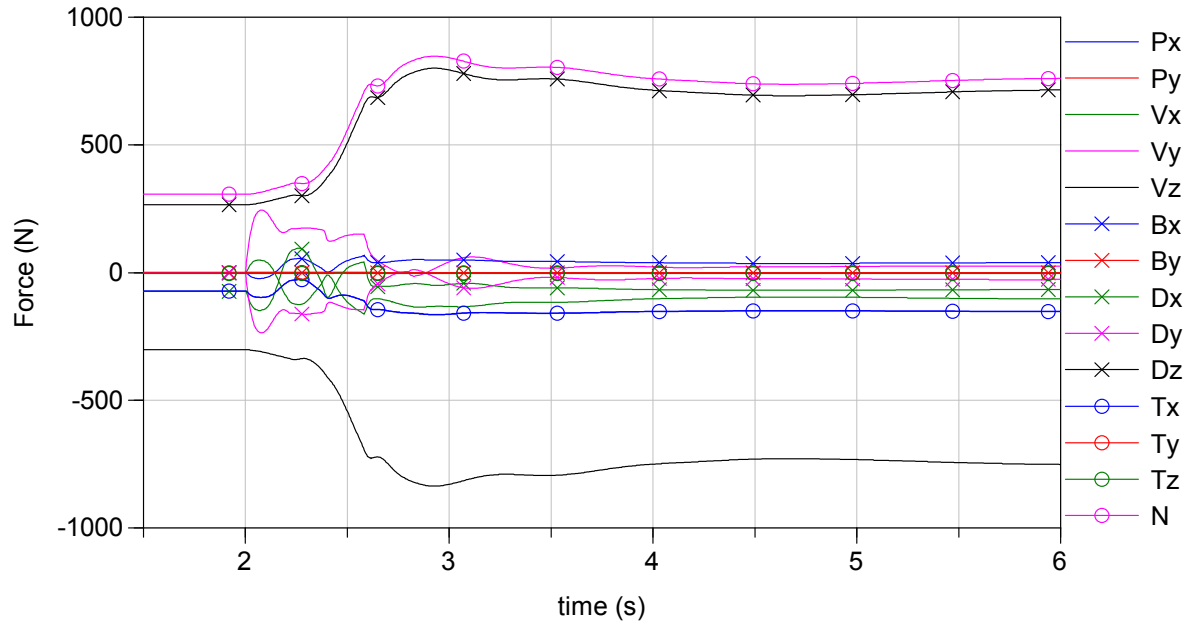


Figure 3.47: Case 3b, legs retracted, arms down – forces on leg 1 (outside leg, facing same way as torso). The combined rotational and linear acceleration is much smaller than in 3a.

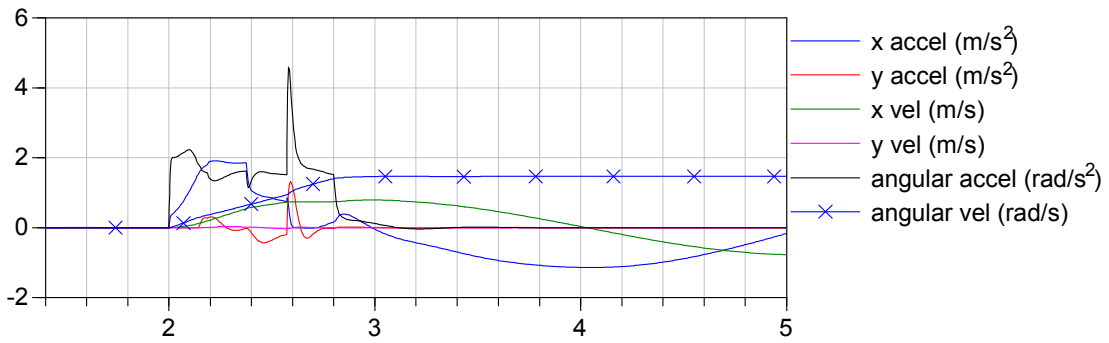


Figure 3.48: Case 3a, legs extended, arms horizontal - velocity and acceleration.

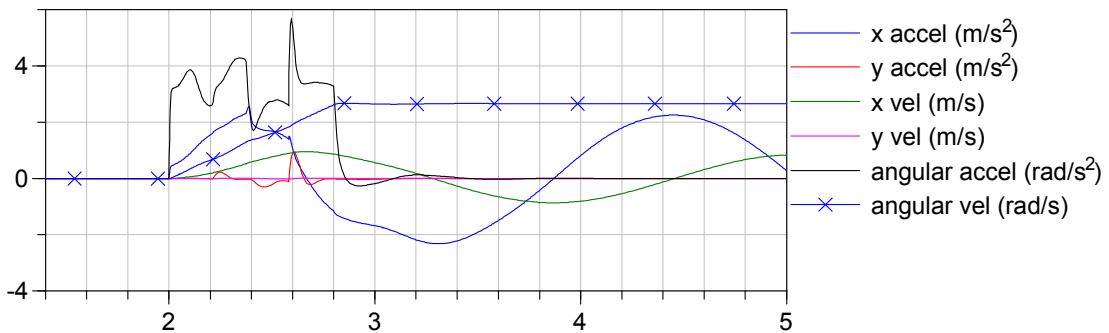


Figure 3.49: Case 3b, legs retracted, arms down - velocity and acceleration

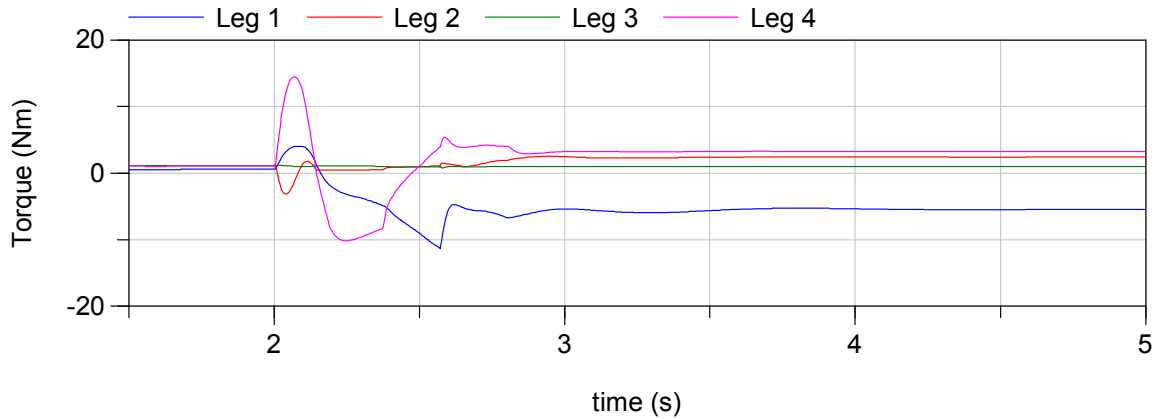


Figure 3.50: Case 3a, legs extended, arms horizontal - torque to hold leg position.

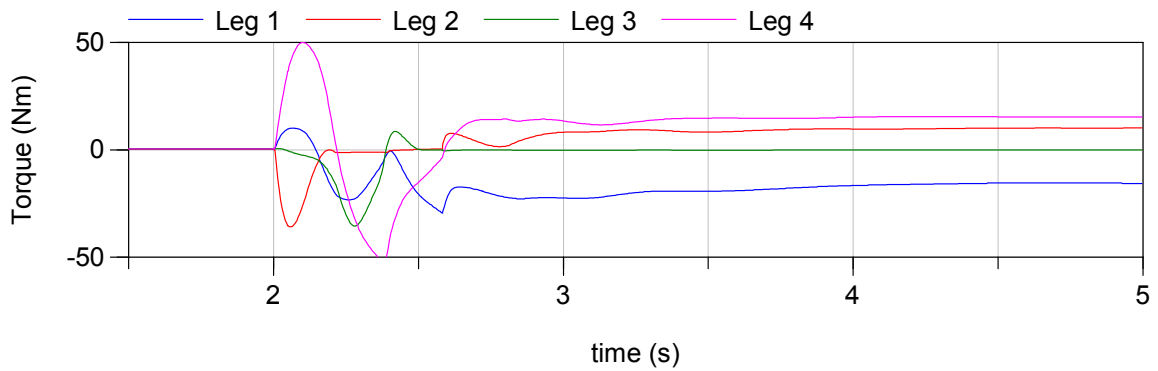


Figure 3.51: Case 3b, legs retracted, arms down - torque to maintain leg position. The torque peaks and levels out higher than case 3a.

3.3.4.4 Discussion

Simulation results show forces that are in some cases significantly higher than the maximums determined by the preceding simplified dynamic analysis. This is primarily due to the effect of differing upper-body positions, which change the weight distribution and the forces due to acceleration. In particular, it should be noted that putting the upper body in a position away from the centre can cause a significant moment on the base. Table 3.9 summarizes the maximum forces and the conditions at which they were recorded.

Generally, because smaller wheelbases cannot stably support high loads and accelerations, the maximum observable forces at these wheelbases are lower than at large wheelbases. The simplified analysis suggests large forces could occur, but in practice the system becomes unstable first.

The most demanding situation is case 1b, linear acceleration with the maximum payload and horizontally extended arms opposite the direction of acceleration, although it does not result in the highest leg holding torque. This occurs during combined angular and linear acceleration, case 3b, where a torque of 52 Nm is observed.

Table 3.9: Maximum forces for simulated cases. Forces are resolved in the base; positive x is away from base, positive z is down

case			1ref	1ref	1a	1b	1c	1d	2a	2b	3a	3b
payload/arm	kg		7.5	7.5	7.5	7.5	1.5	1.5	1.5	7.5	7.5	7.5
forward accel	m/s ²		0	-2	-2	-2	-2	-2	0	0	0.748	0.78
angular accel	rad/s ²		0	0	0	0	0	0	2.768	6.494	1.842	3.328
angular velocity	rad/s		0	0	0	0	0	0	3.46	5.195	1.473	2.662
leg with max load			Leg 2	Leg 2	Leg 2	Leg 2	Leg 2	Leg 2	Leg 2	Leg 2	Leg 2	Leg 2
Force	Unit	MAX										
Px	N	-2695	-766	-1065	-1583	-2695	-642	-2632	-1732	-142	-2464	-164
Vx	N	-270	0	-76	-112	-249	-268	-270	45	137	-186	-163
Vy	N	338	0	-1	-112	-42	-73	-50	77	208	338	245
Vz	N	-1057	-298	-435	-637	-1057	-973	-1044	-679	-528	-969	-836
Bx	N	206	-30	46	81	123	64	150	-51	-59	206	66
Dx	N	-2459	-766	-996	-1536	-2459	-429	-2374	-1714	-301	-2363	-148
Dy	N	-329	0	1	105	42	73	50	-70	-201	-329	-236
Dz	N	1020	262	401	600	1020	937	1007	643	467	934	800
Tx	N	-2696	-766	-1065	-1484	-2696	-643	-2633	-1733	-143	-2464	-166
Ty	N	4	0	0	-1	0	0	0	4	1	1	1
Tz	N	-5	-3	-3	-5	-3	-3	-3	4	-5	-3	-5
N	N	1074	303	443	646	1074	993	1062	685	536	979	848
Tau (any leg)	Nm	-52	1.1	-3.7	-4.7	-16.0	-40.3	-16.8	6.3	30.4	-11.3	-52.0

3.4 Drive Selection

3.4.1 Requirements

Because of the asymmetric geometry (see section 9.7.2) and because Justin has a clearly defined front, there will generally be one tip-over axis (see section 4.1.1) that is more in need of support than the others. Extension of only the pair of legs that form the boundary of that axis is preferable to extending all the legs simultaneously, which would cause unneeded footprint enlargement. The pair in question will change depending on the torso orientation and the loading, thus it is desirable to be able to actuate the legs individually.

Situations requiring leg extension:

- Centre of mass moves towards tip-over axis
 - o because of addition of mass
 - o because of movement of upper-body
- acceleration introduces dynamic forces which increase the moment around the tip-over axis
- angular velocity introduces dynamic forces which increase the moment around the tip-over axis

Situations where leg retraction is desired:

- footprint reduction for improved mobility whenever stability allows
- footprint reduction in order to fit through narrow spaces which may require upper body reconfiguration and/or a reduction in acceleration to improve stability

It is difficult to determine what leg extension speed is necessary. While it would be nice to be able to use the leg extension to react to imminent tip-over, there are times when this would require instantaneous movement, for instance when a load is placed on or released from the manipulator. Thus, since a reactionary approach is not guaranteed to be successful, it is preferred to have leg-extension act in a proactive manner. Control can certainly be set up to attempt a reactionary movement when necessary, but actuation design will be for the proactive case in order to reduce power needs and mass. The velocity then becomes a matter of being fast enough to not unduly delay the operation of the robot. Since the leg only travels a short distance (0.376 m from minimum to maximum extension), the acceleration will also play a significant role in determining the extension time. For instance, using a 1/3-1/3-1/3 trapezoidal velocity profile, the necessary speed and acceleration to complete a full extension in one second are

$$a = 4.5 \frac{\Delta x_l}{t^2} = 4.5 \frac{0.396}{1^2} = 1.692 \text{ m/s}^2 \quad (3.74)$$

$$1.5 \frac{\Delta x_l}{t} = 1.5 \frac{0.396}{1} = 0.564 \text{ m/s.} \quad (3.75)$$

There are several different possible actuation methods that will be explored in detail below.

3.4.2 Vertical Linear Drive on Base

One possible point of actuation is the vertical slider at the base (y_l). While initially this appears to be a simple location to implement some sort of linear drive, particularly because of the fairly large space available that could extend into the base proper, there are several drawbacks to actuating here. The simplest actuator, a belt drive, takes up some space at top, reducing available height by at least the pulley diameter, which would be on the order of 5 cm. Spindle drives are heavier and take up more space along the axis. In addition, because of the tangent relationship between x_l and y_l , the velocities required of the drive become high at large extensions (3.8). Similarly, forces due to acceleration and slider friction become high at small and large extensions (3.55, 3.33) respectively.

The power needed to extend the leg at constant velocity, ignoring friction, is to overcome the force in the vertical slider due to the leg mass and the platform acceleration load. At a constant horizontal leg extension velocity of 1 m/s and a platform acceleration of 2m/s^2 , this leads to a peak power of 84W at 70° and 113 W at 80° of leg extension (Figure 3.52),

$$P_{linear} = P_y \cdot \dot{y} \quad (3.76)$$

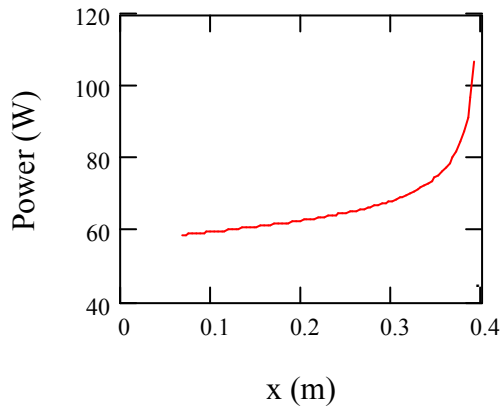


Figure 3.52: Power for constant velocity extension of 1 m/s at body acceleration of 2 m/s with 15 kg load and leg mass of 1 kg.

3.4.3 Rotary Drive

An actuator for the VFM could be placed at any of the leg rotary joints. Placement of an actuator at the leg intersection T involves some difficulty in terms of packaging, and an actuator at this location would increase the leg mass, which needs to be accelerated during leg extension. On the other hand, it would not take up any space in the base around the slider. Placement of an actuator on one of the outside joints (B and V) increases the mass of the wheel upright, which must also be accelerated, and space in the upright is at a premium as well. The top inside joint and top outside joints (L and B) both sit on sliders, making mounting difficult. L is subjected to vertical acceleration and B experiences vertical and horizontal acceleration during leg movement. Thus the most logical place for rotary actuation is the bottom inside joint D , which does not move during leg extension and has sufficient space around it.

The power needed to extend the leg at constant x-velocity of 1 m/s against a 1 kg leg mass and 2 m/s² acceleration load using the centre joint is 84W at 70° and 113W at 80° of leg extension, where power is simply

$$P_{centre} = \Gamma(\theta). \quad (3.77)$$

As the values suggest, this is equivalent to the power of the linear actuator.

3.4.4 Using the wheel drive

Another alternative to actuating the VFM is to use the drive and steering actuators. Simply by moving one wheel at a greater rate than the others in the same direction as the leg, it can be made to extend and retract. This has the advantage that no additional actuators are needed, reducing weight and volume requirements. In addition, the wheel velocity translates directly to leg velocity; there is no angle relationship as with the kinematics of the other actuation locations. It will however put some restriction on the drive performance that can be achieved simultaneous to leg motion.

If the platform encounters an obstacle such as a small step, even if the wheel is powered, the leg will retract, which could lead to a tip-over. Thus, a brake is essential. By using the brake, the power requirements for the wheel drive to hold the leg in position become zero. Power is only needed when the wheel is to be extended or retracted; below, it will be shown that it is not necessary to move the leg during high wheel loading, so the brake can maintain the leg's position and power needs can be kept to a minimum.

In most situations, wheel extension should be just as capable as a separate actuator on the VFM, since the wheel drive has more than enough power and sufficient velocity and acceleration capabilities. Only in the following situations are there restrictions:

- When maximum power is already being used to accelerate
 - For maximum forward acceleration, the (front) wheel that would have to accelerate *more* to extend is being unloaded by forward acceleration and shouldn't need to extend. Retracting it simply means releasing the brake and accelerating it less.
 - For max forward acceleration, the rear wheel wants to extend anyway, which is good because it is being loaded by the forward acceleration. It will NOT be possible to retract it, which would require accelerating it more, but this is unlikely to be desired considering it is being loaded by the acceleration.
 - For angular velocity loading (which is highest around a point near one wheel as detailed in 8.2.3.2), the outside leg will want to retract when the opposite would be helpful, but it can be extended by changing the steering angle to spiral the wheel outward.
- When insufficient traction is available
 - Unless the surface is very slippery, this implies that not much load is on the wheel and there shouldn't be any need to extend it at the moment, although a preemptive move may be desired.

Considering the benefits of using wheel actuation for the VFM, it is deemed acceptable to have some restriction of the drive performance during leg movement due to the sharing of the actuators and some restrictions on the leg movement due to drive and platform conditions.

3.5 VFM – Conclusions

The variable footprint is best implemented using a scissor-style mechanism, as it is one of the designs in which the weight of the platform is not carried by the actuated components of the mechanism, and, of these designs, offers the best compromise between extension distance and volume requirements. The analysis of mechanism kinetics shows the loading the VFM will experience in various situations and how these need to be considered in its actuation. In the further development of the mechanism, it will be important to consider these loadings, for instance when designing the structural elements. Different actuation options are explored and the decision is made to use the wheel drive, thus eliminating the need for further actuators.

Chapter 4

Stability

4.1 Stability Measure

As reviewed in section 1.3.4, there are a number of different measures for the stability of a mobile robot. The Force-Angle measure proposed by Papadopoulos [76] is used in this work as it is fairly comprehensive without being unduly complicated to implement.

4.1.1 Theory

At each wheel is a ground contact point p whose location is expressed in the inertial frame by

$$p_i = \begin{bmatrix} x_i + x_l \cos \gamma_i \\ y_i + x_l \sin \gamma_i \\ 0 \end{bmatrix} \quad (4.1)$$

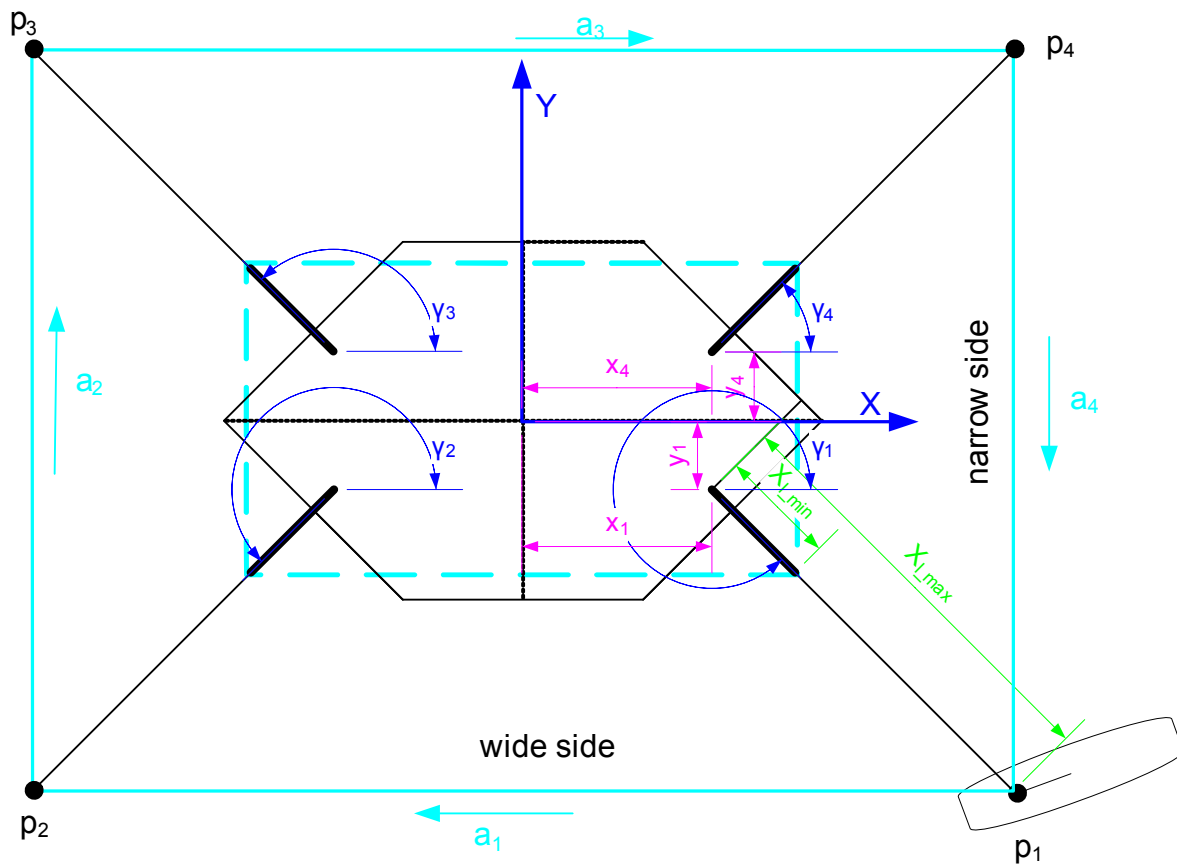


Figure 4.1: Top view of platform showing stability parameters.

where x_i and y_i are the position coordinates of the start of the leg in the base, x_i is the leg extension distance as described in section 3.3.1, and γ_i is the angle of the leg in the horizontal plane. The zero in the third term makes the assumption that the system operates only on level ground. The contact points are numbered in a clockwise fashion when viewed from above for consistency with the method described in [76], as shown in Figure 4.1.

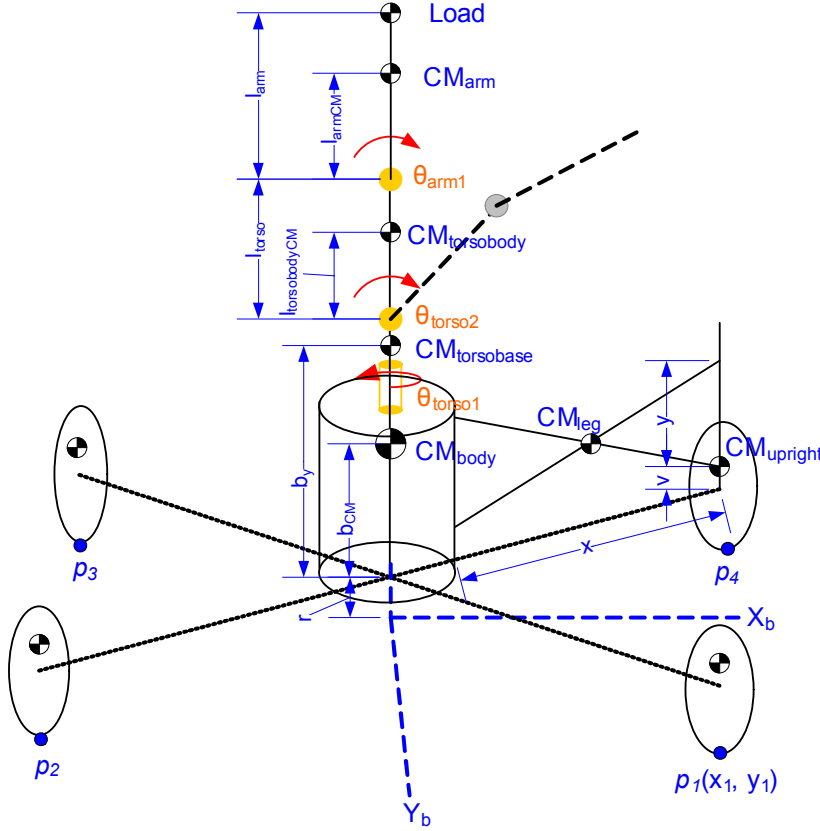


Figure 4.2: platform configuration showing centre of mass locations for stability analysis.

To simplify analysis, we will lump together the torso into one link, the arms into one link, and we will consider these together with the load, the body, the leg pieces and the wheel uprights to each have a point mass, m_j , located at point p_{CMj} , where $j = 1 \dots 12$ (Figure 4.2). The instantaneous location of the system centre of mass p_c in the inertial frame is thus expressed as

$$p_c = \frac{\sum_j p_{CMj} m_j}{m_{total}}. \quad (4.2)$$

The mass of the wheel upright is assumed to be centered over the contact point at the height of the lower leg joints in position $p_{CMupright}$,

$$p_{CMupright_i} = \begin{bmatrix} x_i + x \cos \gamma_i \\ y_i + x \sin \gamma_i \\ v + r \end{bmatrix} \quad (4.3)$$

where v , is the vertical wheel offset distance and r is the wheel radius. The mass of the legs is assumed to act at their geometric centre position p_{CMleg} ,

$$p_{CMleg_i} = \begin{bmatrix} x_i + \frac{x}{2} \cos \gamma_i \\ y_i + \frac{x}{2} \sin \gamma_i \\ \frac{y}{2} \end{bmatrix}. \quad (4.4)$$

The location of the centre of mass of the main body, p_{CMbody} , is defined as

$$p_{CMbody} = \begin{bmatrix} 0 \\ 0 \\ b_{CM} + r \end{bmatrix}. \quad (4.5)$$

The centre of mass position of the moving part of the torso, $p_{CMtorsobody}$, the fixed part of the torso, $p_{CMtorsobase}$, and arms, p_{CMarm} , are calculated from the specifications (Table 4.1) and are added to the inertial frame at a point at the top centre of the base; the arms are assumed to remain extended and parallel to each other, rotating only in the first joint θ_{arm1} to simplify analysis. The torso is simplified to rotate in the vertical axis at θ_{torso1} , where 0° is facing the narrow side between p_1 and p_4 , and in the horizontal axis θ_{torso2} , where 0° is aligned with the horizontal plane.

$$p_{CMtorsobody} = \begin{bmatrix} l_{torsobodyCM} \cos \theta_{torso1} \cos \theta_{torso2} \\ l_{torsobodyCM} \sin \theta_{torso1} \cos \theta_{torso2} \\ b_y + r + l_{torsobodyCM} \sin \theta_{torso2} \end{bmatrix} \quad (4.6)$$

$$p_{CMtorsobase} = \begin{bmatrix} 0 \\ 0 \\ b_y + r \end{bmatrix} \quad (4.7)$$

$$p_{CMarm} = \begin{bmatrix} (l_{torso} \cos \theta_{torso2} + l_{armCM} \cos \theta_{arm1}) \cos \theta_{torso1} \\ (l_{torso} \cos \theta_{torso2} + l_{armCM} \cos \theta_{arm1}) \sin \theta_{torso1} \\ b_y + r + l_{torso} \sin \theta_{torso2} + l_{armCM} \sin \theta_{arm1} \end{bmatrix} \quad (4.8)$$

Table 4.1: Simplified Arm & Torso geometry

	Mass (kg)	CM location (m)	Endpoint location (m)
Arm & Hand	$m_{arm} = 14.7$	$l_{armCM} = 0.440$	$l_{arm} = 0.928$
Torso	$m_{torso} = 18.6$		
base	$m_{torsobase} = 4.4$	$l_{torsobaseCM} = -0.033$	$l_{torsofixed} = 0.1055$ (vertical)
body	$m_{torsobody} = 12.2$	$l_{torsobodyCM} = 0.418$ (when horizontal)	$l_{torso} = 0.6$ (when horizontal)
Head	$M_{head} = 2.5$	$l_{head} = 0.282$	

Finally, the load is assumed to be located at the end of the arm in position p_{load} :

$$p_{load} = \begin{bmatrix} (l_{torso} \cos \theta_{torso2} + l_{arm} \cos \theta_{arm1}) \cos \theta_{torso1} \\ (l_{torso} \cos \theta_{torso2} + l_{arm} \cos \theta_{arm1}) \sin \theta_{torso1} \\ b_y + r + l_{torso} \sin \theta_{torso2} + l_{arm} \sin \theta_{arm1} \end{bmatrix}. \quad (4.9)$$

Thus, the system CM position is:

$$p_c = \frac{p_{CMbody} m_b + \sum_i^{i=4} (p_{CMleg_i} m_{leg} + p_{CMupright_i} m_{upright}) + \left(p_{CMtorsobase} m_{torsobase} + p_{CMtorsobody} m_{torsobody} \right) + 2p_{CMarm} m_{arm} + p_{load} m_{load}}{m_b + 4(m_{leg} + m_{upright}) + m_{torsobase} + m_{torsobody} + 2m_{arm} + m_{load}} \quad (4.10)$$

The potential tip-over axes a are found by connecting the support points,

$$a_i = p_{i+1} - p_i \quad (4.11)$$

which in our case will give a quadrilateral that varies in size depending on the leg extension, as indicated by the two cyan rectangles in Figure 4.1.

The tip-over axis normals l_i which pass through the system CM are found as follows:

$$l_i = \left(I_{3 \times 3} - \frac{a_i}{\|a_i\|} \left(\frac{a_i}{\|a_i\|} \right)^T \right) (p_{i+1} - p_c) \quad (4.12)$$

Papadopoulos [76] defines the net force and net moment acting on the system CM which affects tip-over stability, f_r and n_r respectively, as

$$f_r = \sum f_{grav} + \sum f_{ee} + \sum f_{dist} - \sum f_{inertial} \quad (4.13)$$

$$n_r = \sum n_{ee} + \sum n_{dist} - \sum n_{inertial} \quad (4.14)$$

where *grav*, *ee*, *dist* and *inertial* subscripts represent the gravitational, end-effector, additional outside disturbance and inertial forces and moments respectively.

With no outside disturbance forces and potential inertia forces due to acceleration assumed to be limited to the horizontal direction, f_r simplifies to the gravitational load,

$$f_r = m_{tot} g \quad (4.15)$$

and n_r simplifies to

$$n_r = -\sum n_{inertial} \quad (4.16)$$

For each tip-over axis, the force and moment component acting about that axis can be found

$$\text{as } f_i = \left(I_{3 \times 3} - \frac{a_i}{\|a_i\|} \left(\frac{a_i}{\|a_i\|} \right)^T \right) f_r, \quad (4.17)$$

$$n_i = \left(I_{3 \times 3} - \frac{a_i}{\|a_i\|} \left(\frac{a_i}{\|a_i\|} \right)^T \right) n_r. \quad (4.18)$$

The moment component is converted into an equivalent force couple, f_{ni} , at the centre of mass by

$$f_{ni} = \frac{l_i}{\|l_i\|} \times n_i. \quad (4.19)$$

The effective net force vector, f_i^* , is simply the sum of the force component and the force couple acting at the axis,

$$f_i^* = f_i + f_{ni}. \quad (4.20)$$

The minimum length vectors d_i from the tip-over axes a_i to f_i^* are found by finding the projections of the tip-over axes normals l_i onto f_i^* and adding them to the negative of the normals l_i ,

$$d_i = -l_i + \left(l_i^T \cdot \frac{f_i^*}{\|f_i^*\|} \right) \frac{f_i^*}{\|f_i^*\|}. \quad (4.21)$$

The angle θ_i for the stability measure is found as

$$\theta_i = \sigma_i \cos^{-1} \left(\frac{f_i^*}{\|f_i^*\|} \cdot \frac{l_i}{\|l_i\|} \right) \quad (4.22)$$

whereby $0 \leq \theta_i$ and σ is defined as

$$\sigma_i = \begin{cases} +1 & \left(\frac{f_i^*}{\|f_i^*\|} \times \frac{l_i}{\|l_i\|} \right) \cdot \frac{a_i}{\|a_i\|} > 0 \\ -1 & \text{otherwise} \end{cases} \quad (4.23)$$

in order to give a positive value when the net force vector is directed inside the support quadrilateral.

Finally, the Force-Angle stability measure for a particular axis is defined as

$$\beta_i = \theta_i \cdot \|d_i\| \cdot \|f_i^*\| \quad (4.24)$$

which, as an angle times a distance times a force, gives a value in Newton-metres (Nm). Essentially, the measure considers how large the sum of all forces is and how close its direction is to being perpendicular to the tip-over axis, which indicates marginal stability. It includes the effect of top-heaviness, that is the reduced stability experienced when the centre of mass is located up high. It is easily calculated and it can deal with inertial and external forces. To determine the overall stability measure, the minimum of all axes must be found. The system becomes unstable at values below zero.

4.2 Analysis

The analysis is based on a VFM as decided upon in section 3.3.3.1 and the platform geometry described in section 9.7.2, with the effect of caster offset ignored.

4.2.1 Static

As the leg angle of all legs is simultaneously increased, the footprint grows, and naturally the stability increases as can be seen in Figure 4.3. With the torso upright and the arms also vertical, the centre of mass is in the centre of the footprint, making the torso rotation θ_{torso1} irrelevant in this position. The stability decreases slightly with increasing load, as the centre of mass is raised (the payload being at the end of the arms), offsetting the increased downward force.

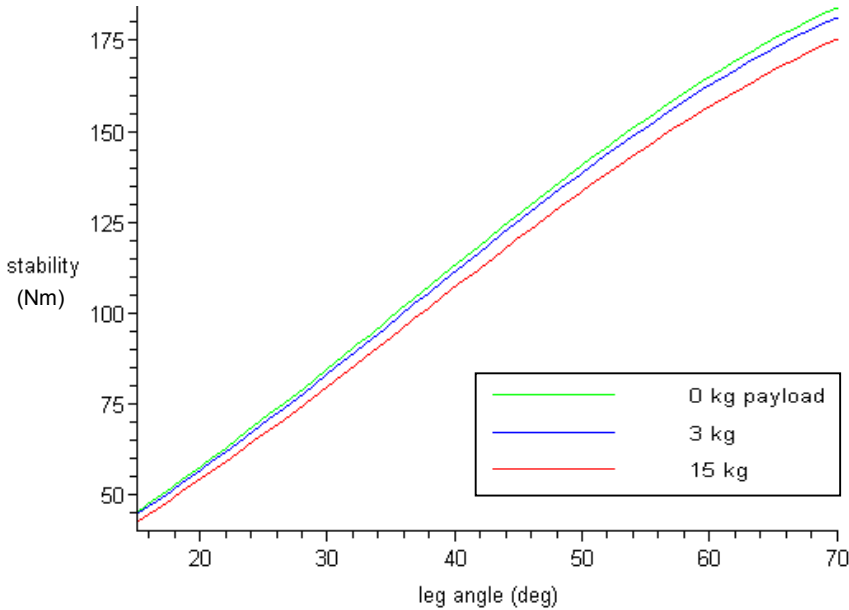


Figure 4.3: Torso and arms vertical, stability as a function of leg-extension angle at three different payloads.

With the torso or arms bent at θ_{torso2} or θ_{arm1} , the most stable torso rotation angle θ_{torso1} is not, as one might expect, such that the torso is aligned facing a contact point, because this gives a poorer stability value for the wide tip axis than an angle further over the narrow side. The most stable point is where the stability value for the wide and narrow axis become equal, which lies somewhere over the narrow side depending on the load. As can be seen in Figure 4.4, for torso and arms extended horizontally—the worst position for static stability—with a 3 kg payload and legs extended all the way out, the maximum stability occurs at about $\theta_{torso1} = 21^\circ$ (and at angles corresponding to symmetric positions), reaching a value of about 130 Nm. The stability value is substantially lower when the torso is rotated to face between the legs, with the narrow side reaching a minimum stability of 24 Nm at $\theta_{torso1} = 0^\circ$ and the wide side a value of 1.4 Nm at 90° . In other words, the platform can statically support 3 kg with the torso at any vertical torso rotation θ_{torso1} , but only barely. It can statically support a maximum of 5 kg aligned with the wide side in this configuration. Figure 4.5 shows how stability varies with payload for this configuration; the zero-plane, below which the configuration becomes unstable, is shaded grey.

Figure 4.6 and Figure 4.7 show the stability with varying payload for the torso in the upright position ($\theta_{torso2} = 90^\circ$) with arms extended horizontally ($\theta_{arm1} = 90^\circ$), a configuration that is expected to occur fairly frequently. Figure 4.6 is with the legs fully retracted; 15 kg cannot be supported over

the wide side in this configuration. Figure 4.7 shows the stability with the legs fully extended; now the platform is very stable. In fact, even over the middle of the wide side, the platform can statically handle a load of 30 kg in this configuration, as is apparent in Figure 4.8 and Figure 4.9, which show the effect of leg extension.

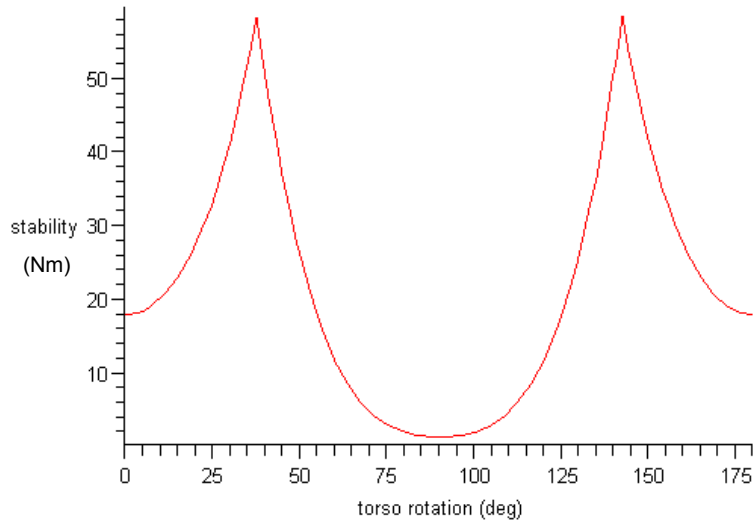


Figure 4.4: Stability with payload of 3kg and varying vertical torso rotation (θ_{torso1}), torso and arms horizontal, no acceleration, legs extended at 70°.

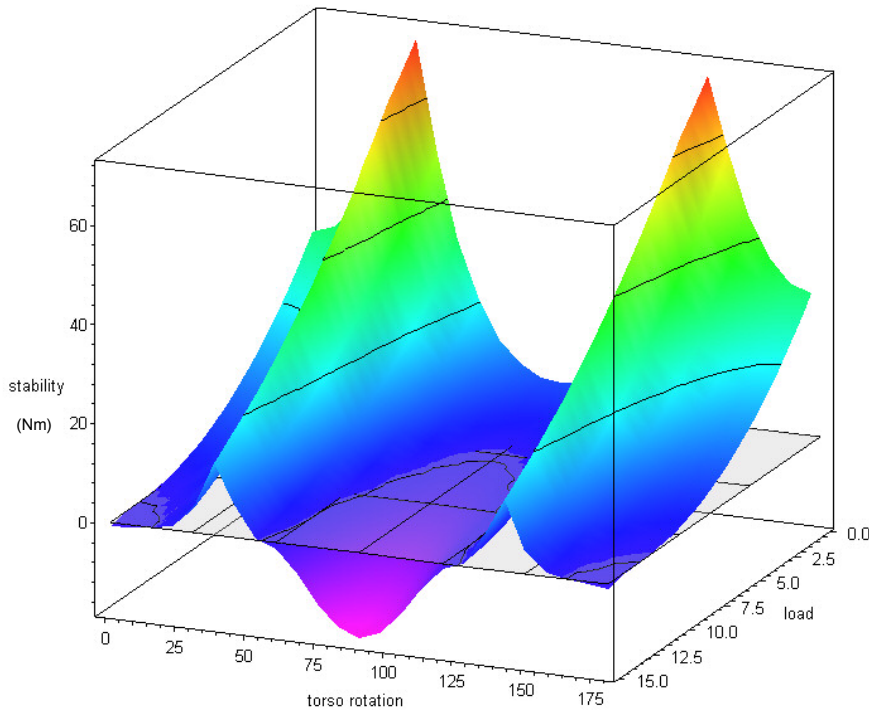


Figure 4.5: Stability for varying payload and vertical torso rotation with torso and arms horizontal, no acceleration, legs extended at 70°.

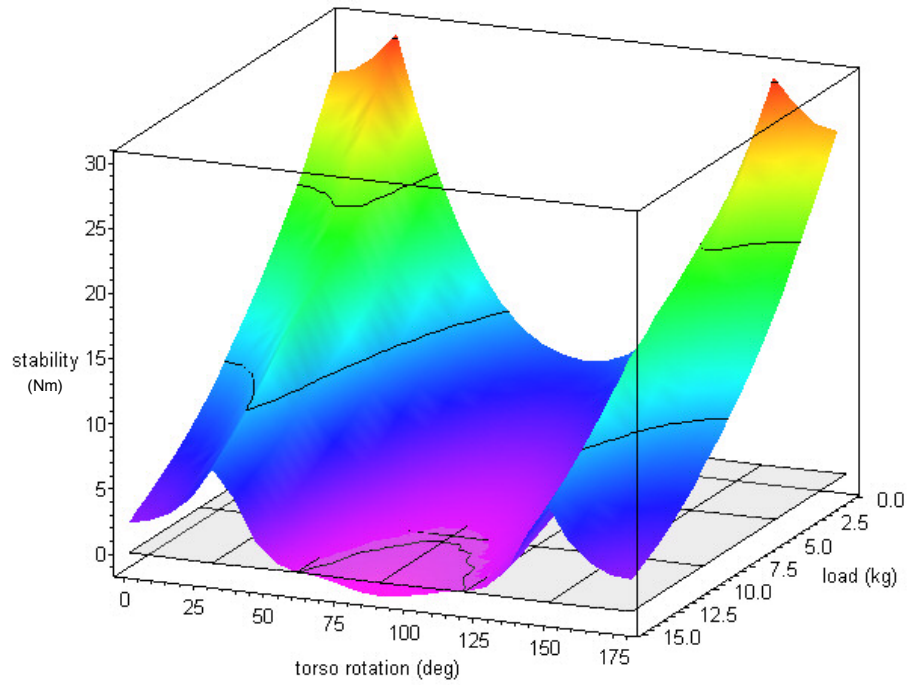


Figure 4.6: Stability for varying payload and vertical torso rotation with torso vertical, arm horizontal, no acceleration, legs retracted to 15°.

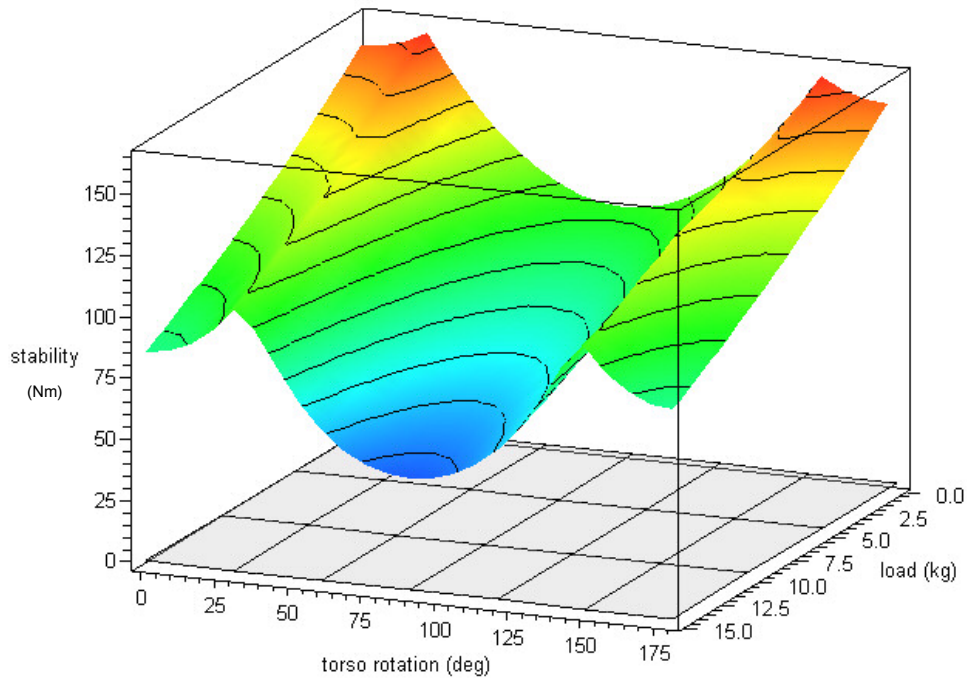


Figure 4.7: Stability for varying payload and vertical torso rotation, torso vertical, arms horizontal, no acceleration, legs extended to 70°.

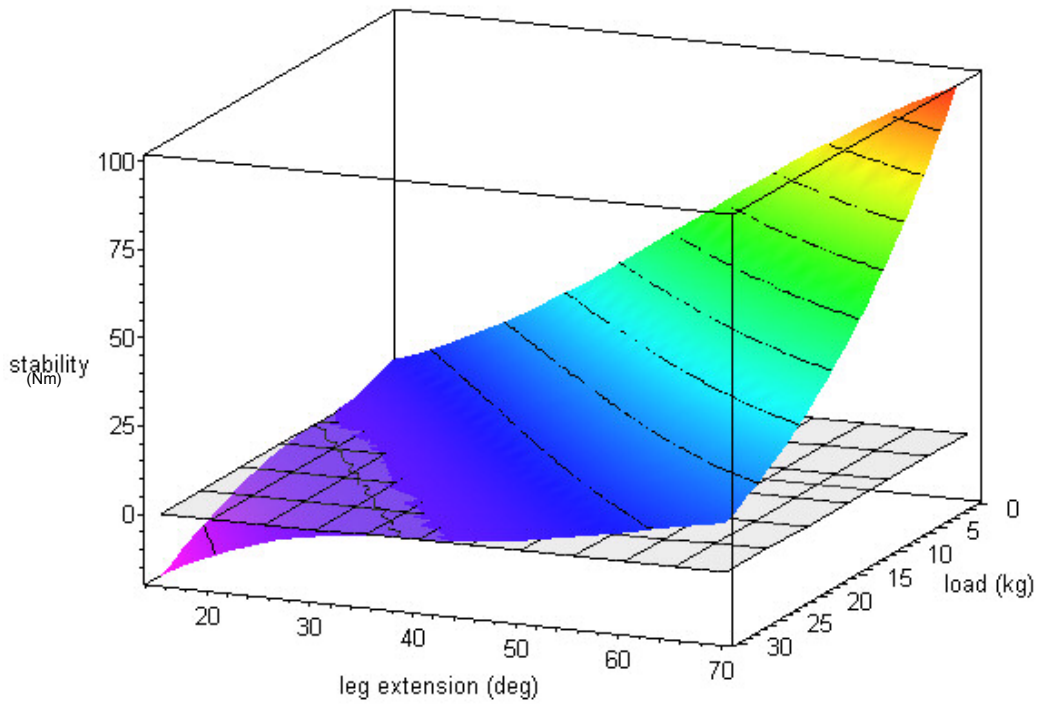


Figure 4.8: Stability for varying leg extension and load, torso vertical, arm horizontal and extended over wide side ($\theta_{torso1} = 90^\circ$), no acceleration.

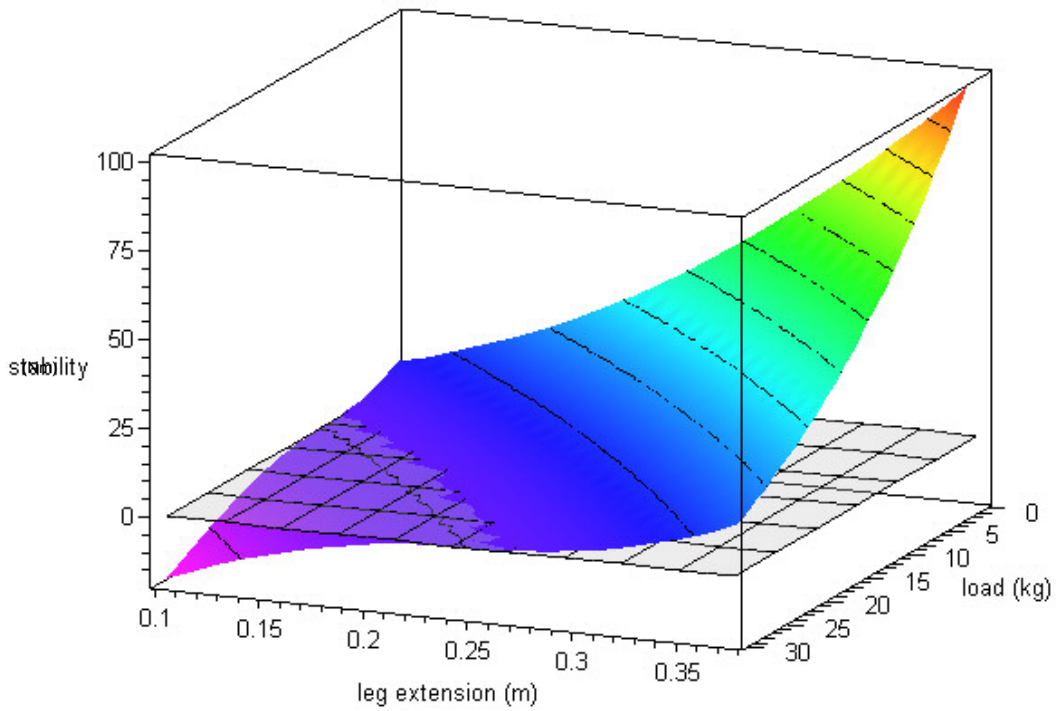


Figure 4.9: Same as above but leg extension expressed in metres.

4.2.2 With acceleration

Because of the platform's relatively high centre of mass, its significant acceleration capabilities are expected to have a considerable impact on stability. Indeed, the effect is pronounced; the inertial forces attempt to rotate the platform in the vertical plane contrary to the acceleration direction, causing a large reduction in stability on the side facing away from the acceleration direction, a large increase on the side facing the acceleration, and a mixed effect on the perpendicular side. This highlights how it may be possible to accelerate with a particular load and configuration, but unless the configuration is changed, deceleration (which will act in the opposite direction) can cause instability. Figure 4.10 through Figure 4.14 show the stability for various configurations and varying payloads. A number of key stability values are tabulated in Table 4.2.

4.2.3 Other Considerations

The stability measure as developed is fairly rudimentary. Some factors that should be considered if it is to be used for critical control purposes are:

- Effect of torso dynamics – significant inertial forces are transferred to the base
- Effect of caster – slightly different footprint size and shape depending on caster position
- Effect of suspension – causes tilt, which causes weight shift
- Effect of grade – traveling up a slope introduces a new variable and shifts the CM

The above factors could be implemented as additional geometric parameters and disturbance forces in the stability measure. Design and operation based on the stability measure should occur with some safety margin to ensure stability in the light of unaccounted for disturbance factors.

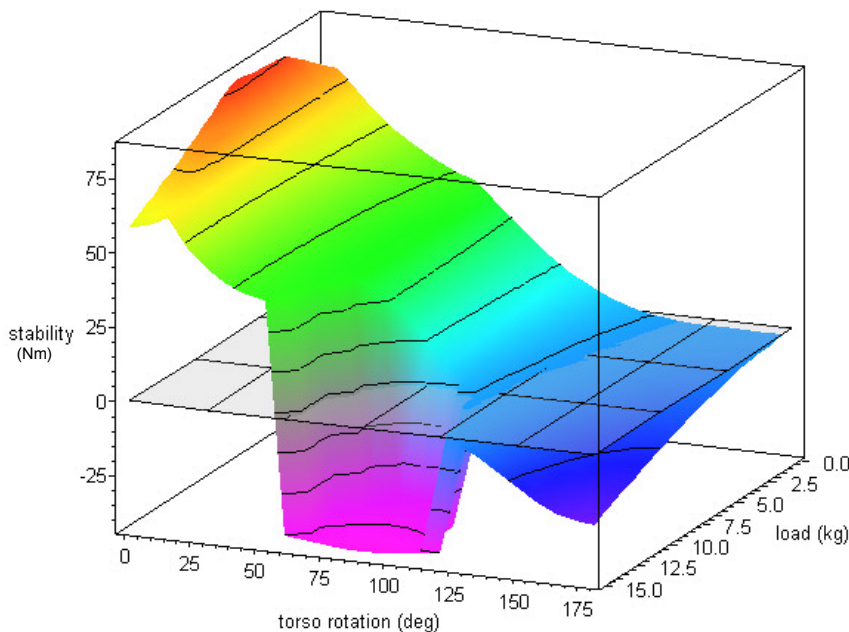


Figure 4.10: Stability for varying payload and vertical torso rotation, torso vertical, arms horizontal, acceleration at 2 m/s^2 in the x-direction (0°), legs retracted to 15° .

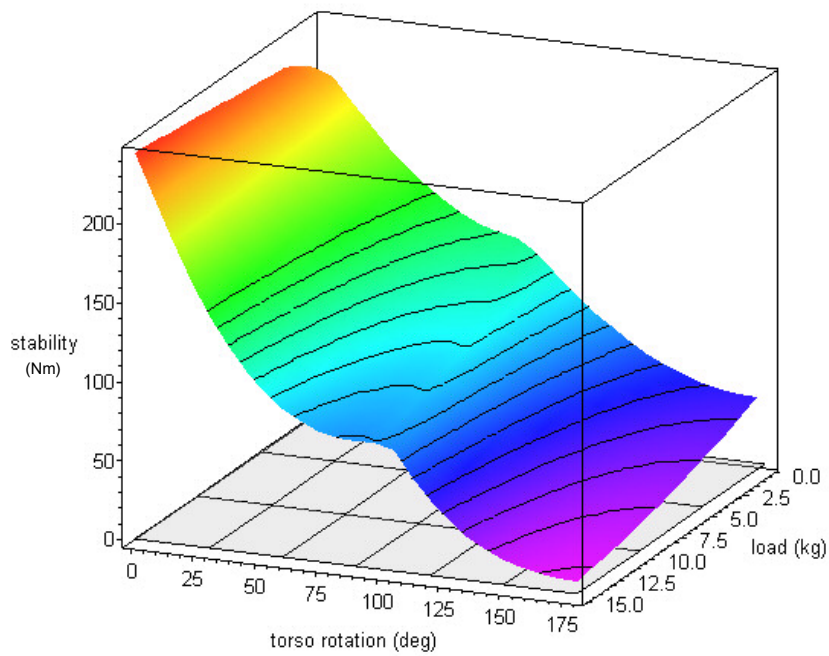


Figure 4.11: Stability for varying payload and vertical torso rotation, torso vertical, arms horizontal, acceleration at 2 m/s^2 in the x-direction (0°), legs extended to 70° .

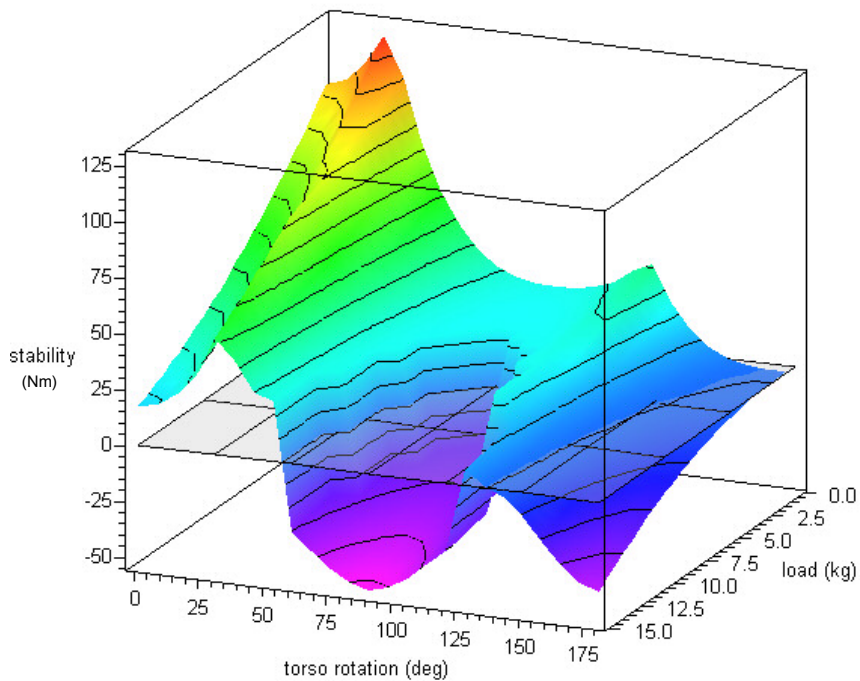


Figure 4.12: Stability for varying payload and vertical torso rotation, torso and arms horizontal, acceleration at 2 m/s^2 in the x-direction (0°), legs extended to 70° .

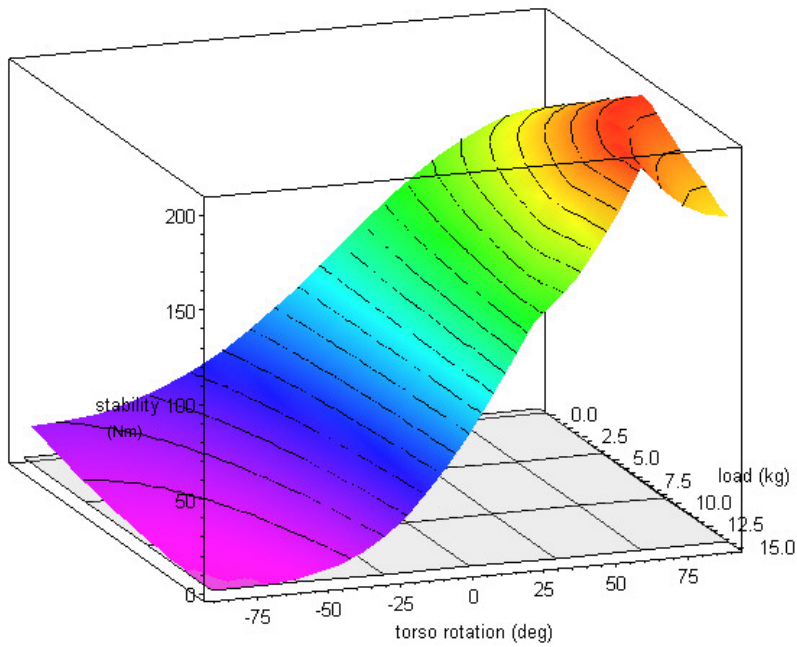


Figure 4.13: Stability for varying payload and vertical torso rotation, torso vertical, arms horizontal, acceleration at 2 m/s^2 in the y-direction (90°), legs extended to 70° .

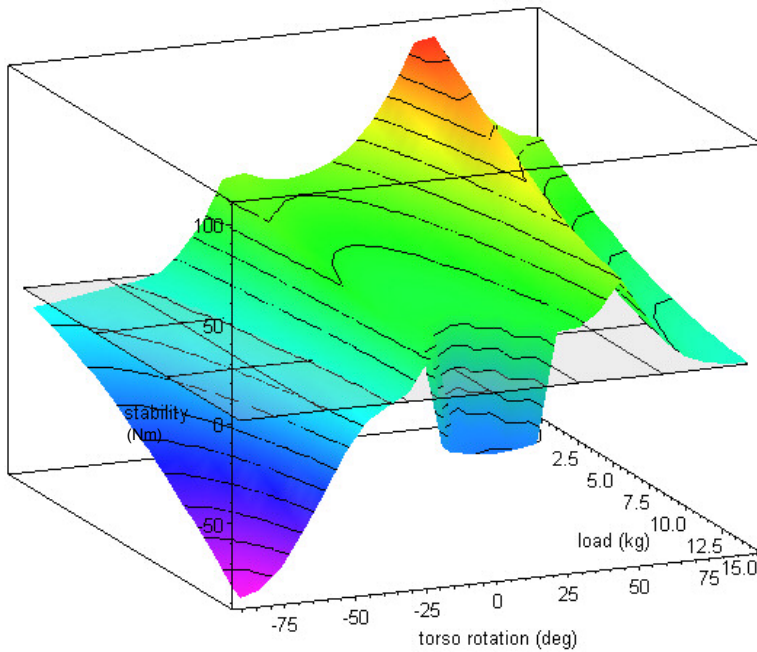


Figure 4.14: Stability for varying payload and vertical torso rotation, torso and arms horizontal, acceleration at 2 m/s^2 in the y-direction (90°), legs extended to 70° .

Table 4.2: Stability values for different configurations.

Situation	Leg Position	Load	Torso Position		Arm Position	Stability (Nm) Beta
			Rotation in Vertical Axis	Tilt at first horizontal axis	Tilt in first axis	
	deg	kg	deg	deg	deg	
No acceleration						
Ultimate Maximum load with Torso, Arm Horizontal	70	30	40.5	0	0	0.03
Largest fully statically stable load with Torso, Arm Horiz	70	5	90.0	0	0	0.04
15kg load, Torso, Arm Horizontal min	70	15	90.0	0	0	-17.85
15kg load, Torso, Arm Horizontal max	70	15	39.4	0	0	16.7
3kg load, Torso, Arm Horizontal min	70	3	90.0	0	0	1.36
3kg load, Torso, Arm Horizontal max	70	3	37.6	0	0	58.6
no load, Torso, Arm Horizontal min	70	0	90.0	0	0	7
no load, Torso, Arm Horizontal max	70	0	36.9	0	0	74
no load, Torso, Arm Vertical min=max	70	0	na	90	90	184.42
15kg load, Torso, Arm Vertical min=max	70	15	na	90	90	175.51
no load, Torso, Arm Vertical min=max	15	0	na	90	90	45.79
15kg load, Torso, Arm Vertical min=max	15	15	na	90	90	43.01
no load, Torso, Arm Horizontal max	15	0	36.9	0	0	-0.02
3kg load, Torso, Arm Horizontal max	15	3	37.6	0	0	-2.26
15kg load, Torso Vert, Arm Horiz min	15	15	90.0	90	0	-1.08
15kg load, Torso Vert, Arm Horiz max	15	15	32.5	90	0	8.26
3kg load, Torso Vert, Arm Horiz min	15	3	90.0	0	0	3.88
3kg load, Torso Vert, Arm Horiz max	15	3	25.3	0	0	25.3
15kg load, Torso Vert, Arm Horiz min	70	15	90.0	90	0	45.2
15kg load, Torso Vert, Arm Horiz max	70	15	32.6	90	0	110
3kg load, Torso Vert, Arm Horiz min	70	3	90.0	0	0	91.1
3kg load, Torso Vert, Arm Horiz max	70	3	25.3	0	0	154
with acceleration of 2m/s² in the x-direction:						
3kg load, Torso Vert, Arm Horiz min	70	3		90	0	37.2
3kg load, Torso Vert, Arm Horiz Torso to side	70	3	90.0	90	0	116
3kg load, Torso Vert, Arm Horiz max	70	3	0.0	90	0	233
15kg load, Torso Vert, Arm Horiz min	70	15	180.0	90	0	8.14
15kg load, Torso Vert, Arm Horiz Torso to side	70	15	90.0	90	0	78.9
15kg load, Torso Vert, Arm Horiz max	70	15	0.0	90	0	244
3kg load, Torso Vert, Arm Horiz min	20	3	180.0	90	0	-0.18
3kg load, Torso Vert, Arm Horiz min	20	3	90.0	90	0	22.7
3kg load, Torso Vert, Arm Horiz max	20	3	0.0	90	0	92.7
3kg load, Torso Vert, Arm Horiz min	20	15	180.0	90	0	-15.2
3kg load, Torso Vert, Arm Horiz min	20	15	90.0	90	0	-41
3kg load, Torso Vert, Arm Horiz max	20	15	0.0	90	0	79.28
15kg load, Torso, Arm Horizontal min (Torso to side)	70	15	90.0	0	0	~-52
15kg load, Torso, Arm Horizontal Torso away from accel	70	15	180.0	0	0	~-29
15kg load, Torso, Arm Horizontal max	70	15	~30	0	0	~-52
3kg load, Torso, Arm Horizontal Torso to side	70	3	90.0	0	0	23.58
3kg load, Torso, Arm Horizontal min (Torso away from accel)	70	3	0.0	0	0	-0.436
3kg load, Torso, Arm Horizontal max	70	3	~21	0	0	~-130
with acceleration of 2m/s² in the y-direction:						
3kg load, Torso Vert, Arm Horiz max	70	3	90.0	90	0	175.8
3kg load, Torso Vert, Arm Horiz Torso to side	70	3	0.0	90	0	75.1
3kg load, Torso Vert, Arm Horiz min	70	3	-90.0	90	0	13.64
15kg load, Torso Vert, Arm Horiz max	70	15	~60	90	0	~200
15kg load, Torso Vert, Arm Horiz Torso to side	70	15	0.0	90	0	~70
15kg load, Torso Vert, Arm Horiz min	70	15	-90.0	90	0	0.11
15kg load, Torso, Arm Horizontal min	70	15	-90.0	0	0	-89.6
15kg load, Torso, Arm Horizontal Torso to side	70	15	0.0	0	0	-30.6
15kg load, Torso, Arm Horizontal Torso away from accel	70	15	90.0	0	0	~0
15kg load, Torso, Arm Horizontal max	70	15	~45	0	0	~45
3kg load, Torso, Arm Horizontal min	70	3	-90.0	0	0	-13.85
3kg load, Torso, Arm Horizontal max	70	3	~50	0	0	~90

Chapter 5

Step Passing Behaviour

While most design studies for mobile robots consider the actuator loads that occur under acceleration and peak velocity, e.g. [16], [81], and sometimes consider surmounting grades, they generally do not consider the power needed to surmount small steps, even though such steps occur frequently at door sills and at floor-covering transitions. The torque for overcoming a step—particularly at low speeds—can pose the highest torque requirement. ‘Maximum bump height’ is also the 8th most important engineering criteria for this system (see section 1.4.4). In order to be able to properly determine the step passing torque requirements for the system, which is to overcome steps of 3 cm in height, this problem will be analyzed in detail below. The resulting torque will then be compared to other torque requirements to size the drive actuator appropriately as detailed in Appendix E.

The chapter starts by presenting a simple static model of step passing. To investigate the validity of this model, some experiments were conducted. The first group of experiments in 5.3 were performed to determine the properties of the experimental system. Then, the experiments with small steps under different conditions are described in 5.4. The simple model does not adequately describe the experimentally observed behaviour, so an advanced model which includes system dynamics and tire elasticity is presented in 5.5. This model is simulated for comparison to the experimental results in 5.6. In section 5.7, the model is extended to other conditions and adjusted to match the system as designed, with simulations again being performed. Finally, this leads to conclusions in 5.8 about step passing in general and applications to the mobile platform drive actuator design.

5.1 Background

Ferriere [30, 32] states “the European Federation of Handling Industry recommends a ratio H/R_w smaller than 0.06 if the wheel stiffness is important (as for polyurethane) and a ratio of 0.1 for pneumatic tires or tires covered with an elastic material,” where H is step height and R_w is wheel radius. He also considers basic statics and says that in addition to sufficient horizontal force, the wheel may not slip at the corner, which depends on the friction coefficient and the vertical load on the tire; for a friction coefficient of 0.5, the maximum bump is 20% of the wheel radius. In sizing the spherical wheel, he considers a 0.06 ratio as the limit for dynamic step passing at 4km/h in order to limit vibrations and a 0.2 ratio the upper limit for static surmountable step height.

5.2 Simple Theory

Some tire models designed for car tires can handle steps [82], [83], but these cannot be easily translated to typical robot tires and their complexity makes it difficult to understand the underlying phenomenon in passing over steps. Often, they are specifically for pneumatic tires. Tire models available in Dymola as well as many other dynamics simulation packages do not allow for two points of contact; the tire model used in other parts of this thesis (Appendix D) is unsuitable for simulating step passing because it requires ground disturbances to have radii at least as large as the tire radius

[84]. This is a situation that occurs in sill climbing when the tire impacts the corner but before it has lifted from its ground contact point where it stopped rolling.

5.2.1 Rigid-Wheel Model

To create a simple rigid-element model (Figure 5.1), the front wheel of radius r is replaced by a rigid link (CF) pin-jointed at one end to the ground and to the cart at the other end. The rear wheel is replaced by a pin joint attached to a slider joint at R . It is assumed that the vehicle is front-wheel driven and that the wheels are aligned perpendicular to the step with a radius larger than the step height h . The mass and inertia of the wheels are neglected.

Described in this way, the problem is similar to a slider-crank, a mechanism that is often used as an example in literature, e.g. [85], where the front wheel resembles the crank. There are several differences from the typical representation of a slider-crank as a device to convert linear into rotational motion: the slider is vertically offset from the crank origin by distance e ; the ‘connecting rod’ (RF) of length b (the vehicle) has a large mass m and inertia I with CM at B which is a distance c_x and c_y from F ; and, most importantly, the torque T_f is applied not at the ‘crank origin’ C but at the front wheel centre F . Introducing a torque in the middle of the mechanism means that its reaction also plays a role, acting both on α , the angle of the platform from horizontal, and θ , the angle of CF from horizontal. The reaction torque from the motor acts to effectively shift some of the load off the front wheel, reducing the necessary torque. This differentiates the problem from a slider crank, where the reaction torque is to the ground and does not affect the mechanism.

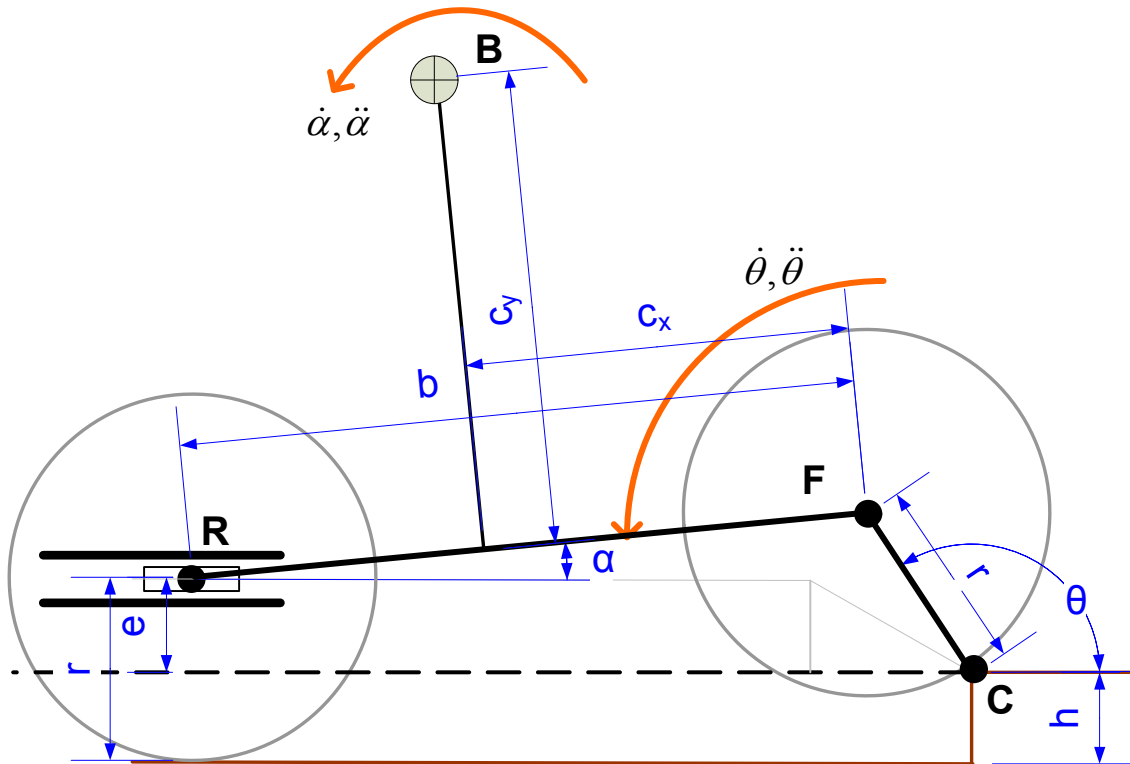


Figure 5.1: Rigid system model showing similarities to a slider-crank.

5.2.1.1 Statics

The maximum torque T_{max} required for static balance of this mechanism occurs with the system at the base of the step and is

$$T_{max} = \frac{1}{2} \frac{mgbr \cos \theta_{init}}{b - r \cos \theta_{init}} \quad (5.1)$$

when $c_x = b/2$. The cosine of the starting angle θ_{init} can be found as follows:

$$\cos \theta_{init} = -\sqrt{h(2r-h)}/r \quad (5.2)$$

Alternatively, define x_{init} the initial horizontal distance from the step corner to the wheel centre as

$$x_{init} = -r \cos \theta_{init} \quad (5.3)$$

Thus the torque can also be expressed as

$$T_{max} = \frac{1}{2} \frac{mgbx}{b + x_{init}} \quad (5.4)$$

Torque in (5.1) is directly proportional to system load. Combining (5.1) and (5.2) using three non-dimensionalized (ND) groups, T_{max}/mgb , b/r , h/r , results in the ND expression for torque

$$\frac{T_{max}}{mgb} = \frac{1}{2} \left(\frac{\sqrt{\frac{h}{r} \left(2 - \frac{h}{r} \right)}}{\left(\frac{b}{r} + \sqrt{\frac{h}{r} \left(2 - \frac{h}{r} \right)} \right)} \right) \quad (5.5)$$

which allows for the observation of generalized trends that hold true for the more advanced model to follow and which are visible in Figure 5.2:

- ND peak torque decreases with increasing wheelbase (b), though the benefits are minimal for large wheelbase-to-wheel-radius ratios (b/r). Compared to applying a torque at the origin C as in a typical slider-crank, $b/(b + r \cos \theta_{init})$ less peak torque is required.
- A larger wheel radius increases ND peak torque (the moment arm is larger), though the effect is reduced for small step heights.
- ND peak torque increases with step height

As is apparent from Figure 5.2, increasing the wheelbase, which increases the b/r ratio, significantly reduces the necessary torque and allows for climbing higher sills even within the same friction limitations—an advantage for having a variable footprint.

An important additional consideration is that the friction between the corner and the wheel must be sufficient to prevent slip. Experiments show that the effective friction factor is higher at the corner than on a flat surface, in some cases even exceeding one, as discussed in section 5.3.4.1. Nevertheless, the available normal force decreases with increasing h/r , reaching zero when $h=r$, at which point a front-wheel-driven platform has reached its ultimate step height limit. With higher static friction between the wheel and the ground, larger sill heights can be surmounted.

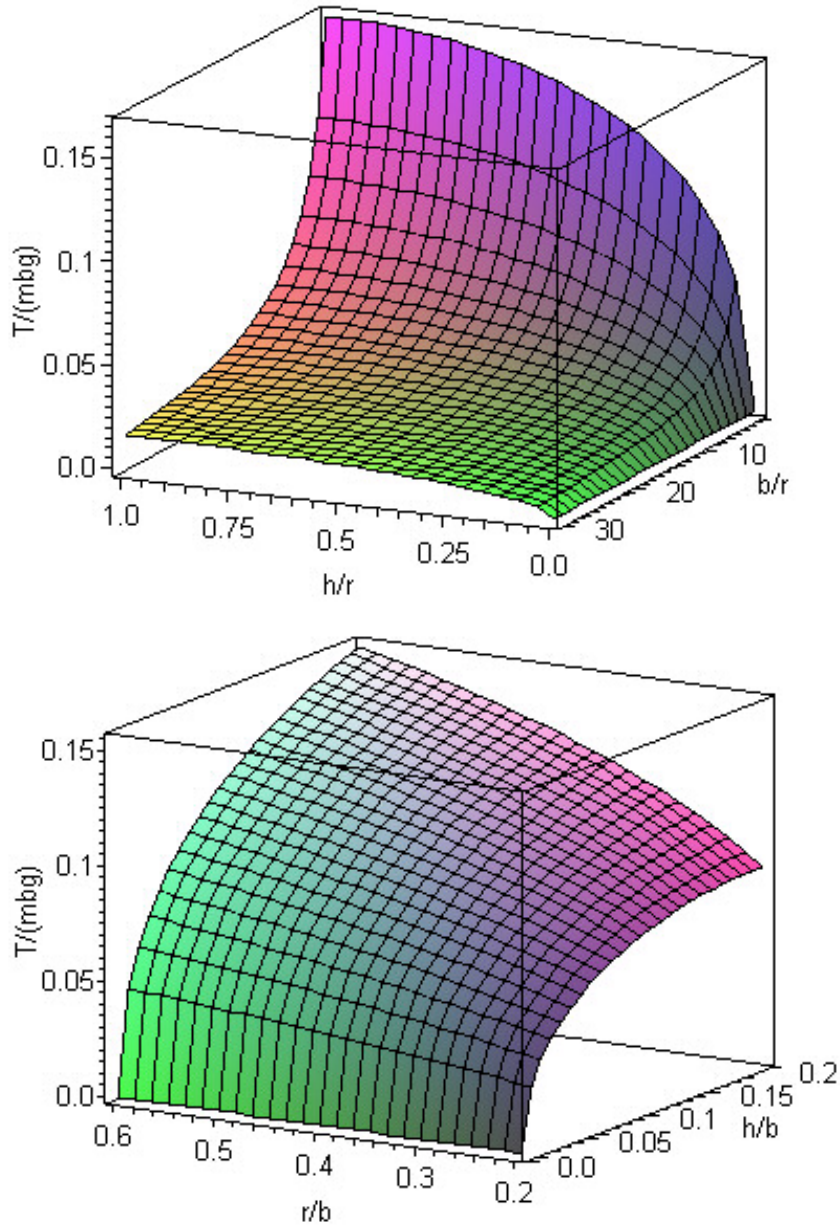


Figure 5.2: Static torque relationship for non-dimensionalized parameters.

5.3 Experimental System Characterization

Little data exists for wheels of the size and type suitable for use on the mobile platform. This experiment investigates the ground interface behaviour of the drive wheel of the previous DLR platform, which is similar to the wheel intended for the new platform. Quantifying the friction behaviour between the tire and the ground is crucial for understanding step passing, which of course relies on the ground-tire interface.

5.3.1 Setup

5.3.1.1 Tire Properties

The wheel is similar to a wheelchair caster wheel with a custom aluminium hub and a tire that has foam rather than air filling. Details are given in Table 5.1.

Table 5.1: Wheel specifications.

Tire Manufacturer and Model	IMPAC 32-86 IS300
Nominal Dimensions	6" x 1 ¼" (152.4 mm x 31.75 mm)
Measured Dimensions	147.6 mm x 31 mm
Tire Surface Material	Polyamide
Tire Filling	Polyurethane foam filled
Hub Diameter	100mm

Simple calliper measurements with the wheel unit successively loaded with a weight of up to 94 N in addition to the 88 N load of the drive unit and then unloaded show a wheel diameter hysteresis of 0.138 \pm 0.025 mm, which amounts to 0.09% of the measured diameter.

5.3.1.2 The Drive Unit

Identical to the units in the previous generation platform, the experimental drive unit includes motors, gearing and torque control for both wheel propulsion and steering. It is a steered wheel configuration; the steering axis intersects the drive axis perpendicularly. The drive wheel is powered through the centre of the steering axis using a bevel gear and belt drive combination, as visible in Figure 5.3 and detailed in Table 5.2 [86].

5.3.1.3 The Test Stand

The drive unit was mounted in a test stand such that it was only supported horizontally but free to slide vertically along the aluminium profile pieces (Figure 5.4). The friction factor between the drive unit's steel back-plate and the aluminium profile piece was experimentally determined using the inclined plane method [87]. The drive unit could be moved forward such that the drive wheel came in contact with the floor surface or test pieces could be placed underneath the wheel in the position shown in Figure 5.6.

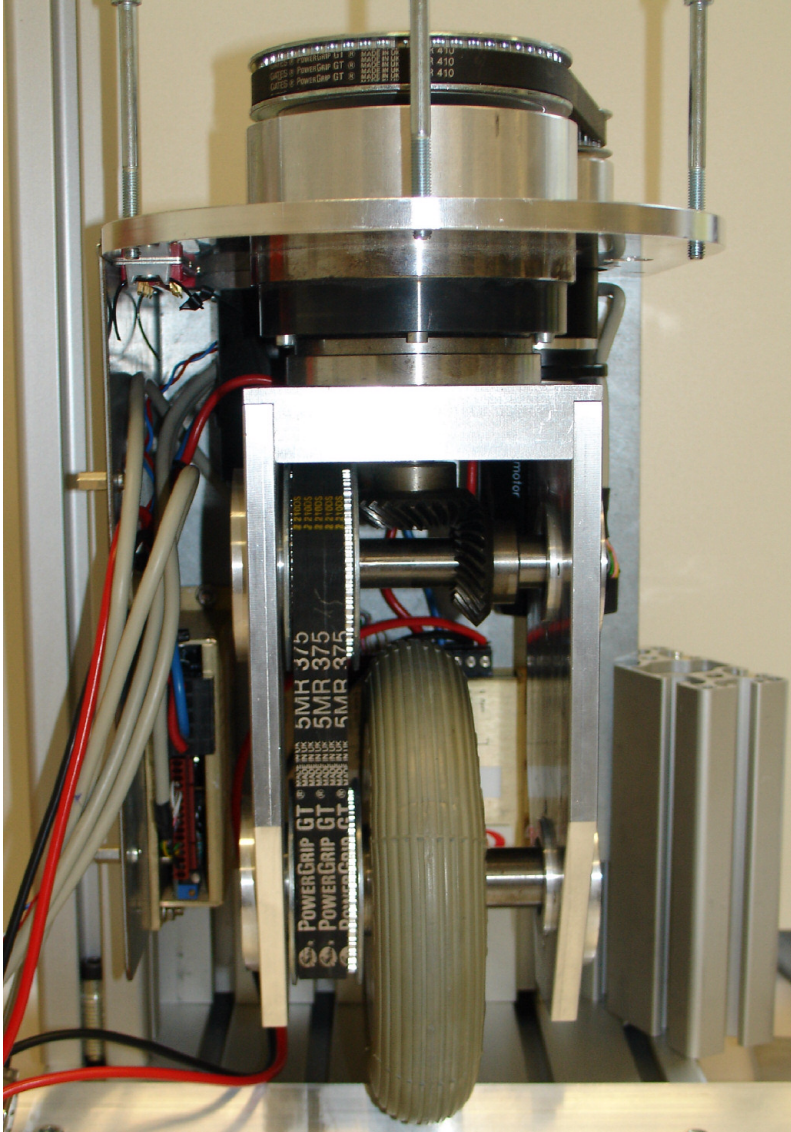


Figure 5.3: Front view of drive unit in test stand with belt drive to left of and bevel gear above tire.

5.3.2 Test Procedure

5.3.2.1 Test Stand Friction

With the back of the drive unit placed on top of the aluminium profile piece which it contacts in the test stand, the angle of the piece, θ_{slip} , was slowly increased until the drive unit started to slip, at which point the angle was recorded in order to calculate the friction factor, μ_{wall} :

$$\mu_{wall} = \tan(\theta_{slip}) \quad (5.6)$$

After several trials, the friction factor was found to be 0.233 ± 0.007 .

Table 5.2: Drive unit specifications.

Unit Chassis	Weight:	8967 g
	Approx. Dimensions:	25.5 cm high, 21.4 cm deep, 18.2 cm wide
Controllers	Manufacturer and Model:	Copley Controls 4122CE
	Specifications:	20 A peak, 10 A continuous
Drive and Steer Motor	Manufacturer and Model:	Maxon RE 40 – 148877
	Specifications:	DC Brush, 150 W, 48 V, Rated 0.148 Nm @ 7000 rpm, Peak 2.5 Nm Weight: 480 g Torque Constant: 0.0603 Nm/A
Drive Gearing	30:1 Reduction:	15:1 - Maxon GP 42C – 203116, 2 Stage, 7.5 Nm max continuous rated output 2:1 – Toothed Pulley
	Rated Speed at Wheel:	233.3 rpm (1.86 m/s)
	Rated Torque at Wheel:	4.5 Nm
	Efficiency:	81% Planetary, 98% Belt, 99% Bevel, 98% Belt = 79% max at rated torque
Steering Gearing	127.5 Reduction:	51:1 - Harmonic Drive 2.5:1 – Toothed Pulley
	Rated Speed at Wheel:	54.9 rpm (0.92 rev/s)
	Rated Torque at Wheel:	23.7 Nm

5.3.2.2 Wheel Output Torque

The relationship between the reference input voltage V_{ref} of the Copley torque controller and the output torque at the wheel was determined by loading the free wheel with a known torque and increasing the reference voltage until the wheel began to move. This method includes all electrical and mechanical losses in the drive train yet has limited sources of error compared to calculating the relationship of each stage individually. Multiple measurements were made with different loadings as suggested in [88] to come up with the following linear fit relationship,

$$T_{wheel} = aV_{ref} - b \quad (5.7)$$

where the coefficients a and b are shown in Table 5.3 for different wheel velocities. This allows for interpolation based on the observed velocity. For the following investigation in section 5.3.2.3, the relationship at 0 rpm was used, since the static friction factor at zero velocity is of interest. This relationship was also used for step climbing from a standing start as investigated below in 5.4, as

again the wheel starts at zero velocity, and it does not gain much speed when it reaches the point of maximum torque that is early in the step climb.

Table 5.3: Coefficients for relationship between input reference voltage and wheel output torque at different wheel speeds.

Wheel Velocity	a	b
rpm	Nm/V	Nm
0	2.86 ± 0.07	0.32 ± 0.09
100	2.84 ± 0.02	0.36 ± 0.02
200	2.92 ± 0.01	0.21 ± 0.01



Figure 5.4: test stand with drive unit.

Torque was controlled using the Copley controller run in torque mode, where a reference and monitor signal are set and recorded by a PC-based controller/DAQ at 10kHz. Controller reaction times were found to be significantly smaller than observed physical behaviour. A GUI with corresponding C code was created to allow for easy adjustment to the torque set-point voltage and for observing torque monitor voltage and wheel encoder data. Further coding created a setup with PI velocity feedback to allow for operation at a set velocity. Power was provided by a DC power supply set to 48V.

5.3.2.3 Drive Wheel Friction

With the drive unit in the test stand and the wheel on the desired test surface, the reference input voltage of the torque controller was slowly increased while monitoring the wheel for signs of slip. The reference input voltage from the controller was recorded when wheel slip occurred.

Using the experimentally determined relationship between input voltage and wheel output torque (T), the experimentally determined friction factor between the test stand and the drive unit (μ_{wall}), the known mass of the drive unit (m), and the effective radius of the wheel as measured when under load, the friction factor between the wheel and the ground (μ_{ground}) can be calculated as detailed in Figure 5.5.

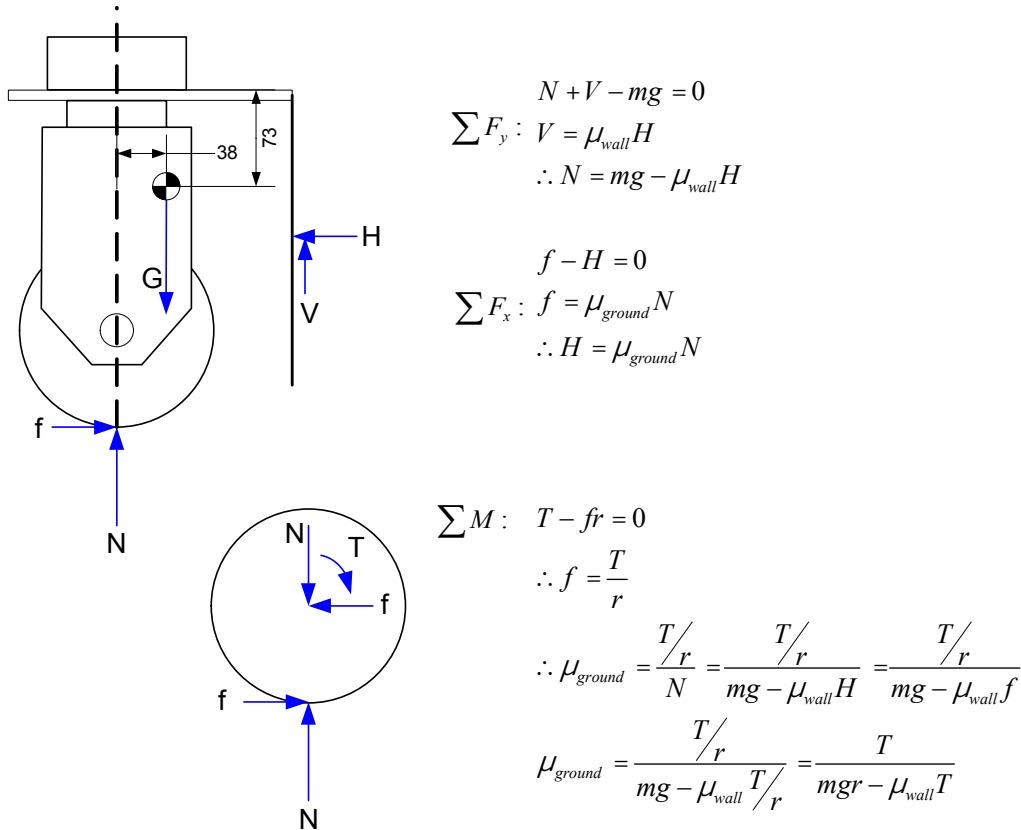


Figure 5.5: static force balance used to calculate wheel/ground friction factor.

5.3.3 Results

5.3.3.1 Drive Wheel Friction

The results for two types of floor, laminate and short-pile carpet, with three different loadings are shown in Table 5.4. The friction factor for laminate floor is higher than that for the carpet; in both cases, the friction factor varies somewhat with loading. The wheel was also placed on top of the corner of an aluminium angle piece as shown in Figure 5.6 to resemble the conditions that might be encountered at a metal door sill; results were found to have large variations between trials; a range is given in Table 5.4. For the angle piece, rather than a smooth slip at a certain torque, the drive unit would actually jump up while trying to move forward once movement occurred.

Table 5.4: drive wheel friction on different surfaces - experimental results.

Condition	Load	Wheel Torque	Effective Load	Ground Force	Friction Factor
		Nm	N	N	
Laminate floor	Drive unit only (8.967 g)	3.5±0.3	77±1	47±5	0.62±0.06
	+4.806 g	5.1±0.4	120±1	69±6	0.57±0.05
	+4.781 g	6.6±0.6	162±2	90±7	0.56±0.05
	Average				0.58±0.02
Carpet	Drive unit only (8.967 g)	2.4±0.3	80±1	32±4	0.39±0.04
	+4.781 g	3.9±0.3	123±1	53±5	0.43±0.04
	+4.806 g	6.5±0.5	162±2	87±7	0.54±0.05
	Average				0.45±0.04
Aluminium angle piece	Drive unit only (8.967 g)	4.2 – 5.6	75 - 70	57 - 75	0.76 – 1.1

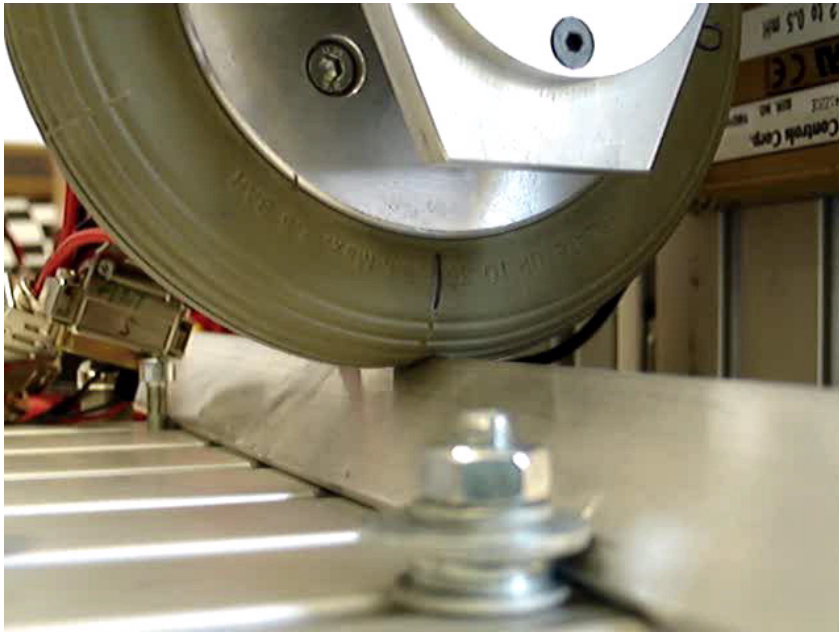


Figure 5.6: Aluminium angle piece fixed in test stand to simulate a step edge.

5.3.4 Analysis

5.3.4.1 Drive Wheel Friction

The range of results corresponds with values in literature for similar materials (Table 5.5). Also apparent from this listing is the variability in friction factor values.

While in theory, the normal load should not affect the value of the friction factor, the experimental results suggest otherwise. For linoleum, there is a small trend towards lower friction values at higher loading. It is hypothesized that the tire-ground interface changes depending on the size of the contact area, affecting adhesion. This is visually confirmed by the skid marks left in the linoleum; with a low load, the tire does not deform much and so a small contact area digs deeply into the floor surface (Figure 5.9). With a higher load, deformation is higher and the contact area increases (Figure 5.7 and Figure 5.8), reducing the amount the wheel digs in and thus reducing the adhesion of the tire.

For carpet (Figure 5.10), there is a small opposite trend towards higher friction values at higher loading. It is hypothesized that here the compression of the carpet fibres under higher loads provides better adhesion, increasing the friction factor.

Intuitively, a high “friction factor” is expected at the angle piece, because it digs into the tire, as can be seen in Figure 5.6. That the classical definition of the friction factor as being dependent on the normal load, as utilized in 5.3.2.3, may not be applicable in this situation is illustrated by calculated results that exceed 1. Such results are nonetheless possible when with the effect of tire material adhesion and deformation are considered. The elastic nature of the tire thus helps provide excellent hold at a corner, an observation that must be considered for step climbing.

Table 5.5: Friction factors from literature.

Tire Type	Surface	Static Friction Factor	Source
Foam filled wheelchair tire (polyisoprene polymer in polyethylene tube)	<i>Indoor surface:</i> smooth finished concrete, sealed and polished	0.43	[89]
Molded polyurethane wheelchair tire		0.55	
Pneumatic wheelchair tire		0.65	
Foam filled wheelchair tire (polyisoprene polymer in polyethylene tube)	<i>Outdoor surface:</i> Concrete sidewalk	0.70	
Molded polyurethane wheelchair tire		0.65	
Pneumatic wheelchair tire		0.78	
Rubber	Concrete	0.8	[22]
Car tire	Road, dry	0.7	[90]



Figure 5.7: Top view of skid marks and slight damage of floor under heaviest load; note large width of indentation and low depth due to wider contact area. Lower ruler scale in cm.

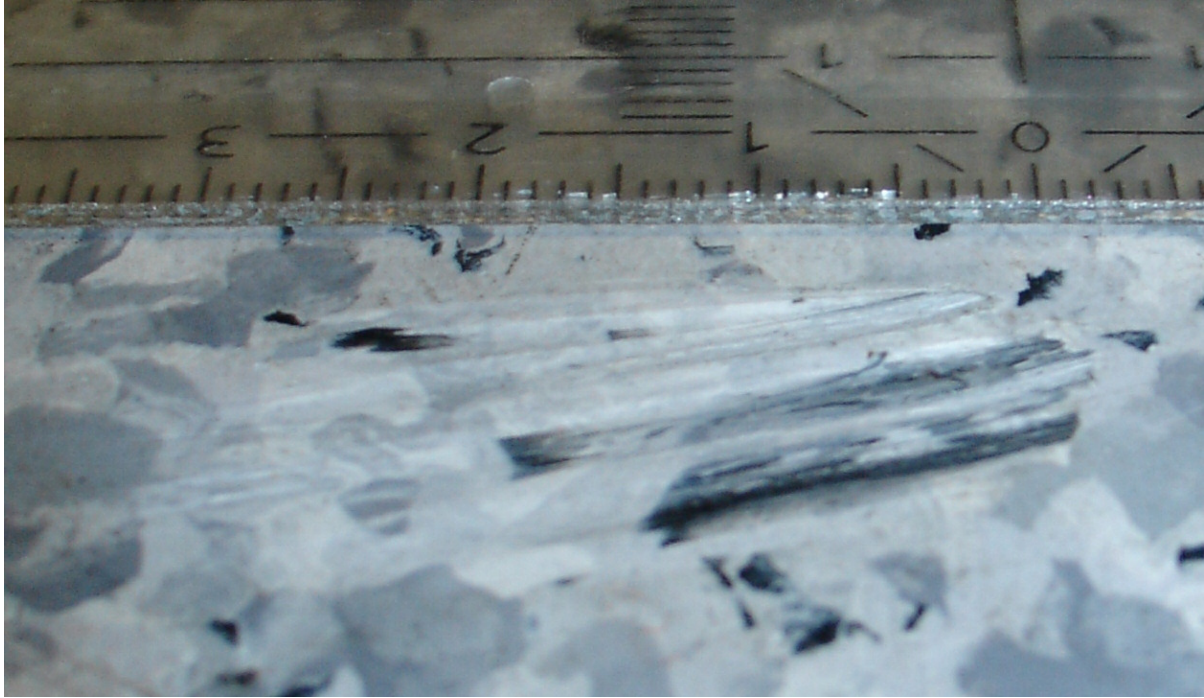


Figure 5.8: Side view of skid marks and slight damage of floor under heaviest load; note large width of indentation and low depth due to wider contact area. Ruler in cm.



Figure 5.9: Top view of indentation of floor under lightest load; note narrow width of indentation and high depth due to wider contact area. Lower ruler scale in cm.



Figure 5.10: Close-up of short-pile commercial carpet test surface.

5.3.5 Conclusions

The friction factor between different ground surfaces and the tire lie in the middle of expected ranges, suggesting published values can be used to define boundary values for simulation and calculation results. The results will also be considered in analysis of the step-passing experiments.

5.4 Step Passing Behaviour Experiment

5.4.1 Setup

5.4.1.1 Motor & Geartrain Properties

Using the drive unit from the old DLR platform (described in 5.3.1.2), a three-wheeled cart was assembled (Figure 5.11, Table 5.6). Consisting of ITEM aluminium profile pieces, the cart was easily re-configured for different wheelbases and centre of mass locations. The two rear fixed-caster wheels were chosen to be very similar to the drive wheel. A solid model of the entire cart was created which included mass and inertial data obtained from part specifications and, in the case of the wheels and drive unit, measurement. The total mass, centre of mass and inertia for the cart was calculated from the model in software. Torque control of the drive unit was performed as in 5.3.2.2.

The small steps for the experiment were constructed of wood sheets of different thickness with a laminate surface. Two different step heights—8.42 mm and 16 mm or 11% and 22% of undeformed tire radius, representing 84% and 105% of rated motor torque for static balance—were tested. An initial torque of 0.73 Nm was applied to eliminate play in the system and bring the wheel into contact with the corner.

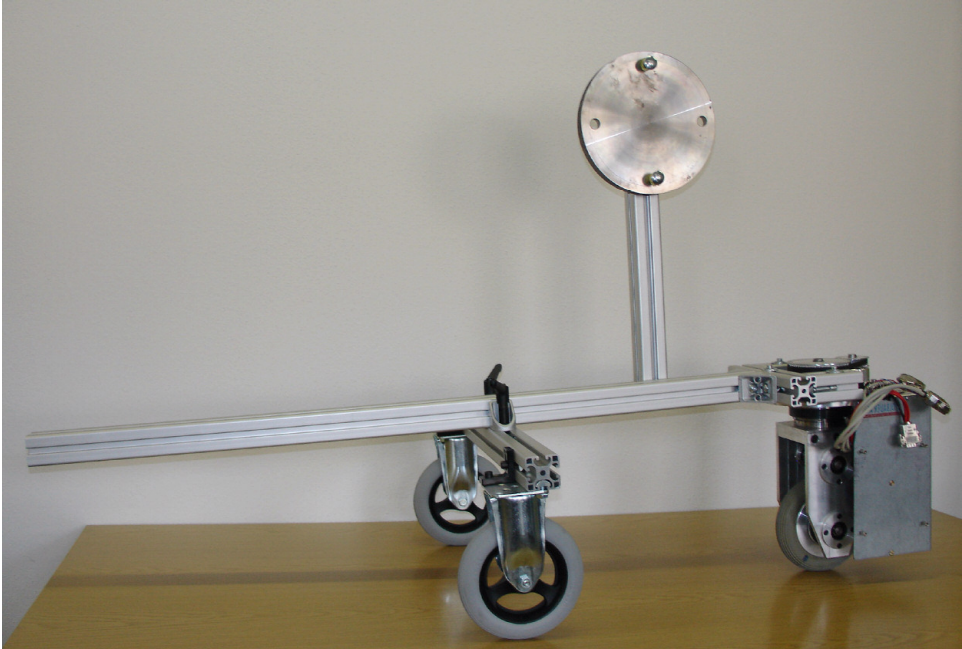


Figure 5.11: experimental cart, side view with short wheelbase.

Table 5.6: Experimental cart specifications.

Component	Details
Drive Motor & Geartrain	As in Table 5.2
Drive Wheel	As in Table 5.1
Wheelbase	0.477 m
Cart Mass	20.64 kg
Cart Inertia (kg·m ²)	$I_{xx}:0.929, I_{xy}:-0.256, I_{xz}:0.001, I_{yy}:1.24, I_{yz}:0.007, I_{zz}:1.959$, relative to CM, where x is forward, z is up
Cart CM	0.25 m above tire centre, 0.215 m behind tire centre

5.4.2 Results

Slowly increasing current (and thus torque) to achieve a near static condition—increasing torque in small increments and waiting for motor rotation to settle—causes the platform to pass over the step within range of the calculated static value using the simple model in 5.2.1. However, increasing the current from 0.73 Nm to the test value in one step requires a smaller value to pass over the step, behaviour that is not explained by the static model. It is hypothesized that the dynamics and the elasticity of the tire need to be included to accurately represent this situation. A model that does this is presented below in section 5.5, and its simulated results in section 5.6.2 agree with the step-increase torque experiment, suggesting the hypothesis is correct. The results of the simple static

model and the advanced model are compared to the experimental results in Table 5.7; the simple model theoretical static torque value is calculated from equation (5.1), where uncertainty is propagated from the measurement uncertainty in the physical variables (r , h , m , c_x , c_y , b).

5.5 Advanced Theory

It has been found that modifying the model above in the following way better describes the non-linear dynamics of small-step passing: the rigid ‘crank’ (FC) is replaced with an ideal spring-damper element with spring constant k_c , damping constant k_d and displacement c (Figure 5.12). Also, it is essential to include a ground support force at the base of the tire. This is realized by a vertical spring-damper with spring constant k_v , damping constant k_b and displacement d which only acts when in contact with the ground.

Two different spring constants are used to reflect the fact that the tire behaves differently when compressed on a level surface versus compression on a corner. Tire spring forces become non-linear for large deformations such as at corners, but this simplification has proven effective. The model will lose validity towards the top of the step, where the compression point reverts from a corner to a flat surface and the tire’s standard spring constant for level surfaces should begin to apply again. However, this region does not play a role in determining peak torque requirements, since, as is evident from (5.1), torque required decreases towards zero as cosine θ approaches 90° .

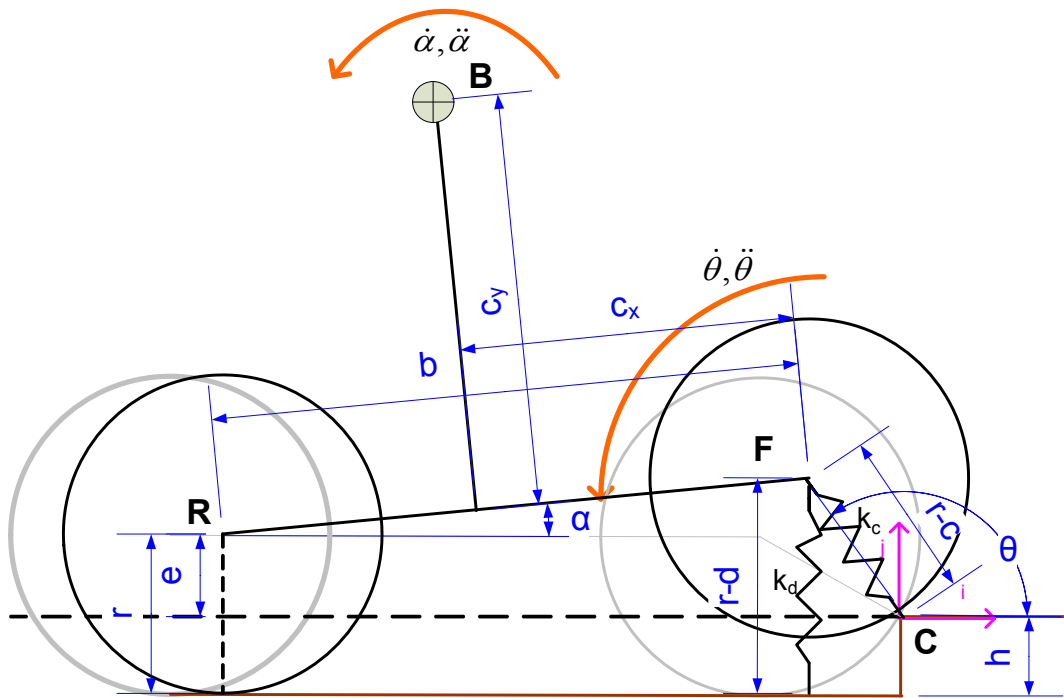


Figure 5.12: Improved system model with spring-damper wheel.

With the tire in contact with the ground, the kinetic energy of the system, T , can be expressed as

$$T = \frac{1}{2} m_b (\dot{v}_b i^2 + \dot{v}_b j^2) + \frac{1}{2} I_{cm} \dot{\alpha}^2 \quad (5.8)$$

where the velocity of B is

$$\begin{aligned} v_b \hat{i} &= c_x \dot{\alpha} \sin \alpha - c_y \dot{\alpha} \cos \alpha - \dot{c} \cos \theta - R \dot{\theta} \sin \theta \\ v_b \hat{j} &= -c_x \dot{\alpha} \cos \alpha - c_y \dot{\alpha} \sin \alpha - \dot{c} \sin \theta + R \dot{\theta} \cos \theta \end{aligned} \quad (5.9)$$

where R is the effective radius,

$$R = r - c \quad (5.10)$$

and the potential energy, U , can be expressed as

$$U = \frac{1}{2} k_c c^2 + \frac{1}{2} k_d d^2 + m_b g (R \sin \theta - c_x \sin \alpha + c_y \cos \alpha) \quad (5.11)$$

where time derivatives are expressed in dot notation.

To express the motion of the system using Lagrange's equations, four generalized coordinates, α , θ , c , d are chosen and are related by the constraint equations

$$C_1 = \lambda_1 (b \sin \alpha - R \sin \theta + e) \quad (5.12)$$

$$C_2 = \lambda_2 (e - d - R \sin \theta) \quad (5.13)$$

that relate α to θ and d to c & θ respectively, where λ_1, λ_2 are Lagrange multipliers and where

$$e = r - h. \quad (5.14)$$

The Lagrangian L is

$$L = T - U - C_1 - C_2. \quad (5.15)$$

External forces are expressed in the generalized coordinates as

$$Q_\alpha = T_f \quad (5.16)$$

$$Q_\theta = -T_f \quad (5.17)$$

$$Q_c = k_d \dot{c} \quad (5.18)$$

$$Q_d = k_d \dot{d} \quad (5.19)$$

The four dynamic equations are thus found using

$$\frac{d}{dt} \left(\frac{\partial L}{\partial \dot{q}} \right) - \left(\frac{\partial L}{\partial q} \right) = Q_q \quad (5.20)$$

where q stands for the generalized coordinates α , θ , c , d :

$$d : k_v d - \lambda_2 = -k_v d \quad (5.21)$$

$$\begin{aligned} \theta : m_b & \left(\begin{aligned} & (c_x \dot{c} \dot{\alpha} - R c_x \ddot{\alpha}) \cos(\gamma) + 4 R \dot{c} \dot{\theta} + 2 R^2 \ddot{\theta} \\ & + R \dot{\alpha} (c_x \sin(\gamma) X + c_y \cos(\gamma) H) + (R c_y \ddot{\alpha} - c_y \dot{c} \dot{\alpha}) \sin(\gamma) \\ & - (c_x \dot{c} \dot{\alpha} + R c_y \dot{\alpha} \dot{\theta}) \cos(\gamma) + (c_y \dot{c} \dot{\alpha} - R c_x \dot{\alpha} \dot{\theta}) \sin(\gamma) \end{aligned} \right) \\ & + m_b g (R \cos \theta) - \lambda_1 R \cos \theta - \lambda_2 R \cos \theta = -T_f \end{aligned} \quad (5.22)$$

$$\alpha : m_b \left(\begin{array}{l} 2\ddot{\alpha}(c_y^2 + c_x^2) + (c_x\ddot{c} - \dot{c}c_y\dot{\theta} + Rc_y\ddot{\theta})\sin(\gamma) \\ + (c_x\dot{c} + Rc_y\dot{\theta})\cos(\gamma)H + (\dot{c}c_x\dot{\theta} + c_y\ddot{c} - Rc_x\ddot{\theta})\cos(\chi) \\ + (Rc_x\dot{\theta} - c_y\dot{c})\sin(\chi)X - (c_x\dot{c}\dot{\alpha} + Rc_y\dot{\alpha}\dot{\theta})\cos(\gamma) \\ + (c_y\dot{c}\dot{\alpha} - Rc_x\dot{\alpha}\dot{\theta})\sin(\chi) \end{array} \right) + I_{cm}\ddot{\alpha} + m_b g(-c_x \cos \alpha - c_y \sin \alpha) + \lambda_1 b \cos \alpha = T \quad (5.23)$$

$$c : m_b \left(\begin{array}{l} (c_x\ddot{\alpha} + c_y\dot{\alpha}\dot{\theta})\sin(\gamma) + c_x\dot{\alpha}\cos(\gamma)H + 2\ddot{c} \\ + (c_y\ddot{\alpha} - c_x\dot{\alpha}\dot{\theta})\cos(\chi) - c_y\dot{\alpha}\sin(\chi)X - 2R\dot{\theta}^2 \end{array} \right) + k_c c - m_b g \sin \theta + \lambda_1 \sin \theta + \lambda_2 \sin \theta = -k_d \quad (5.24)$$

and the following substitutions are made to conserve space:

$$\chi = \theta + \alpha \quad (5.25)$$

$$\gamma = \theta - \alpha \quad (5.26)$$

$$X = \dot{\theta} + \dot{\alpha} \quad (5.27)$$

$$H = \dot{\theta} - \dot{\alpha} \quad (5.28)$$

d can be eliminated by substituting the constraint relationship and its derivative,

$$d = -R \sin \theta + e \quad (5.29)$$

$$\dot{d} = \dot{c} \sin \theta - R \dot{\theta} \cos \theta \quad (5.30)$$

into (5.25), which we can then be solved for λ_2 :

$$\lambda_2 = (\dot{c} - R)k_v \sin \theta + ek_v - Rk_v \dot{\theta} \cos \theta. \quad (5.31)$$

Eliminating the Lagrange multipliers at this point is preferable to including them in the numerical integration [91]. Solving for λ_1 using (5.23) and substituting λ_1, λ_2 into (5.22) and (5.24) gives (5.32) and (5.33) that are time-dependent functions of $\ddot{\alpha}, \dot{\alpha}, \alpha, \ddot{\theta}, \dot{\theta}, \theta, \ddot{c}, \dot{c}, c$ only:

$$\begin{aligned} & m_b \left(\begin{array}{l} (c_x\dot{c}\dot{\alpha} - Rc_x\ddot{\alpha})\cos(\chi) + (Rc_y\ddot{\alpha} - c_y\dot{c}\dot{\alpha})\sin(\gamma) \\ + R\dot{\alpha}(c_x \sin(\chi)X + c_y \cos(\gamma)H) \\ + 4R\dot{c}\dot{\theta} + 2R^2\ddot{\theta} - (c_x\dot{c}\dot{\alpha} + Rc_y\dot{\alpha}\dot{\theta})\cos(\gamma) \\ + (c_y\dot{c}\dot{\alpha} - Rc_x\dot{\alpha}\dot{\theta})\sin(\chi) \end{array} \right) b \cos \alpha + \\ & m_b \left(\begin{array}{l} 2\ddot{\alpha}(c_y^2 + c_x^2) + (c_x\ddot{c} - \dot{c}c_y\dot{\theta} + Rc_y\ddot{\theta})\sin(\gamma) \\ + (c_x\dot{c} + Rc_y\dot{\theta})\cos(\gamma)H + (c_y\dot{c}\dot{\alpha} - Rc_x\dot{\alpha}\dot{\theta})\sin(\chi) \\ + (\dot{c}c_x\dot{\theta} + c_y\ddot{c} - Rc_x\ddot{\theta})\cos(\chi) \\ + (Rc_x\dot{\theta} - c_y\dot{c})\sin(\chi)X - (c_x\dot{c}\dot{\alpha} + Rc_y\dot{\alpha}\dot{\theta})\cos(\gamma) \end{array} \right) R \cos \theta \\ & + m_b g R \cos \theta (b \cos \alpha - c_x \cos \alpha - c_y \sin \alpha) \\ & + I_{cm}\ddot{\alpha}R \cos \theta + T_f (b \cos \alpha - R \cos \theta) \\ & - ((\dot{c} - R)k_v \sin \theta + ek_v - Rk_v \dot{\theta} \cos \theta) R b \cos \theta \cos \alpha = 0 \quad (5.32) \end{aligned}$$

$$\begin{aligned}
& m_b \left(\begin{array}{l} (c_x \ddot{\alpha} + c_y \dot{\alpha} \dot{\theta}) \sin(\gamma) + k_c c + k_d + (\dot{c} - R) k_v b \sin^2 \theta \\ + e k_v b \sin \theta + (c_y \ddot{\alpha} - c_x \dot{\alpha} \dot{\theta}) \cos(\gamma) - c_y \dot{\alpha} \sin(\gamma) \\ + 2\dot{c} - 2R\dot{\theta}^2 - R k_v b \dot{\theta} \cos \theta \sin \theta + c_x \dot{\alpha} \cos(\gamma) \end{array} \right) b \cos \alpha \\
& - m_b \left(\begin{array}{l} (2\ddot{\alpha}(c_y^2 + c_x^2) + (c_x \ddot{c} - \dot{c} c_y \dot{\theta} + R c_y \ddot{\theta}) \sin(\gamma) \\ + (c_x \dot{c} + R c_y \dot{\theta}) \cos(\gamma) \text{H} + (c_y \dot{c} \dot{\alpha} - R c_x \dot{\alpha} \dot{\theta}) \sin(\gamma) \\ + (\dot{c} c_x \dot{\theta} + c_y \ddot{c} - R c_x \ddot{\theta}) \cos(\gamma) \\ + (R c_x \dot{\theta} - c_y \dot{c}) \sin(\gamma) \text{X} - (c_x \dot{c} \dot{\alpha} + R c_y \dot{\alpha} \dot{\theta}) \cos \gamma \\ g(c_x \cos \alpha + c_y \sin \alpha - b \cos \alpha) \end{array} \right) \sin \theta \\
& - I_{cm} \ddot{\alpha} \sin \theta + T_f \sin \theta = 0
\end{aligned} \tag{5.33}$$

Similarly, α can be eliminated using

$$\sin \alpha = (R \sin \theta + e) / b \tag{5.34}$$

$$\cos \alpha = \sqrt{b^2 - (R \sin \theta + e)^2} / b \tag{5.35}$$

$$\dot{\alpha} = (-\dot{c} \sin \theta + R \dot{\theta} \cos \theta) / (b \cos \alpha) \tag{5.36}$$

$$\ddot{\alpha} = \frac{\left(\begin{array}{l} r \ddot{\theta} \cos \theta - r \dot{\theta}^2 \sin \theta - \dot{c} \sin \theta + \dot{c}^2 \cos \theta \\ - \dot{c} \dot{\theta} \cos \theta - c \ddot{\theta} \cos \theta + c \dot{\theta}^2 \sin \theta + \dot{\alpha}^2 b \sin \alpha \end{array} \right)}{b \cos \alpha} \tag{5.37}$$

We are left with two equations that can be rearranged into the form

$$\ddot{\theta} = f(\dot{\theta}, \theta, \dot{c}, c) \tag{5.38}$$

$$\ddot{c} = f(\dot{\theta}, \theta, \dot{c}, c) \tag{5.39}$$

which can then be integrated numerically. Integration must be stopped when $d > 0$ and the final coordinates used as initial conditions for the system equations without ground contact that are described below.

To model the dynamics when the tire is not touching the ground, the potential energy and damping force of the ground contact spring-damper is set to zero, eliminating the external work Q_d and making the new potential energy term

$$U_{\text{offground}} = \frac{1}{2} k_c c^2 + m_b g (R \sin \theta - c_x \sin \alpha + c_y \cos \alpha) \tag{5.40}$$

Only three generalized coordinates α, θ, c and one constraint equation, (5.16), are now needed, which are solved in the same manner as before. Numerical integration is performed until $d < 0$, at which point the first set of dynamic equations must be used, and the process repeated *ad infinitum*.

In order to easily compare different mobile platforms, the equations and results can be non-dimensionalized with the following 18 ND groups:

$$\frac{c_x}{b}, \frac{c_y}{b}, \frac{h}{r}, \frac{b}{r}, \frac{T}{mgb}, k_c \frac{b}{mg}, k_v \frac{b}{mg}, k_d \frac{b^{3/2}}{m\sqrt{g}}, \frac{I_{CM}}{mb^2},$$

$$\theta, \dot{\theta}, \sqrt{\frac{b}{g}}, \ddot{\theta} \frac{b}{g}, \frac{c}{r}, \frac{\dot{c}}{\sqrt{gb}}, \frac{\ddot{c}}{g}, \frac{d}{r}, \frac{\dot{d}}{\sqrt{gb}}, \frac{\ddot{d}}{g}$$

To determine what friction factor, μ_c , is necessary at the corner to prevent slip, one must determine the radial normal force,

$$F_N = k_c c + k_d \dot{c} \quad (5.41)$$

and the tangential force,

$$F_T = T_f / R \quad (5.42)$$

The friction factor to prevent slippage is

$$\mu_c = F_T / F_N \quad (5.43)$$

Note that there is an additional friction force at the ground contact point so long as $d < 0$, during which time the above equations do not apply.

Since μ_c fluctuates somewhat due to the changes in tire compression c which change the normal force F_N , for a corner with a particular friction factor there will be a range of parameters creating a border-line case where some slippage occurs. The tire will slip when the normal force is low, because the friction factor necessary to prevent slippage, μ_c , is higher than the actual friction factor at the corner. When the normal force increases, that is when the tire is more compressed, the necessary friction factor decreases, and the tire has traction. In the border-line case, periods of traction while the tire is more compressed and the normal force is higher are sufficient such that the wheel will still surmount the step. Determining for what parameters this case occurs would require extending the model to include slip.

Other possible extensions include consideration of non-powered wheels, where the external force comes from a different point, and of rear wheels, which are loaded more heavily because platform tilt moves the CM towards the back, thus causing them to need more torque. Also, approaching the step with a velocity or acceleration lowers the torque requirements but can lead to undesired oscillations and lift-off after impact.

5.6 Simulation

5.6.1 Setup

The vertical spring constant was determined experimentally, as no published data was available for the tire. The radial spring constant was found by calibrating the model to fit the experimental data. The model will be poor for step heights much greater or lower than those used during calibration. For example, for no step, the radial spring constant should be the same as the tire's normal spring constant for flat ground. Thus, calibration should be performed to include the expected maximum step height to ensure the model is accurate when finding the peak torque required for this height. The spring constants that correspond to the experimental set-up are 62,000 N/m at the corner and 130,000 N/m

for the vertical spring. A damping value for both dampers of 200 N·m/s was chosen; results were found to have low sensitivity to changes in damping within a range (50–500) typical for tires as detailed in Table 6.2.

The simulation was created using the Dymola/Modelica (see Appendix B), allowing for animation and easy programming of loss-of-contact conditions. It was run using the ‘Dassl’ integrator set to a tolerance of 1e-5. Results were compared to direct numerical integration of the dynamic equations from section 5.5 in Maple using the Runge-Kutta Fehlberg method [92] and found to be identical. Parameters for wheelbase, mass, inertia, centre of mass, wheel radius and step height were chosen to match the experimental setup (Table 5.6). Note that the 3D functionality of the library was made use of to include the cart’s off-diagonal inertia terms in order to improve agreement with experiment.

Simulations were also performed using different model configurations at different levels of complexity to confirm model behaviour. The simplest model used only a rigid link between the tire centre and the corner; results agreed with theory (see 5.2.1) for this case. Next this link was replaced by a spring-damper element. It was found that starting off with a ground support force is essential, otherwise the cart will drop below ground level while the radial spring is undergoing compression since the radial spring has not built up enough vertical force to hold the cart up. This drop below ground level is sufficient to prevent the cart from climbing the step in some situations as weight also shifts forward and the sill gets effectively higher. Thus the spring damper element connecting the tire center vertically with the ground is essential. Including gear-train elasticity and backlash, and adding motor dynamics all had negligible impact. Adding a vertical spring-damper at the rear tire shows its elasticity to have no significant influence.

5.6.2 Results & Analysis

Because the elastic tire compresses, the effective wheel radius is reduced. The small reduction due to compression, on the order of 3% with the parameters used in the simulation, causes a 1.7% reduction in torque in the static analysis. However, the reduction in radius is not the only benefit of an elastic tire.

Figure 5.13 to Figure 5.15 show results for the 16 mm step. It is apparent that the elastic tire first absorbs energy in the radial spring element while the cart is still partially supported by the ground. The spring compresses, spring potential energy increases, and it only slowly starts contributing to the total vertical support force. The vertical ground contact spring expands, releasing stored energy as its component of the vertical support force diminishes until it vanishes completely when ground contact is lost at 3.07 seconds. The radial spring then continues damped oscillations, contributing a vertical force component that puts the vertical force on average at the same level as the rigid system—this despite a lower torque and thus a lower contribution from the torque reaction to the vertical force.

Since the system is nearly conservative with small losses due to damping, the elasticity only acts to redistribute the energy over time, but this is sufficient to reduce the peak torque. In effect, energy is initially stored in the spring while the tire is still partially supported by the ground – this energy is later released, reducing the peak torque required.

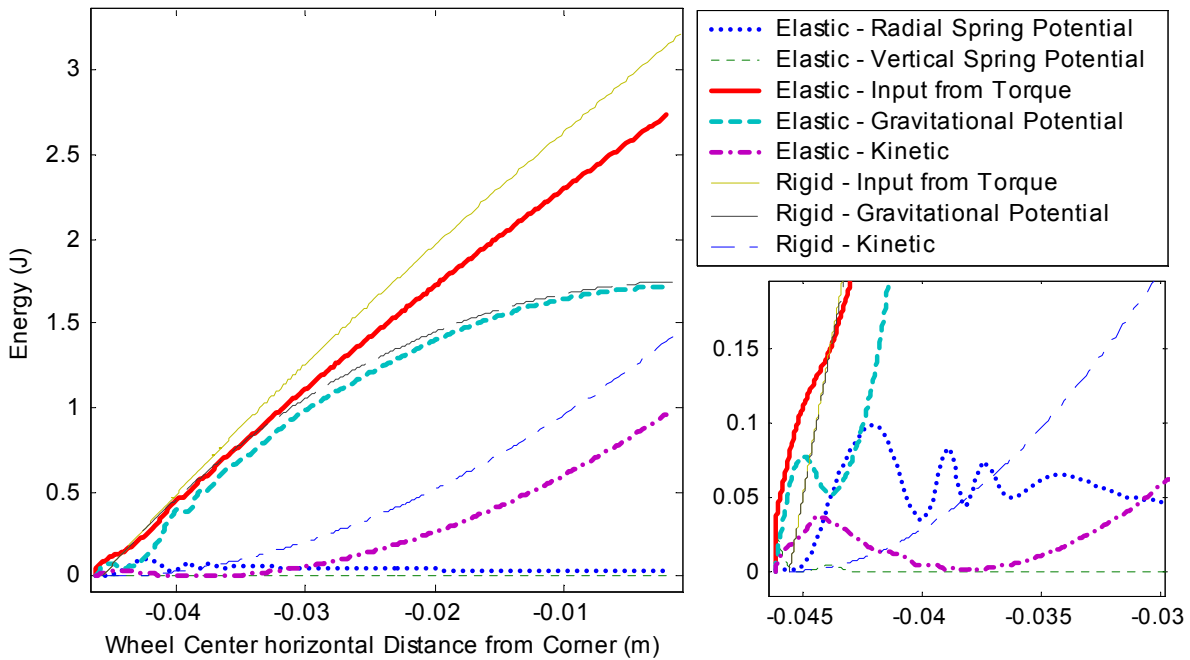


Figure 5.13: Energy for 16 mm step height, comparing rigid and elastic tire. The sub-figure on the right is an enlargement of the start of the step climb using the same units as the main figure.

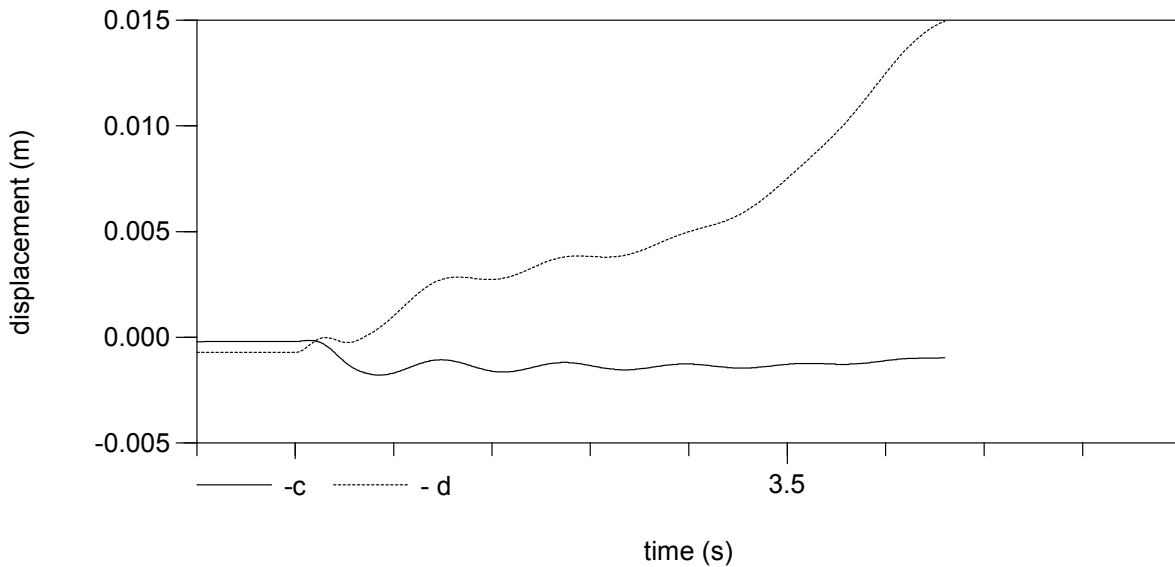


Figure 5.14: Radial (c) and vertical (d) spring compression, 16 mm step height, torque step from 0.73 to 3.91 Nm at 3 s, tire lifts off ground at 3.07 s.

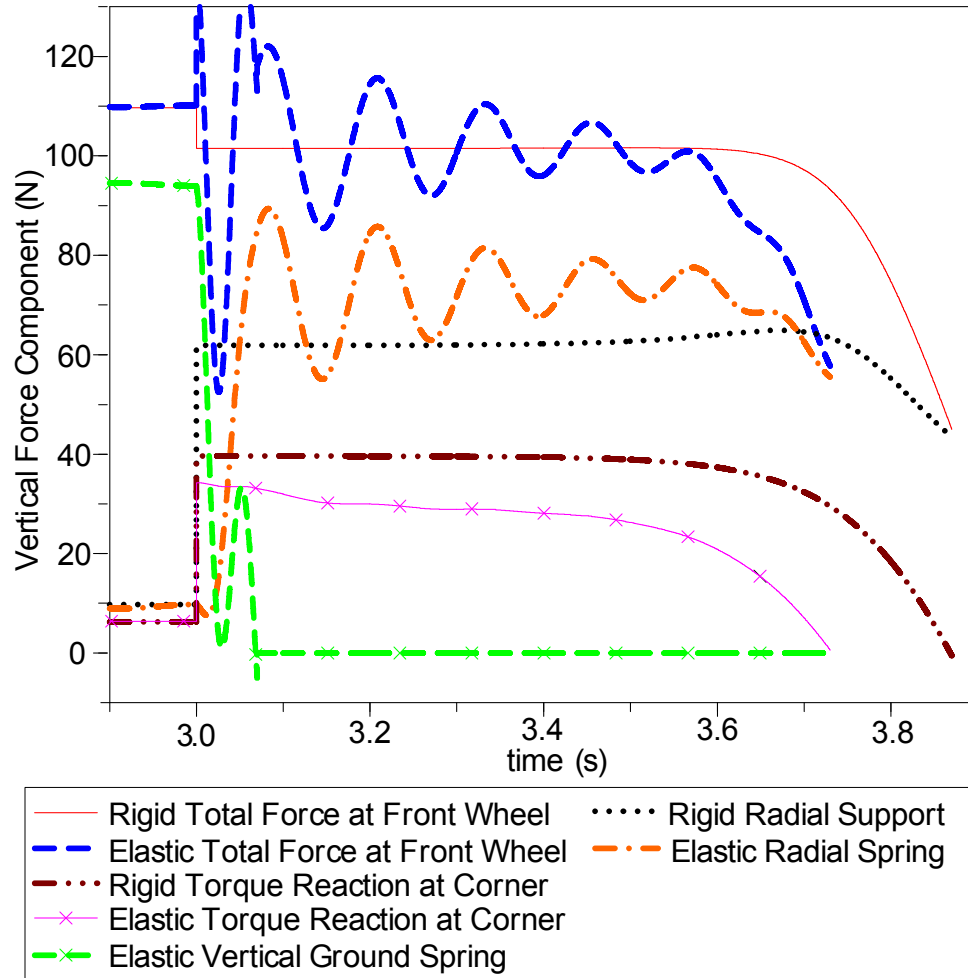


Figure 5.15: Forces at front wheel resolved into vertical components for both spring-damper and rigid model, 16 mm step height. Torque step from 0.73 to 3.91 Nm at 3 s for elastic wheel, 0.73 to 4.63 Nm for rigid wheel. Elastic wheel reaches top of step at 3.66 s, rigid wheel at 3.86 s.

Table 5.7: Experimental and simulation results.

Step Height (mm)	Theoretical Static Torque ^a (Nm)	Torque Input Type	Experimental Torque (Nm)	% difference to static torque	Simulation Torque (Nm)	% difference to experimental torque
8.42	3.53±0.29	step	2.67±0.05	-24	2.67	0.0
		ramp	3.23±0.13		3.19	
16.00	4.63±0.43	step	3.89±0.06	-16	3.91	0.3
		ramp	5.07±0.17		4.44	-12

^abased on the wheel radius as measured on a flat surface

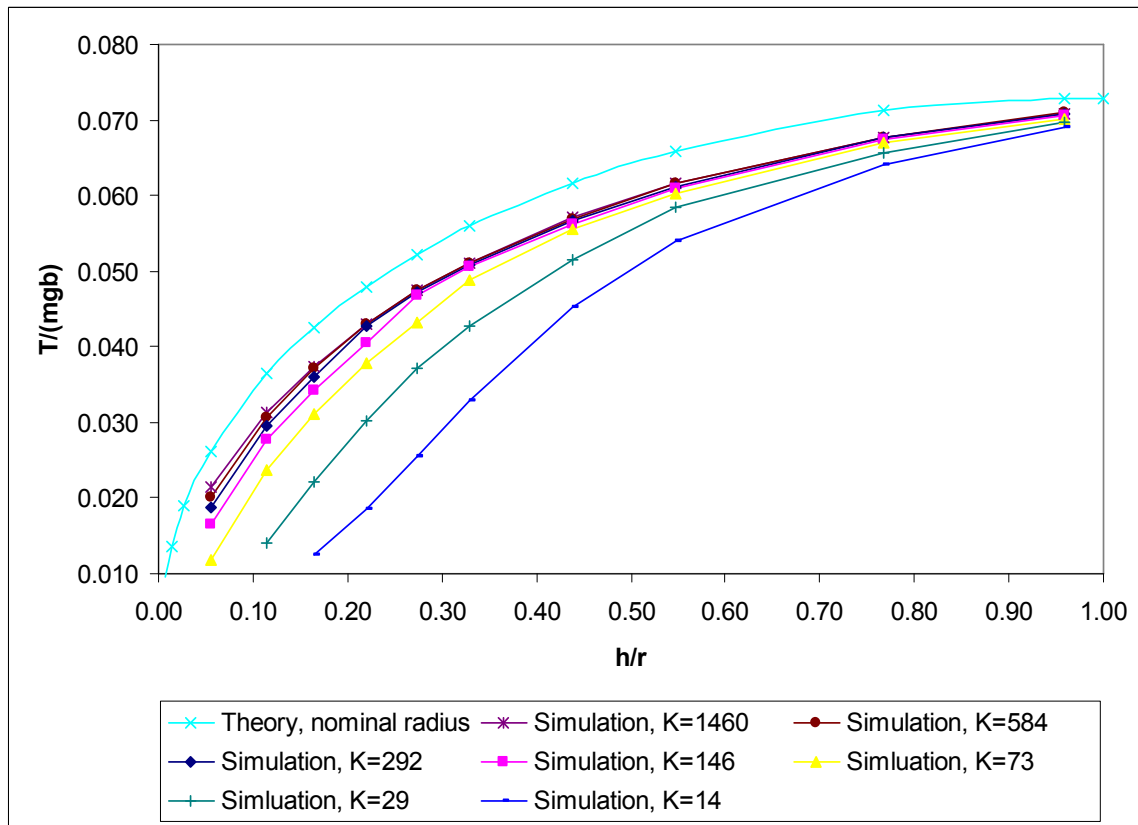


Figure 5.16: ND static torque compared to simulation results showing effect of different ND spring constants, where $K = k_c b/mg$ and all other ND groups are held at experimental conditions. $K=146$ is experimental setup.

5.6.2.1 Parametric Analysis of Dynamic Response

From Figure 5.16 a number of observations can be made. The reduction in ND peak torque with the elastic tire, both in relative and absolute terms, is largest at small step-height-to-radius ratios and with soft spring constants. It gets relatively small quickly as the step height to radius ratio increases, and also decreases in absolute terms, though this decrease is at a fairly low rate, particularly for hard spring constants. At high h/r ratios, the curves converge, approaching but not reaching the static curve.

In general, a softer spring increases the time period over which energy can be stored and released, reducing the peak torque required. Its ability to do so appears dependent on the h/r ratio (likely because of the initial contact angle, θ_{init}). Of course, a softer tire may have unwanted repercussions in the vehicle's overall behaviour, where high stiffness is often desirable for instance to improve positioning accuracy of a mounted sensor or end-effector. Thus, the benefits of a large soft tire for step passing must be weighed against potential negatives for each application.

A larger wheel can climb higher steps because its initial contact angle θ is higher, increasing the radial normal force and thus decreasing the necessary friction factor. However, it requires more torque, takes up more space, weighs more, and tends to have a higher rolling resistance.

5.7 Applications to Platform Design

The platform design is all-wheel drive with a varying wheelbase. To investigate the torque that will be necessary for it to overcome steps in the indoor environment, the simulation is modified to reflect this design. A torque acting on the rear rotational joint is added as well as a force F proportional to the torque acting where the rear wheel would contact the ground to represent the horizontal ground reaction force due to friction,

$$F = \frac{T_R}{r} \quad (5.44)$$

This is necessary because otherwise the rear torque causes no forward force in the rear slider, which is modelled as a frictionless free slider. As with the front tire, a check needs to be performed to ensure there is sufficient normal force at the rear tire to support the horizontal ground reaction force due to the desired torque. This will also depend on the current friction factor between tire and ground.

The condition for static balance at the beginning of the step becomes

$$-T_F b + T_F r \cos \theta - T_R b \sin \theta + T_R \cos \theta = mg(b - c_x)r \cos \theta \quad (5.45)$$

If front and rear torque are both set equal to T and the CM is located halfway along the base, $c_x = b$, (5.49) becomes

$$T = \frac{m_{sys} g r \cos(\theta)}{2r \cos \theta - b \sin \theta - b} \quad (5.46)$$

This is less than front wheel drive alone by the factor

$$\frac{b \sin \theta + b - 2r \cos \theta}{b - r \cos \theta} \quad (5.47)$$

Thus the advantage of all wheel drive is highest for no step and decreases as the step height increases. The decrease becomes more pronounced for a larger wheelbase, as shown in Figure 5.17.

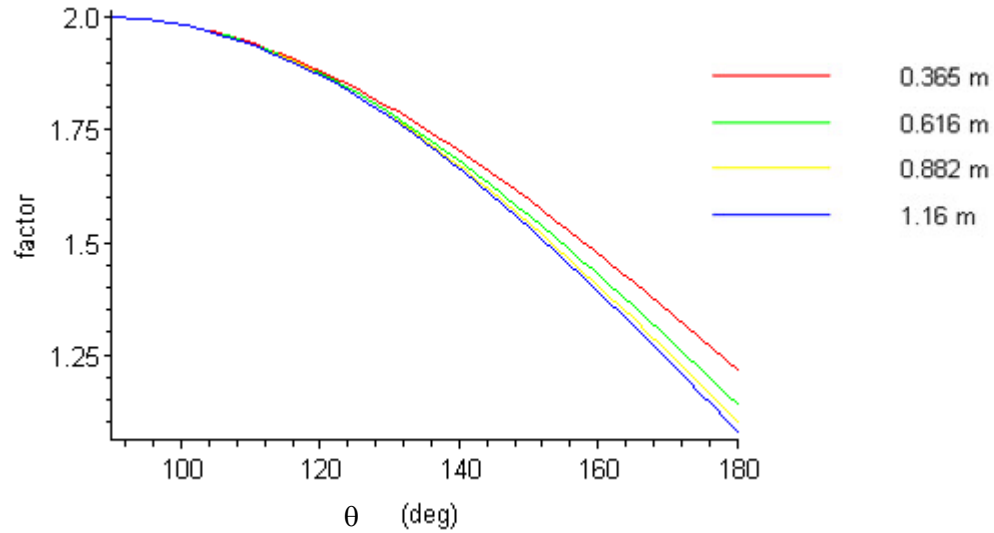


Figure 5.17: The factor by which front-wheel drive torque is larger than all-wheel drive torque is shown here for different wheelbase lengths, wheel radius = 0.1 m.

The cart body parameters are changed to reflect the base as designed, with the torso modelled as a cylinder representing the upright position with arms down and a 7.5 kg payload per arm. Details are given in Table 5.8. Since the platform has four wheels, they are lumped together into a front and rear set in order to match the 2D simulation.

Table 5.8: Cart parameters to represent upper-body and base as designed.

Segment	Geometry	Mass (kg)	Inertia
Base	cylinder, radius: 0.2 m, height: 0.55 m	65	uniform cylinder
Upper-body including payload mass	cylinder radius: 0.13 m height: 0.7 m	65	uniform cylinder
Wheels	radius: 0.1 m	mass-less	

In addition, the worst-case scenario is expected to be with the front wheel already up the step and the rear wheel at the edge, since the platform will be tilting backwards and thus loading the rear wheel more than the front. The shorter the wheelbase, the larger the tilt angle; the tilt angle α reaches a maximum with the front wheel all the way up ($\theta = 90^\circ$) and the rear wheel still down, reducing (5.34) to

$$\sin \alpha = \frac{h}{b}. \quad (5.48)$$

The platform tilt angle for a step height of 3 cm and varying wheelbase approximately from minimum wheelbase to maximum effective leg extension spread is shown in Figure 5.18.

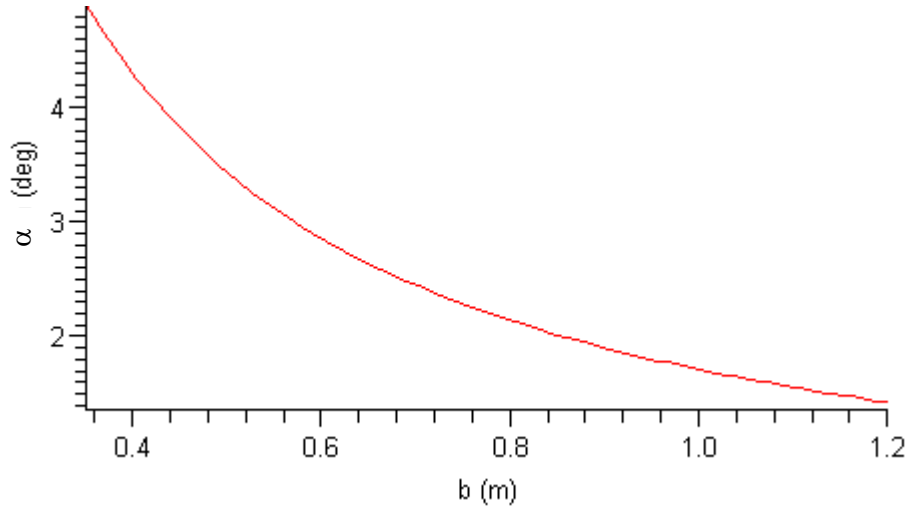


Figure 5.18: Maximum platform tilt angle α for a step height of 3 cm.

The static balance with equal front and rear torque T for this situation where the front wheel set has already surmounted the step and the rear wheel set is resting on the step corner (Figure 5.19) is

$$T = \frac{-m_{sys} gr \cos \theta (c_x \cos \alpha + c_y \sin \alpha)}{2r \cos \theta + b \cos \alpha (1 + \sin \theta) - h \cos \theta} \quad (5.49)$$

The height of the centre of mass c_y now becomes a factor due to the platform tilt α . In terms of the simulation setup, the front and rear tire switch, with the front tire becoming rigid and the rear tire being modelled with two springs.

The position of the upper body as well as the payload mass and its position will further affect the step-passing ability, however, rather than expect the system to be able to climb steps in all configurations, it will be assumed that the payload can be held close to the centre of the base during step passing. Thus, the upper-body configuration is approximated by a cylinder as described in Table 5.8 that does not change position. This will prevent the torque requirements from becoming excessively large in order to meet a situation such as climbing a step with a load extended backwards that is unlikely and typically preventable.

For simplicity, the assumption of edge contact with two wheels will be maintained. If the platform surmounts the edge with only one trailing wheel, the weight shift onto this wheel will not be as severe, because the other wheels will have already raised the platform, reducing the platform tilt angle.

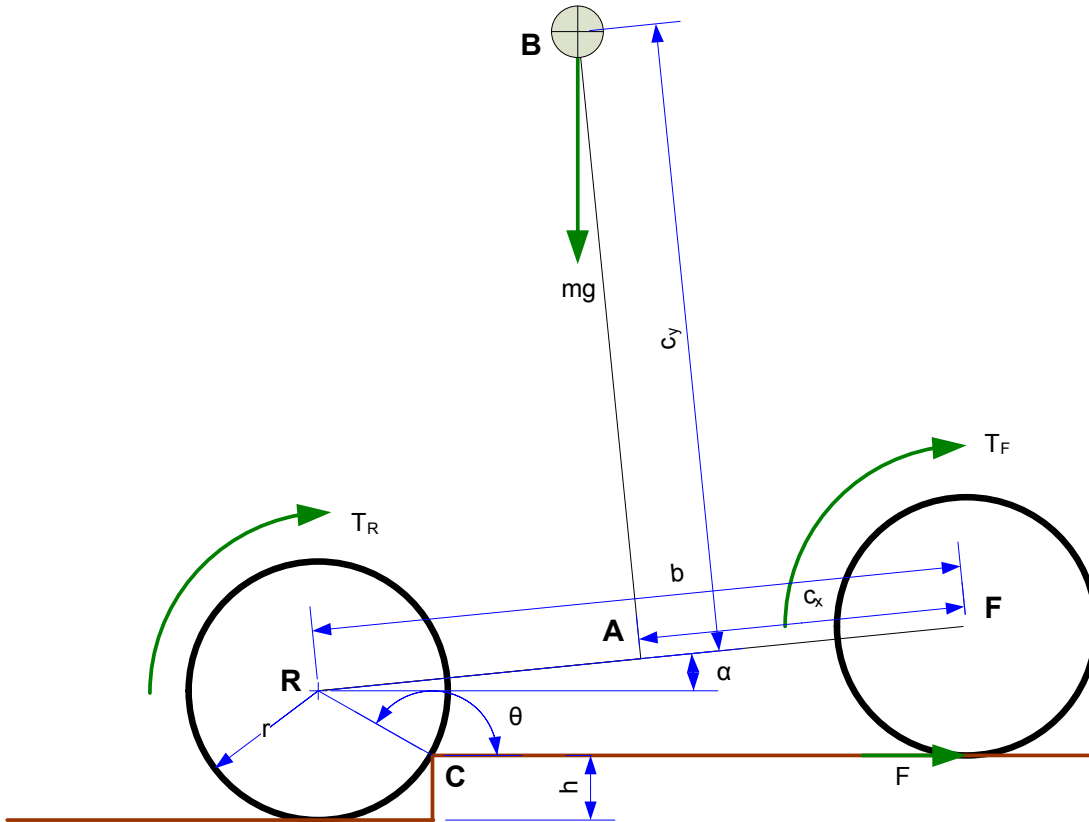


Figure 5.19: Rear wheel set at the step corner; the tilt α causes higher loading at the rear.

5.7.1 Simulation Setup

The dynamic model in Dymola was modified to reflect the system as designed (Table 5.8). Different versions were created in order to investigate all-wheel drive and the situation where the rear wheel is at the step as described above. Torque is increased using a step function as in 5.6.1 with preload of 0.73 Nm and the initial position adjusted so that the platform is static with the wheel at the step. It is assumed the tire will be similar to the one used in the experiment, as it has similar material and construction. The larger radius should not be a factor in the tire elasticity, so the same spring constant values that were found to match experimental results (62,000 N/m at the corner, 130,000 vertical) were used in these simulations.

5.7.2 Simulation Results

The results for the different configurations are shown in Figure 5.20 compared to the static balance conditions: (5.46), all wheel drive with the front wheel at the step, and (5.49), all wheel drive with the rear wheel at the step. The torque values are for a set of two wheels. The non-dimensionalized form is shown in Figure 5.21, which adds static balance condition (5.1), front wheel drive with the front wheel at the step. The condition with the rear wheel at the step is investigated at two wheelbases, 0.616 m and 1.16 m[A1]. The shorter wheelbase requires more torque than the longer wheelbase, with the difference increasing with increasing step-height. This mirrors the trend in the static theory. The

reduction in required torque with a step torque increase due to the tire elasticity is more significant with the rear wheels driven than with only front wheel drive. It is also more significant for the rear wheel than the front wheel at the step. For small steps, the simulation results for the rear wheel at the step lie very close to those for the front wheel at the step despite the static theory suggesting the rear wheel at the step should require significantly more torque.

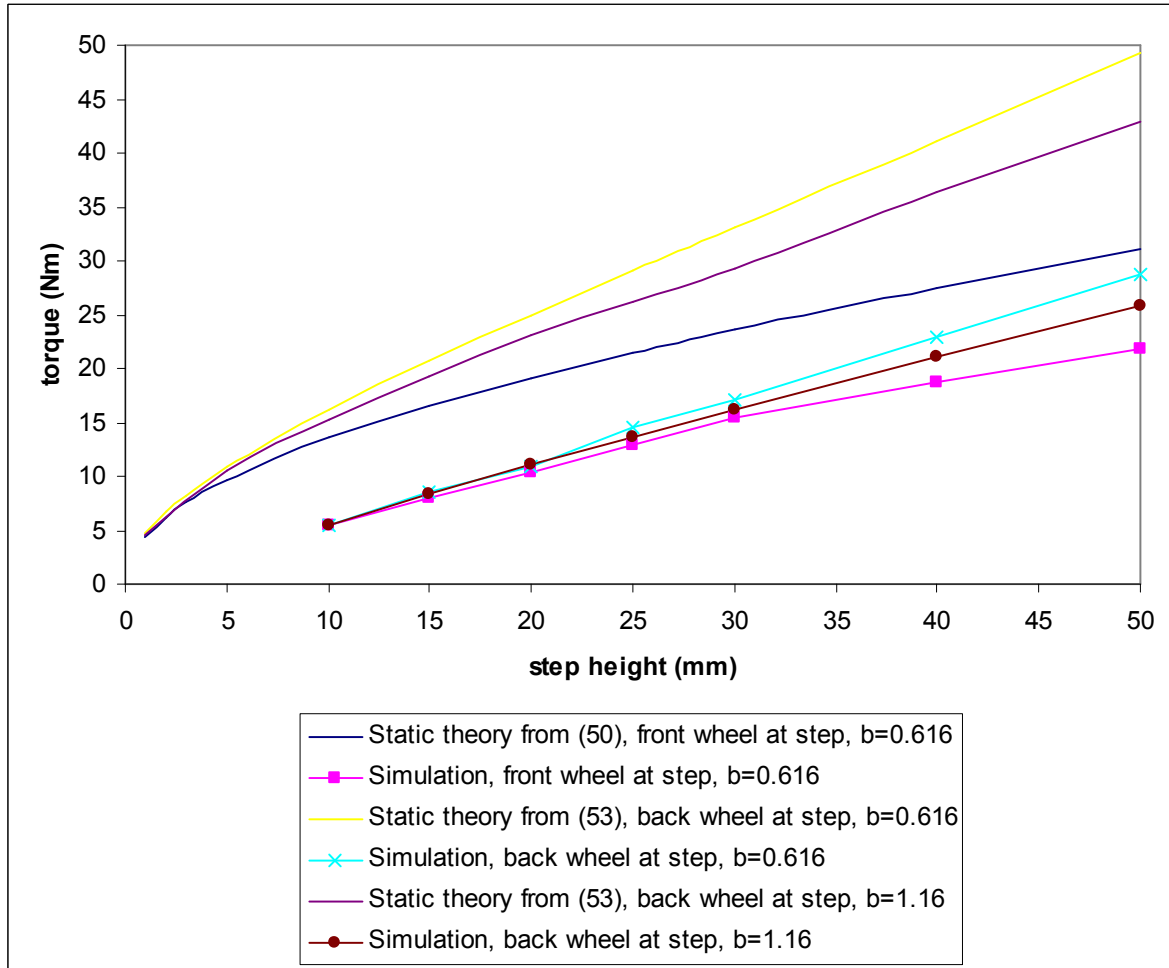


Figure 5.20: Torque for surmounting step with all wheels driven, $r = 0.1$ m, $k_c = 62000$.

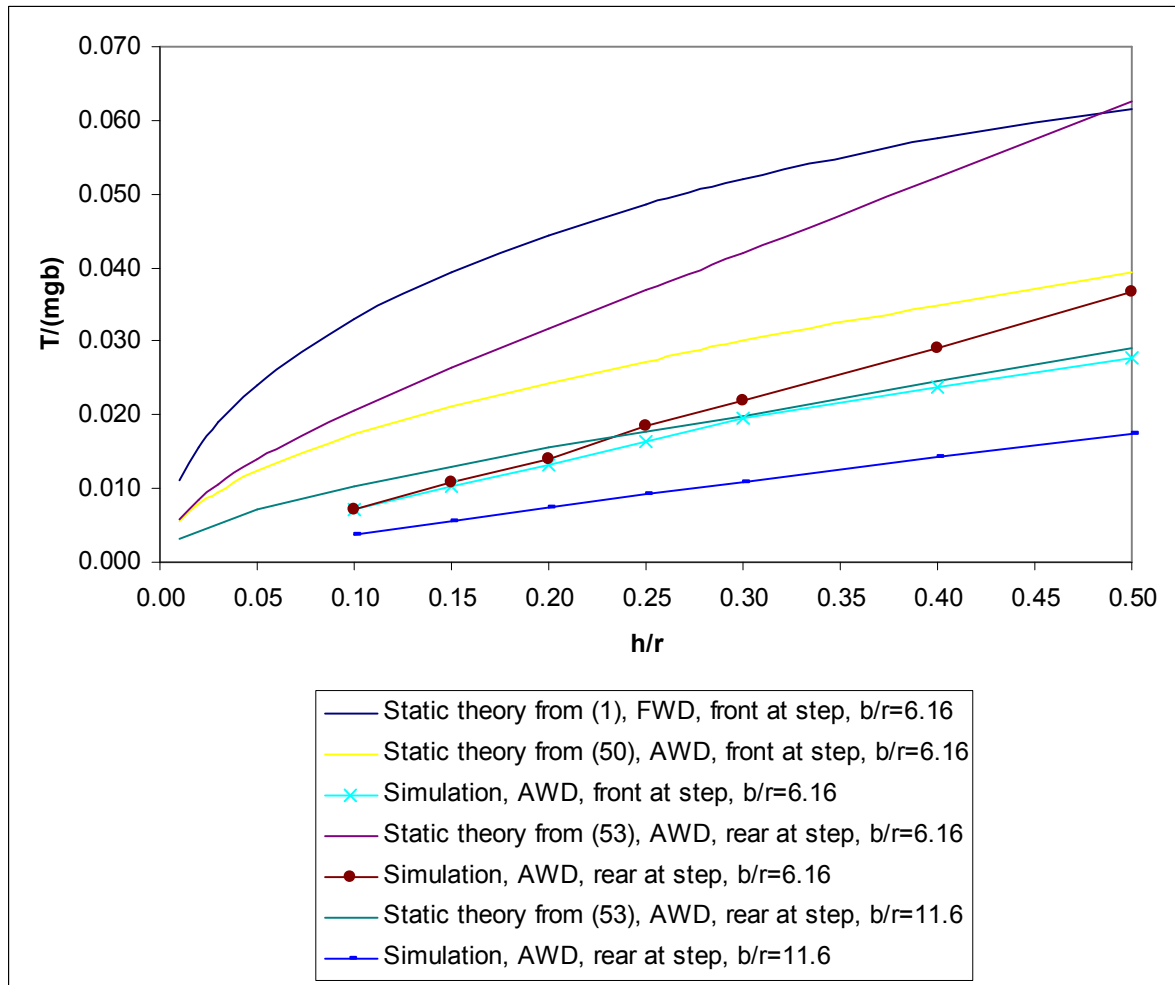


Figure 5.21: ND static torque compared to simulation results for different situations. K for $b/r = 6.16$ is 30, for $b/r = 11.6$ is 56.

The normal force for the tire not at the edge was recorded to see what minimum friction factor would be necessary to support the desired torque; selected values are listed in Table 5.9. While the tire at the corner also relies on friction, the effective friction factor at the corner was observed to be higher due to tire indentation, so it is assumed that the other tire is the limiting element. At a step height of 3 cm, the target goal to be surpassed, the highest friction factor required is 0.51 with the short wheelbase; this is available on many surfaces. Climbing a 5 cm step with this wheelbase would require a friction factor of 1.94, which is not normally possible.

The highest torques are observed for the rear wheel at the step with a short wheelbase, however, these cannot be achieved in practice due to the lack of normal force at the front tire and resultant inability to generate enough frictional force for the torque. A longer wheelbase reduces the tilt angle, which reduces the shift in normal force, allowing for better traction and thus the surpassing of higher steps. These higher steps have higher torque requirements than the largest of those achievable with the short wheelbase as is apparent in Table 5.9.

Table 5.9: Friction factor required to support torque for climbing selected step heights.

Wheelbase, b (m)	Scenario	Step Height, h (m)	Torque, T (Nm)	Necessary Friction Factor
0.616	front wheel at step	0.25	12.82	
		0.30	15.40	0.35
		0.40	18.68	0.33
		0.50	21.74	0.37
	back wheel at step	0.25	14.56	0.37
		0.30	17.13	0.51
		0.40	22.86	0.94
		0.50	28.76	1.94
1.16	back wheel at step	0.25	13.70	
		0.30	16.18	0.35
		0.40	21.02	0.49
		0.50	25.88	0.66

5.8 Conclusions

The dynamic model of step-climbing presented in section 5.5 is much better at predicting the necessary torque to overcome the step than a static rigid model. It accurately demonstrates the reduced torque required due to energy storage in an elastic tire, as is evident from the agreement between experimental and model results. Using the ND parameters, different mobile robot designs can be evaluated and compared for their step-climbing ability. Since climbing small steps is a significant torque requirement, especially when approached at slow speed, and potentially the highest torque requirement in some mobile robotics applications, modeling this situation more accurately will lead to lower actuator requirements with associated benefits for mass and power consumption. It will also allow for better selection of tire characteristics—choosing between suspension and step-passing qualities.

For this system, the tire has already been selected. However, the model will help determine appropriate drive actuator requirements. Given the goal of surpassing 3 cm high steps, the peak step-climbing torque requirement is 17.1 Nm or 8.6 Nm per wheel.

Chapter 6

Suspension

6.1 Problem Definition and Goals

Because the mobile platform has more than three points of support—it is hyperstatic—some form of suspension is needed in order to ensure that all four wheels have ground contact at all times. While a suspension cannot eliminate the effects of gravity and acceleration that reduce the normal force on a wheel, it can keep the wheel on the ground to take advantage of any traction that is available. In a car, the purpose of the suspension is to isolate the body from ground disturbances while ensuring good wheel ground contact for improved road handling. In the case of a mobile manipulator, there are additional disturbance sources that arise due to interaction of the manipulator with the environment as well as the inertial forces created by upper-body movement. In addition, the system mass changes due to varying payloads, which, together with the upper-body position, changes the mass distribution. Thus, the goal of the platform suspension is to:

- isolate the disturbances from
 - the ground
 - manipulator/environment interaction
 - inertial forces
- provide good traction

These goals should be met over the entire range of operating variables. Inherent suspension factors are the platform's mass and its natural frequency response, as well as its centre of mass, footprint and load. While mass and natural frequency are to a certain extent design variables, their range of adjustment is limited. Footprint (due to the variable footprint design) and load are operational variables whose range is determined in the design phase. The centre of mass is a function of design and operational variables. In addition to the limited inherent design variables, there are numerous suspension options which can be added that range in complexity and benefit.

6.2 Background

The simplest suspension is that of an elastic wheel, such as a rubber or pneumatic tire. More complex systems are often derived from automotive applications, on which much work has been done; see for instance [93]. Traditionally, such suspensions use a spring in parallel with a damper. This low cost, low complexity mechanism can be quite effective but must be tuned for specific conditions; other conditions will result in degraded performance. Because it is passive, no energy is required to power the suspension nor is it possible to add energy to the system.

One interesting method to improve upon simple passive spring-damper systems is by using a semi-active damper, which can change its damping rate and thus can be used to achieve improved suspension performance. This means that natural frequency resonance can be almost completely suppressed and kinetic energy removed more quickly than with a passive damper [94]. The most promising method to do so is using a magneto-rheological (MR) fluid, which changes its characteristics when exposed to a magnetic field—this approach is more effective than similar electro-rheological (ER) dampers, mainly because it uses less energy [95]. Since only the damper is modified, and its response depends solely on velocity, no long-term change to the suspension position is possible in this semi-active approach. A weight shift will result in the damper to sag to a lower level.

Another way to change the suspension behaviour is to change its geometry such that the spring or damper displacement changes in relation to the disturbance input path. By changing the geometry horizontally, the adjustment actuation does not need to carry the weight of the system. A variable geometry has the advantage that it changes the spring constant, which affects the critical damping value and allows the suspension height to be changed. The range of adjustment is limited by geometry and actuator constraints. Such systems tend to be fairly mechanically complex and have been used in only a limited number of applications [96].

Fully active suspension options allow an even greater deal of control by adding a force independent of suspension conditions to support or counteract suspension movement. This means the height of the platform can be controlled. The range of motion that can be influenced depends upon the bandwidth and power of the system. Often, the actuator is placed in series and/or in parallel with a spring so that they can work in concert to reduce actuator load and improve isolation of high frequency disturbances. When placed in parallel, the spring carries the majority of the load and the actuator acts to add or remove energy from the spring. A series placement is beneficial because most actuators cannot respond quickly enough for all disturbances.

Linking the suspension mechanism between two or more wheels can improve stability, such as the rocker-bogie design used on several planetary exploration rovers that passively averages the position of the chassis relative to the height of each wheel [97]. Another system with a rocker-bogie and omni-wheels has been developed by Yamashita et al. [98]. The shrimp rover uses a wheel mounted on a front fork which has a virtual centre of rotation below the wheel; this helps the wheel to passively surmount vertical obstacles up to 1.5 times the wheel diameter [8].

6.3 Review of Options

In general, suspension options make a trade off between complexity (in terms of control and mechanics) and improved performance. Furthermore, while more compliance is desirable for dealing with road disturbances, low movement at the end-effector is important for its precision. The different options available are shown in Figure 6.1 and compared in Table 6.1. Because only limited ground disturbances are expected in the indoor environment, and in order to keep the complexity of the wheel unit, which is already expected to be crowded, manageable, only tire and passive spring & damper suspension options will be considered in detail.

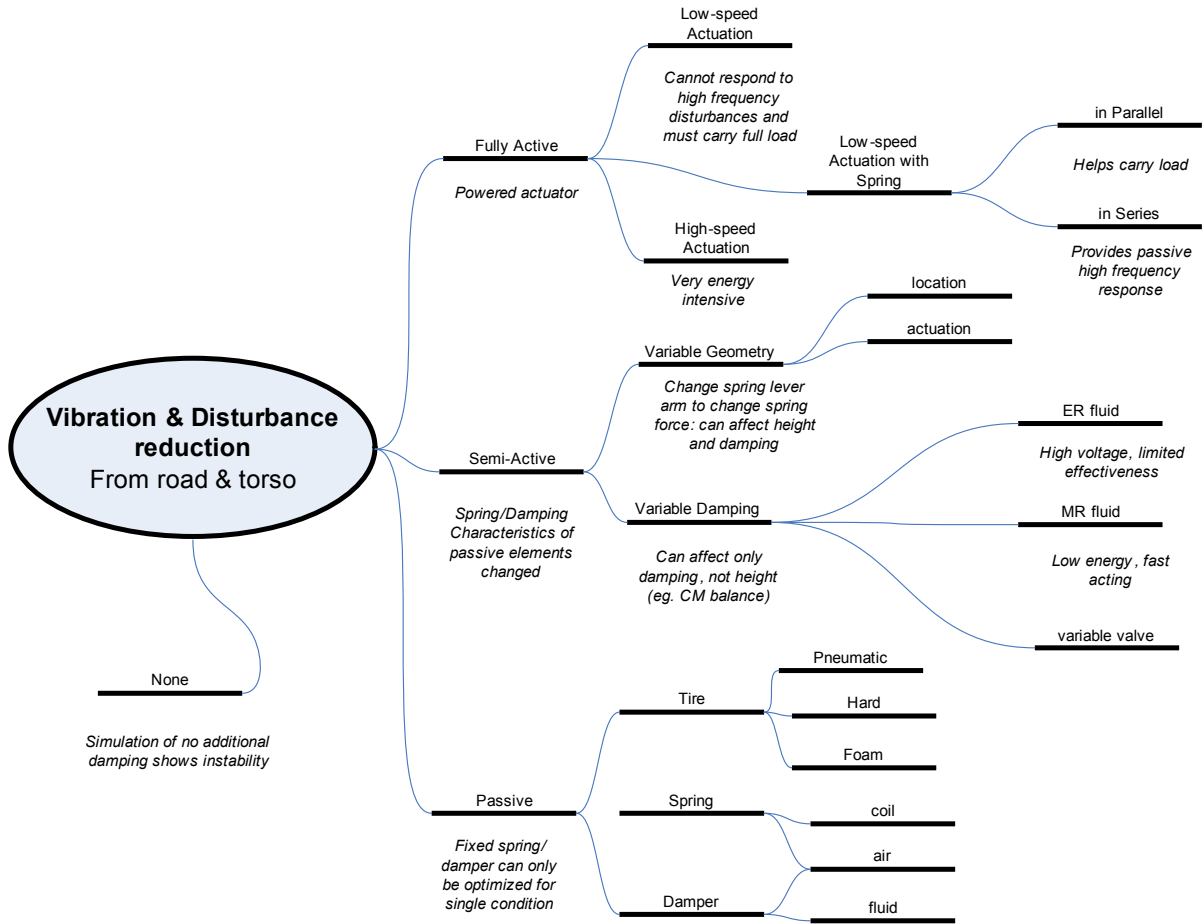


Figure 6.1: Suspension options.

Table 6.1: Comparison of suspension options

	Passive Spring Damper	Variable Damper	Variable Geometry	Active in Parallel	Fully Active	Compensate in Upper Body
<i>Complexity:</i>						
Control Complexity	no control	average	average	average	average	high
Mechanical Complexity	low	average	very high	very high	high	none
Design	simple	average	high	high	high	none
<i>Costs:</i>						
Weight	low	average	above avg	average	very high	none
Energy Use	none	above avg	above avg	above avg	very high	none
<i>Disturbance Reduction:</i>						
Ground Disturbances	ok	good	very good	very good	average	?
Change in Mass/Mass Distribution	poor	poor	good	good	good	?
Torso/ Arm Movements	ok	ok	?	?	?	poor

6.4 Tire Only

An elastic tire is the simplest form of suspension and is often the only suspension found on indoor mobile robots. Some typical values for tire spring and damping constants are found in Table 6.2 below.

Table 6.2: Different tire spring and damping constants from literature.

Tire Type	Spring Constant (kN/m)	Damping Constant (Ns/m)	Details	Source
Bicycle	134	272	Tire make: Radical, 3.65 kg	[99]
Bicycle	200	250	Tire make: Ostrad Adagio, 0.25m radius, 5.85 kg	
Bus	500	15020		[100]
Car	200	125		[101]
Car	70	233		[102]
Car	90	10		[103]
Car	100-250	200 at 6 mm	Damping varies with $amplitude^{-0.64}$	[104]
Wheelchair	118		Tire material: grey rubber, pneumatic	[89]
Wheelchair	144		Tire material: circular polyurethane foam	
Wheelchair	244		Tire material: tapered polyurethane foam	
Wheelchair	607		Tire material: molded polyisoprene	

6.4.1 Frequency Response - Quarter-Car Model

To investigate the response of the suspension to a range of frequencies originating from ground disturbances, a simplified second-order ‘quarter-car’ model is used which represents only one wheel unit and a quarter of the system mass, $m_{sys/tire}$, as shown in Figure 6.2. It has one degree of freedom representing the tire position relative to the ground, x_1 . The equation of motion is:

$$m_{sys/tire}\ddot{x}_1 = kx_0 + c\dot{x}_0 \quad (6.1)$$

where x_0 is the ground height, k is the tire spring constant and c is the tire damping constant. A softer tire (lower spring constant) will result in more travel, where the displacement is inversely proportional to Hooke’s law:

$$x_1 = \frac{F}{k} \quad (6.2)$$

Under equally distributed static loading with no payload, the tire will deflect between 0.5 and 4 mm for the softest to the hardest values in Table 6.7. The maximum static load on one wheel could be just under half the system mass, assuming the configuration and loading is such as to be near the point of tip-over instability. The system mass ranges from $115 \text{ kg} / 4 = 28.75 \text{ kg}$ which is no payload over four wheels to $141.4 \text{ kg} / 2 = 70.7 \text{ kg}$ which is the maximum payload over two wheels. For a system mass of a 141.4 kg over two wheels, this is a load of 693 N . The opposing set of wheels from the tip-over axis would then have near zero loading. With the dynamic effects of acceleration, wheel loading could be as high as 800 N , which would result in tire compression between 1 and 11 mm. Tires, irregardless of material, generally do not provide very high levels of damping, so additional suspension components are required if more damping is needed. As detailed below, this is the case for the platform.

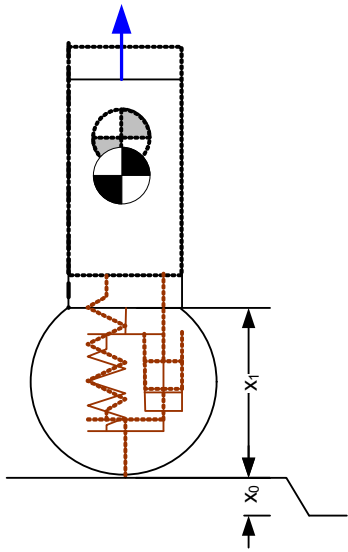


Figure 6.2: Quarter-car model.

For frequency analysis, a sinusoidal input is applied to x_0 .

The transfer function for the quarter car can be found analytically and is

$$X = \sqrt{\frac{1 + (2r\zeta)^2}{(1 - (r)^2)^2 + (2r\zeta)^2}} \quad (6.3)$$

where r is the wheel radius and ζ is the damping ratio, defined as

$$\zeta = \frac{c}{c_{critical}} \quad (6.4)$$

where $c_{critical}$ is the critical damping, which can be found with

$$c_{critical} = 2\sqrt{k \cdot m_{sys/tire}} \quad (6.5)$$

The damping ratio is 1 for a critically damped system. Critical damping is desired since it is the fastest way to reach steady-state without any oscillations. For a system mass of 115 kg , or

28.75 kg/tire, a range of tire spring constants of 70-600 kN/m gives critical damping values from 4443 to 13 008 Ns/m, which generally exceed a tire's actual damping constant. Figure 6.3 shows the frequency response of the quarter car model for different levels of damping and spring constant. Higher damping reduces the amplitude of the response particularly around the resonant frequency. A lower spring constant moves the resonant peak to a lower frequency and slightly reduces its amplitude.

As is apparent from (6.5) and shown graphically in Figure 6.4, critical damping is dependent on the spring constant and the system mass. Since the mass of the system will vary depending on the payload, the damping ratio will change as well.

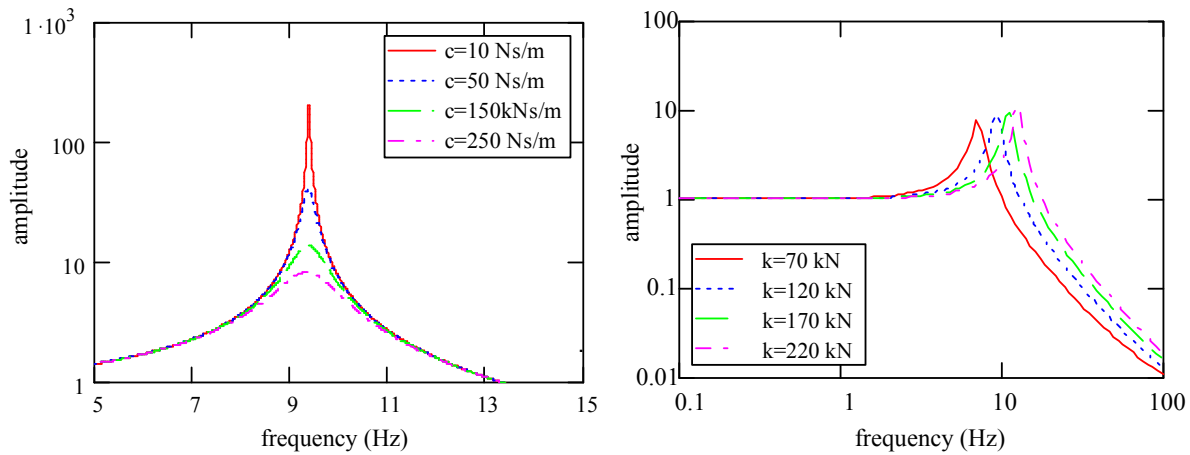


Figure 6.3: frequency response under maximum load for different damping constants at a spring constant of 120 kN (left) and for different spring constants at a tire damping constant of 250 Ns/m (right).

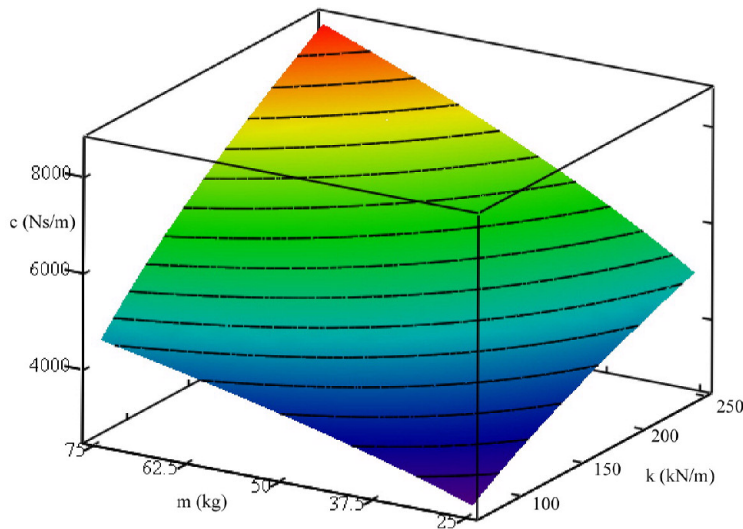


Figure 6.4: The damping c required for critical damping depends on the spring constant k and the system mass m , which are shown here for potential tires and payloads.

6.4.2 Upper Body Disturbance - Simulation

A multi-body physics simulation is performed in the Dymola/Modelica environment using an accurate upper-body model, a realistic platform and an elastic tire model as described in Appendix D. It includes all four tires, each with full freedom relative to the ground.

Disturbances due to the inertial effects of upper-body motion are investigated by applying a demanding motion trajectory to the upper-body as shown in Figure 6.6. The scenario investigated is lifting a 3 kg mass from the fully extended position with the torso and arms horizontal to a position where the torso is vertical and the arms horizontal. Movement begins at 2 s with the 2nd torso joint (the first torso joint rotates the torso around a vertical axis) accelerating with maximum torque to the maximum joint speed (100 deg/s), which is maintained until the torso nears the upright position. Maximum torque is again used to decelerate, which leads to a much higher deceleration rate due to the reduced loading on the joint in the upright position. Because the base itself can accelerate both due to suspension travel and movement of the entire platform—the wheels are prevented from turning but have a frictional ground contact that allows slip—the forces between the base and the upper-body are not as high as the forces between the upper-body and a fixed surface as shown in Appendix C.

The test is done with the torso facing the ‘narrow’ side of the base and the legs extended to 70°. Repeating the same scenario with legs extended half their maximum horizontal distance (36.9°) causes the platform to tip, highlighting the significant effect of upper body disturbances and the potential importance of an improved suspension.

The pitch angle, angular velocity and angular acceleration of the base as well as the vertical position of the top of the base centre and its acceleration are recorded during the trajectory for four different tire spring constants from 70 kN/m to 220 kN/m with a constant damping of 200 Ns/m and results are recorded in Figure 6.7 to Figure 6.10. The results show significant oscillation for all spring constants as expected for damping below critical. Table 6.3 lists maximum and minimum angular and vertical acceleration values for the different spring constants. The peak acceleration values are all relatively similar, with the highest absolute angular value occurring for 120 kN/m and the highest vertical value occurring for 220 kN/m.

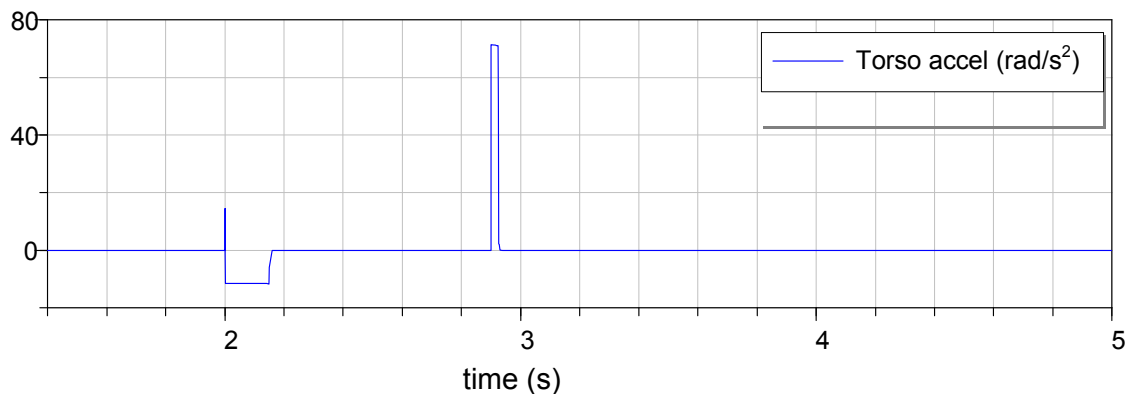


Figure 6.5 Second torso joint acceleration used to generate an example of a severe disturbance due to the upper-body.

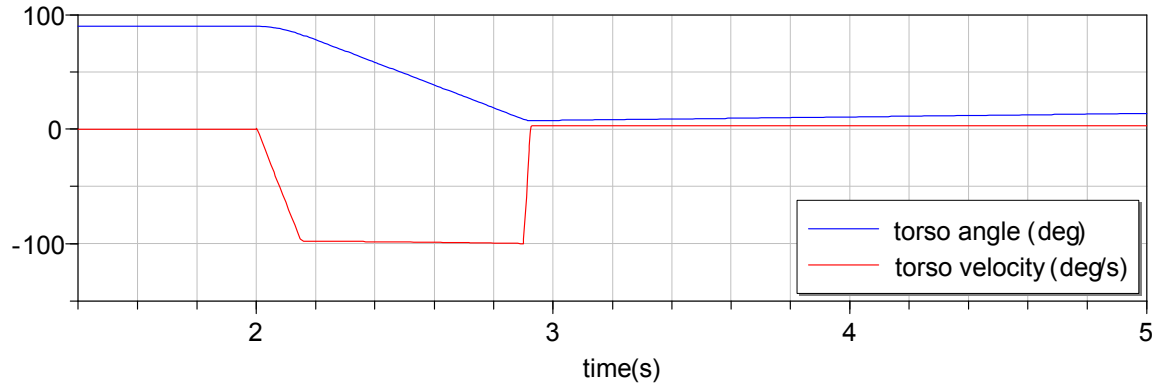


Figure 6.6: Second torso joint angle and velocity used to generate upper-body disturbance.

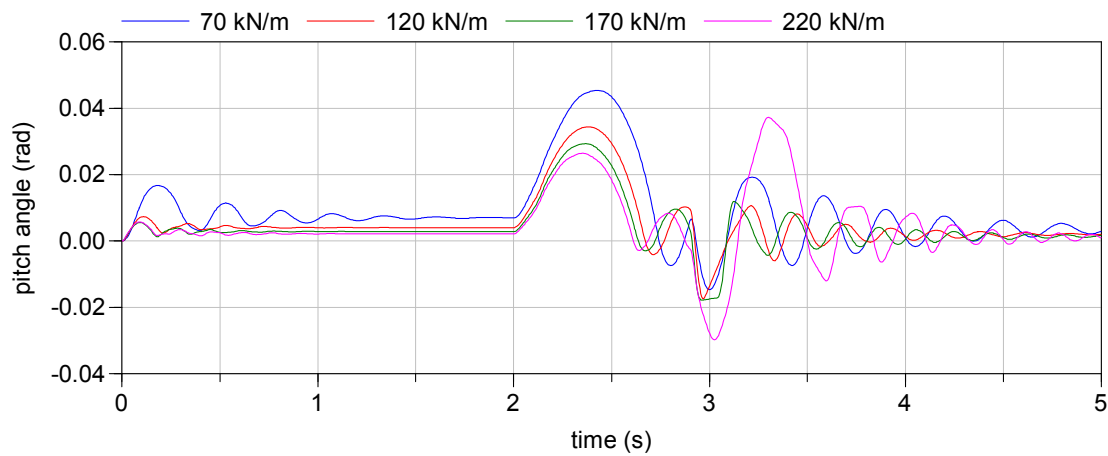


Figure 6.7: pitch angle of base for torso disturbance (raising 3 kg from horizontal torso & arm position to vertical torso, horizontal arm) for different tire spring constants, constant damping at 200 Ns/m. Legs extended to 70°, torso facing narrow side.

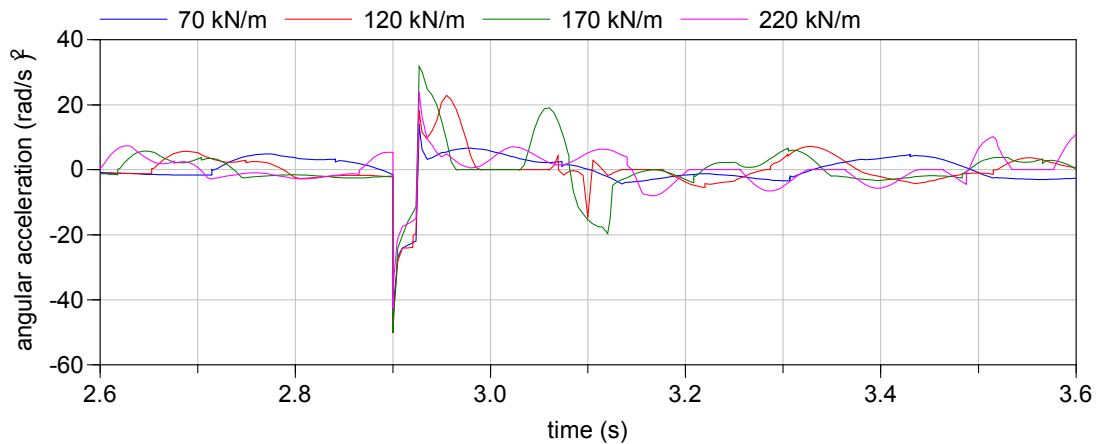


Figure 6.8: angular acceleration due to torso disturbance as described above for different tire spring constants.

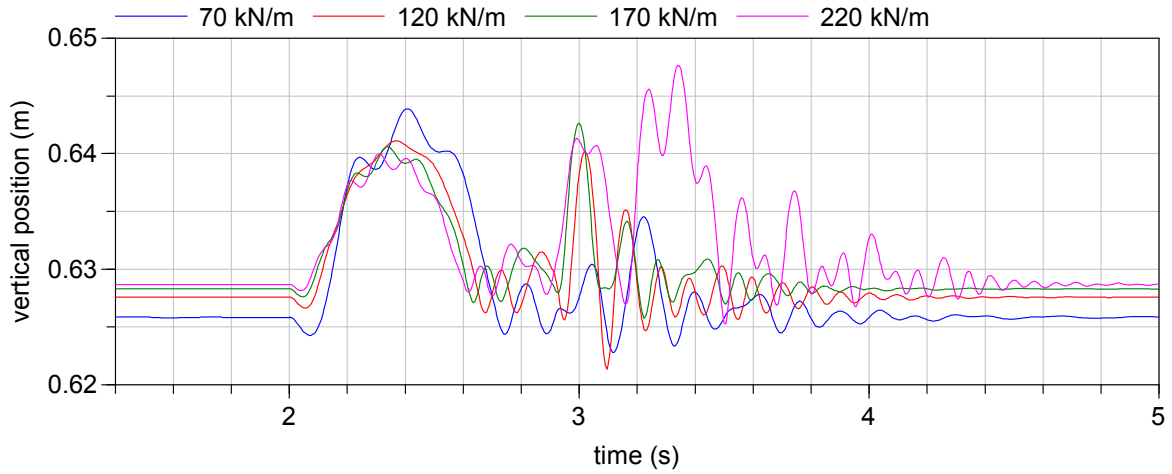


Figure 6.9: vertical position of top of base during torso disturbance as described above for different tire spring constants.

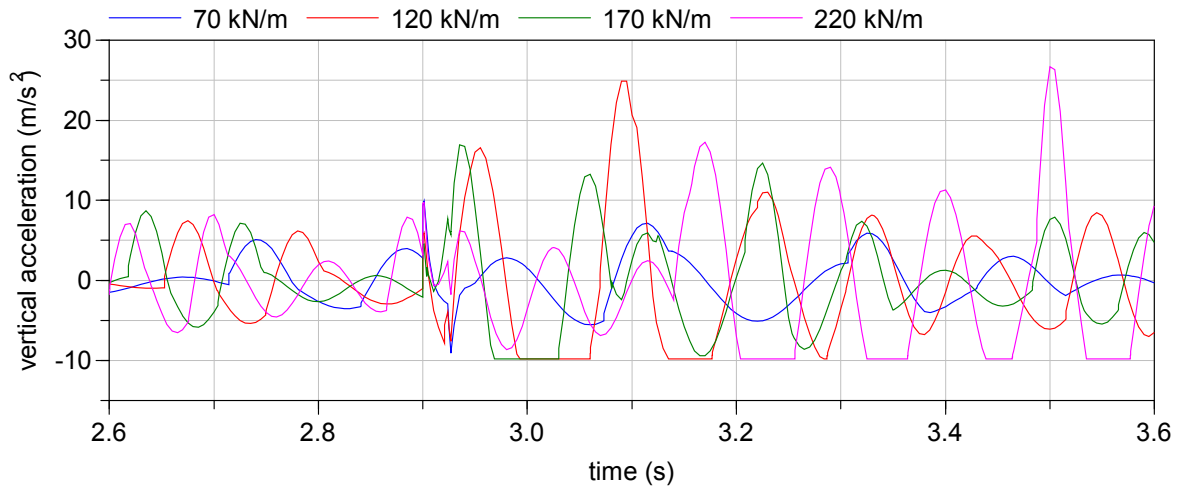


Figure 6.10: vertical acceleration of top of base during torso disturbance as described above for different tire spring constants.

Table 6.3: Maximum and Minimum angular and vertical base acceleration do to torso disturbance for different tire spring constants, damping 200 Ns/m.

Spring constant	Min/Max angular acceleration	Min/Max vertical acceleration
70 kN/m	-49.3/14.1 rad/s ²	-9.1/9.9 m/s ²
120 kN/m	-50.3/22.9 rad/s ²	-9.8/24.9 m/s ²
170 kN/m	-50.0/31.7 rad/s ²	-9.8/16.9 m/s ²
220 kN/m	-42.6/24.0 rad/s ²	-9.8/26.7 m/s ²

6.5 Passive Spring & Damper

A common way to provide for a improved vehicle suspension is to use a spring and damper in parallel between the wheel and body. The softest allowable spring constant is determined based on the suspension travel that is desired under maximum loading and the availability of space for suspension travel. The suspension travel will take away from the vertical slider travel, reducing the leg extension distance. Thus the goal is to keep the travel as small as possible while satisfying the performance goals.

Given the maximum loading per wheel F found in section 6.4.1, the spring constant k necessary for a given amount of travel x can be found,

$$k = \frac{F}{x} \quad (6.6)$$

and a range of results is shown in Figure 6.11 and tabulated in Table 6.4. Note that this travel is in addition to the compression of the tire itself.

Table 6.4: Suspension travel at maximum load for different spring constants.

Travel at maximum load	Spring constant (kN/m)	Critical damping constant (Ns/m)
1 cm	80	3315
2 cm	40	2344
3 cm	27	1914
4 cm	20	1658

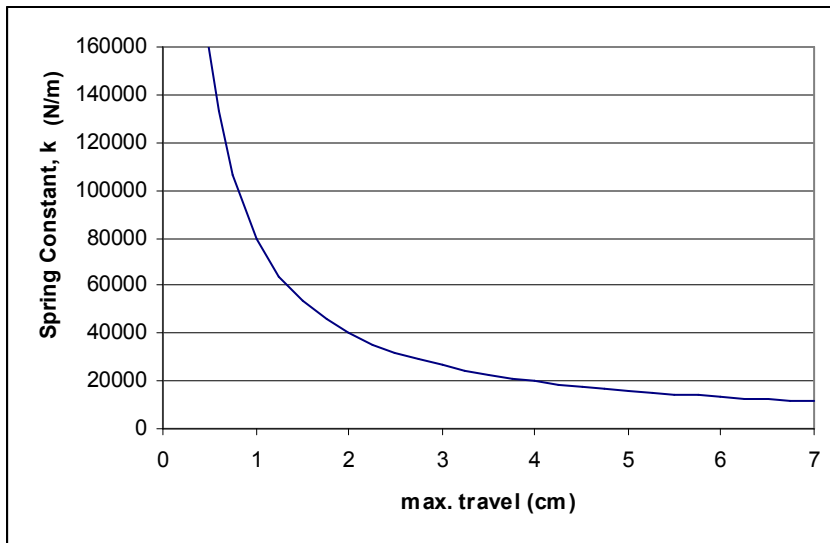


Figure 6.11: Spring constant necessary to give the indicated suspension travel under maximum load (800N).

6.5.1 Frequency Response - Quarter Car Model

To investigate the response of the suspension with a spring/damper, the quarter car model is extended to two degrees of freedom, one for the tire as before and a second for the body, x_2 , as shown in Figure 6.12.

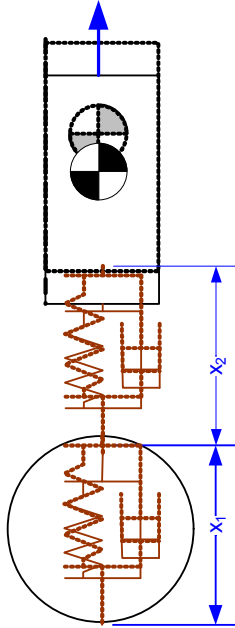


Figure 6.12: Quarter-car model with added spring-damper element in addition to tire.

The equations of motion become:

$$m_2 \ddot{x}_2 + c_2 (\dot{x}_2 - \dot{x}_1) + k_2 (x_2 - x_1) = 0 \quad (6.7)$$

$$m_1 \ddot{x}_1 - c_2 \dot{x}_2 + (c_1 + c_2) \dot{x}_1 - k_2 x_2 + (k_1 + k_2) x_1 = x_1 x_0 + k_1 x_0 \quad (6.8)$$

where m_2 is the body mass, m_1 is the ‘un-sprung mass,’ which consists of the wheel and other suspension components that are attached below the spring-damper, k_1 is the tire spring constant, c_1 is the tire damping constant, k_2 is the added spring constant and c_2 is the added damping constant.

In this analysis, the un-sprung mass is assumed to be 1 kg, and the body mass is as before except that the un-sprung mass is subtracted, ranging from $m_a = 111/4 = 27.75$ kg to $m_b = 137.4/2 = 68.7$ kg.

Due to changes in mass and weight distribution, the damping ratio can go from 1 at full load over two tires to 1.635 at no load over four tires. The change in mass from m_a to m_b by a factor of 2.5 causes a change in damping ratio between c_a and c_b of 1.6 due to the square-root relationship; since $c_c = 2\sqrt{km}$ (as approximated by a 1 DoF system),

$$\frac{c_a}{c_b} = \frac{2\sqrt{km_a}}{2\sqrt{km_b}} = \sqrt{\frac{m_a}{m_b}} \quad (6.9)$$

If the mass for the first system is twice the mass of the second system,

$$\frac{c_a}{c_b} = \sqrt{2} \tag{6.10}$$

Looking at the results from the quarter car model in Figure 6.13 to Figure 6.15, it can be seen that a softer spring (lower spring constant) provides better isolation around the natural frequency. Softer springs also have poorer high frequency isolation, but this is hardly noticeable.

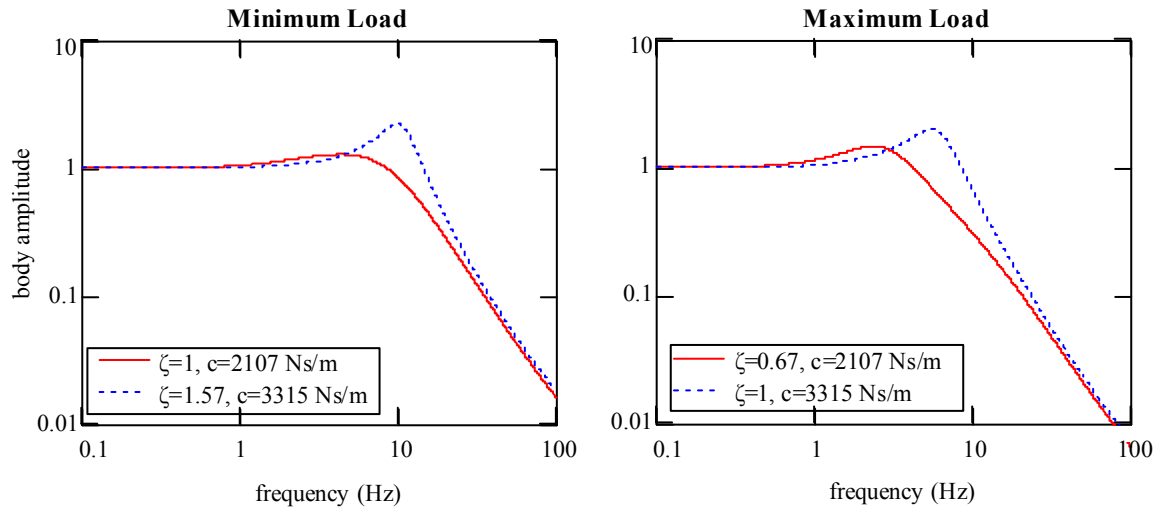


Figure 6.13: Frequency response of quarter car with spring constant of 40 kN/m, showing effect of varying damping ratio from 0.64 to 1 at minimum load (left) and 1 to 1.57 at maximum load (right), tire spring constant is 150 kN/m, tire damping constant is 250 Ns/m.

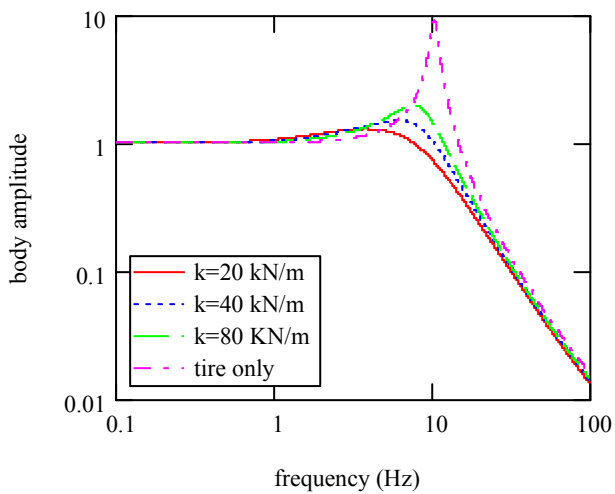


Figure 6.14: Frequency response of quarter car model for different suspension spring constants, critically damped for full load over four tires (as in Table 6.4), full load applied, tire 150 kN/m, 250 Ns/m

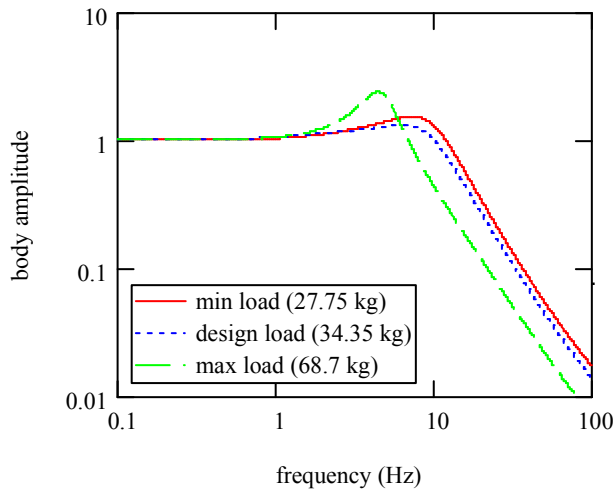


Figure 6.15: Frequency response at different loading, spring constant is 40 kN/m, damping constant is 2344 Ns/m (critically damped for maximum load over four wheels, 34.35 kg).

6.5.2 Upper-Body Disturbance - Simulation

As in 6.4.2, a representative upper-body motion is used to investigate effects from the upper-body on the suspension. Ideal spring-dampers are added to each wheel directly above the wheel axis and are vertically aligned with the base. Three different spring constants—20, 40 and 80 kN/m—are investigated. The damping is set to be critically damped for the maximum load distributed over four wheels. The tire has a spring constant of 150 kN/m and a damping constant of 250 Ns/m.

In Figure 6.16, the suspension travel is compared, which is inversely proportional to the spring constant as expected. In Figure 6.17 to Figure 6.20, the angular and vertical position and acceleration are compared. The softer the spring, the larger the displacement but the smaller the acceleration of the body. The maximum and minimum angular and vertical accelerations are tabulated in Table 6.5.

Table 6.5: Maximum and minimum angular and vertical acceleration do torso disturbance with passive spring-damper suspension and varying spring constants.

Spring Constant	Min/max angular acceleration	Min/max vertical acceleration
20 kN/m	-46.9/20.3 rad/s ²	-9.9/6.6 m/s ²
40 kN/m	-48.1/20.6 rad/s ²	-9.9/8.0 m/s ²
80 kN/m	-50.2/21.2 rad/s ²	-9.9/12.0 m/s ²

[A2]

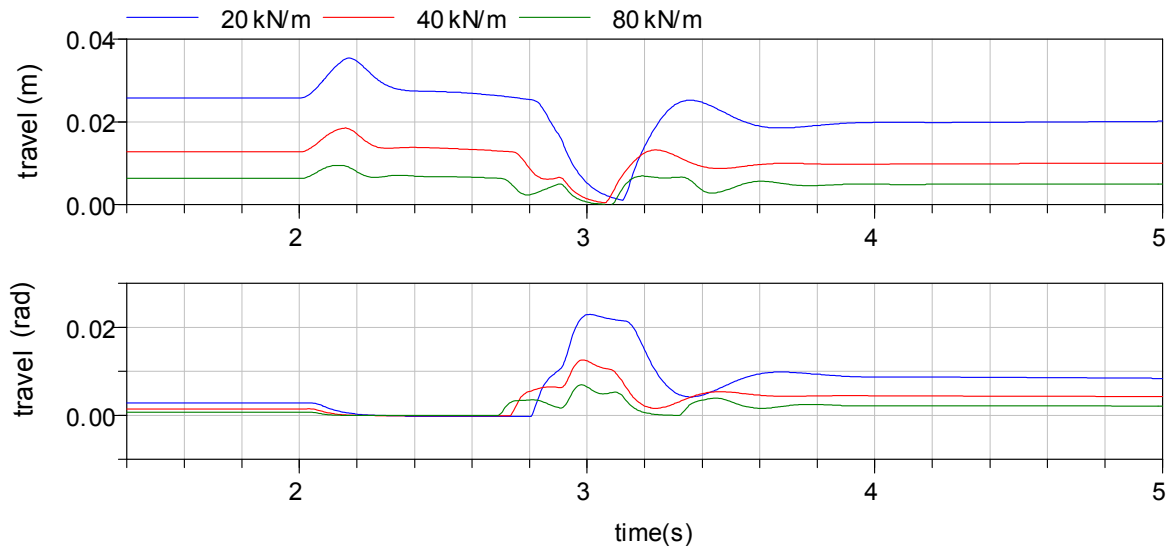


Figure 6.16: Right (top) and left (bottom) suspension travel for torso disturbance (raising 3 kg from torso & arm in horizontally extended position to vertical torso, horizontal arm) for different spring constants, critically damped for maximum load over four wheels. Legs extended to 70°, torso facing narrow side.

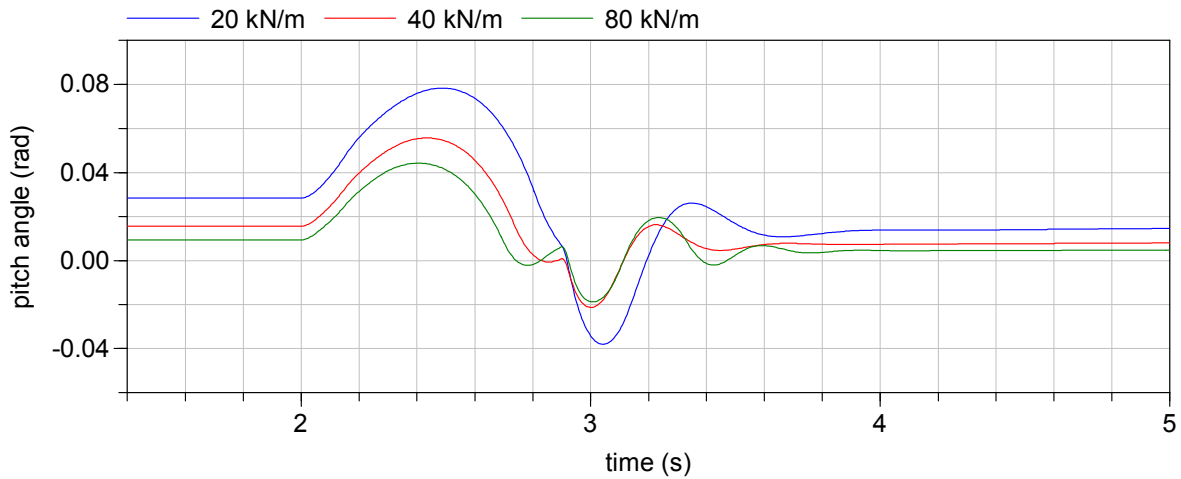


Figure 6.17: Base pitch angle for different spring constants during torso disturbance as above.

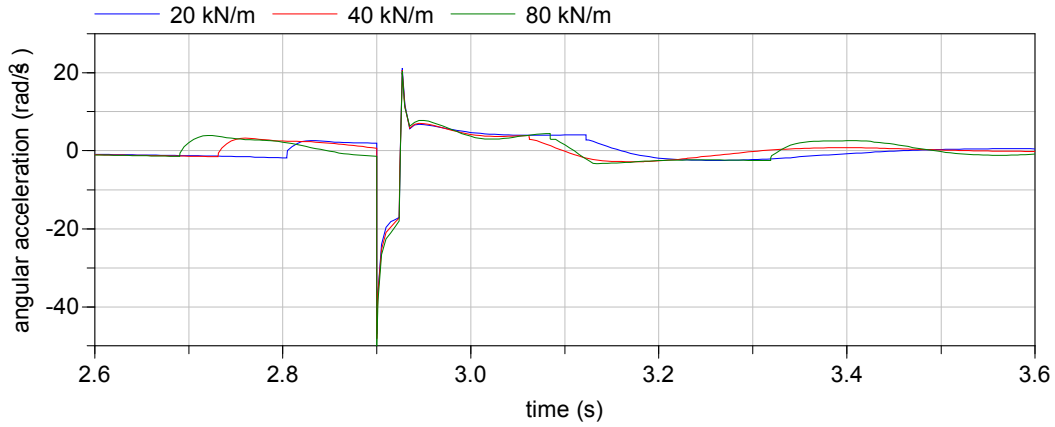


Figure 6.18: Angular acceleration for different spring constants, torso disturbance as above.

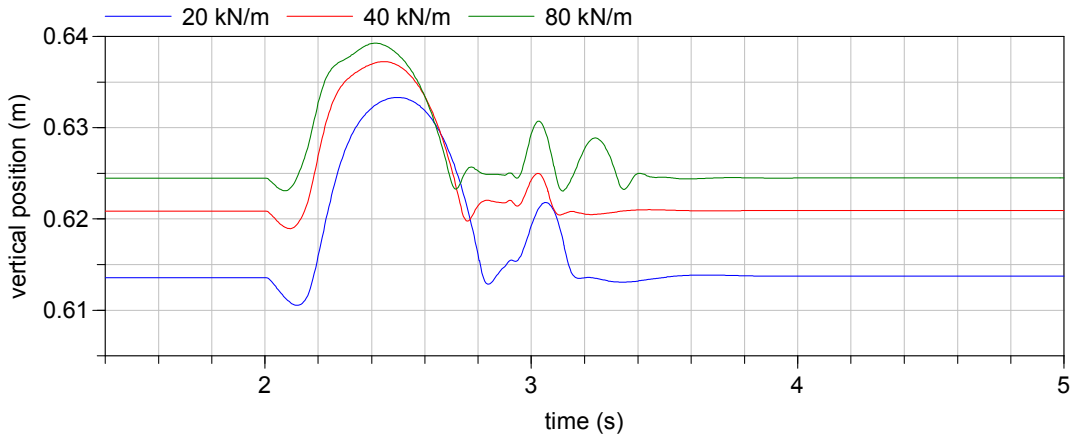


Figure 6.19: Vertical position of top of base for different spring constants, torso disturbance as above.

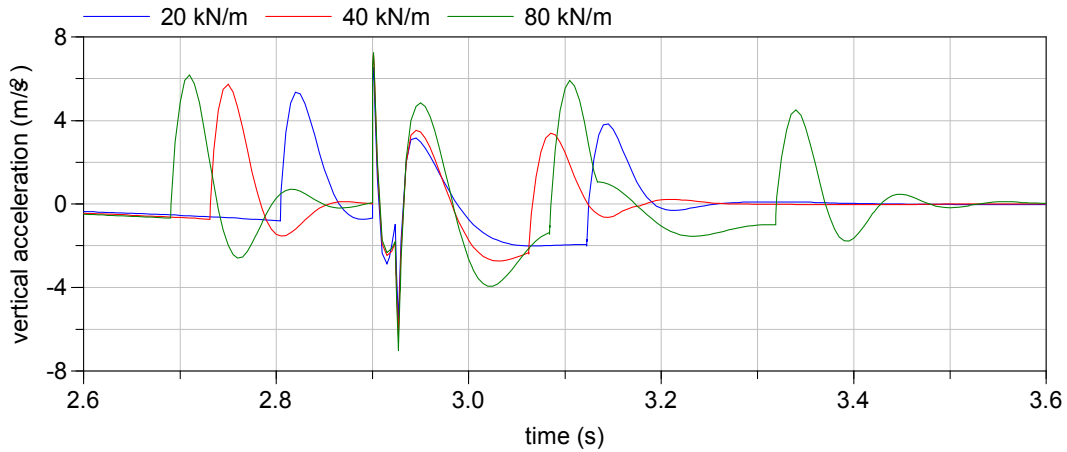


Figure 6.20: vertical acceleration of base for different spring constants, torso disturbance as described above.

In Figure 6.21 to Figure 6.23, the response of the tire only suspension with tire spring constant of 150 kN/m and tire damping constant of 250 Ns/m is compared to the passive spring-damper suspension with spring constant of 40 kN/m critically damped for maximum load over four wheels at 2344 Ns/m. The spring-damper suspension uses the same values for its tire as the tire-only suspension. The comparison is performed at a leg extension of 70° and 50°. Maximum and minimum angular and vertical acceleration are tabulated in Table 6.6. The largest absolute angular acceleration occurs with the tire only and the leg at 70°, although it is only about 4% higher than the value with suspension. The largest vertical acceleration occurs with the tire only and the leg at 50°, and is twice as high as the value with suspension.

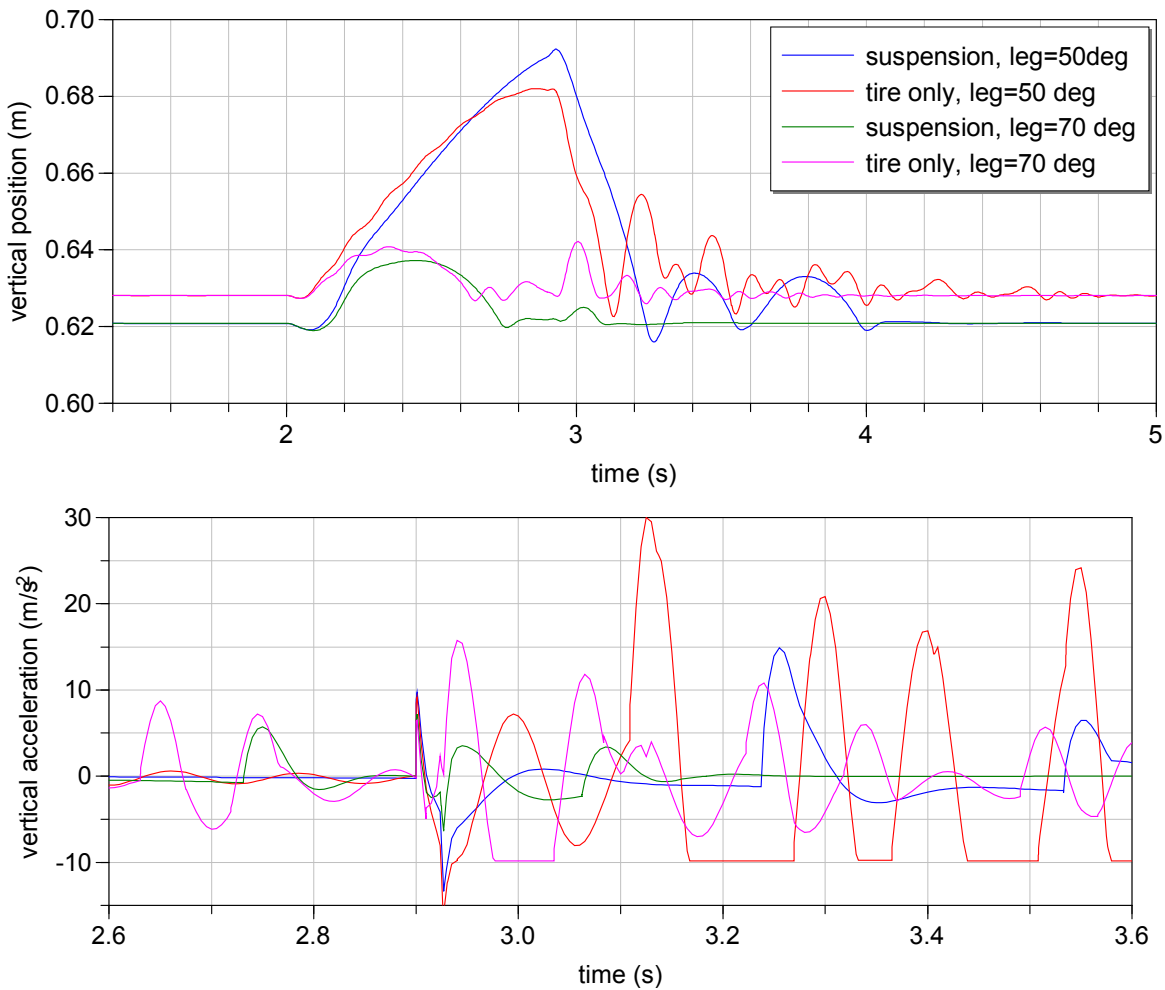


Figure 6.21: Vertical base position and acceleration during torso disturbance at two different leg extensions with tire only (tire spring constant of 150 kN/m and tire damping constant of 250 Ns/m) and passive spring-damper suspension (spring constant of 40 kN/m, damping constant of 2344 Ns/m).

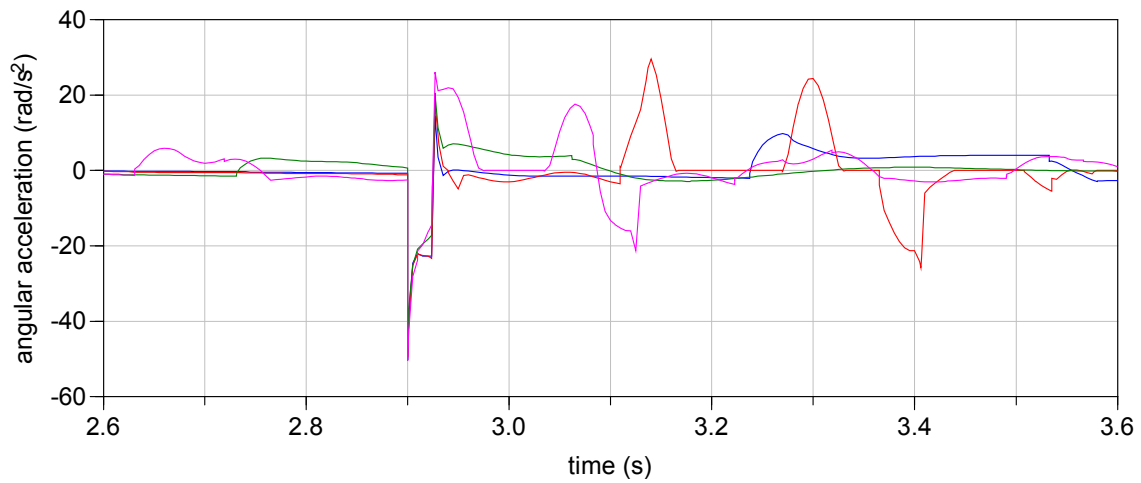
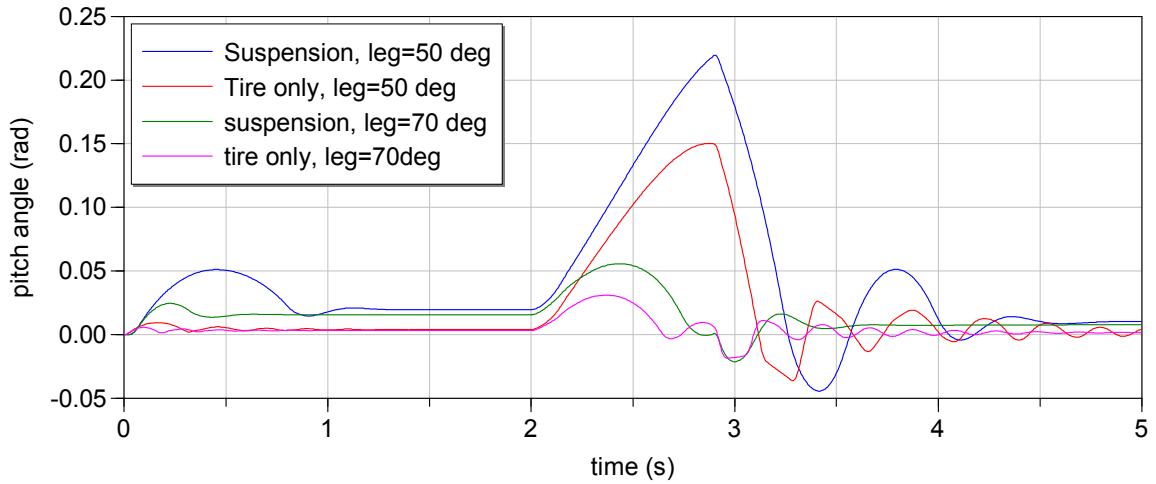


Figure 6.22: Angular base position and acceleration during torso disturbance comparing tire only and passive spring-damper suspension at two different leg lengths as described above.

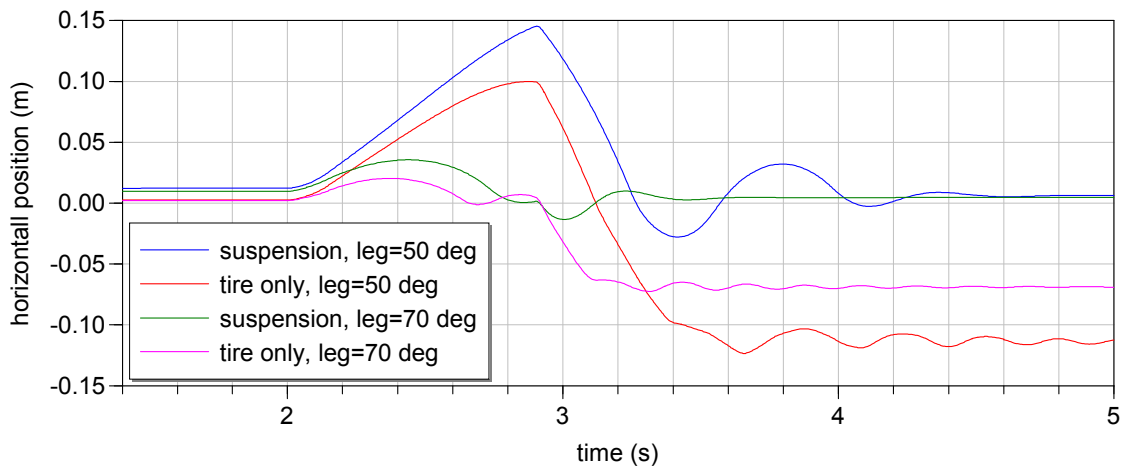


Figure 6.23: horizontal position of base during torso disturbance comparing tire only to passive spring-damper suspension at two different leg lengths as described above.

Table 6.6: Maximum and minimum angular and linear base acceleration do to torso disturbance for tire only and passive spring-damper suspension at leg extensions of 50° and 70°.

Scenario	Max/Min angular acceleration	Max/Min vertical acceleration
Suspension, leg at 50°	-50.2/14.6 rad/s ²	-13.4/14.9 m/s ²
Tire only, leg at 50°	-49.6/29.6 rad/s ²	-16.1/30.0 m/s ²
Suspension, leg at 70°	-48.1/20.6 rad/s ²	-9.9/8.1 m/s ²
Tire only, leg at 70°	-50.5/26.1 rad/s ²	-9.8/15.6 m/s ²

The simulation results show that a spring-damper suspension provides better isolation than a tire only suspension, generally causing less oscillation and significantly lower acceleration. However, the displacement amplitude is higher, both under constant load and dynamic loading.

Figure 6.23 shows that the reaction force of the torso disturbance causes the platform to jump and slide horizontally; the steady-state distance moved is most severe with the tire only suspension, whereas the spring-damper suspension causes a larger oscillation amplitude that decays to near the original position. This is evidence of sliding in the case of the tire only suspension as opposed to horizontal motion due to suspension travel with the spring-damper. The movement is more pronounced with the smaller leg extension angle.

6.5.3 Conclusions Passive Spring & Damper

A softer spring provides better isolation, but requires more travel room. Thus, the spring constant is limited by the travel room, which is determined by the maximum expected loading.

The passive spring damper suspension can only be tuned for one condition. It is desirable to have this condition be the one that is expected to occur most often on average, while ensuring that all other conditions perform satisfactorily and all limits are met. However, for ease of positioning the upper body, a slower, overdamped response is preferable to the large amounts of oscillation that occurs with an underdamped system. In addition, underdamping can lead to loss of stability, because the larger the pitch angle that occurs during overshoot, the larger the weight shift. Setting damping to be critical for the maximum load over four wheels provides reasonable performance over the typical operating range from minimum to maximum loading over four tires while still responding sufficiently well to extreme loading such as maximum load on two wheels.

Spring-dampers normally intended for use with mountain bikes are readily available and meet the requirements for travel length, spring constant and damping constant. Some models also feature a 'lockout' which effectively turns the spring-damper into a rigid link. This feature could be used when less suspension travel is required during slow precision upper-body manoeuvres.

6.6 Suspension: Conclusion

The advantage of a passive spring-damper system over only an elastic tire outweighs the increase in complexity and weight. Thus, the mobile platform design will include such a system. Limiting the travel to 2 cm at peak load (800 N) gives adequate performance and results in a spring constant of 40 kN/m. Damping is chosen to correspond to critically damped at maximum payload distributed evenly over four wheels, which gives a damping value of 2344 Ns/m.

The tires typically used on indoor mobile robots are most similar to wheelchair caster tires; this makes sense, since they operate in the same indoor environment and with similar loading as wheelchairs. Literature on tires for wheelchairs [105] suggests that pneumatic wheelchair tires perform best if properly inflated, with foam-filled tires coming close in performance without the need to monitor air pressure. Air-filled tires are undesirable for the robot suspension because along with their performance degradation due to air loss, their characteristics also change, throwing off the results from calculations that depend on these characteristics. A relatively soft tire however is desired for good traction characteristics, particularly at small steps (section 5.6.2), making a foam-filled tire a suitable choice. A potential candidate was chosen for its low mass and suitable load capacity; it is assumed to have a spring constant of 150 kN and a damping constant of 250 Ns/m, which is in line with literature for foam wheelchair tires and with experimental results on a similar tire used on the previous generation platform; its specifications (Table 6.7) are used in further analysis.

Table 6.7: candidate wheel properties

Manufacturer	Tente
Model	, PNP200x50-Ø8
Load Capacity	100 kg
Diameter	200 mm
Width	50 mm
Mass	0.4 kg
Material	Tire: foamed polyurethane Rim: hard plastic
Estimated inertia	Along axis: 0.00177 kg·m ² Perpendicular: 0.000948 kg·m ²

Chapter 7

Locomotion System

Although the general platform configuration was determined in section 2.5 and the basic locomotion concept along with it – four wheels with steering – the details of the wheel type and geometry are yet to be determined. Four wheel-types as shown in Figure 7.1 could be applied to the design:

- steered wheel
- split steered wheel
- powered caster
- powered split caster

Synchronized steered wheels are not considered in this research given the complexity of the resulting drive mechanism in combination with a variable footprint. Furthermore, Justin cannot rotate completely in the vertical axis, so an additional rotational stage would be necessary.

In general, there is a trade-off between increased mobility on the one hand and low complexity on the other. There is also a trade-off between reduced steering torque and increased size. The pros and cons for the different wheel types are summarized in qualitative terms in Table 7.1, where the steering scrubbing torque refers to the torque required to overcome the resistance to rotation around the vertical axis as a result of friction between the tire and the ground.

Table 7.1: Summary of attributes of the different wheel types

	Steered	Split Steered	Powered Caster	Powered Split Caster
Mobility	Omnidirectional	Omnidirectional	Omnidirectional Holonomic	Omnidirectional Holonomic
Complexity	Low	Low; lower if hub driven	Medium	Medium
Mass	Low	High	Medium	Highest
Steering Scrubbing Torque	High	Low	Medium	Low
Steering Acceleration Torque	Low	Medium	Medium	High
Footprint	Smallest	Medium	Medium	Largest

7.1 Footprint Geometry

The effective footprint radius r_{eff} for different wheel types is shown in Figure 7.1. For the steered wheel, the footprint radius is simply equal to the wheel radius, r . For the split steered wheel, the footprint radius increases with split offset distance, o ,

$$r_{eff_split_steer} = \sqrt{r^2 + \left(\frac{o}{2}\right)^2} \quad (7.1)$$

For the caster wheel, the footprint radius is simply the wheel radius plus the caster offset, c ,

$$r_{eff_caster} = r + c, \quad (7.2)$$

and for the split offset caster, the footprint is a function of split offset and caster distance,

$$r_{eff_split_caster} = \sqrt{(r + c)^2 + \left(\frac{o}{2}\right)^2} \quad (7.3)$$

Thus, the steered wheel always has the smallest footprint. The relative size of the split steered wheel versus the powered caster varies, for instance, for the split steered wheel to have a larger footprint than the powered caster with wheel radius of 0.1 m, the following inequality must hold:

$$o > \sqrt{4c(0.2 + c)} \quad (7.4)$$

Thus, a 2 cm caster is equivalent to a 5.7 cm split distance. The powered split caster is always largest given the same caster or offset distance.

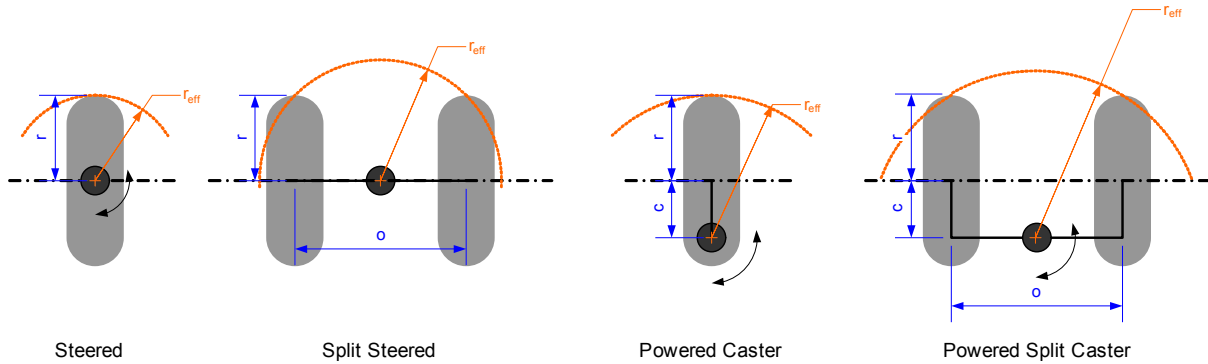


Figure 7.1: Wheel type footprint geometry

7.2 Mobility

One important consideration is that only holonomic solutions allow the VFM to be adjusted at any time without need to re-orient the wheels first, a substantial benefit that allows maximum utility to be obtained from the variable footprint. Holonomic motion is also the preferred solution as determined in 1.4.4.3. Thus, this leaves the powered caster and the powered split-caster as viable options. The kinematics and dynamics of these options will be considered below.

7.3 Kinematics & Dynamics

For the powered split-caster, the drive motor velocity $\dot{\rho}$ required to rotate the wheel unit at a steering velocity $\dot{\phi}$ depends on the side offset o and the wheel radius r ,

$$\dot{\rho} = \dot{\phi} \frac{o}{2r} \quad (7.5)$$

For offsets smaller than the wheel diameter, the drive motor velocity will be smaller than the steering velocity required, decreasing up to an undetermined situation at zero offset. Spenko et al. find the torque to overcome rolling resistance at steady-state on the other hand decreases with *increasing* offset at a non-linear rate dependent on the elasticity of the ground tire interface. More elastic contact reduces the effect of increased separation distance o in reducing the frictional resistance torque. Spenko et al. find the frictional resistance torque and power in their split-offset design to be about 2/3 the amount for a comparable single caster [18].

The torque to accelerate the steering of the unit depends on its inertia. The mass of a split caster is likely to be at least one-and-a-half times that of a single caster, even given that lighter tires can be used since the load is distributed between both. The inertia increases considerably more since the mass is moved outward from the centre; the larger the side-offset o , the larger this effect. Thus, it is assumed that the acceleration torque would be at least twice as large for a split-offset caster compared to a single caster with the same caster length c and tire load capacity.

So, while a split offset reduces the constant velocity torque, it increases the acceleration torque due to the increased inertia of the split caster; in terms of peak power, whether the savings of the one outweigh the gains of the other depends on the configuration geometry and the mass. In terms of energy use, it also depends on the duty cycle as to the ratio between time spent accelerating the steering versus steering at a constant velocity. In most cases, the steering is only actuated a short period of time and then stays constant, meaning acceleration predominates.

7.4 Selection of Wheel Type

The smaller footprint of a single caster is considered to be more significant than the fractional decrease in the constant velocity torque and power for the split-offset caster, so the decision is made to use the former. The length of the caster will be determined in Chapter 8 by simulating the torque and power requirements for varying lengths.

Chapter 8

Drive System Kinetics

8.1 Co-operating Manipulators Model Derivation

The kinematics and dynamics of a powered-caster system can be determined using the method of co-operating manipulators [16]. In this method, each powered-caster leg unit is treated as a manipulator with its base at the wheel ground contact point and its end-point at the centre of the platform, as shown in Figure 8.1 and Figure 8.2.

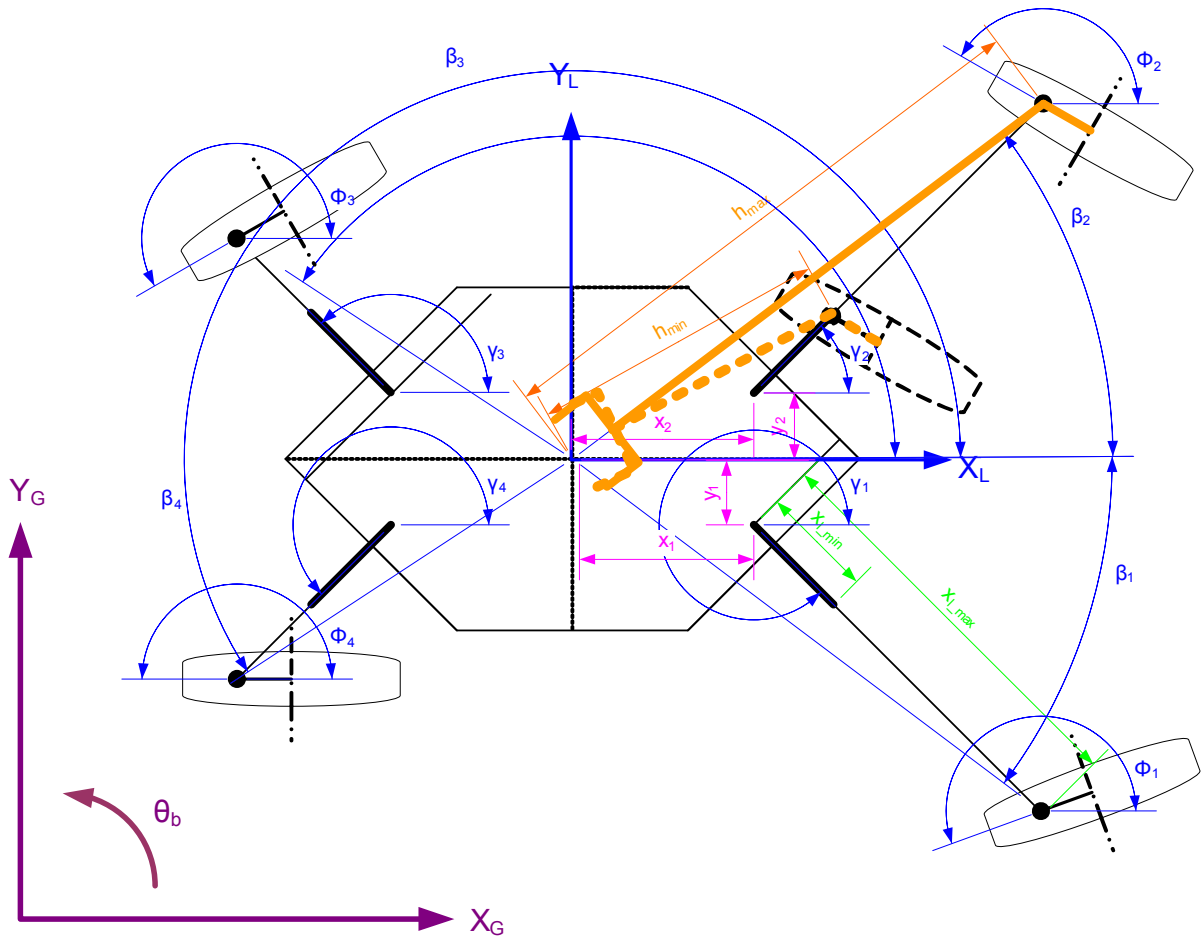


Figure 8.1: Top view of platform showing drive kinematic parameters, where the ‘cooperating manipulator’ is highlighted in orange.

The variables associated with the changing footprint will be considered to remain static with respect to time in this analysis. X_L - Y_L represents the local base co-ordinate frame and is attached to the centre of the base of the platform. X_G - Y_G represents the global ground reference frame and θ_b is

the angle of the base frame relative to the ground frame. The steering angles $\phi_{1..4}$ and the horizontal leg extension direction angle $\gamma_{1..4}$ are measured relative to the local base co-ordinate frame's X-axis.

The effective leg length h can be found from the horizontal leg extension distance x_i , the angle γ , and the horizontal leg origin position given in the local base frame as (x_i, y_i) , using

$$h_i = \sqrt{(x_i + x_i \cos(\gamma))^2 + (y_i + x_i \sin(\gamma))^2} \quad (8.1)$$

The effective leg angle β can be found as follows:

$$\beta_i = \arctan\left(\frac{y_i + x_i \sin(\gamma)}{x_i + x_i \cos(\gamma)}\right) \quad (8.2)$$

where inverse tangent must be resolved to the appropriate quadrant (or the function *arctan2* can be used). The average leg angle is 38.5° .

Initially, only one leg 'manipulator' will be considered; later, when the platform as a whole consisting of four co-operating manipulators is examined, the subscript i will be added to the joint variables to indicate wheels 1-4.

The Denavit-Havenberg parameters for the powered-caster leg manipulator are given in Table 8.1.

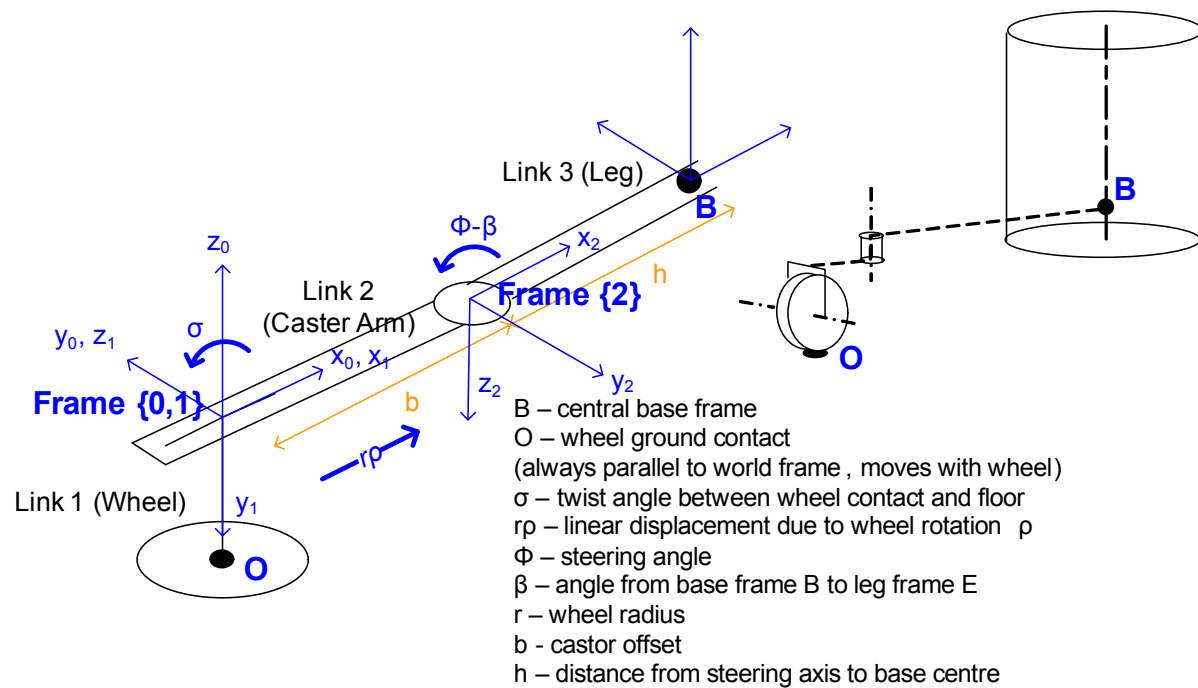


Figure 8.2: One leg of the platform as a manipulator with end-effector at base centre.

Table 8.1: D-H parameters for leg ‘manipulator’

	twist α	length a	rotation θ	offset d
OH	$-\pi/2$	0	σ	0
HG	$-\pi/2$	$r\rho$	0	0
GF	0	0	$\Phi-\beta$	0

The transformation matrices for the manipulator are:

$$T_0^1 = \begin{bmatrix} \cos(\sigma) & 0 & -\sin(\sigma) & 0 \\ \sin(\sigma) & 0 & \cos(\sigma) & 0 \\ 0 & -1 & 0 & 0 \\ 0 & 0 & 0 & 1 \end{bmatrix} \quad (8.3)$$

$$T_1^2 = \begin{bmatrix} 1 & 0 & 0 & r\rho \\ 0 & 0 & 1 & 0 \\ 0 & -1 & 0 & 0 \\ 0 & 0 & 0 & 1 \end{bmatrix} \quad (8.4)$$

$$T_0^2 = \begin{bmatrix} \cos(\sigma) & \sin(\sigma) & 0 & \sin(\sigma)r\rho \\ \sin(\sigma) & -\cos(\sigma) & 0 & \cos(\sigma)r\rho \\ 0 & 0 & -1 & 0 \\ 0 & 0 & 0 & 1 \end{bmatrix} \quad (8.5)$$

$$T_2^3 = \begin{bmatrix} \cos(\phi-\beta) & -\sin(\phi-\beta) & 0 & 0 \\ \sin(\phi-\beta) & \cos(\phi-\beta) & 0 & 0 \\ 0 & 0 & 1 & 0 \\ 0 & 0 & 0 & 1 \end{bmatrix} \quad (8.6)$$

$$T_0^3 = \begin{bmatrix} \cos(\sigma)\cos(\phi-\beta)-\sin(\sigma)\sin(\phi-\beta) & -\cos(\sigma)\sin(\phi-\beta)-\sin(\sigma)\cos(\phi-\beta) & 0 & \cos(\sigma)r\rho \\ \sin(\sigma)\cos(\phi-\beta)+\cos(\sigma)\sin(\phi-\beta) & \cos(\sigma)\cos(\phi-\beta)-\sin(\sigma)\sin(\phi-\beta) & 0 & \sin(\sigma)r\rho \\ 0 & 0 & 1 & 0 \\ 0 & 0 & 0 & 1 \end{bmatrix} \quad (8.7)$$

The centre of mass of the first link, the wheel, is naturally at the wheel centre, the origin of frame $\{0\}$:

$$c1_o = \begin{bmatrix} 0 \\ 0 \\ 0 \\ 1 \end{bmatrix} \quad (8.8)$$

The second link, the caster, consists of all the parts that move with the steering except for the wheel. The inertia of these parts will be expressed from the origin of frame $\{1\}$,

$$c2_{HG} = \begin{bmatrix} 0 \\ 0 \\ 0 \\ 1 \end{bmatrix} \quad (8.9)$$

which is transformed to frame $\{0\}$,

$$c2_o = T_0^2 c2_{HG} = \begin{bmatrix} \cos(\sigma)r\rho \\ \sin(\sigma)r\rho \\ 0 \\ 1 \end{bmatrix} \quad (8.10)$$

The mass of the third link represents a quarter of the platform mass (for each wheel unit). The inertia will be expressed in GF such that the four legs add up to the total platform inertia centered in its middle,

$$c3_{GF} = \begin{bmatrix} -h \\ 0 \\ 0 \\ 1 \end{bmatrix} \quad (8.11)$$

which transformed into the $\{0\}$ frame is:

$$c3_o = T_0^3 c3_{GF} = \begin{bmatrix} -(\cos(\sigma)\cos(\phi-\beta) - \sin(\sigma)\sin(\phi-\beta))h + \cos(\sigma)r\rho \\ -(\sin(\sigma)\cos(\phi-\beta) + \cos(\sigma)\sin(\phi-\beta))h + \sin(\sigma)r\rho \\ 0 \\ 1 \end{bmatrix}. \quad (8.12)$$

The transformation matrices are used to find the link Jacobians by differentiation. When differentiating $r\rho$ with respect to σ and ϕ , the result is considered to be the constant b , but when differentiating with respect to ρ , it is considered as a time variable and results in $r\dot{\rho}$. The link 1 linear and angular Jacobians are

$$J1_v = \begin{bmatrix} 0 & 0 & 0 \\ 0 & 0 & 0 \\ 0 & 0 & 0 \end{bmatrix} \quad (8.13)$$

$$J1_\omega = \begin{bmatrix} 0 & 0 & 0 \\ 0 & 0 & 0 \\ 1 & 0 & 0 \end{bmatrix}. \quad (8.14)$$

The link 2 linear and angular Jacobians are

$$J2_v = \begin{bmatrix} 0 & \cos(\sigma)r & 0 \\ 0 & \sin(\sigma)r & 0 \\ 0 & 0 & 0 \end{bmatrix} \quad (8.15)$$

$$J2_{\omega} = \begin{bmatrix} 0 & 0 & 0 \\ 0 & 0 & 0 \\ 1 & 0 & 0 \end{bmatrix}. \quad (8.16)$$

The link 3 linear and angular Jacobians are

$$J3_v = \begin{bmatrix} h \sin(\beta) - b \sin(\phi) & \cos(\sigma)r & -h \sin(\beta) \\ -h \cos(\beta) + b \cos(\phi) & \sin(\sigma)r & h \cos(\beta) \\ 0 & 0 & 0 \end{bmatrix} \quad (8.17)$$

$$J3_{\omega} = \begin{bmatrix} 0 & 0 & 0 \\ 0 & 0 & 0 \\ 1 & 0 & -1 \end{bmatrix}. \quad (8.18)$$

Since the system operates in the x-y plane, only rows 1 and 2 of the linear velocity Jacobian and row 3 of the angular velocity Jacobian, representing x_b , y_b , and θ_b , are of interest. These are combined to form the overall Jacobian for one leg ‘manipulator,’ expressed in frame $\{0\}$:

$${}^0J = \begin{bmatrix} -h \sin(\phi - \sigma - \beta) - b \sin(\sigma) & \cos(\sigma)r & h \sin(\phi - \sigma - \beta) \\ -\cos(\phi - \sigma - \beta) + bh \cos(\sigma) & \sin(\sigma)r & -h \cos(\phi - \sigma - \beta) \\ 1 & 0 & -1 \end{bmatrix} \quad (8.19)$$

At this point, in order to use a joint vector, q , with joints in the following order,

$$q_i = \begin{bmatrix} \phi \\ \rho \\ \sigma \end{bmatrix} \quad (8.20)$$

The columns 1 and 3 of 0J are swapped,

$${}^0J = \begin{bmatrix} h \sin(\phi - \sigma - \beta) & \cos(\sigma)r & -h \sin(\phi - \sigma - \beta) - b \sin(\sigma) \\ -h \cos(\phi - \sigma - \beta) & \sin(\sigma)r & -\cos(\phi - \sigma - \beta) + bh \cos(\sigma) \\ -1 & 0 & 1 \end{bmatrix}. \quad (8.21)$$

Since it is desired to have the Jacobian expressed in the base frame at B , it is rotated by the following rotation matrix extracted from T_0^3 in (8.7):

$$R_O^B = \begin{bmatrix} \cos(\phi - \sigma) & -\sin(\phi - \sigma) & 0 \\ \sin(\phi - \sigma) & \cos(\phi - \sigma) & 0 \\ 0 & 0 & 1 \end{bmatrix} \quad (8.22)$$

which results in the following:

$${}^B J = \begin{bmatrix} -h \sin(\beta) & \cos(\phi)r & h \sin(\beta) - b \sin(\phi) \\ h \cos(\beta) & \sin(\phi)r & -h \cos(\beta) + b \cos(\phi) \\ 1 & 0 & 1 \end{bmatrix}. \quad (8.23)$$

As a result, σ , the ground contact angle, which cannot be controlled or measured, is removed from the equation. The first two rows of the Jacobian enforce the non-holonomic constraints posed by ideal

rolling, while the third row is a holonomic constraint that stipulates platform rotation fulfill the condition

$$\theta_b = \sigma - \phi. \quad (8.24)$$

This allows one to find the base velocity if the joint velocities are known:

$$\begin{bmatrix} \dot{x} \\ \dot{y} \\ \dot{\theta} \end{bmatrix} = {}^B J \begin{bmatrix} \dot{\phi} \\ \dot{\rho} \\ \dot{\sigma} \end{bmatrix} \quad (8.25)$$

Inverting the Jacobian gives

$${}^B J^{-1} = \begin{bmatrix} -\frac{\sin(\phi)}{b} & \frac{\cos(\phi)}{b} & \frac{h \cos(\phi - \beta)}{b} & -1 \\ \frac{\cos(\phi)}{b} & \frac{\sin(\phi)}{b} & \frac{h \sin(\phi - \beta)}{b} & 0 \\ -\frac{r \sin(\phi)}{b} & \frac{r \cos(\phi)}{b} & \frac{h r \cos(\phi - \beta)}{b} & 0 \end{bmatrix} \quad (8.26)$$

The first two rows of the inverse Jacobian representing the ideal rolling constraints are used to form the constraint matrix C_i , where the subscript i indicates the leg number:

$$C_i = \begin{bmatrix} -\frac{\sin(\phi_i)}{b_i} & \frac{\cos(\phi_i)}{b_i} & \frac{h \cos(\phi_i - \beta_i)}{b_i} & -1 \\ \frac{\cos(\phi_i)}{r} & \frac{\sin(\phi_i)}{r} & \frac{h \sin(\phi_i - \beta_i)}{r} & 0 \end{bmatrix} \quad (8.27)$$

Constraint matrices for each wheel are augmented to form the whole platform constraint matrix

$$C = \begin{bmatrix} C_1 \\ \vdots \\ C_n \end{bmatrix} \quad (8.28)$$

which lets one find the steering and drive joint velocities for a given base velocity,

$$\dot{q} = C \dot{X}_{body} \quad (8.29)$$

where \dot{q} is the augmented joint velocity vector for all wheels,

$$\dot{q} = \begin{bmatrix} \dot{q}_1 \\ \vdots \\ \dot{q}_4 \end{bmatrix} \quad (8.30)$$

and X and its derivative are simply the vectors of base position and velocities,

$$\dot{X}_{body} = \begin{bmatrix} \dot{x}_b \\ \dot{y}_b \\ \dot{\theta}_b \end{bmatrix}. \quad (8.31)$$

The joint accelerations can be found by differentiating (8.29) with respect to time such that

$$\ddot{\mathbf{q}} = \dot{\mathbf{C}}\ddot{\mathbf{X}}_{body} \quad (8.32)$$

8.2 Kinematics

8.2.1 Number of Actuators

In order to achieve holonomic motion in the plane, only three degrees of freedom need to be actuated. However, in order to avoid singularities and for ease of torque distribution, a higher degree of actuation can be beneficial, allowing for improved load distribution [81, 106]. Yi et al. find that the norm of the actuation effort in their three-wheeled fully-actuated system (with 6 actuators) is $\frac{1}{4}$ less than that for minimum actuation (requiring only 3 actuators). When more than two wheels are fully actuated, singularity-free planar omnidirectional motion is assured [107]. Thus, it is decided to actuate all wheels in this design fully for steering and drive joints, i.e. 8 actuators in total.

8.2.2 Requirements

For an isotropic maximum linear velocity v_{\max} , the relationship $v_{\max} = \sqrt{\dot{x}^2 + \dot{y}^2}$ must hold. According to DLR requirements for the base, the maximum linear velocity is required to be 1.6 m/s (6 km/h), which corresponds to a brisk walking pace. The isotropic maximum linear acceleration a_{\max} is targeted to be 2 m/s^2 . Acceleration from standstill to peak velocity should thus take only 0.8 s.

An angular velocity together with a linear velocity can put additional load on the drives. Thus, requirements are quite different for simultaneously maintaining an isotropic maximum linear *and* angular velocity versus an isotropic maximum linear *or* angular velocity. That is to say, allowing for a reduction in maximum linear velocity during peak angular velocity or vice versa places much lower requirements on the actuators. Angular velocity is considered to be of secondary importance, since the torso itself has 340° of movement in this same axis at about $100^\circ/\text{s}$. Thus, angular velocity is not considered as a factor in determining drive speed. Similarly, angular acceleration is also considered secondary. Both will be allowed to vary with the leg extension; smaller angular acceleration and velocities at full extension are considered acceptable.

The requirements are set for steady-state motion, because this will determine the size of the motor for continuous operation. Simulation results will be checked for higher transient peak speeds and requirements will be adjusted accordingly.

8.2.3 Parametric Analysis

Of the design parameters affecting the drive kinematics, the wheel radius is determined in Appendix E, the leg length was set in section 3.2 and the resulting variable footprint geometry is determined in section 9.7.2. The caster distance however is still undecided at this point. The leg angle β is fixed at its average value for this analysis, 38.5° . A larger caster requires greater space, which is at a premium in the design. The effects of caster length on the drive kinetics performance will be evaluated below so that an optimum caster length can be chosen.

8.2.3.1 Global Frame to Body Frame Conversion

In order to express global velocities in the robot's local frame, one only needs to rotate the velocity vector by the robot's angular position,

$$\dot{X}_b = \begin{bmatrix} \cos\theta_b & \sin\theta_b & 0 \\ -\sin\theta_b & \cos\theta_b & 0 \\ 0 & 0 & 1 \end{bmatrix} \dot{X}_G. \quad (8.33)$$

8.2.3.2 Drive Velocity

The relationship between the platform linear and angular velocities and the wheel drive speed is taken from the second row of the matrix result from (8.29):

$$\dot{\rho} = \frac{\cos(\phi_i)\dot{x}}{r} + \frac{\sin(\phi_i)\dot{y}}{r} + \frac{h_i \sin(\phi_i - \beta)\dot{\theta}}{r} \quad (8.34)$$

Drive speed depends on wheel radius, leg position, steering angle, as well as linear and angular velocities. The drive speed is inversely related to radius, but radius is fixed at 0.1 m.

When a velocity without an angular component is desired, the drive velocity will vary sinusoidally with steering angle. This is most evident if the relationship between $\dot{\rho}$ and the linear x and y velocities is expressed in polar co-ordinates, where

$$v = \sqrt{\dot{x}^2 + \dot{y}^2} \quad (8.35)$$

is the velocity magnitude and where

$$\lambda = \arctan\left(\frac{\dot{x}}{\dot{y}}\right) \quad (8.36)$$

is the angle of the velocity.

Thus, for linear velocity only, the drive speed at maximum linear velocity is

$$\dot{\rho} = \frac{v_{\max}}{r} \cos(\phi - \lambda) \quad (8.37)$$

which reaches a maximum when the steering angle is equal to the velocity angle, that is, when the wheel is pointing in the same direction as the velocity. At v_{\max} (1.6 m/s), the drive speed is thus 16 rad/s or 153 rpm. A minimum of zero is reached when the wheel is perpendicular to the desired velocity direction, as seen in Figure 8.3, i.e. $\phi - \lambda = 90^\circ$.

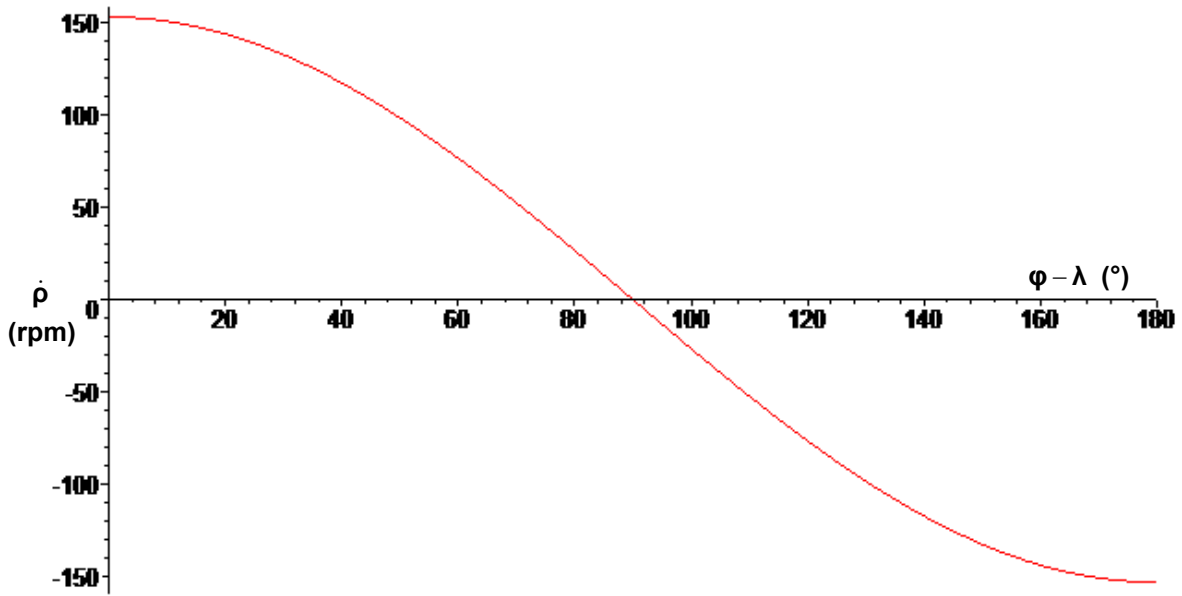


Figure 8.3: Drive rotational speed for different velocity angle (λ) and steering angle (ϕ) combinations at maximum x-velocity of 1.6. Peak is at 153 rpm.

If the wheel is in line with the leg, that is, the steering angle is equal to the leg angle, the wheel drive plays no part in providing angular velocity. If the wheel is perpendicular to the leg, the contribution to angular velocity is

$$\dot{\rho} = \frac{h_i}{r} \dot{\theta} \quad (8.38)$$

which means that drive speed required increases as the wheelbase increases. By limiting the drive speed to that needed for maximum linear velocity, the maximum continuous angular velocity occurs when the wheels are perpendicular to a radial line from the platform centre (Figure 8.4), which occurs as determined by the following equation at an angle dependent on the caster length and the wheelbase:

$$\phi_{\text{angularonly}} = \arcsin\left(\frac{\sqrt{h^2 - b^2}}{h}\right) - \beta \quad (8.39)$$

With β equal to zero,

$$\sin(\phi) = \frac{\sqrt{h^2 - b^2}}{h} \quad (8.40)$$

Substituting into (8.34) with linear velocities set to zero and $\beta = 0$,

$$\dot{\rho} = \frac{h \sin(\phi)}{r} \dot{\theta} = \frac{\sqrt{h^2 - b^2}}{r} \dot{\theta} \quad (8.41)$$

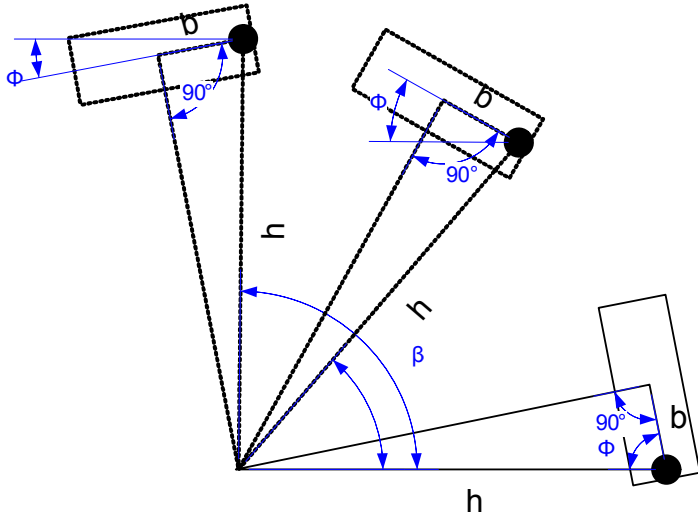


Figure 8.4: Steering angle for steady-state pure angular motion is such that the wheel is perpendicular to a line radial to the base centre

Solving for the angular velocity with $\dot{\rho} = v_{\max}/r$, the maximum continuous angular velocity is

$$\dot{\theta}_{\max_cont} = \frac{v_{\max}}{\sqrt{h^2 - b^2}} \quad (8.42)$$

which can be conservatively approximated assuming that the caster length is much shorter than the wheelbase by

$$\dot{\theta}_{\max_cont} = \frac{v_{\max}}{h} \quad (8.43)$$

For a wheelbase ranging from 0.3 to 0.7, this translates to a maximum turn rate of 5.3 to 2.3 rad/s (51 to 22 rpm). A half rotation at full leg extension in 1.4 s is considered adequate performance.

Angular velocity adds or subtracts from the drive speed for linear velocity depending on the direction and steering angle (Figure 8.5). Looking at the entire platform, there will always be at least one leg where the desired rotation increases the necessary drive speed. If angular velocity is desired simultaneously with linear velocity, and the restriction on the maximum drive velocity is to be upheld, either or both the maximum linear velocity and maximum angular velocity must be reduced such that the following condition derived from (8.34) and (8.37), is true:

$$v_{\max} = v_{linear} \cos(\phi - \lambda) + h\dot{\theta} \sin(\phi - \beta) \quad (8.44)$$

For continuous linear and angular velocity, the limiting condition is

$$v_{\max} = v_{linear} + h\dot{\theta} \quad (8.45)$$

which occurs when the steering angle is equal to the velocity angle and perpendicular to the leg angle, or $\phi = \lambda \perp \beta$. At one extreme, if linear velocity is to be maintained at v_{\max} , there can be a configuration where up to two wheels (since opposing legs are parallel) cannot support any rotational velocity without breaking the velocity restriction. If the remaining wheel drives have sufficient torque

reserves, they could push the wheels that can't support rotational velocity to go beyond v_{\max}/r , or of course these motors themselves could exceed this maximum if their capacity permits. This will depend on the torque load and the motor maximum velocity.

To stay within the limits imposed by the maximum linear velocity, (8.34) can be, using (8.43) to substitute for the angular velocity and (8.35) and (8.36) for the linear velocity, expressed as

$$\dot{\rho} = \alpha_a \frac{v_{\max} \cos(\phi - \lambda)}{r} + \alpha_b \frac{v_{\max} \sin(\phi_i - \beta)}{r} \quad (8.46)$$

where α_a and α_b represent the fraction of the maximum velocity allowance that is dedicated to linear and angular velocity respectively; they can add up to no more than one.

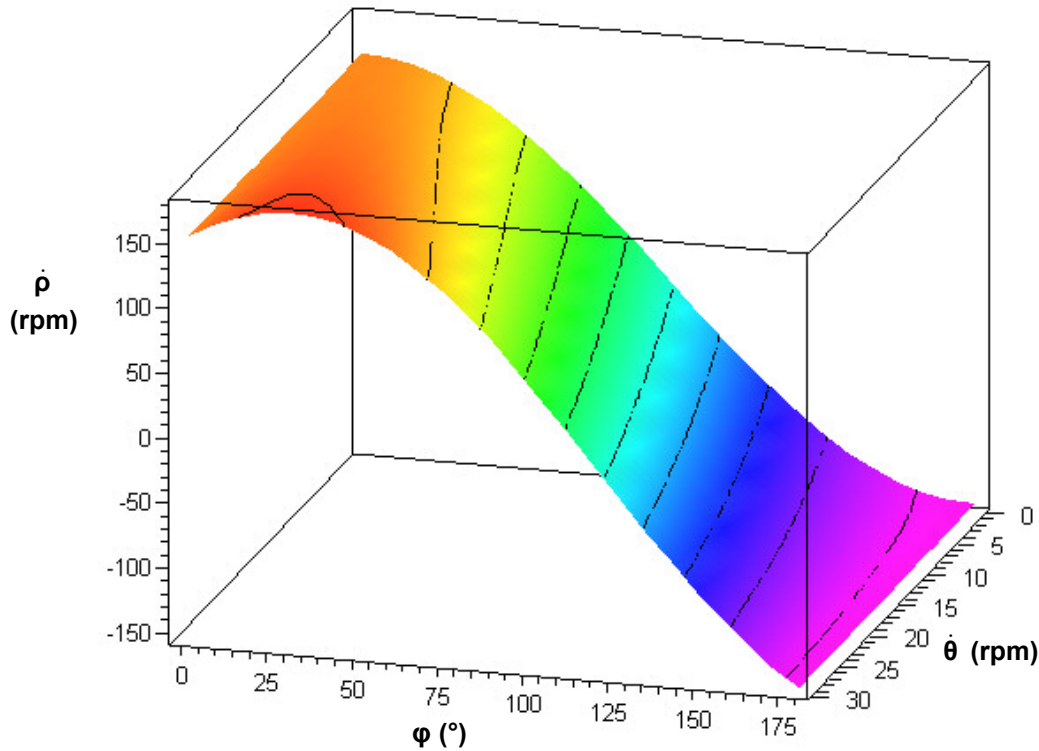


Figure 8.5: Plot of (36) with $\dot{x}=1.6$, $h=0.308$ m: increasing the base rotational velocity ($\dot{\theta}$) increases drive speed ($\dot{\rho}$) and shifts the steering angle (ϕ) at which the drive speed reaches a maximum away from zero.

8.2.3.3 Steering Velocity

The general relationship between the steering joint velocity and the body velocities, taken from the first row of the resultant matrix from (8.29), is

$$\dot{\phi}_i = -\frac{\sin(\phi_i)\dot{x}}{b} + \frac{\cos(\phi_i)\dot{y}}{b} + \frac{h_i \cos(\phi_i - \beta_i)\dot{\theta}}{b} - \dot{\theta}. \quad (8.47)$$

The required steering speed varies sinusoidally depending on the steering position. Naturally, steer speed requirement is highest when steering angle is perpendicular to desired direction and zero when in line with direction. In the former case, the desired velocity must be provided entirely by the steering speed, in the latter, entirely by the drive speed.

For instance, for a desired x -velocity of 1.6 m/s, with no y or θ velocity, the steer speed is

$$\dot{\phi}_i = -\frac{1.6 \sin(\phi_i)}{b} \quad (8.48)$$

The relationship to y -velocity is the same but offset 90° . Steer speed is inversely proportional to caster offset distance, approaching infinity at zero offset. Equation (8.48) is shown graphically in Figure 8.6.

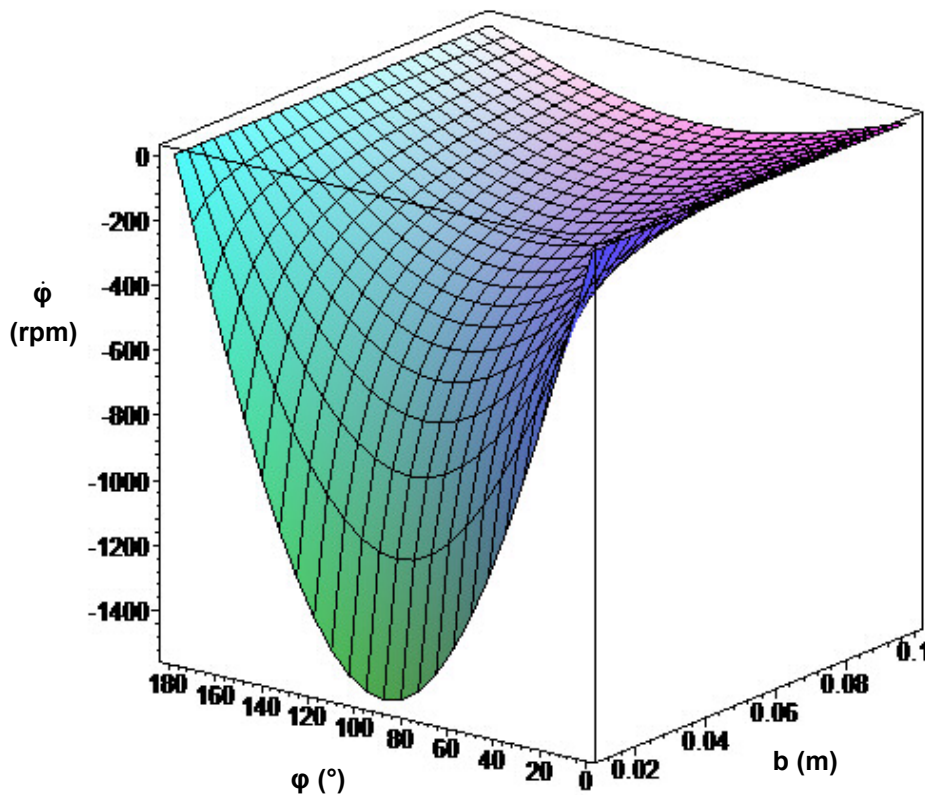


Figure 8.6: Required steering axis rotation speed to achieve x -velocity of 1.6 m/s for different steering angles (ϕ) and casters offsets (b).

For pure rotation with no linear velocity, the steering speed reduces to

$$\dot{\phi}_i = \frac{h_i \cos(\phi_i - \beta_i) \dot{\theta}}{b} - \dot{\theta} \quad (8.49)$$

The steering will be active until the wheel is aligned perpendicular to a radial line from the centre, at which point the steering angle becomes

$$\phi_{\text{angularonly}} = \arccos\left(\frac{b}{h}\right) - \beta. \quad (8.50)$$

This when substituted into (8.49) makes the steering speed zero. Alternately, the steering speed is largest when the caster is lined up with the leg—that is when the steering angle ϕ is equal to the leg angle β —where it becomes

$$\dot{\phi}_i = \frac{h_i \dot{\theta}}{b} - \dot{\theta} = \dot{\theta} \left(\frac{h_i}{b} - 1 \right). \quad (8.51)$$

Since in our consideration the wheelbase will always be larger than the caster offset, $h/b > 1$, the maximum steering speed due to angular velocity only will always be larger than and in the same direction as the angular velocity, increasing with a larger wheelbase and decreasing with increased caster length. The effect of caster length is shown in Figure 8.7 for different steering angle positions.

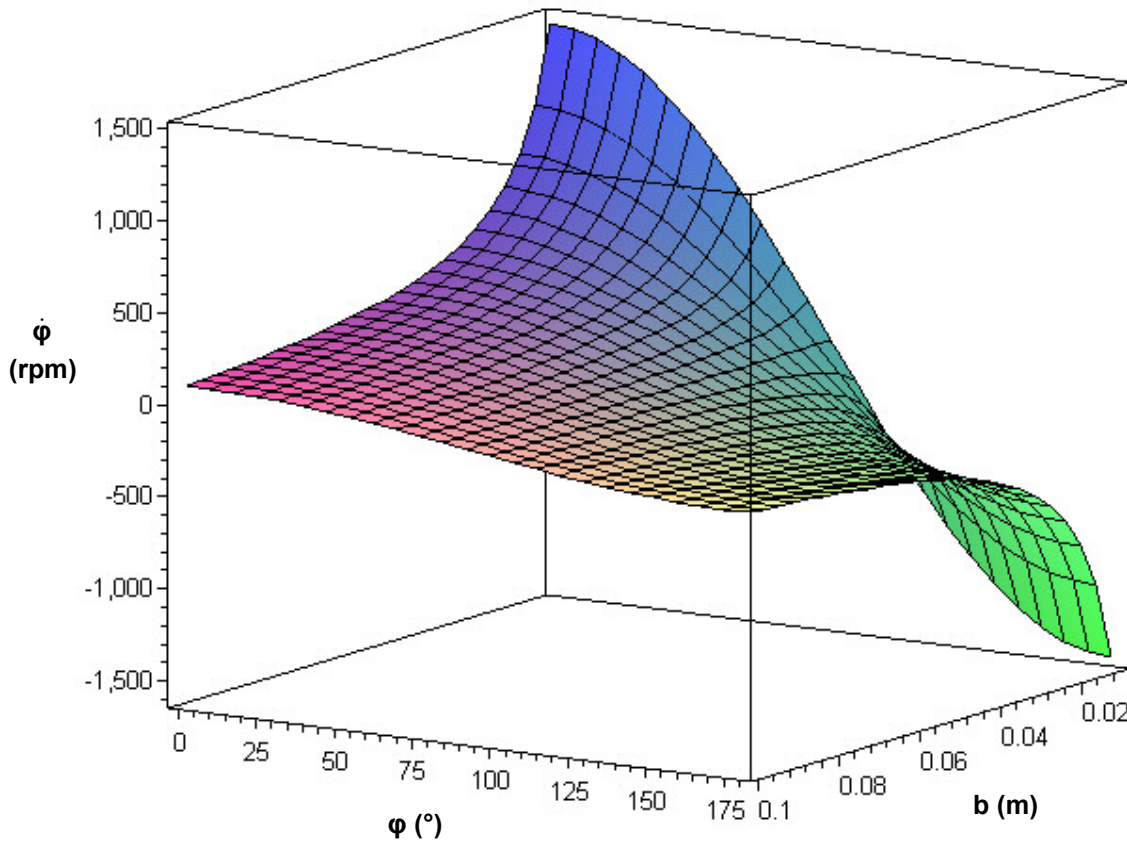


Figure 8.7: Steering speed for angular velocity only at $h = 0.308$, $\dot{\theta} = 1.6/0.308$, for different caster lengths, b , and at different steering positions, ϕ .

If linear and angular velocities are desired simultaneously, the steering speed can be higher or lower than either alone depending on the direction, leg angle or steering angle. In order to maintain the limits imposed by the maximum linear velocity, the steering speed becomes

$$\dot{\phi}_i = -\frac{\alpha_a v_{\max} \sin(\phi_i - \lambda)}{b} + \frac{\alpha_b v_{\max} \cos(\phi_i - \beta_i)}{b} - \frac{\alpha_b v_{\max}}{h} \quad (8.52)$$

by substituting (8.35), (8.36) and (8.43) into (8.47), where α_a and α_b represent the fraction of the maximum velocity allowance that is dedicated to linear and angular velocity respectively; they can add up to no more than one. The worst-case configuration is when the steering angle is perpendicular to the velocity angle ($\phi \perp \lambda$), and opposite to the leg angle ($\phi - \beta = \pi$), which reduces (8.52) to

$$\dot{\phi}_i = -\frac{\alpha_a v_{\max}}{b} - \frac{\alpha_b v_{\max}}{b} - \frac{\alpha_b v_{\max}}{h} \quad (8.53)$$

Thus the absolute worst-case scenario occurs with only angular velocity, $\alpha_b=1$, $\alpha_a=0$, which reduces the equation to

$$\dot{\phi}_i = -v_{\max} \left(\frac{1}{b} + \frac{1}{h} \right) \quad (8.54)$$

The steering speed will be highest with a small caster and small wheelbase, as seen in Figure 8.8. Since $b < h$, the caster offset has a bigger effect than the steering speed. For a wheel base of 0.308 m and a caster of 0.02 m, the steering speed is 85 rad/s (or 815 rpm) for the maximum linear velocity restriction of 1.6 m/s. For a wheelbase of 0.578 m, this decreases to 52 rad/s.

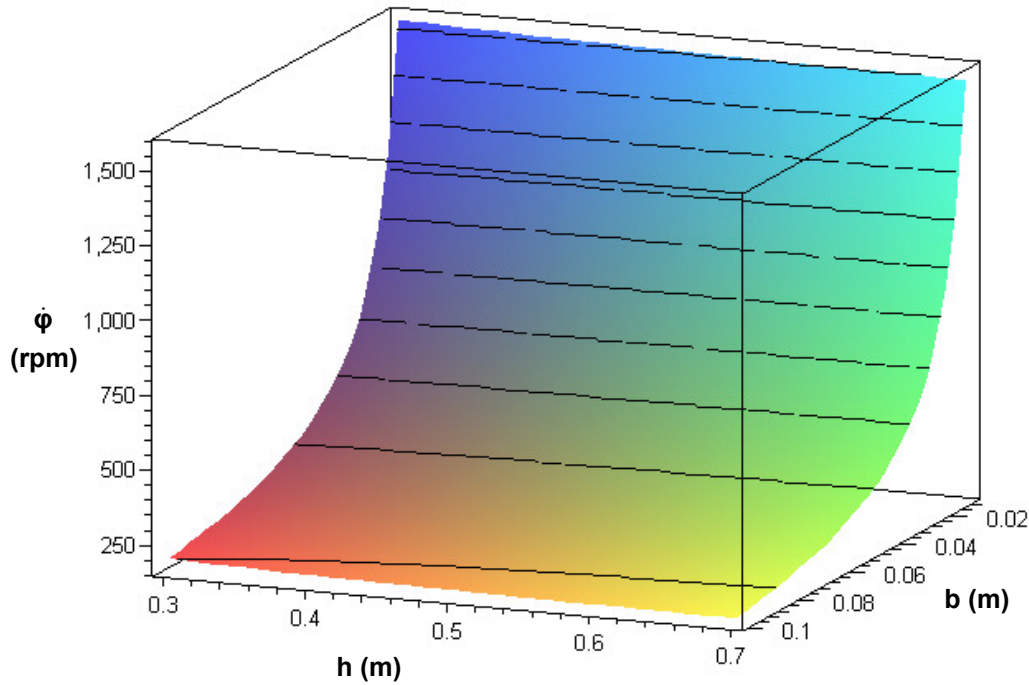


Figure 8.8: Maximum steering velocity as defined by the maximum linear velocity of 1.6 m/s in relation to the caster length b and the effective leg extension h .

8.3 Dynamics

The dynamics of a single powered-caster ‘manipulator’ in the manipulator base frame can be expressed using Lagrangian dynamics as follows [108]:

$$\tau_{jnts} = \begin{bmatrix} A & v \end{bmatrix} \begin{bmatrix} \ddot{\phi} \\ \dot{\rho} \\ \ddot{\sigma} \end{bmatrix} + \begin{bmatrix} \dot{\phi} \\ \dot{\rho} \\ \dot{\sigma} \end{bmatrix} \quad (8.55)$$

Where τ_{jnts} is the joint torque vector consisting of torques for the steer joint between frame {0} and {1}, the roll joint between {1} and {2}, and the twist joint between {2} and the platform base frame as indicated in Figure 8.2. A is the inertia matrix and v is the vector of centripetal and coriolis terms. Gravity is ignored (the manipulator is assumed to operate on a level surface). The inertia matrix is found by using the mass and inertia (expressed in frame {0}) together with the Jacobian for each link, which is determined using the centre of mass for each link:

$$A = J1_v^T \cdot m_{caster} \cdot J1_v + J1_w^T \cdot I_{caster_O} \cdot J1_w + J2_v^T \cdot m_{caster} \cdot J2_v + J2_w^T \cdot I_{caster_O} \cdot J2_w + J3_v^T \cdot m_{leg-base} \cdot J3_v + J3_w^T \cdot I_{leg-base_O} \cdot J3_w \quad (8.56)$$

The wheel inertia is defined as

$$I_{wheel} = \begin{bmatrix} I_{wheel_{xx}} & 0 & 0 \\ 0 & I_{wheel_{yy}} & 0 \\ 0 & 0 & I_{wheel_{zz}} \end{bmatrix} \quad (8.57)$$

and expressed in frame {0},

$$I_{wheel_O} = R_0^1 \cdot I_{wheel} \cdot (R_0^1)^T = \begin{bmatrix} \cos^2(\sigma)I_{wheel_{xx}} + I_{wheel_{zz}} - \cos^2(\sigma)I_{wheel_{zz}} & \cos(\sigma)\sin(\sigma)(-I_{wheel_{zz}} + I_{wheel_{xx}}) & 0 \\ \cos(\sigma)\sin(\sigma)(-I_{wheel_{zz}} + I_{wheel_{xx}}) & \cos^2(\sigma)I_{wheel_{xx}} + I_{wheel_{zz}} - \cos^2(\sigma)I_{wheel_{zz}} & 0 \\ 0 & 0 & I_{wheel_{yy}} \end{bmatrix} \quad (8.58)$$

The caster inertia is defined as

$$I_{caster} = \begin{bmatrix} I_{caster_{xx}} & 0 & 0 \\ 0 & I_{caster_{yy}} & 0 \\ 0 & 0 & I_{caster_{zz}} \end{bmatrix} \quad (8.59)$$

and expressed in frame {0},

$$I_{caster_O} = R_0^2 \cdot I_{caster} \cdot (R_0^2)^T = \begin{bmatrix} \cos^2(\sigma)I_{caster_{xx}} + I_{caster_{yy}} - \cos^2(\sigma)I_{caster_{yy}} & \cos(\sigma)\sin(\sigma)(-I_{caster_{yy}} + I_{caster_{xx}}) & 0 \\ \cos(\sigma)\sin(\sigma)(-I_{caster_{yy}} + I_{caster_{xx}}) & \cos^2(\sigma)I_{caster_{yy}} + I_{caster_{xx}} - \cos^2(\sigma)I_{caster_{xx}} & 0 \\ 0 & 0 & I_{caster_{zz}} \end{bmatrix} \quad (8.60)$$

The leg inertia is defined as

$$I_{leg-base} = \begin{bmatrix} I_{leg_{xx}} & 0 & 0 \\ 0 & I_{leg_{yy}} & 0 \\ 0 & 0 & I_{leg_{zz}} \end{bmatrix} \quad (8.61)$$

$$I_{leg-base_O} = R_0^3 \cdot I_{leg} \cdot (R_0^3)^T \quad (8.62)$$

which can be expressed in the same fashion as (8.60).

Thus, from (8.56), and substituting (8.13)-(8.18) as well as (8.60) and (8.62), the inertia matrix becomes

$$A = \begin{bmatrix} I_{wheel_{yy}} + I_{caster_{zz}} - 2m_{leg}hb \sin(\phi - \beta) & & \\ + m_{leg}b^2 + m_{leg}h^2 + I_{leg_{zz}} & -m_{leg}rh \sin(\phi - \beta) & -m_{leg}h^2 + m_{leg}hb \sin(\phi - \beta) - I_{leg_{zz}} \\ -m_{leg}rh \sin(\phi - \beta) & m_{caster}r^2 + m_{leg}r^2 & m_{leg}rh \sin(\phi - \beta) \\ -m_{leg}h^2 + m_{leg}hb \sin(\phi - \beta) - I_{leg_{zz}} & m_{leg}rh \sin(\phi - \beta) & m_{leg}h^2 + I_{leg_{zz}} \end{bmatrix}$$

The centripetal and coriolis vector is found according to the following formula [108]:

$$v_i = \sum_{j=1}^3 \sum_{k=1}^3 \left(\frac{\partial A_{jk}}{\partial q_k} - \frac{1}{2} \frac{\partial A_{jk}}{\partial q_i} \right) \dot{q}_j \dot{q}_k \quad (8.63)$$

$$v = \begin{bmatrix} v_1 \\ v_2 \\ v_3 \end{bmatrix} \quad (8.64)$$

where i, j and k denote the joints 1 through 3. Performing the appropriate operations in (8.63), the centripetal and coriolis vector for the leg ‘manipulator’ becomes

$$v = \begin{bmatrix} m_{leg} \left(-2rh\dot{\sigma}\dot{\rho} \cos(\phi - \beta) + 2\dot{\sigma}\dot{\phi}hb \sin(\phi - \beta) + 2br\dot{\sigma}\dot{\rho} - r^2\dot{\phi}\dot{\rho}h \sin(\phi) - \dot{\phi}^2hb \sin(\phi - \beta) \right) \\ m_{leg} \left(-\dot{\sigma}^2h \cos(\phi - \beta) - \dot{\phi}^2h \cos(\phi - \beta) + \dot{\sigma}^2b + 2\dot{\sigma}\dot{\phi}h \cos(\phi - \beta) \right) \\ \dot{\sigma}m_{leg}h \left(-\dot{\sigma}b \sin(\phi - \beta) + 2r\dot{\rho} \cos(\phi - \beta) \right) \end{bmatrix}. \quad (8.65)$$

To express the dynamics in the base frame by the method of operational space dynamics [16], the inertia matrix A and vector v can be converted to operational space, where they are denoted by Λ and μ respectively,

$$\Lambda = J^{-T} \cdot A \cdot J^{-1} \quad (8.66)$$

$$\mu = J^{-T} \left(A \cdot J^{-1} \begin{bmatrix} \dot{x}_b \\ \dot{y}_b \\ \dot{\theta}_b \end{bmatrix} + v \right) \quad (8.67)$$

where $x_b, y_b,$ and θ_b are the position of the base in the local robot frame X_L-Y_L and their time derivatives are indicated using dot notation. The force/torque vector at the end-effector (the platform centre) is thus

$$F = \Lambda \dot{X}_{body} + \mu. \quad (8.68)$$

In order to determine the dynamics of the entire robot, the force vectors, operational space inertia matrices and centripetal and coriolis vectors are simply summed,

$$\Lambda = \sum_i^4 \Lambda_i \quad (8.69)$$

$$\mu = \sum_i^4 \mu_i \quad (8.70)$$

$$F = \sum_i^4 F_i. \quad (8.71)$$

The force/torque vector for the entire robot is related to the joint torques by the constraint matrix C ,

$$F = C^T \cdot \Gamma_{jnts} \quad (8.72)$$

where Γ_{jnts} is the vector of drive and steering joint torques for all legs. In order to find the joint torques as a function of the base's local velocity co-ordinates, an inverse relationship for (8.72) must be found. The approach of Holmberg and Khatib, which minimizes the contact forces developed by the wheels [16], is used here. Other approaches, for instance to minimize the actuator power, also exist.

To minimize the contact forces developed by the wheels, the velocities of the wheels' ground contact points, \dot{p} , must first be found using the joint velocities, which can be found from sensors and the block-diagonal invertible matrix C_q :

$$\dot{q} = C_q \dot{p} \quad (8.73)$$

where

$$C_{q_i} = \begin{bmatrix} \frac{-\sin(\phi_i)}{r} & \frac{\cos(\phi_i)}{r} \\ \frac{b_i \cos(\phi_i)}{r} & \frac{b_i \sin(\phi_i)}{r} \end{bmatrix} \quad (8.74)$$

$$C_q = \begin{bmatrix} C_{q_1} & & \\ & \ddots & \\ & & C_{q_4} \end{bmatrix}. \quad (8.75)$$

If ideal rolling holds true, there is also a relationship between the wheel contact point velocities and the local body velocities,

$$\hat{p} = C_p \dot{X}_{body} \quad (8.76)$$

where the matrix C_p is defined as

$$C_{p_i} = \begin{bmatrix} 1 & 0 & -h \sin(\beta_i) - b \sin(\phi_i) \\ 0 & 1 & h \cos(\beta_i) + b \cos(\phi_i) \end{bmatrix} \quad (8.77)$$

$$C_p = \begin{bmatrix} C_{p_1} \\ \vdots \\ C_{p_4} \end{bmatrix}. \quad (8.78)$$

The inverse of this non-square matrix is found using the Moore-Penrose pseudo-inverse and denoted C_p^+ . In practice, due to slippage, generally the actual contact point velocity is not equal to theory,

$$\dot{p} \neq \hat{\dot{p}}. \quad (8.79)$$

Using the pseudo-inverse to find the local body velocity will minimize the difference between \dot{p} and $\hat{\dot{p}}$, which thus minimizes the perceived slip,

$$\dot{X}_{body} = C_p^+ \dot{p}. \quad (8.80)$$

Combining (80) and (73), a relationship between the joint velocities and the local body velocities is found:

$$\dot{X}_{body} = C_p^+ C_q^{-1} \dot{q} \quad (8.81)$$

This can also be used to relate the operational space forces to the joint space torques,

$$\Gamma_{jnts} = (C_p^+ C_q^{-1})^{-T} \cdot F, \quad (8.82)$$

which minimizes the wheel contact forces by least-squares. Spreading the force as evenly as possible between all the wheels provides the best possible traction. Substituting (8.68) into the above, we can find the joint torques necessary to accelerate the platform at a given acceleration level:

$$\Gamma_{jnts} = (C_p^+ C_q^{-1})^{-T} \cdot (\Lambda \ddot{X}_{body} + \mu) \quad (8.83)$$

8.4 Control

To investigate the dynamic performance of the platform in simulation, a PD-controller was implemented as in [16] to generate a control force, F^* ,

$$F^* = -K_p (X_{body} - X_{body_desired}) - K_v (\dot{X}_{body} - \dot{X}_{body_desired}) + \ddot{X}_{body}. \quad (8.84)$$

where K_p and K_v are the position and velocity gains respectively. $X_{body_desired}$ and its derivatives are the desired position, velocity and acceleration in the body frame X_L - Y_L , which are found from the desired platform trajectory. This can be created from a global frame velocity trajectory by using the rotational matrix in (8.33) to convert the desired velocity from the global frame X_G - Y_G to the local robot frame, differentiating to find the desired local acceleration and integrating to find the desired local position.

The control force is used to generate the desired joint torques, which would be sent to the actuator control systems:

$$\Gamma_{jnts} = (C_p^+ C_q^{-1})^{-T} (\Lambda F^* + \mu) \quad (8.85)$$

Elementary tuning of the PD gains was performed by solving (8.68) from the dynamic model for \ddot{X}_{body} and linearizing

$$\delta\ddot{X}_{body} = A_{lin}\delta\dot{X} + B_{lin}\delta F \quad (8.86)$$

with a nominal set point of a steering angle of $\varphi=90^\circ$ for all wheels, maximum load, a caster length of 0.02 m, and a leg extension of 0.3 m. Although the system is highly non-linear, performance with the controller gains derived from this linearization as detailed below was found to be adequate for investigating the platform dynamics in the simulation. The transfer function for this open loop system was then found from the linearized state space model above,

$$\frac{Y(s)}{R(s)} = \frac{0.0192s^2 + 0.0105s - 2.4705}{s^2(s^2 + 0.545s - 128.4654)} \quad (8.87)$$

which factors to

$$\frac{Y(s)}{R(s)} = \frac{(s - 11.073)(s + 11.62)}{s^2(s - 11.065)(s + 11.64)} \quad (8.88)$$

which is approximately equal to

$$\frac{Y(s)}{R(s)} = \frac{1}{s^2} \quad (8.89)$$

Applying a PD controller, the closed-loop transfer function is

$$\frac{Y(s)}{R(s)} = \frac{K_d s + K_p}{s^2 + K_d s + K_p} \quad (8.90)$$

Thus

$$K_d = 2\xi\omega_n \quad (8.91)$$

and

$$K_p = \omega_n^2 \quad (8.92)$$

which makes

$$K_d = 2\xi\sqrt{K_p} \quad (8.93)$$

For a damping ratio ξ of 1,

$$K_d = 2\sqrt{K_p} \quad (8.94)$$

A high position gain K_p of 10000 is chosen for a fast response and the appropriate velocity gain K_d found using the above equation. The control system is found to be stable with no discernable error in the simulation.

8.5 Simulation

8.5.1 Setup

A 3D-multibody dynamics simulation is implemented in Dymola/Modelica (Appendix B). A simplified model is used in which the upper body is represented by a cylinder and the VFM is replaced by a single fixed link. Model parameters are shown in Table 8.2. Tests are performed at the maximum leg extension, $h = 0.578$ m. The wheels are driven with an ideal torque source; motor and gearbox dynamics are neglected. The tire model used is described in Appendix D; it allows for slip and includes rolling friction (using a coefficient of 0.045) and turning friction (using a coefficient of 0.8).

Table 8.2: Simulation parameters

Component	Geometry	Mass	Inertia
Upper Body as cylinder	Height: 70 cm Radius: 0.13 m	50 kg plus payload	uniform cylinder
Lower Body as cylinder	Height: 55 cm Radius: 0.2 m	59 kg	uniform cylinder
Ground Clearance	0.08 m		
VFM		mass-less link	
Suspension	$k=40000$ N/m, $c=2344$ Ns/m		
Caster Structure as cylinder	Height: 0.15 m Radius: 0.05 m	1 kg	uniform cylinder
Wheels	radius: 0.1 m width: 0.05 m caster: 0.02 m	0.5 kg	torus
TOTAL		115 kg	

8.5.1.1 Sensitivity Study

The integration routine DASSL was used, which is a variable step-size routine capable of handling differential algebraic equations and stiff systems. The integrator error tolerance was varied to investigate simulation sensitivity. The differences between $1e-03$ (default) and $1e-05$ were on the order of 0.01% for joint power peaks, but a 5% difference was observed in tire-ground normal force. At $1e-04$, there was still a difference of about 0.5%. Between $1e-05$ and $1e-07$, differences were below 0.01% for the power and the force. Thus a tolerance of $1e-05$ was chosen.

Simulation data points were recorded every 0.01 s, 0.001 s, 0.0001 s, and 0.00001 s and at discrete events at a tolerance of $1e-5$. Again, the differences observed were minimal and on the order of 0.01% for joint power peaks, so 0.01 s was considered a sufficient sampling time.

8.5.1.2 Test Trajectory

A test trajectory was conceived consisting of a range of motion types at the velocity and acceleration design limits; details can be found in Table 8.3, the path is shown in Figure 8.9, and the velocity and acceleration profiles are shown in Figure 8.10.

Table 8.3: Test trajectory description

Motion Type	Velocity	Acceleration	Start Time	End Time	Figure 8.9 Reference
Stopped			0	1	
Linear acceleration, starting from rest at (0,0) with all casters facing inwards	$\dot{x} = 0$ to 1.6 m/s	$\ddot{x} = 2 \text{ m/s}^2$	1	1.8	
Constant linear velocity	$\dot{x} = 1.6 \text{ m/s}$		1.8	3.0	1
Linear acceleration Caster reversal	$\dot{x} = 1.6$ to -1.6 m/s	$\ddot{x} = -2 \text{ m/s}^2$	3.0 ~4.1	4.6 ~4.4	2
Constant linear velocity	$\dot{x} = -1.6 \text{ m/s}$		4.6	5.8	3
Linear acceleration	$\dot{x} = 0$ to 1.6 m/s	$\ddot{x} = 2 \text{ m/s}^2$	5.8	6.6	
Linear acceleration perpendicular to caster starting position	$\dot{y} = 0$ to 1.6 m/s	$\ddot{y} = 2 \text{ m/s}^2$	6.6	7.4	4
Constant linear velocity	$\dot{y} = 1.6 \text{ m/s}$		7.4	9	5
Curve from y to x direction by maximum acceleration change	$\dot{x} = 0$ to 1.6 m/s $\dot{y} = 1.6$ to 0 m/s	$\ddot{y} = -2 \text{ m/s}^2$ $\ddot{x} = 2 \text{ m/s}^2$	9	9.8	6
Constant linear velocity	$\dot{x} = 1.6 \text{ m/s}$		9.8	10.2	7
Linear acceleration	$\dot{x} = 1.6$ to 0.8 m/s	$\ddot{x} = -2 \text{ m/s}^2$	10.2	10.6	
Constant linear velocity	$\dot{x} = 0.8 \text{ m/s}$		10.6	12	
Angular acceleration with constant linear velocity	$\dot{x} = 0.8 \text{ m/s}$ $\dot{\theta} = 0$ to 13.2 rpm (1.38 rad/s)	$\ddot{\theta} = 33.0 \text{ rpm/s}$ (3.46 rad/s ²)	12	12.4	8
Constant linear velocity with constant angular velocity	$\dot{x} = 0.8 \text{ m/s}$ $\dot{\theta} = 13.2 \text{ rpm}$		12.4	13.0	
Linear acceleration with	$\dot{x} = 0.8$ to 0 m/s	$\ddot{x} = -2 \text{ m/s}^2$	13.0	13.4	

constant angular velocity					
Linear acceleration with constant angular velocity	$\dot{x} = 0$ to -0.57 m/s $\dot{y} = 0$ to -0.57 m/s $\dot{\theta} = 13.2$ rpm	$\ddot{x} = -1.41$ m/s ² $\ddot{y} = -1.41$ m/s	13.4	13.8	9
Constant linear ($v=0.8$ m/s), and angular velocity ($\dot{\theta}=0.8$ m/s)	$\dot{x} = -0.57$ m/s $\dot{y} = -0.57$ m/s $\dot{\theta} = 13.2$ rpm		13.8	20.2	10
Linear acceleration with constant angular velocity	$\dot{x} = -0.57$ to 0 m/s $\dot{y} = -0.57$ to 0 m/s $\dot{\theta} = 13.2$ rpm	$\ddot{x} = 1.41$ m/s ² $\ddot{y} = 1.41$	20.2	20.6	11
Constant angular velocity	$\dot{\theta} = 13.2$ rpm		20.6	22	
Angular acceleration	$\dot{\theta} = 13.2$ to 26.5 rpm (2.77 rad/s)	$\ddot{\theta} = -33.0$ rpm/s (3.46 rad/s ²)	22	22.4	
Constant angular velocity	$\dot{\theta} = 26.5$ rpm		22.4	23	
Angular acceleration	$\dot{\theta} = 26.5$ to 0 rpm	$\ddot{\theta} = 33.0$ rpm/s	23	23.8	
Stopped			23.8	24	

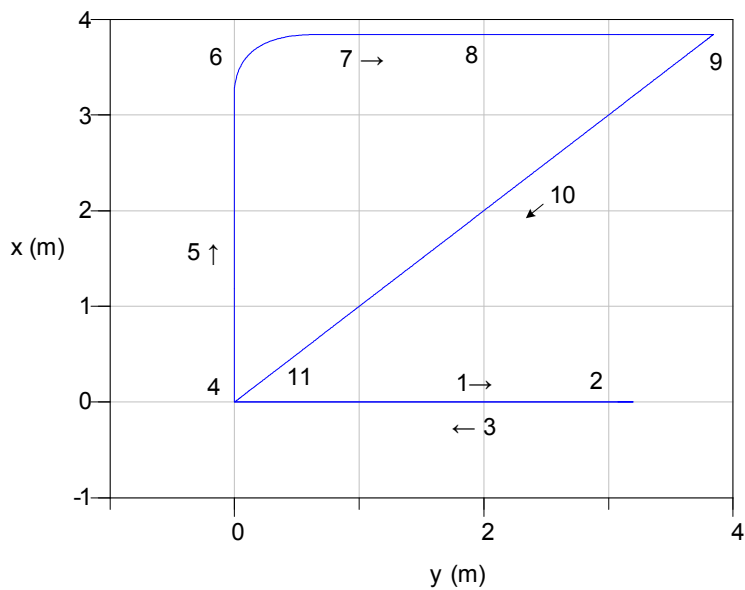


Figure 8.9: x-y path in global co-ordinates with reference numbers to motion described in Table 8.3.

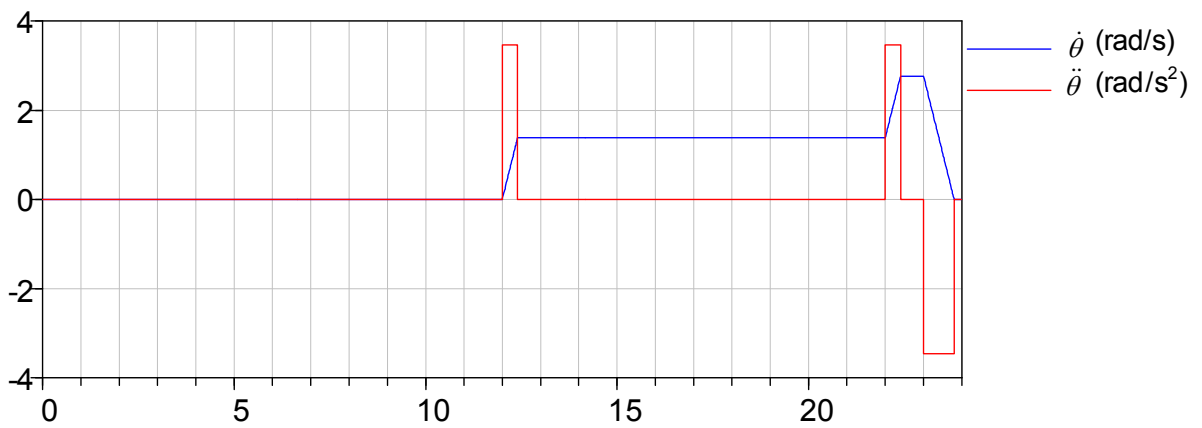
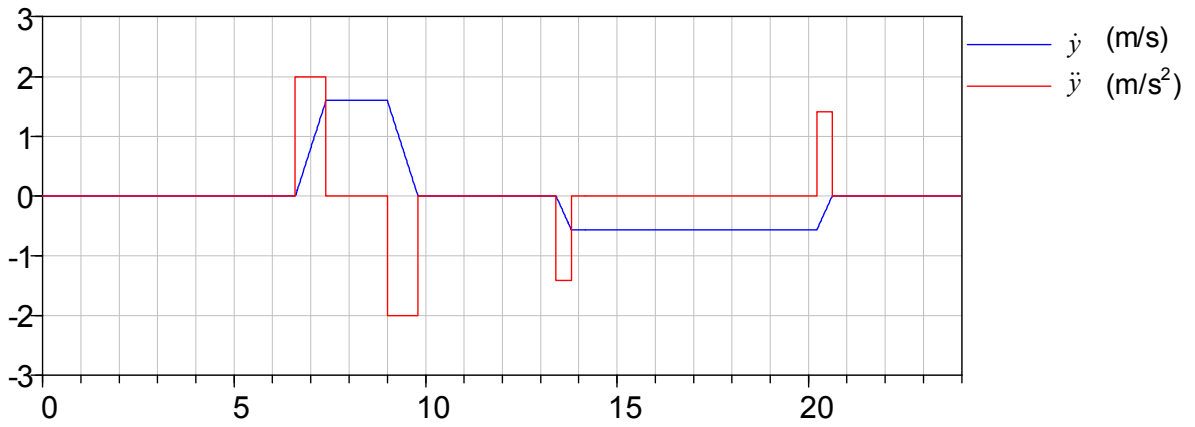
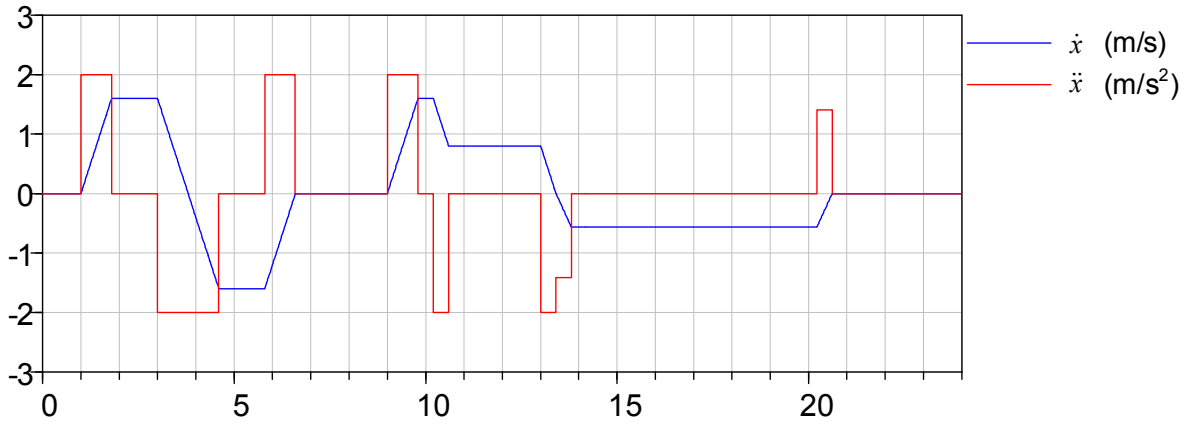


Figure 8.10: x, y, θ velocity and acceleration trajectories (in the global frame).

8.5.2 Results with Different Caster Lengths

The test trajectory was run with seven different caster lengths from 0.5 cm to 4 cm, covering a range of plausible lengths for best performance at a reasonable size. The tests were performed with no payload and at the maximum leg length ($h = 0.578$ m) in order to maximize stability, which reduces traction problems.

The global position error is generally lowest for caster lengths between 2-3 cm (inclusive), although there is no definitive optimum, as some caster lengths lead to larger errors in some places where others do not. It is essentially a measure of how much slip occurred during the trajectory, as the control system itself has no local position error. Caster lengths 0.5 cm and 1.0 cm show significant error after 4.25 s, which is when the casters reverse direction. The other caster lengths do not go significantly off track until combined angular and linear motion start at about 13 s. Figure 8.11 and Figure 8.12 show two situations up close for x-position; y errors are not as severe but show similar trends in relation to caster length. Figure 8.13 shows freeze-frames of the second situation.

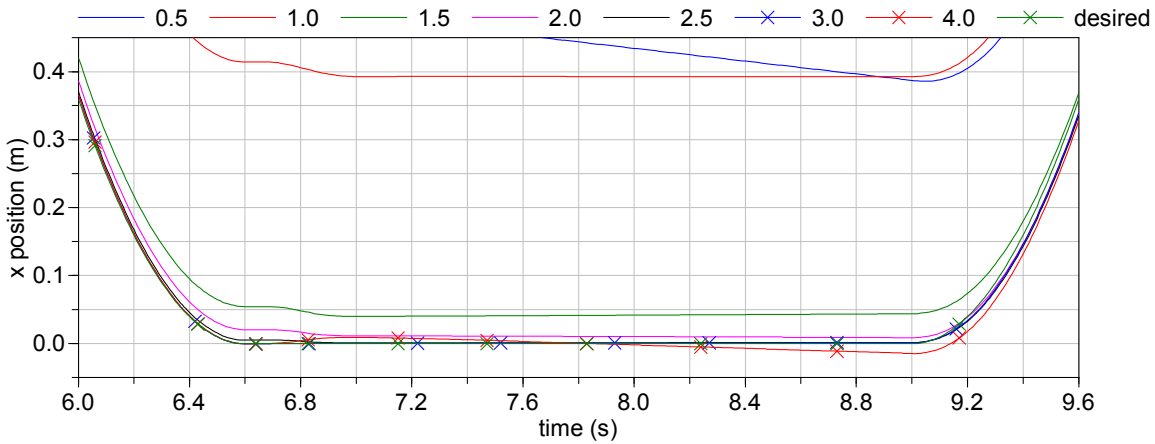


Figure 8.11: Global x-position for different caster lengths (cm) showing the portion of the test trajectory where the base travels along the y-axis.

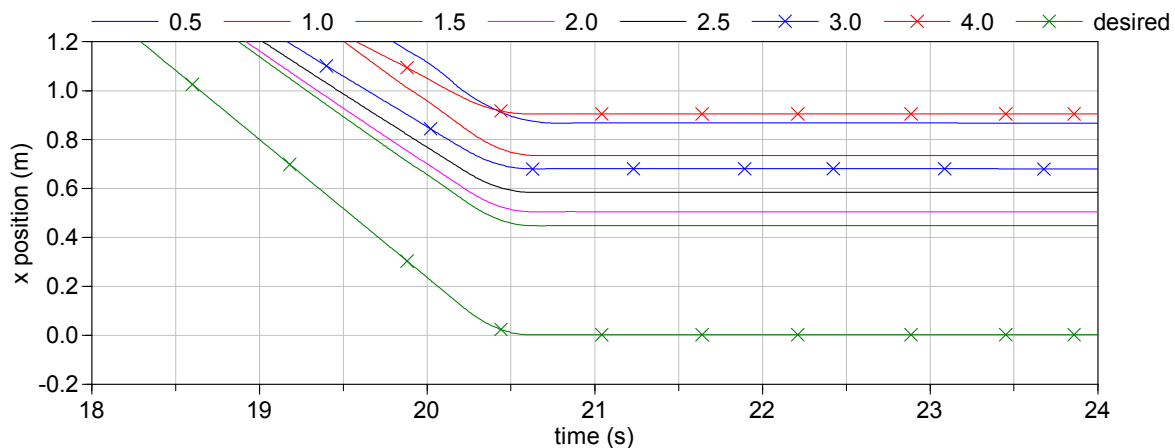


Figure 8.12: Global x-position for different caster lengths (cm), showing the last portion of the test trajectory where the base should return to origin.

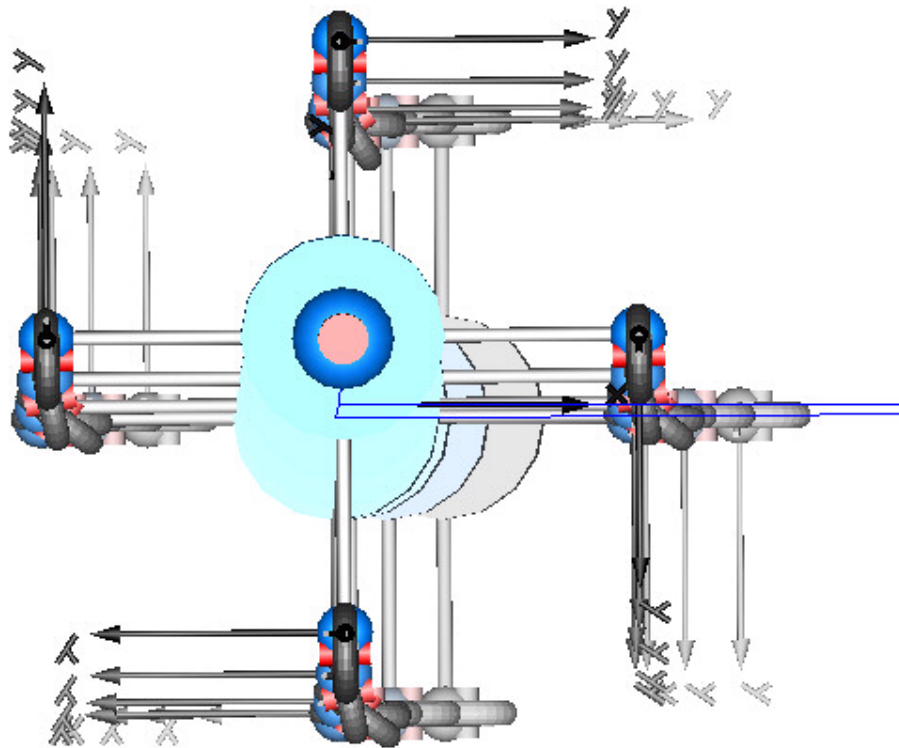


Figure 8.13: Platform decelerating in x-direction, then immediately accelerating in y-direction; final image at 7 s with 8 frames back to about 6.3 s. The path of base is shown in blue, where some deviation is apparent in the return motion (the lower path line) from the starting path that it should return on. Caster length of 0.02 cm.

8.5.2.1 Caster Reversal

If the platform reverses directions, such as at $t = 3.8$ s, the wheels will shortly there-after ‘flip,’ rapidly rotating through 180° so that the caster trail is once again oriented away from the velocity direction. In free casters, this occurs by itself due to disturbance forces and drift in vehicle angle, as anyone using a shopping cart has experienced. In powered casters, the control system reacts to the disturbances and drift in angle to cause very similar behaviour. Interestingly, this makes the timing of reversal unpredictable and dependent on variables such as the caster length, as is apparent in Figure 8.16, which shows the steering angle of Wheel 3 during the reversal. Caster reversal is expected to be one of the worst-case configurations for drive kinetics, as literature suggests this is one of the shortcomings of powered casters [109]. This is born out in simulation, which shows that caster reversal creates the highest power requirements for steering and drive, the highest torques for steering and drive, and the highest joint speed for steering actuation.

Simulations with caster lengths of 0.5 and 1.0 cm show a fair deal of slip during caster reversal, as is evident in Figure 8.14 where the trials with these lengths fall substantially below the desired x-velocity, and Figure 8.15, where there is substantial undesired angular velocity. Lengths from 1.5–

3.0 cm show decreasing amounts of slip in the x-direction, with a caster length of 4.0 cm showing a slight increase in slip over 3.0 cm.

The caster reversal is the period of highest steering joint velocity, which experiences a peak lasting approximately a quarter second that occurs when the steering angle passes through -260° or 10° from perpendicular to the direction of the base velocity (Figure 8.16 and Figure 8.17). Drive joint velocity must switch direction during caster reversal, which is evident in Figure 8.18; trials with caster lengths of 0.5 cm and 1.0 cm have very high drive velocities as a result of wheel slip.

Figure 8.19 and Figure 8.20 show that the steering torque and drive torque is lowest for caster lengths of 2.5 cm and 2.0 cm. It should be noted that due to the unpredictable nature of the caster reversal, each wheel behaves differently at different caster lengths, but the overall trend in torque remains the same.

The drive power during the caster reversal (Figure 8.22) is lowest for lengths of 2.5 cm followed by 3.0 cm and then 2.0 cm, while the steering power (Figure 8.21) is lowest for 2.0 cm, followed by 2.5 cm and then 1.5 cm.

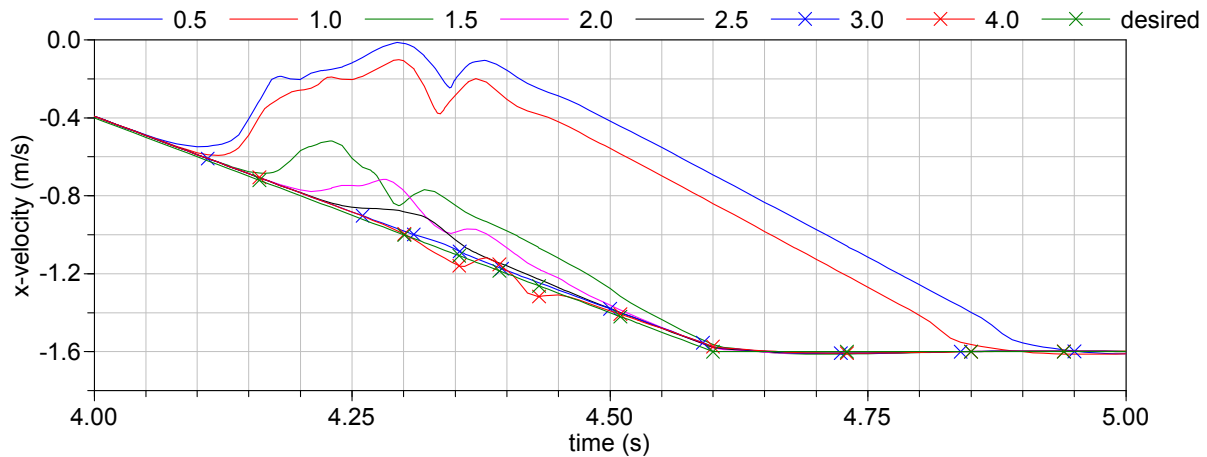


Figure 8.14: Global x-velocity during caster reversal for different caster lengths (cm).

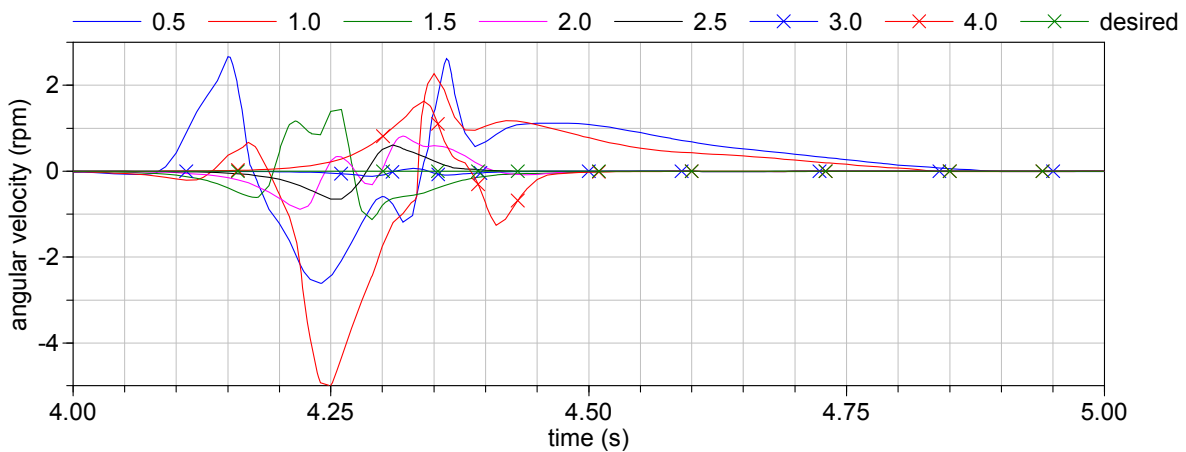


Figure 8.15: Global angular velocity ($\dot{\theta}$) during caster reversal (desired velocity is zero).

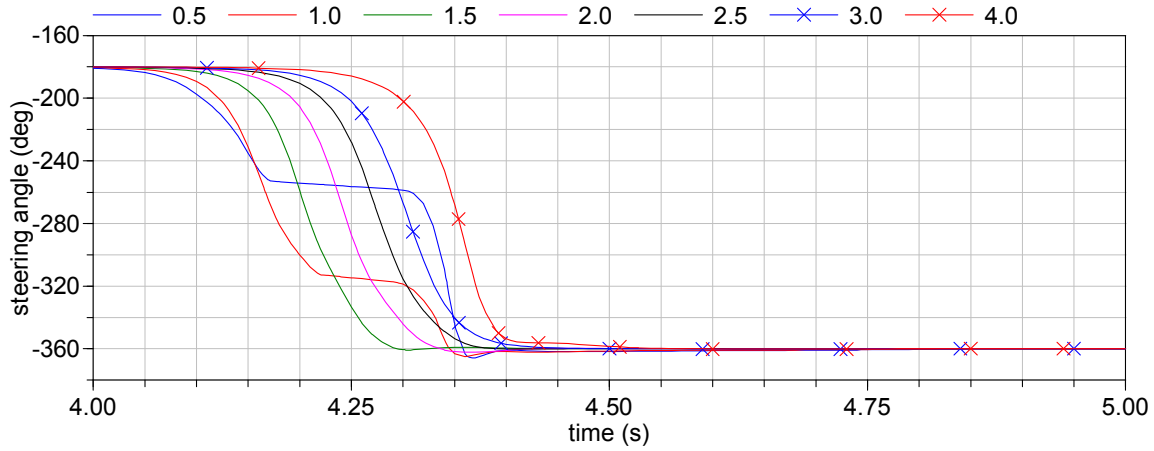


Figure 8.16: Wheel 3 steering angle (ϕ) during caster reversal for different caster lengths (cm).

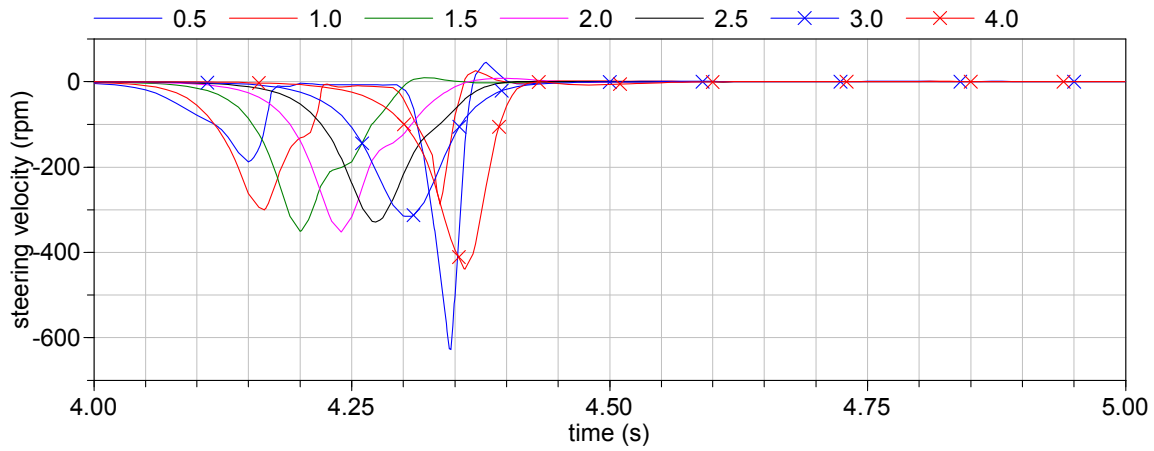


Figure 8.17: Wheel 3 steering velocity ($\dot{\phi}$) during caster reversal, different caster lengths (cm).

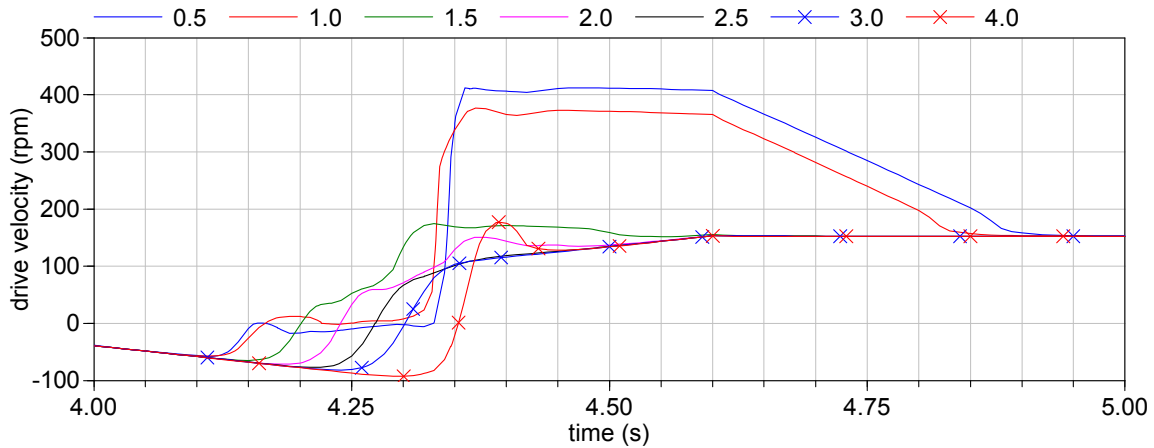


Figure 8.18: Wheel 3 driving velocity ($\dot{\rho}$) during wheel reversal. different caster lengths (cm).

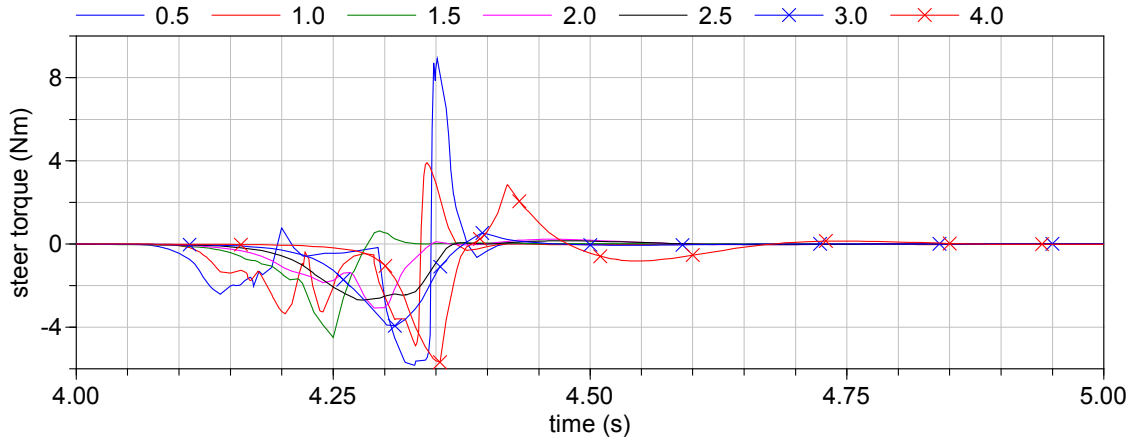


Figure 8.19: Wheel 3 steering torque at caster reversal for different caster lengths (cm).

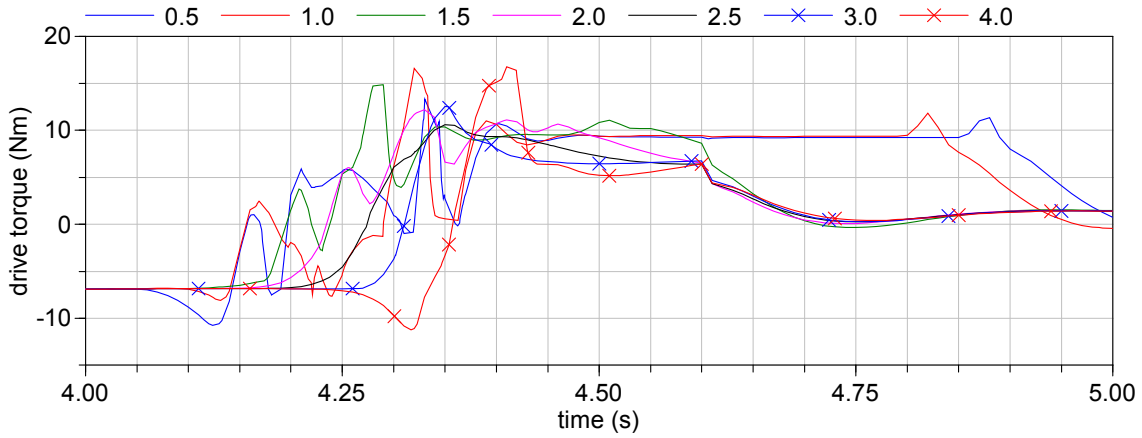


Figure 8.20: Wheel 3 drive torque at caster reversal for different caster lengths (cm).

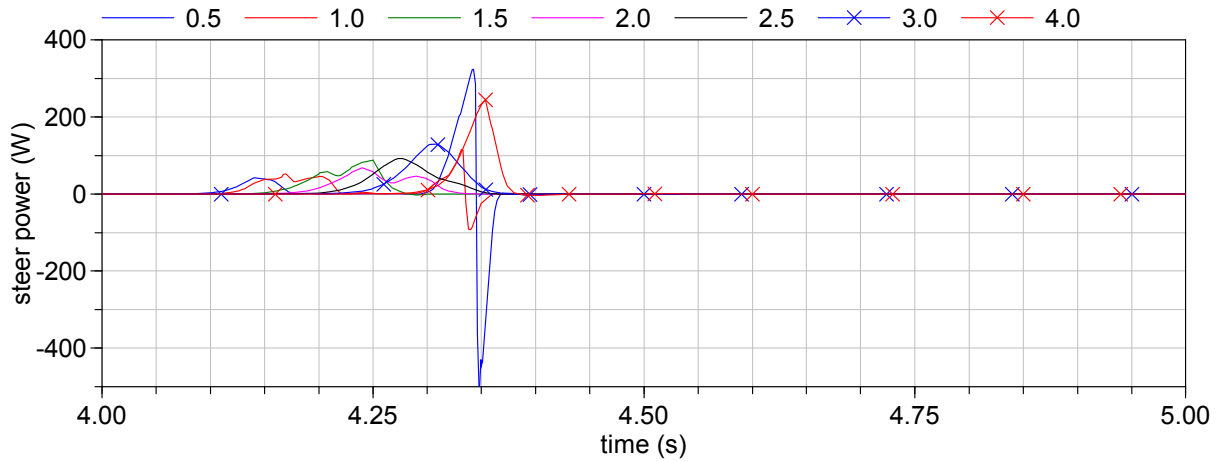


Figure 8.21: Wheel 3 steering joint power during caster reversal, different caster lengths (cm).

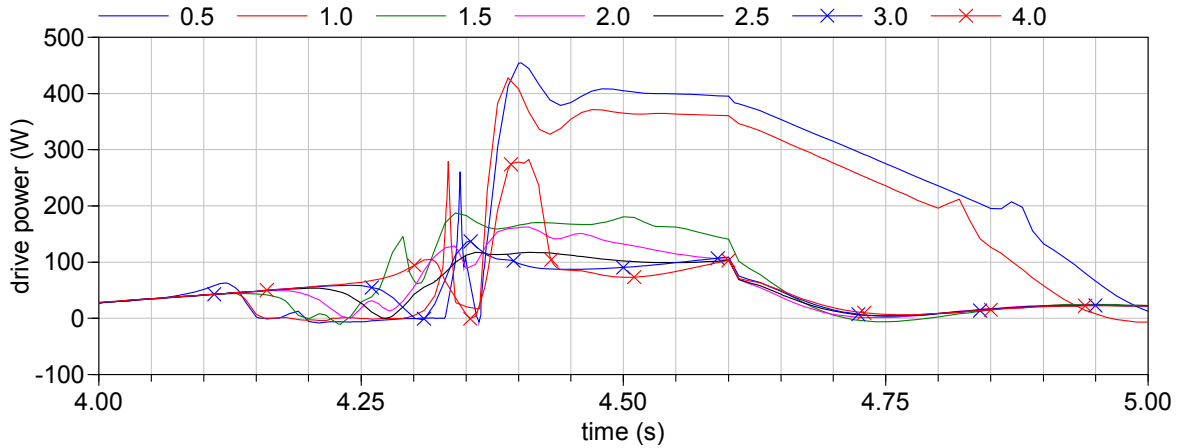


Figure 8.22: Wheel 3 drive joint power during caster reversal for different caster lengths (cm).

8.5.2.2 Curve

During the period from $t = 9$ to 9.8 s, the platform travels a rounded corner at maximum acceleration without changing its orientation, as depicted in Figure 8.24. After a brief period of constant velocity, it then decelerates to half maximum speed between 10.2 to 10.4 s. The following figures show the performance during this period for different caster lengths. Figure 8.23 and Figure 8.25 show some drive and steering velocity drop from desired during the curve, indicating some slip occurring during this maneuver, with the shortest caster length exhibiting more than longer lengths.

Drive power and torque show only a small difference for different caster lengths during this maneuver, which is visible in the close-up of drive power in Figure 8.26; the power decreases from just over 50 W for the shortest caster length to just over 38 W for the longest caster length. Steering torque and power, shown in Figure 8.27 and Figure 8.28, have the opposite pattern, but while there is a significant difference in the fairly strong torque requirements, the power requirements are low due to the low velocity. Torque ranges from -4 Nm at a 4 cm caster length to just over -1 Nm at 0.5 cm caster length, while power ranges from 8.9 to 4.3 W for the same lengths.

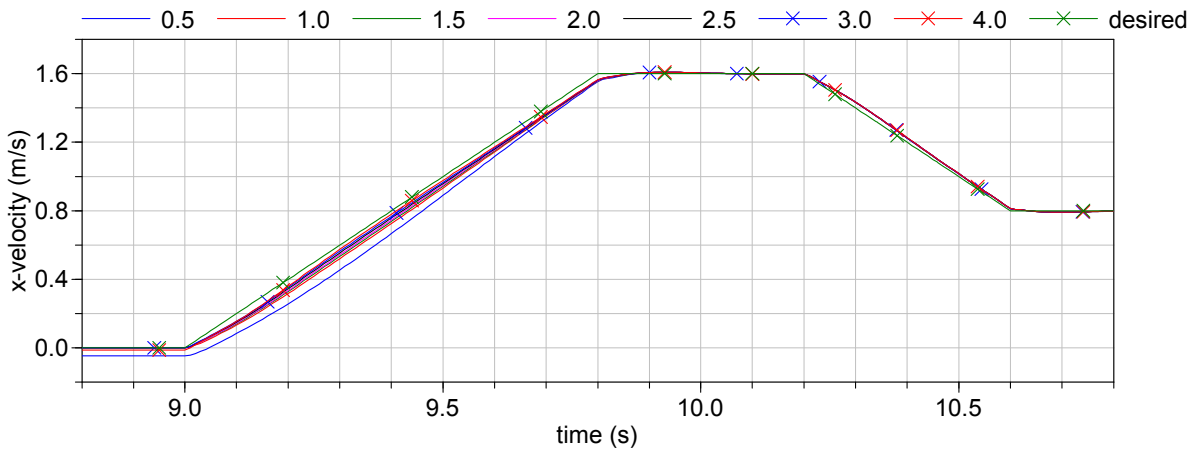


Figure 8.23: Global x velocity during curve for different caster lengths (cm).

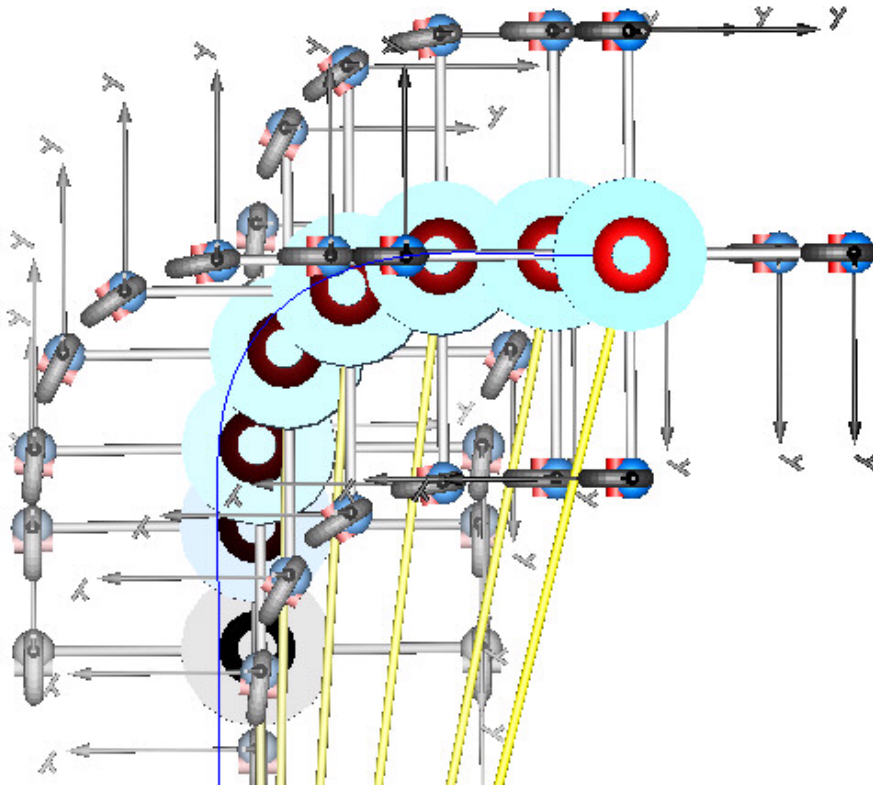


Figure 8.24: Platform motion during curve acceleration. Final image at 10 s with 7 frames back to about 8.7 s. Path of base centre in blue.

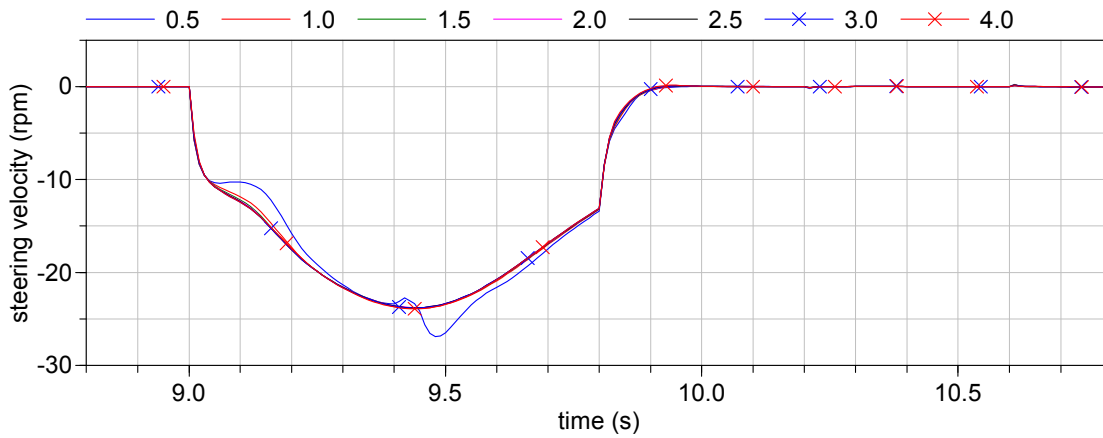


Figure 8.25: Wheel 3 steering velocity during curve for different caster lengths (cm).

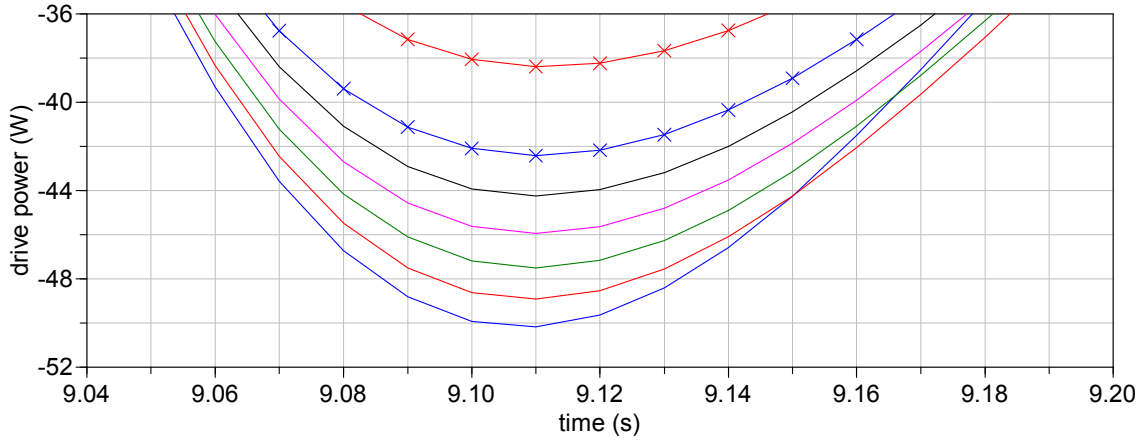


Figure 8.26: Wheel 3 drive power during curve - close-up of negative maximum at 9.11 s.

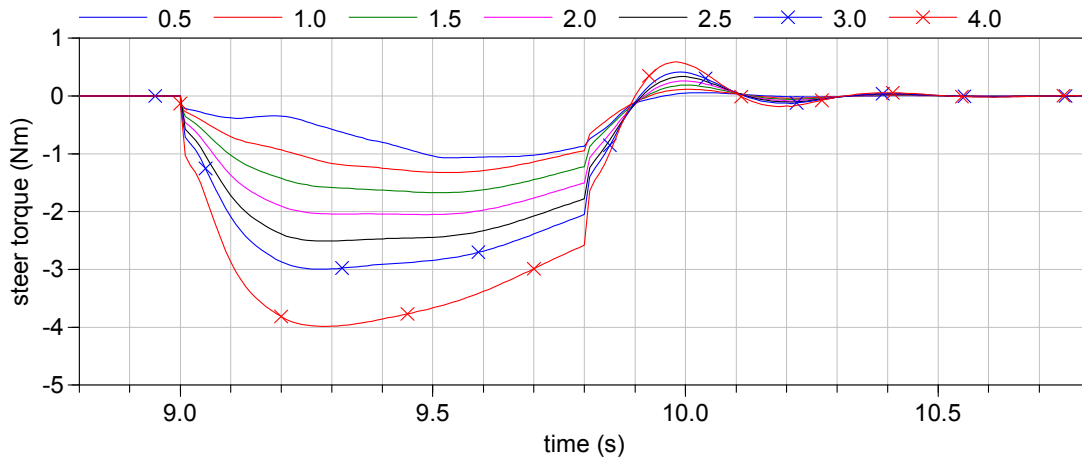


Figure 8.27: Wheel 3 steering torque during curve for different caster lengths (cm).

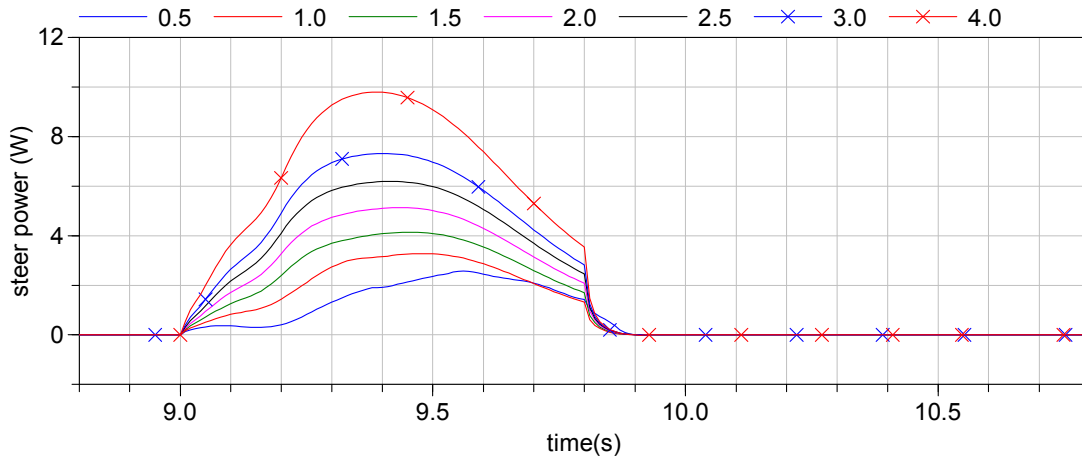


Figure 8.28: Wheel 3 steering joint power during curve for different caster lengths (cm).

8.5.2.3 Simultaneous Angular and Linear Velocity

At 12 s, the platform, travelling at a reduced linear speed of 0.8 m/s, starts to rotate, accelerating at 33.0 rpm/s (the maximum for this leg extension of 0.578 m) up to an angular velocity of 13.2 rpm, the maximum possible for this linear speed as dictated by (11.43). At 13 s, the platform slows its linear speed to a stop before accelerating again towards the origin, all the while continuing to rotate.

The combined linear and angular velocity creates a significant amount of slippage, as evident in the global x-velocity (Figure 8.30), where the longest and the shortest caster lengths are the most affected. The path and motion snapshot is shown in Figure 8.29 for a caster length of 2 cm.

The steering torque peaks at 13.8 s at the end of the linear acceleration and is highest for the longest caster at -2.5 Nm and lowest for the shortest caster, down to -0.6 Nm. The 0.5 cm caster causes large amounts of slippage during the combined motion that is evident in the high and erratic torque and power signals. A second torque peak is apparent at about 14.5 s (Figure 8.31), which is during the period of constant linear and angular velocity when wheel 3 is in a position where its steering actuator must contribute significantly to linear and angular motion. Shortly thereafter the steering velocity peaks (Figure 8.32), which is why there is a power peak here as well; with a magnitude of around 6 W (Figure 8.34) it rivals the peak at 13.8 s that was caused by linear acceleration at constant angular velocity.

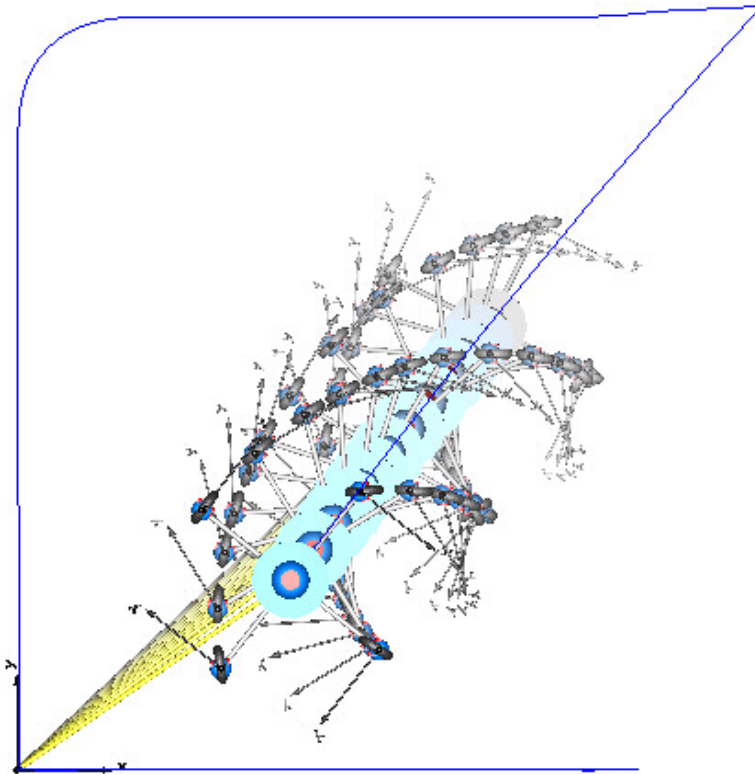


Figure 8.29: Platform during combined linear and angular velocity phase showing path of base and motion history at 0.1 s intervals, caster of 2 cm, $h = 0.578$ m.

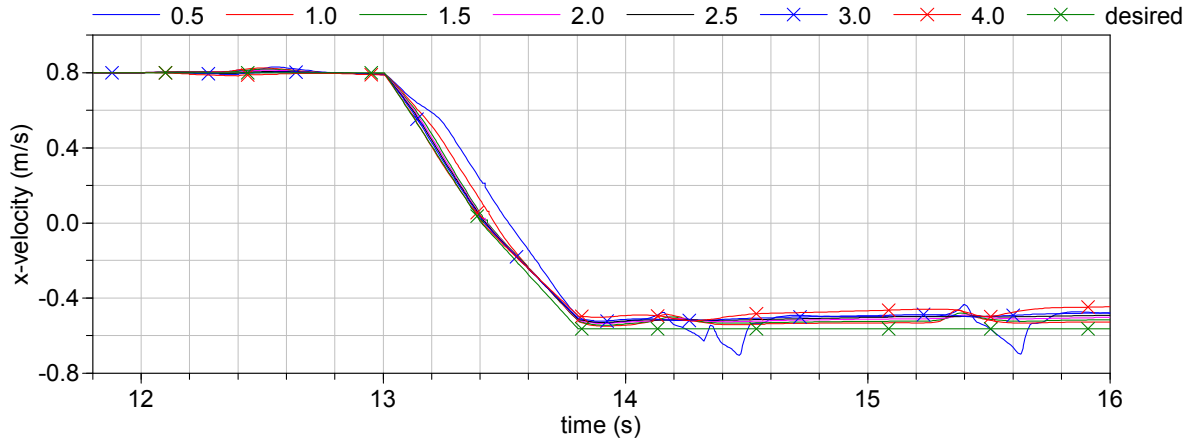


Figure 8.30: Global x velocity during combined linear and angular velocity.

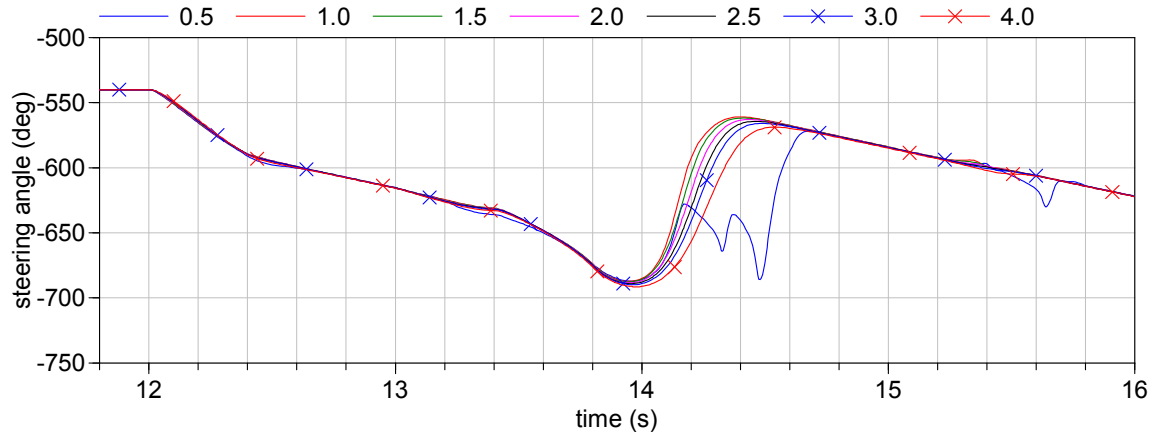


Figure 8.31: Wheel 3 steering angle during combined linear and angular velocity.

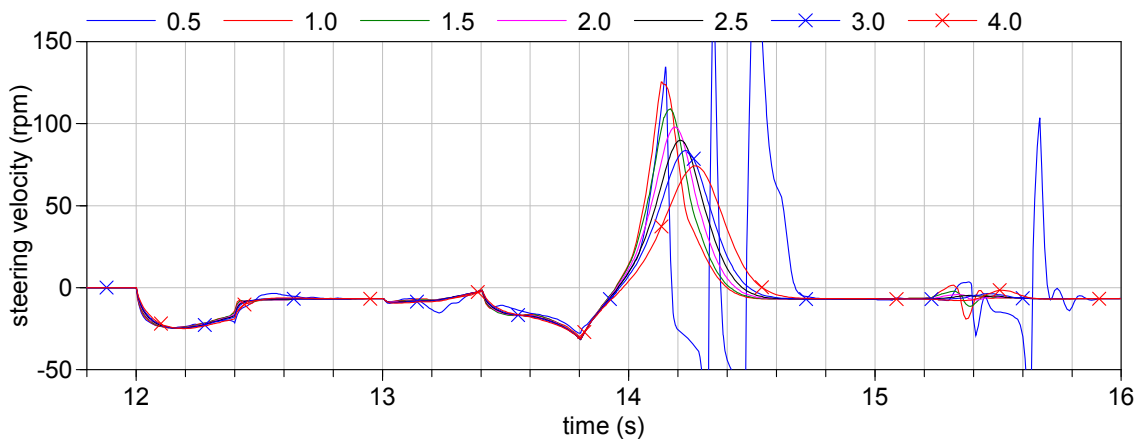


Figure 8.32: Wheel 3 steering velocity during combined linear and angular velocity.

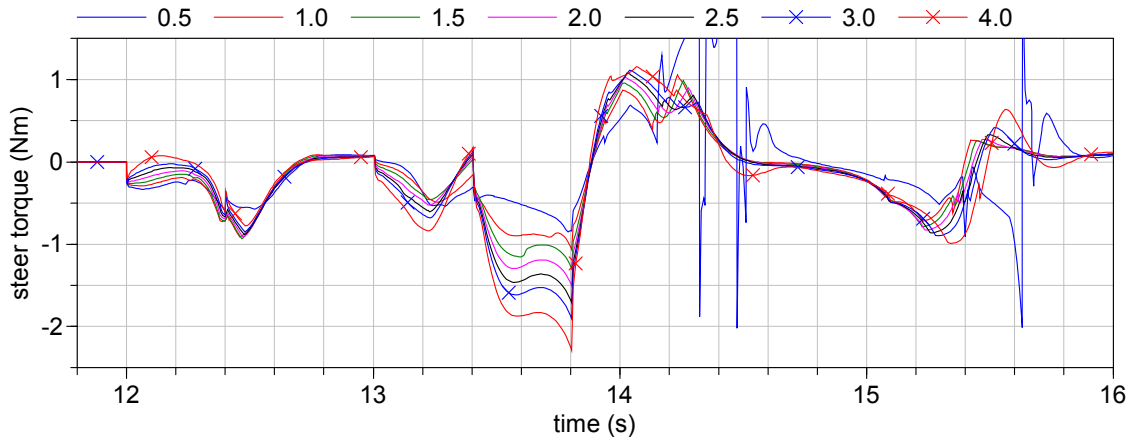


Figure 8.33: Wheel 3 steering joint torque during combined linear and angular velocity.

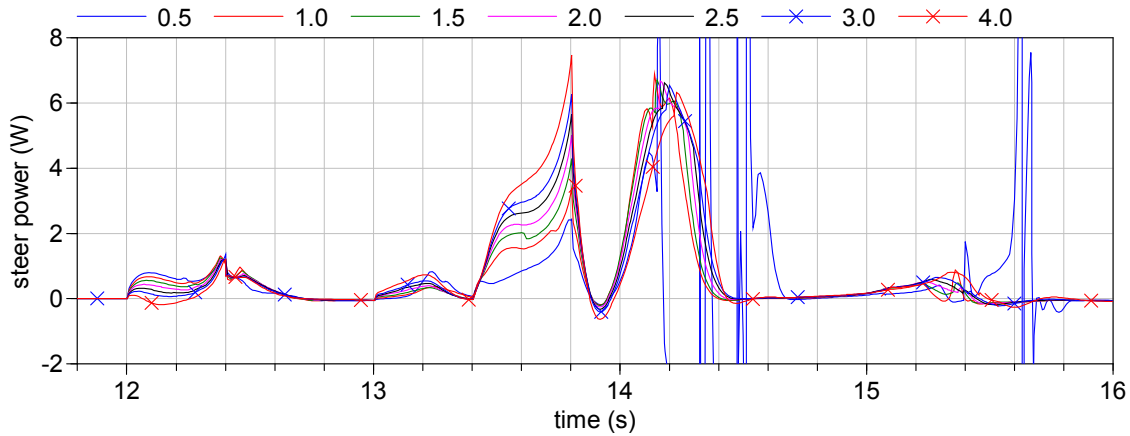


Figure 8.34: Wheel 3 steering joint power during combined linear and angular velocity.

8.5.2.4 Caster Length Selection

The ultimate decision on caster length comes down to choosing a caster as small as possible to conserve space that is not prone to facilitating slip and its associated errors. Based on the simulation results, this narrows down the selection to a length of between 1.5 and 2.0 cm. Although there is a slight velocity and torque advantage to 1.5 cm, the 2.0 cm length has slightly better power and position error performance. 2.0 cm is chosen as the caster length to lean towards reduced slip, since the realism of the model in this regard is unproven and depends on the tire model parameters (see Appendix D). This is the same caster length used by Holmberg and Khatib [16] for similar velocity (1.25 m/s) and acceleration requirements (2.0 m/s^2) as well as similar mass (150 kg), although the tire radius is only 5.5 cm for a caster length to radius ratio of 0.36 instead of 0.1 for the current design. The resulting arrangement of the VFM lower leg joint such that the VFM mechanism does not protrude wider than the wheel envelope while simultaneously trying to place the joint as low as possible as described in 3.2 is shown in Figure 8.35.

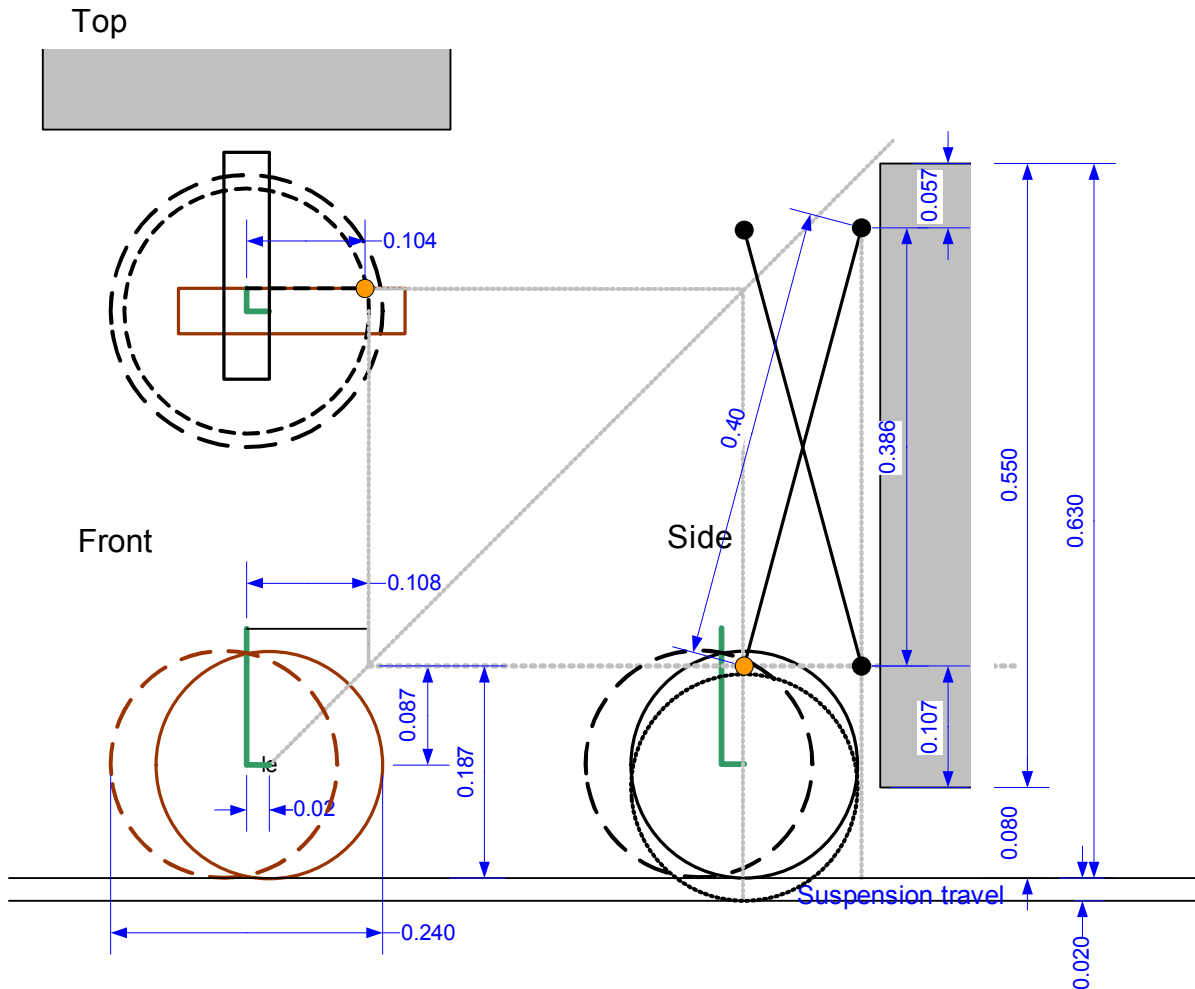


Figure 8.35: Top, front and side view of wheel unit configuration showing vertical and horizontal offset necessary for lower leg joint to clear caster wheel envelope. Caster arm in green with 2 cm caster. Values in (m).

8.5.2.5 Chosen Configuration

The velocity, torque and power for the drive and steering actuators of all the wheels for the chosen caster length with no payload and full leg extension are shown in Figure 8.37 and Figure 8.38.

This shows that forces on all the wheels are similar in magnitude, although there is some variation in timing when the steering angles are not equal, as during combined linear and angular acceleration and velocity. In particular, there is a significant difference during linear acceleration with constant angular velocity between 13.0 – 13.8 s and 20.2 – 20.6 s, where the steering torque for Wheels 1 and 2 peak significantly higher than Wheels 3 and 4. The drive torques also vary, with Wheels 1 and 3 having significantly higher torques than Wheels 2 and 4. This is a result of the position of the wheel and the leg relative to the acceleration direction. The motion at the beginning of the first time period mentioned above is shown graphically in Figure 8.36.

Figure 8.39 compares the velocity, torque and power for the Wheel 3 drive actuator at no payload and at 15 kg payload (the load specified as the maximum for full acceleration). Leg extension is kept at the maximum. As expected, the drive torque and power during periods of acceleration is higher than with no payload, though they do not necessarily increase in a uniform manner; some peaks are 30% higher despite total mass only increasing 13%. Also, the constant velocity drive torque and power are slightly higher due to the increased normal load, which increases the rolling friction. Steering torque (not shown) is very similar at the two different loadings. Maximum values for different motions are summarized in Table 8.4, where the values include simulated rolling and turning friction effects. The absolute maximums all occur at the caster reversal except for the maximum steering torque, which occurs when the platform accelerates perpendicular to the previous direction of travel after $t = 6.6$ s.

Figure 8.40 and Figure 8.41 compare the velocity, torque and power for Wheel 3 drive and steering actuators at maximum ($h = 0.578$ m) and minimum ($h = 0.308$ m) leg extension. Payload is kept constant at 15 kg. For the smaller wheelbase trajectory, the global angular velocity and acceleration are increased to maximums allowed at that wheelbase (Figure 8.42). This changes the pattern of the drive and steering joint velocities as well. The smaller wheelbase causes more significant weight shifts during acceleration, which leads to less traction and consequently more wheel slip (Figure 8.43). In the simulation, this causes the drive velocity during caster reversal to exceed the imposed maximum; in practise, the motor would not be capable of this speed and/or a more sophisticated controller would be capable of limiting slip. The true ground friction behaviour may also be different than the simulated behaviour. A similar slip-induced increased drive velocity is seen during the curve acceleration. Effects are also seen in the power and torque, which are more erratic. Overall, the drive torque is lower with the smaller wheelbase, except for the steady-state linear acceleration and velocity portion of the simulation, in which the torque is of course the same for both wheelbase sizes since linear motion is not affected by the wheelbase size. Drive power during caster reversal is over twice as high with the shorter wheelbase, but this is due to the large slip; the wheels that do not slip have a lower power requirement. The maximums in Table 8.4 are not based on wheels that are slipping; values that are distorted are marked with an asterisk. The required steering speed increases during perpendicular acceleration and constant combined angular and linear velocity, as does torque and power. In other situations, it is slightly lower.

Table 8.4: Maximum velocities, torques and power for drive and steering joints, absolute values at different payload and leg extensions, caster length of 2 cm.

Condition	Leg extension	Payload	Drive Speed (rpm)	Drive Torque (Nm)	Drive Power (W)	Steer Speed (rpm)	Steer Torque (Nm)	Steer Power (W)
Accelerate out of initial position with casters inward	0.578 m	0 kg	153	11.0	108	359	2.86	75.1
		15 kg	153	12.6	121	358	3.23	88.4
	0.308 m	15 kg	287*	10.4	263*	282	3.94	103
Caster reversal (t = 4.2)	0.578 m	0 kg	153	12.9	162	379	3.63	121
		15 kg	153	15.5	186	401	4.46	143
	0.308 m	15 kg	408*	11.0	475*	384	4.03	103
Linear acceleration - peak	0.578 m	0 kg		5.53	72.6			
		15 kg		6.38	81.4			
	0.308 m	15 kg		6.77	*			
Linear acceleration - steady-state	0.578 m	0 kg		4.45				
		15 kg		5.01				
Change of direction (t=3.8 s)	0.578 m	0 kg		7.0				
		15 kg		7.9				
Constant linear or angular velocity	0.578 m	0 kg	153	1.27	20.3	0	0	0
		15 kg	153	1.43	22.9	0	0	0
	0.308 m	15 kg	153	1.43	22.9	0	0	0
Constant linear and angular velocity	0.578 m	0 kg	153	2.99	39.2	133	1.18	8.96
		15 kg	153	3.48	45.7	134	1.39	10.8
	0.308 m	15 kg	153	3.69	51.1	156	1.64	
Acceleration perpendicular to previous direction (t = 6.6...7.4 s)	0.578 m	0 kg		12.1	110	75	3.86	29.0
		15 kg		16.0	125	77	4.62	34.0
	0.308 m	15 kg		15.3	136	116	5.42	14.1
Curve at maximum acceleration (t = 9...9.8 s)	0.578 m	0 kg		6.98	111	24	1.93	4.76
		15 kg		7.85	125	24	2.31	5.59
	0.308 m	15 kg		7.69	160*	~50*	2.28	~12*

Maximum with extended legs	0 kg	153	12.9	162	351	3.86	121
	15 kg	153	15.5	186	401	4.62	143
% Increase, 0 kg to 15 kg		20%	15%	14%	20%	18%	20%
Maximum with retracted legs		*	*	*	384	5.42	103
% Increase					-4%	17%	-29%
ABSOLUTE MAXIMUM		153	15.5	186	401	5.42	143

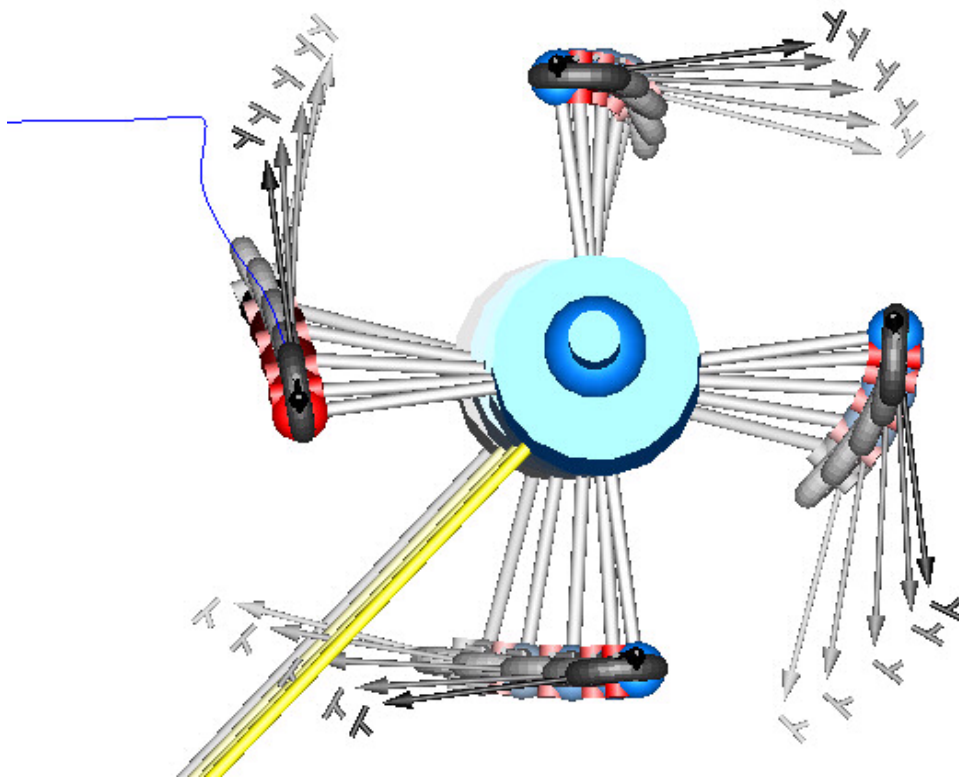


Figure 8.36: Platform during linear deceleration with constant angular velocity at 13.4 s; freeze frames at ~ 0.1 intervals back to 13.0 s. Path of wheel 2 steering axis in blue. 2 cm caster length, $h = 0.578$ m.

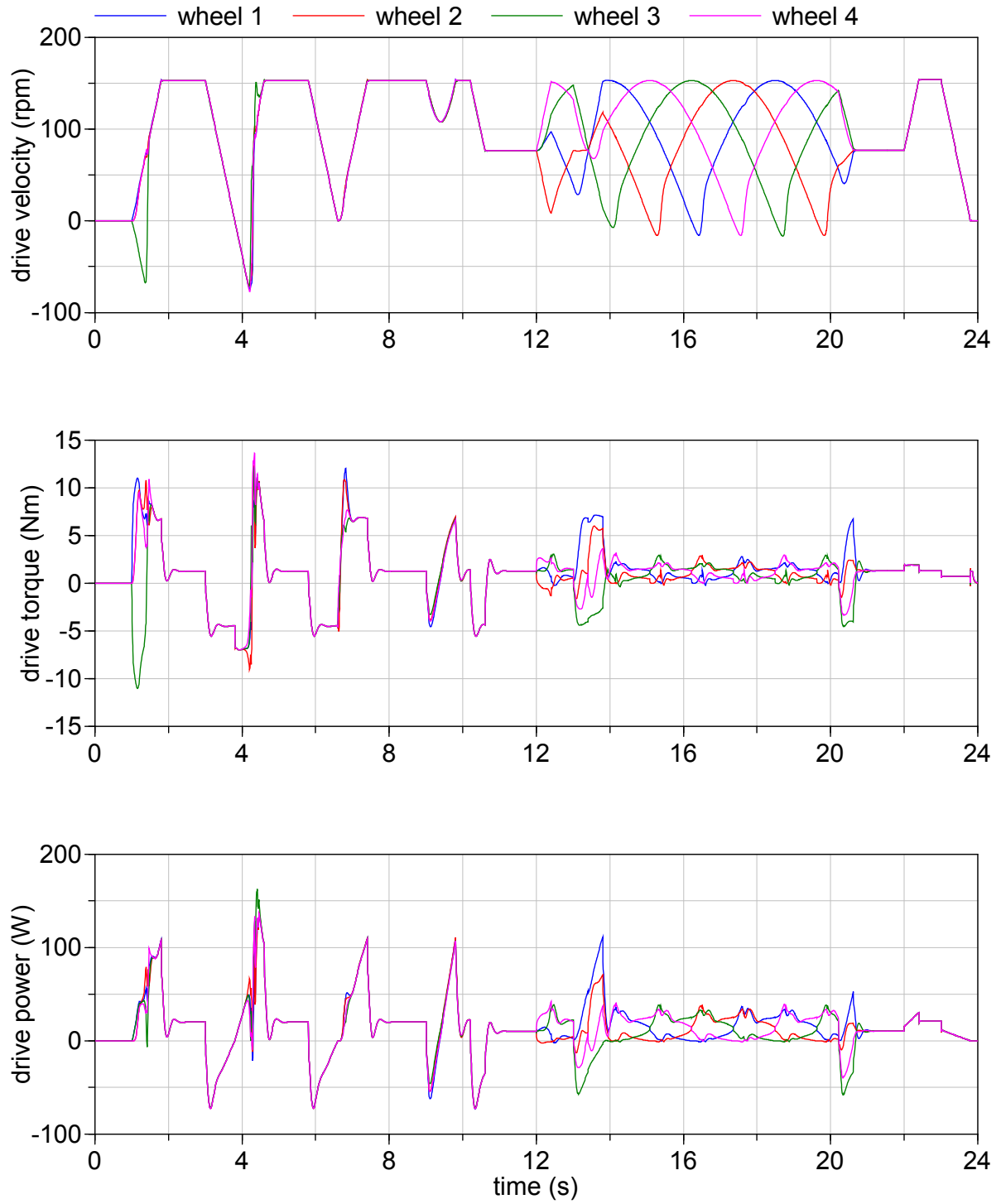


Figure 8.37: Velocity, torque and power for drive joints of all wheels with caster length of 2.0 cm, $h = 0.578$ m, no payload.

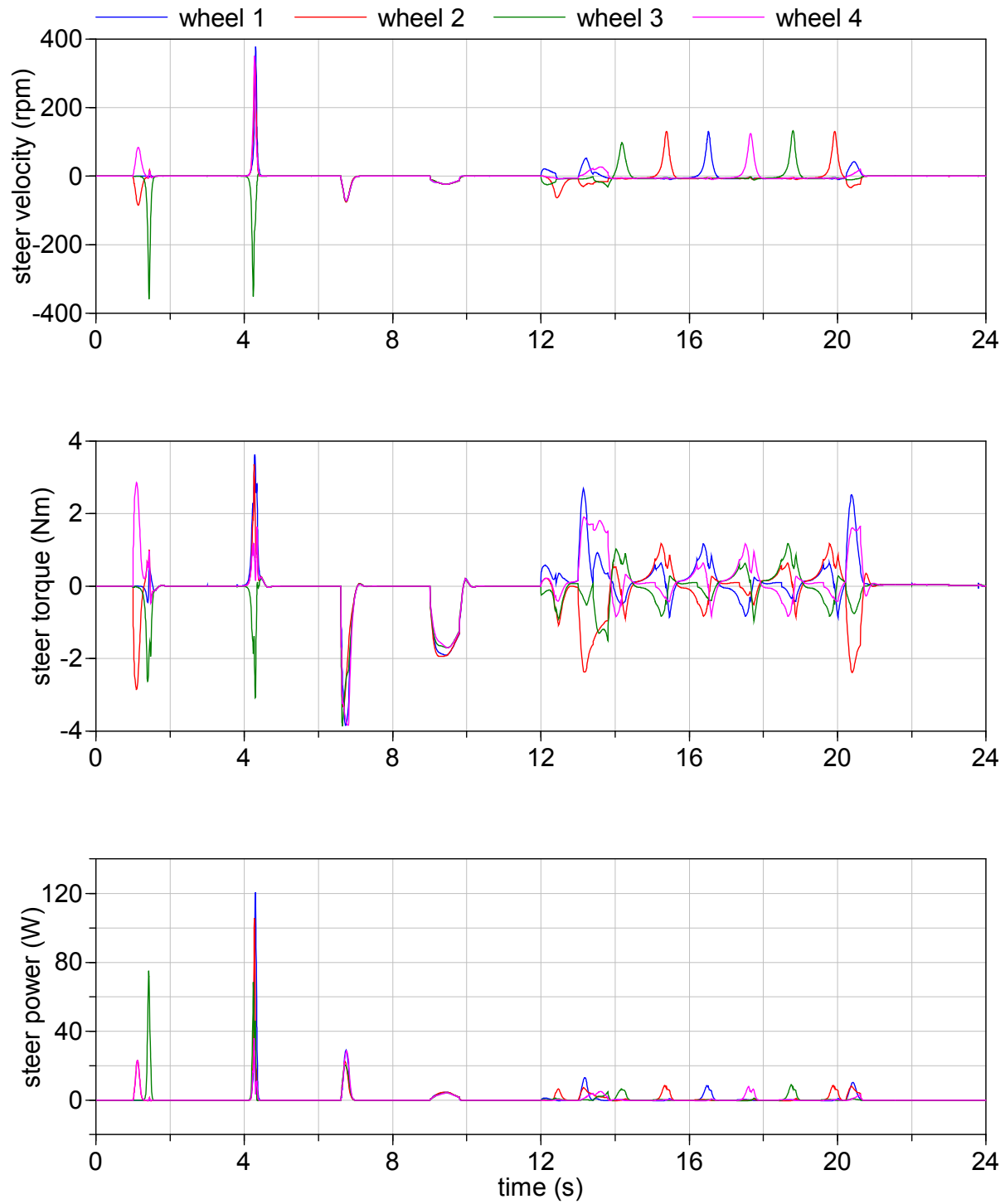


Figure 8.38: Velocity, torque and power for steering joints of all wheels with caster length of 2.0 cm, $h = 0.578$ m, no payload.

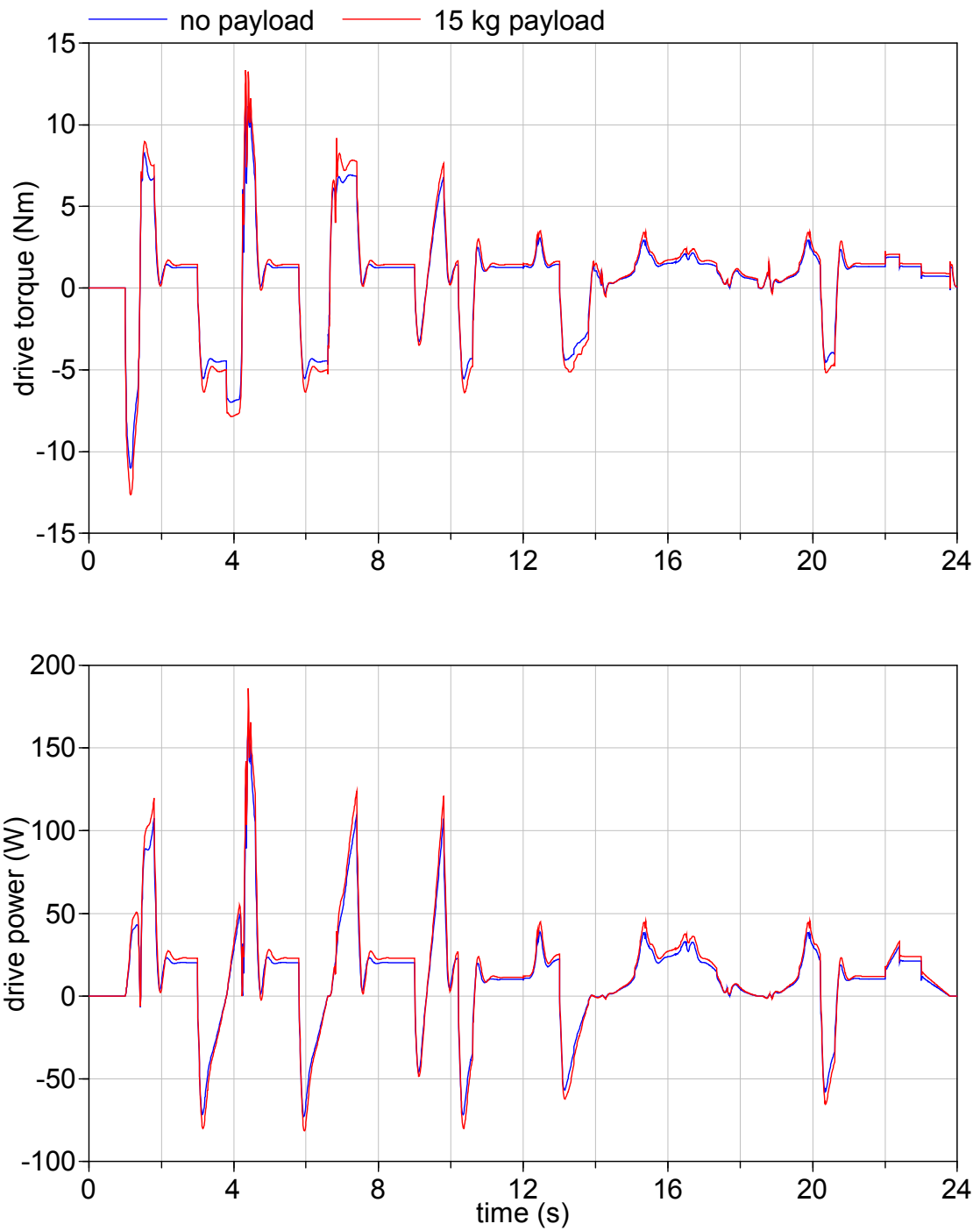


Figure 8.39: Wheel 3 drive torque and power (joint velocity is nearly identical), comparing no payload to maximum payload with acceleration, $h = 0.578$ m, caster of 2.0 cm.

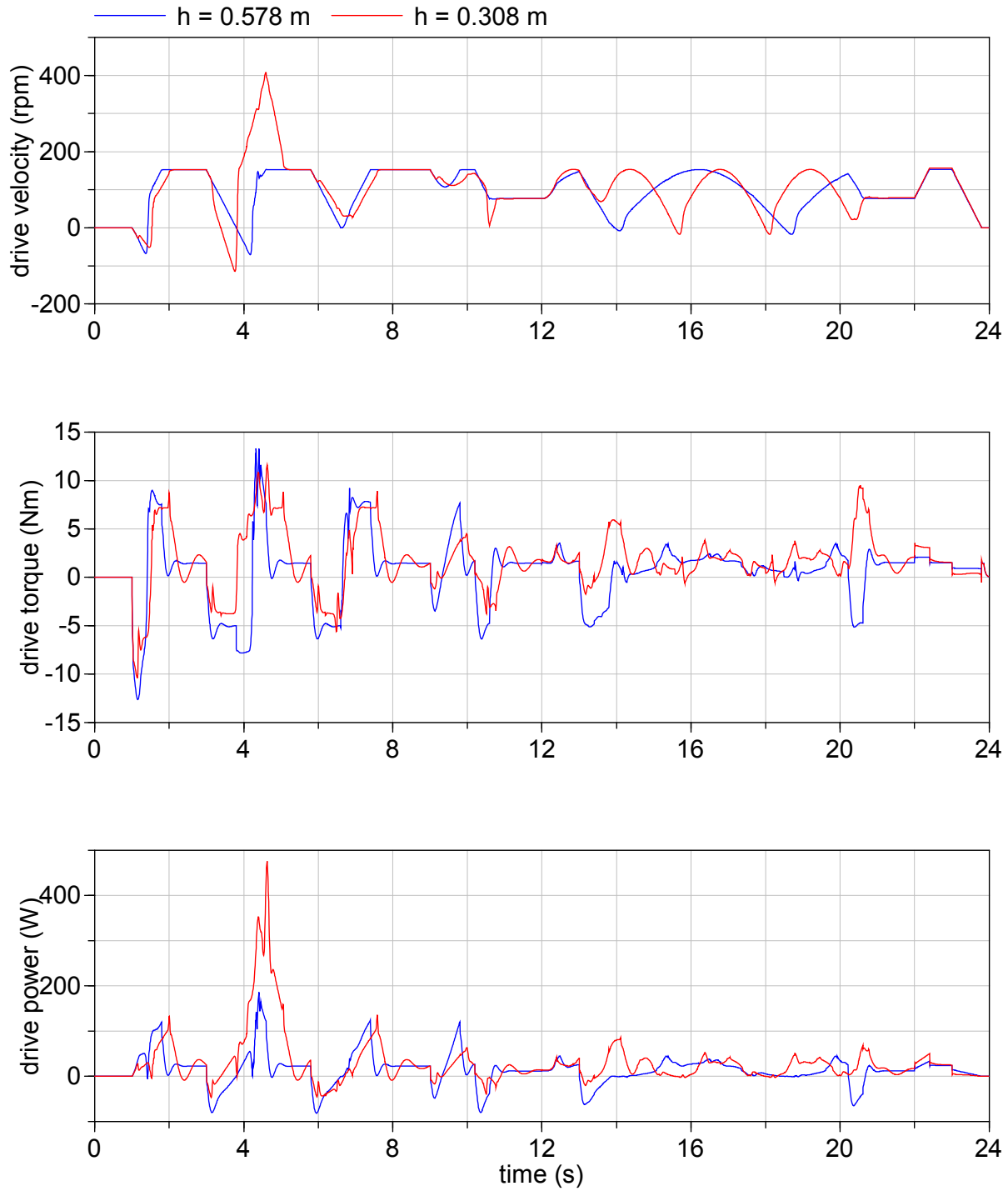


Figure 8.40: Wheel 3 drive joint velocity, torque and power, comparing the smallest wheel base ($h = 0.308$ m) to the largest ($h = 0.578$ m) at a payload of 15 kg. Caster length of 2.0 cm

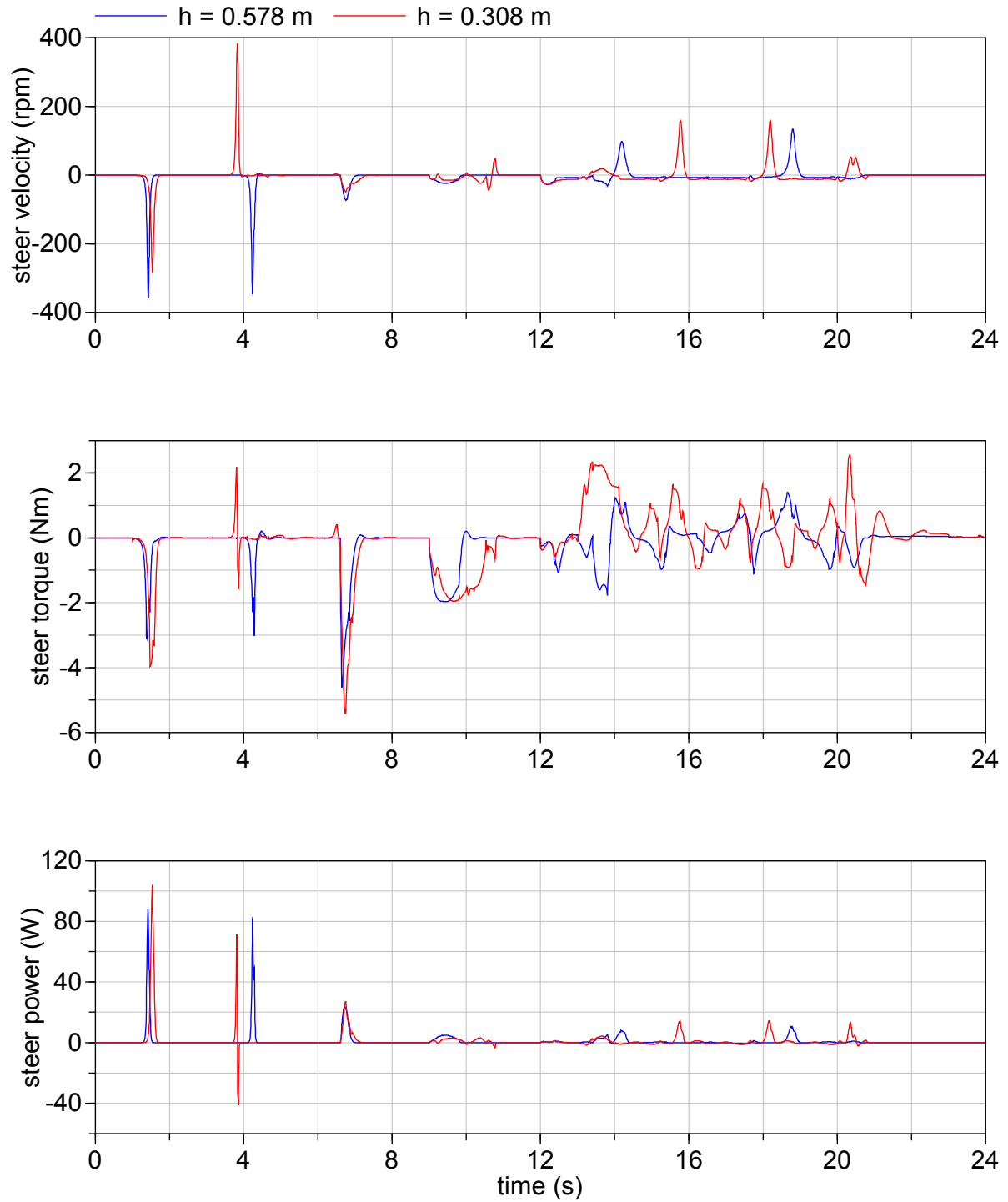


Figure 8.41: Wheel 3 steering joint velocity, torque and power, comparing the smallest wheel base ($h = 0.308$ m) to the largest ($h = 0.578$ m) at a payload of 15 kg. Caster length of 2.0 cm

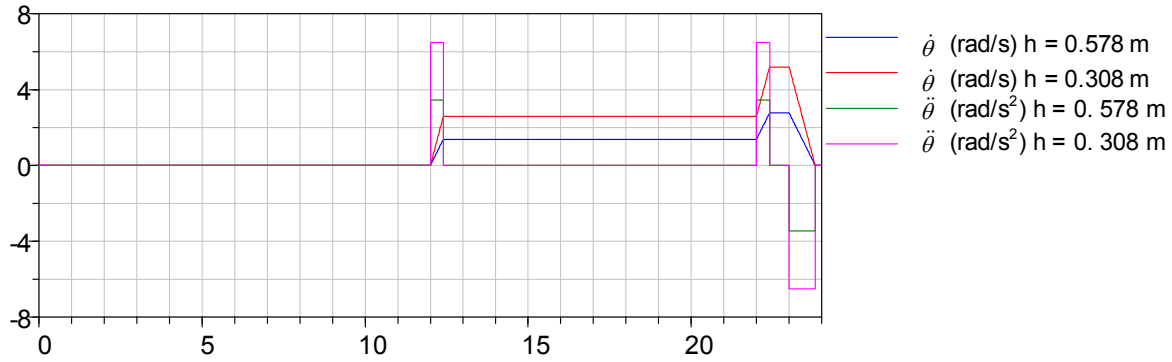


Figure 8.42: Change in angular velocity and acceleration with smaller wheelbase.

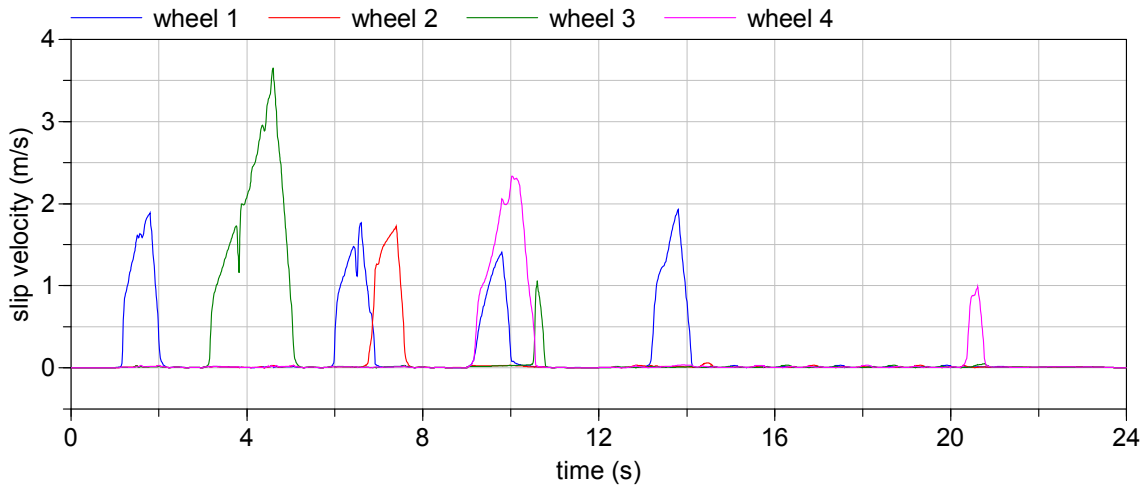


Figure 8.43: The small wheelbase results in large wheel slip.

8.6 Conclusion

The platform will be fully actuated for steering and drive for best performance. Relationships for drive and steering torque, velocity and acceleration given global velocity and acceleration have been derived. The platform is designed to be isotropic for linear velocity and acceleration only, since this is expected to be the most common and important motion type. Global accelerations and velocities are limited by the drive joint acceleration and velocity; the drive joint acceleration and velocity in turn is limited by the maximum linear acceleration and velocity. Thus, maximum angular and linear conditions cannot be achieved simultaneously. Angular motion is also restricted by the size of the wheelbase; thus, the maximum drive joint velocity during angular motion never exceeds that for linear motion. These imposed restrictions on the kinematics prevent the actuators from being oversized for infrequent motions that do not greatly enhance the system’s overall performance.

Simulations with a PD torque controller are performed using a test trajectory to determine the best caster length, which is found to be 2 cm, and the maximum actuator velocities, torques and power requirements, which will be used in determining the requirements for drive and steering actuators in Appendix E.

Chapter 9

Component Volume, Mass, Energy and Power Analysis

In order to ensure the overall design feasibility, a basic investigation of sensing and processing components is done in sections 9.1 and 9.2 below. This is followed by an analysis of estimated power requirements in 9.3, which leads to the energy storage estimates in 9.4. Mass and volume are estimated in sections 9.5 and 9.6. The chapter concludes with the resultant base geometry to accommodate the mass, volume, variable footprint and other design requirements in section 9.7.

9.1 Sensing Components

The platform is to operate autonomously and must be outfitted with the sensors to map and navigate in the human indoor environment. In addition, Justin already has its own imaging system consisting of 3D video and laser range sensors that are mounted on a pan-tilt unit on top of the torso; it will need to be powered by and have its data processed in the base.

9.1.1 Proprioceptive

Proprioceptive sensing is necessary to control and monitor the platform's behaviour; drive speed, steering speed, steering position, leg extension speed, leg position, suspension position, system stability and battery level are some likely values that need to be determined. The components for this are all expected to be small, light and low in power use, and thus are not accounted for individually at this point of the design.

9.1.2 Exteroceptive

9.1.2.1 Requirements

The exteroceptive sensing system must be able to detect obstacles and landmarks in the indoor environment. It should add as little to the weight, volume and power requirements as possible. Due to the holonomic nature of the platform, sensing should be equally effective in all directions in the horizontal plane. Although the platform can only move in one direction at a time, it can change direction without delay, so sensing should be possible in all directions simultaneously as well (precluding the use of a repositionable sensor). Vertically, it is necessary to prevent the robot from confusing the space under tables or chairs as space that can be traversed. Less likely to be encountered but still desirable to be sensed are the edges of stairs, ramps, and sills.

9.1.2.2 Potential Configuration

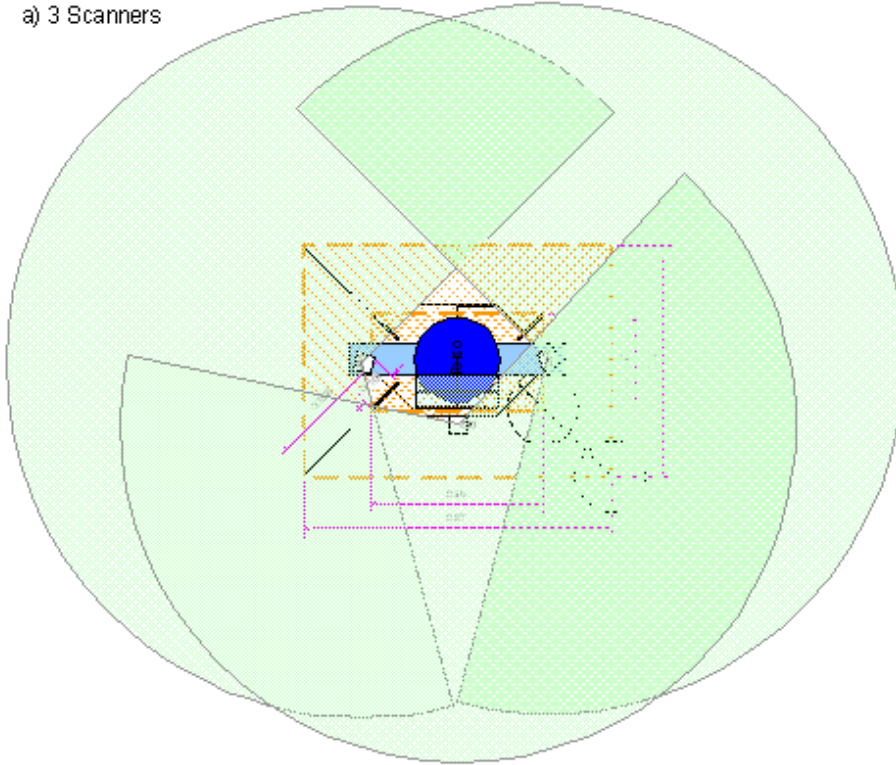
The Hokuyo laser scanner URG-04LX [110] has been specifically developed for mobile robotics and has several advantages over units previously used such as the SICK S300 [111], being significantly smaller, lighter and having lower power consumption; details are given in Table 9.1. Although it has a

shorter range of only 4 m compared to the 50 m range of the SICK laser employed on the DLR’s previous platform [112] and lower accuracy of ± 10 mm at 1 m with an angular resolution of 0.36° , this is deemed adequate for the target indoor environment. At top speed, the platform still has a look-ahead window of 2.5 seconds. The scanner covers a horizontal range of 240° , but because of the geometry of the platform, more than two are required to properly cover areas close to the platform. Three sensors as shown in Figure 9.1 a) provide adequate coverage, where one wide side gets preferential coverage (the opposing side being set to the side of the torso’s vertical rotation limit) in keeping with the philosophy that asymmetry can be more efficient. The overlap could also be used to cover different heights. The sensors need to be mounted above the leg structure (~ 60 cm off the ground) so as not to have a sector obscured by it. Alternatively, four sensors mounted at the end of the leg structure could be used as shown in Figure 9.1 b). Since space and power are at a premium, the solution with three sensors is deemed sufficient.

Table 9.1: Potential laser scanner with volume, mass and power specifications [110].

Component	Manufacturer	Model	length	width	height	volume	mass	peak power	average power
			mm	mm	mm	L	kg	W	W
Laser Scanner	Hokuyo	URG-04LX	50	50	70	0.175	0.16	4	2.5
Quantity: 3									
TOTAL						0.525	0.48	12	7.5

a) 3 Scanners



b) 4 Scanners

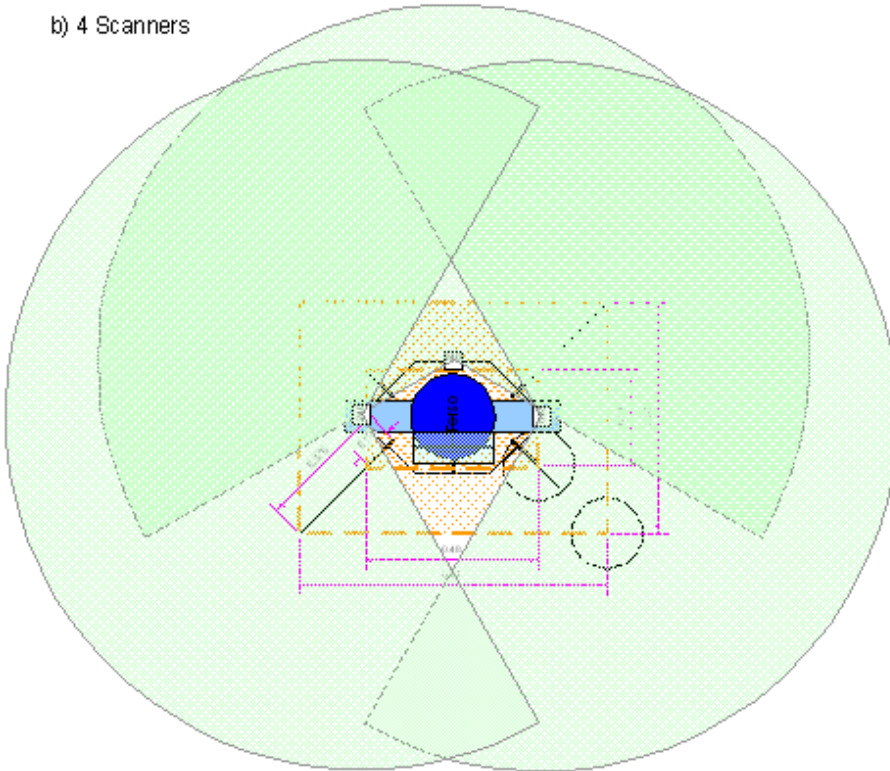


Figure 9.1: Potential laser scanner coverage with a) 3 and b) 4 Hokuyo units.

9.2 Processing Components

9.2.1 Requirements

Computer processing power is required to control Justin and the base. Currently, Justin runs on a number of different computer systems, none of which are optimized for size or electric power consumption. The following six tasks are each expected to require their own processor:

- Arm/Torso control (2 PCI slots)
- Hand control (2 PCI slots)
- Platform control
- Vision system
- Data handling system
- Spare processor for future use

9.2.2 Component Selection

Compact but powerful computers that are also designed with industrial durability are readily available. A potential configuration is shown in Table 9.2.

Table 9.2: Potential computer configuration with volume, mass and power specifications.

Component	Manufacturer	Model	length	width	height	volume	mass	peak power	average power
			mm	mm	mm	L	kg	W	W
Motherboard & CPU	Global American	2804080	170	170	60	1.73	0.32	50	15
Storage		Disk on Module						0.125	0.53
WIFI		WLAN mini-PCI	60	45					
Power Supply	minibox.com	picoPSU-120	31	45	20				
Sub-Total						1.73	0.32	50.1	15.5
<i>power supply efficiency of 90%</i>								5.0	1.6
Quantity: 6									
TOTAL						10.4	1.92	330.6	102.6

9.3 Power Requirements

The estimated power requirements are given in Table 9.3. Each component peak and average power requirement is multiplied by an estimated duty cycle for that component and then multiplied by the quantity of components in the system. Considerations are made for electrical conversion and cable losses as well as the power use of the motor controllers. Their ‘duty cycle’ is actually the loss factor that is applied to the sum of the preceding section to determine the extra power used and is italicized to differentiate it from the component duty cycles. The power requirements are then summed to give the total average and peak power for each subsystem and the overall system.

Values for the arm, torso and existing vision system are based on information available from the DLR about these existing components and on observations made during their operation. Details about the estimated values for other electronic components can be found in sections 9.1 and 9.2. Duty cycles for the upper-body expect it to be operating equivalent to 10% of the system’s operational time at maximum performance, where as the duty cycle for the propulsion and steering expects the base to be in motion equivalent to 60% of the time at the RMS power determined for the test trajectory. The peak value for propulsion and steering is based on the peak value reached during the caster reversal in this trajectory with losses from electrical input to mechanical output estimated at 50%.

Table 9.3: System peak and average power requirements.

	weight	peak power	average power	duty cycle	quantity	volume	weight	peak power	duty average power
	kg	W	W	%		L	kg	W	W
Electronics									
Laser Range	0.16	4	2.5	100%	4	0.70	0.64	16.0	10.0
IMU	0.015		0.678	100%	1	0.01	0.02	0.7	0.7
Computers	0.32	50	15	100%	6	10.40	1.92	300.0	90.0
<i>computer power supply efficiency</i>				90%				30.0	9.0
<i>DC/DC conversion losses</i>				15%				52.0	16.5
SUB-TOTAL ELECTRONICS						11.12	2.58	399	126
Arm/Torso									
Torso Vision System	2.5	5	5	100%	1		2.50	5.0	5.0
Arm/Torso - integrated electronics			120	100%	1				120.0
Arm/Torso - hold zero position			72	90%	1				64.8
Hand	1.8				2		3.60		
Hand/Arm - max	12.9	960		10%	2		25.80	1920.0	192.0
Torso -max	18.7	1152		10%	1		18.70	1152.0	115.2
SUB-TOTAL ARM/TORSO							50.60	3077	497
<i>Cable losses</i>				5%				153.9	24.9
SUB-TOTAL ARM/TORSO							50.60	3231	522
Propulsion									
Drive Motor and Geartrain	0.45	372	64	55%	4		1.80	1488.0	140.8
Motor Controller	0.2			5%	4		0.80	74.4	7.0
Steering motor and Geartrain	0.45	286	14	55%	4		1.80	1144.0	30.8
Motor Controller	0.2			5%	4		0.80	57.2	1.5
<i>Cable losses</i>				5%				138.2	9.0
SUB-TOTAL DRIVING							5.20	2902	189
TOTAL POWER								6531.3	837.2

9.4 Energy Storage

In order to minimize the required volume and mass, a battery type with a high energy density such as lithium-ion should be used. One potential candidate is the Ultralife UBI-2590 [113], details of which are given in Table 9.4.

Table 9.4: Specifications of potential battery, Ultralife UBI-2590 [113].

Manufacturer & Model	length	width	height	volume	weight	voltage	current	energy density		energy
	mm	mm	mm	L	kg	V	A	Wh/kg	Wh/L	W
Ultralife UBI-2590	62.2	111.8	127	0.883	1.4	12	12	120	200	173

Given the average power requirements from 9.3 together with the candidate battery specifications in Table 9.4, the energy storage required for a certain amount of runtime can easily be estimated. The energy storage must also be capable of supplying sufficient current necessary to satisfy the peak power requirements. Since much of the upper-body runs on 48V, it is sensible to arrange the batteries in banks of 4 so as to supply this voltage without requiring additional conversion with its associated losses. As shown in Table 9.5, for a three-hour runtime, 16 batteries are required, which also satisfies the peak current draw.

Table 9.5: Energy supply to meet requirements and its mass.

WEIGHT REQUIREMENTS IN BASE	25 kg
VOLUME REQUIREMENTS IN BASE	25 L
PEAK POWER	6531 W
PEAK CURRENT REQ'D @ 48V	136 A
AVERAGE POWER	837 W
AVERAGE CURRENT @ 48V	17 A
DESIRED RUNTIME	3 h
ENERGY REQUIREMENTS	2512 Wh
Energy Supply	
Ultralife UBI-2590	Quantity 16
	Energy 2768 Wh
Estimated Actual Runtime	3.3 h
	Volume 14 L
	Weight 22 kg
Max Cont Current @ 48V	48 A
Max Peak Current @ 48V	144 A
Max Total Continous Power	2304 W
MASS BASE CONTENT & DRIVING	30 kg
MASS REMAINING FOR 65KG BASE	35 kg
TARGET TOTAL MASS (WITH TORSO)	115 kg

9.5 Mass Estimate

The mass of many system components is listed together with the power requirements in Table 9.3. The masses for the existing arm, torso and vision system components are known, whereas the mass of the electronics, 2.6 kg, and propulsion system, 5.2 kg, is estimated from specifications of potential components. The mass of the energy system is estimated in Table 9.5 to be 22 kg. As calculated in Table 9.5, these components together weigh 30 kg, which leaves 35 kg to reach the base design weight of 65 kg. The remaining 54% of mass is expected to consist primarily of structural and mechanical components such as the base chassis, the leg mechanisms, and the wheel units, but will also include additional electronic components and cabling. If these components do not end up requiring their allotted mass, the weight difference can be made-up for by increasing the energy storage and thus the run-time.

9.6 Volume Estimate

It is important that the design contain sufficient space to house all the components. Of concern is the volume of the base proper, which must house the electronics and the energy storage in addition to structural components and the first joint actuator of the torso. The estimated volume of the electronics and the energy storage is listed in Table 9.3 and Table 9.5 respectively. The volume of the base proper is found by adding the footprint area of the central rectangular section to twice the area of the side triangular section and multiplying by the base height, as detailed in

Table 9.6 and shown in Figure 9.2. The base proper has a theoretical volume of 64 L, of which 41 L remain after electronics and energy storage for structural purposes, cabling and additional electronics or sensors. Some fraction of space will also be lost since the components are of course not moldable.

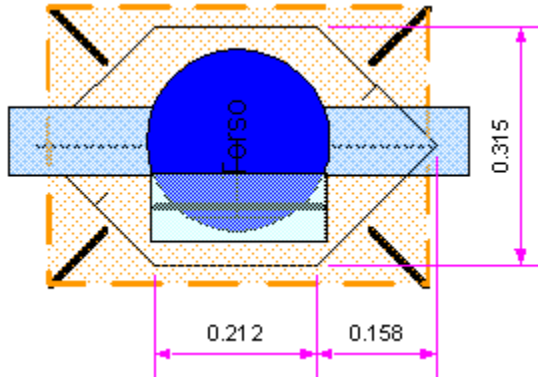


Figure 9.2: Base proper footprint dimensions.

Table 9.6: Volume of base proper remaining after electronics and energy storage.

	Parameters	Area/Volume
centre rectangular section	length: 0.212 m width: 0.315 m	0.06678 m ²
side triangles	base: 0.315 m height: 0.158 m	0.04977 m ²
Total Area		0.11655 m ²
× base height		0.55 m
Total Volume		0.0641 m ³ = 64 L
Volume of electronics		11 L
Volume of energy storage		12 L
Volume remaining		41 L (64%)

9.7 Base Geometry

9.7.1 Platform Height

The height of the platform should be such that the system achieves similar reach characteristics to a human without exceeding the height of a human in its zero configuration. It must also allow pickup of objects on the ground easily. Simultaneously, the height is a factor in the volume of the platform, which must be large enough to fit all components, and in the extension distance of the VFM. Because of the geometry of Justin, human reach is easily exceeded, so choosing the platform height is a trade-off between maintaining a human-scale appearance to ensure the best fit for the human environment, where doors are typically 1.97 m high [114], and providing enough height to create enough volume for components in the base. For Justin's shoulder height to equal that of a 95% male, the distance from floor to base is 63 cm. This makes the height to top of the head 180 cm, which is 3 cm lower than the 95% male height. As is visible in Figure 9.3, at this height, Justin can still easily reach the ground. Considering the suspension travel of up to 2 cm, the height of 65 cm is chosen as the height of the top of the platform from nominal ground level for an overall height of 181±1 cm.

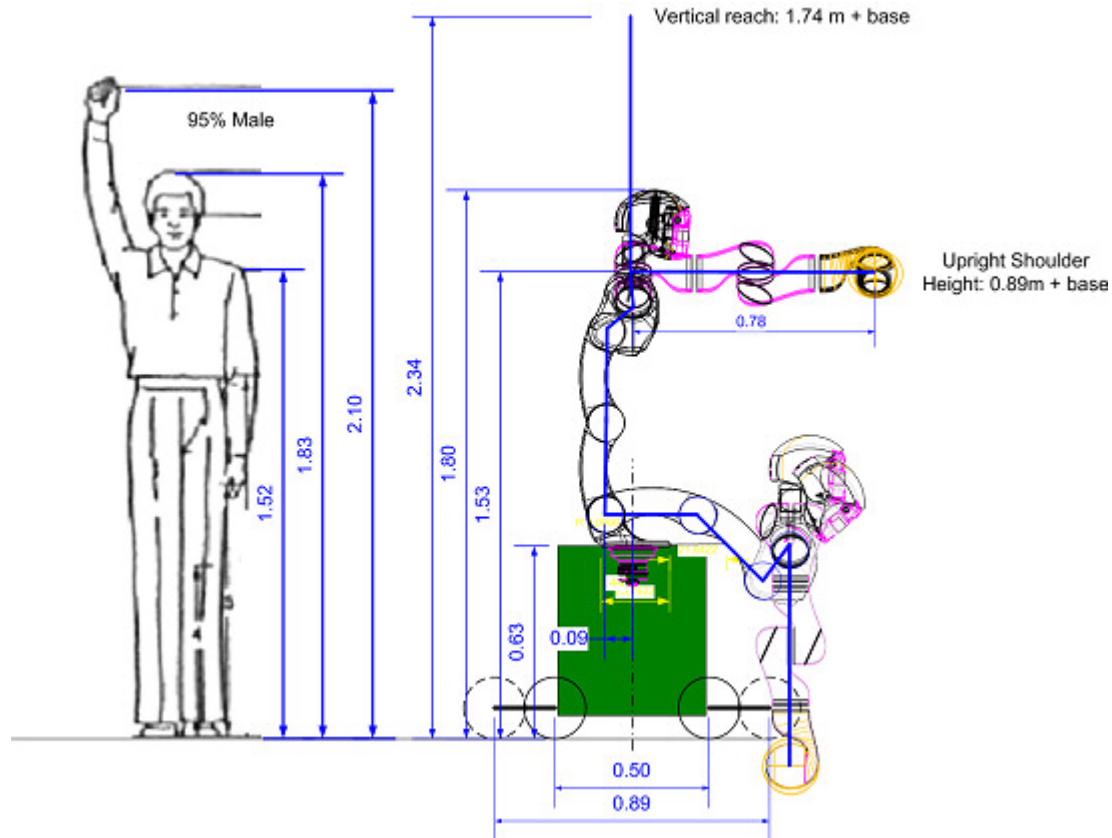


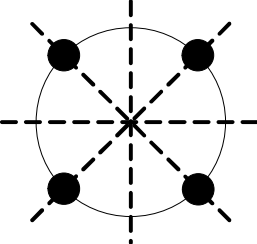
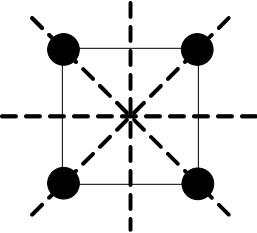
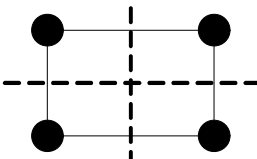
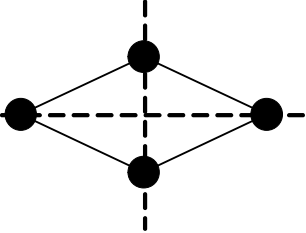
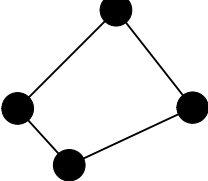
Figure 9.3: Comparison of heights of system and 95% male.

9.7.2 Base Footprint Shape

In order to maximize the possible footprint extension, it makes sense to locate the wheels at the extremes of the base. But what shape of base footprint is best? The merits of different shapes are compared in Table 9.7.

While symmetry makes control easier, because symmetric sides can be treated equally, an asymmetric arrangement allows for optimizing certain sides for certain tasks. With a base capable of turning on the spot and a torso that can rotate $+180/-160^\circ$ on its vertical axis, the appropriate side can always be oriented in the right direction if there is at least one plane of symmetry.

Table 9.7: The merits of different base shapes, with figures indicating wheel positions.

9.7.2.1 Shape	9.7.2.2 Advantages/Disadvantages
<p>Circle</p> 	<ul style="list-style-type: none"> • Full symmetry • No corners to get caught on items in the environment • Maximum use of turning radius area • rectangular components fit poorly into round shape • base extends beyond tip axes
<p>Square</p> 	<ul style="list-style-type: none"> • four planes of symmetry • rectangular components fit well • if wheels are placed at corners, the base sides coincide with tip axes • square footprint has optimal stable surface area
<p>Rectangle</p> 	<ul style="list-style-type: none"> • two planes of symmetry • rectangular components fit well • if wheels are placed at corners, the base sides coincide with tip axes
<p>Diamond (non-90° corners)</p> 	<ul style="list-style-type: none"> • two planes of symmetry • rectangular components fit along sides, but possible problems in corners • if wheels are placed at corners, the base sides coincide with tip axes
<p>Quadrilateral</p> 	<ul style="list-style-type: none"> • rectangular components fit along sides, but problems in corners • if wheels are placed at corners, the base sides coincide with tip axes

A rectangular footprint has two planes of symmetry, a wide side, offering a wide workspace between legs with a short support area, and a narrow side, offering a longer support area to enable more reach over a narrower workspace. Rectangular components fit well into a rectangular base, and the legs can be placed at the corners to maximize the extended distance. Both humans and Justin have a roughly rectangular cross section with a narrow side and wide front, which is their preferred direction for manipulation; Justin will be able to choose whether to use the wide or narrow side of the base to work over—another way the platform resolves the conflicting issues of mobility and stability. While one could specialize each side further, for instance by moving the torso centre towards a side or corner, it must be remembered that sides cannot be switched instantaneously, and there is a 20° sector the torso cannot rotate through—in other words, the system’s workspace flexibility would be hampered.

Together with the shape of the base and the wheel location on the edge of the base, the angle the wheels extend at determines the shape of the support footprint. Starting from a footprint of 0.365×0.495 m, by angling the legs at 45° relative to the base, the VFM can increase the footprint to 0.752×0.885 m, an increase in area by a factor of 3.7. The footprint actually gets somewhat squarer as the wheels extend, from a ratio of 0.74 to 0.85. Compared to a square footprint with the same perimeter as the rectangular one, as detailed in Table 9.8, the retracted position has 98% the area, but a gain in tip over axis distance from centre of 15%, whereas the fully extended position has 99% the area, with a gain over the narrow side in distance of 8%. Setting the angle to be less than 45° towards the narrow side would maintain the reach advantage more, but the ability to lift large heavy objects from the ground at the wide side between the two legs would be restricted; in other words, a larger stable area instead of a larger narrower reach is preferable when the legs are extended, which is when large heavy objects are expected. Because the legs have a significant width, having the legs extend at 45° to the base at the corners unfortunately results in the shape of the base becoming hexagonal, which is less conducive to fitting rectangular components but unavoidable.

Table 9.8: Footprint dimensions related to a square footprint of the same perimeter.

	Footprint Dimensions (m)	Equivalent Square Side Length (m)	Ratio to Square	Area Ratio	Distance from Centre Ratio (m)
Legs retracted	0.365×0.495	0.43	0.74	$0.1807/0.1849 = 0.98$	1.15
Legs extended	0.752×0.885	0.82	0.85	$0.666/0.670 = 0.99$	1.08
increase factor	2.06×1.79	1.91	1.15	1.01	0.94

Because mobility is the number one priority ahead of stability, the platform is kept small at the expense of the size of the stable workspace. If a larger reach and or payload capacity were desired, the dimensions of the base footprint would need to be increased. The base shape and footprint as designed are shown in Figure 9.4, which also shows a human cross-section (dimensions from [80]) and standard door sizes for comparison. German door openings are typically 820 mm wide, with 695 mm being used for narrow spaces, 570 mm for some closets, and 945 mm for extra wide doors [114, 115].

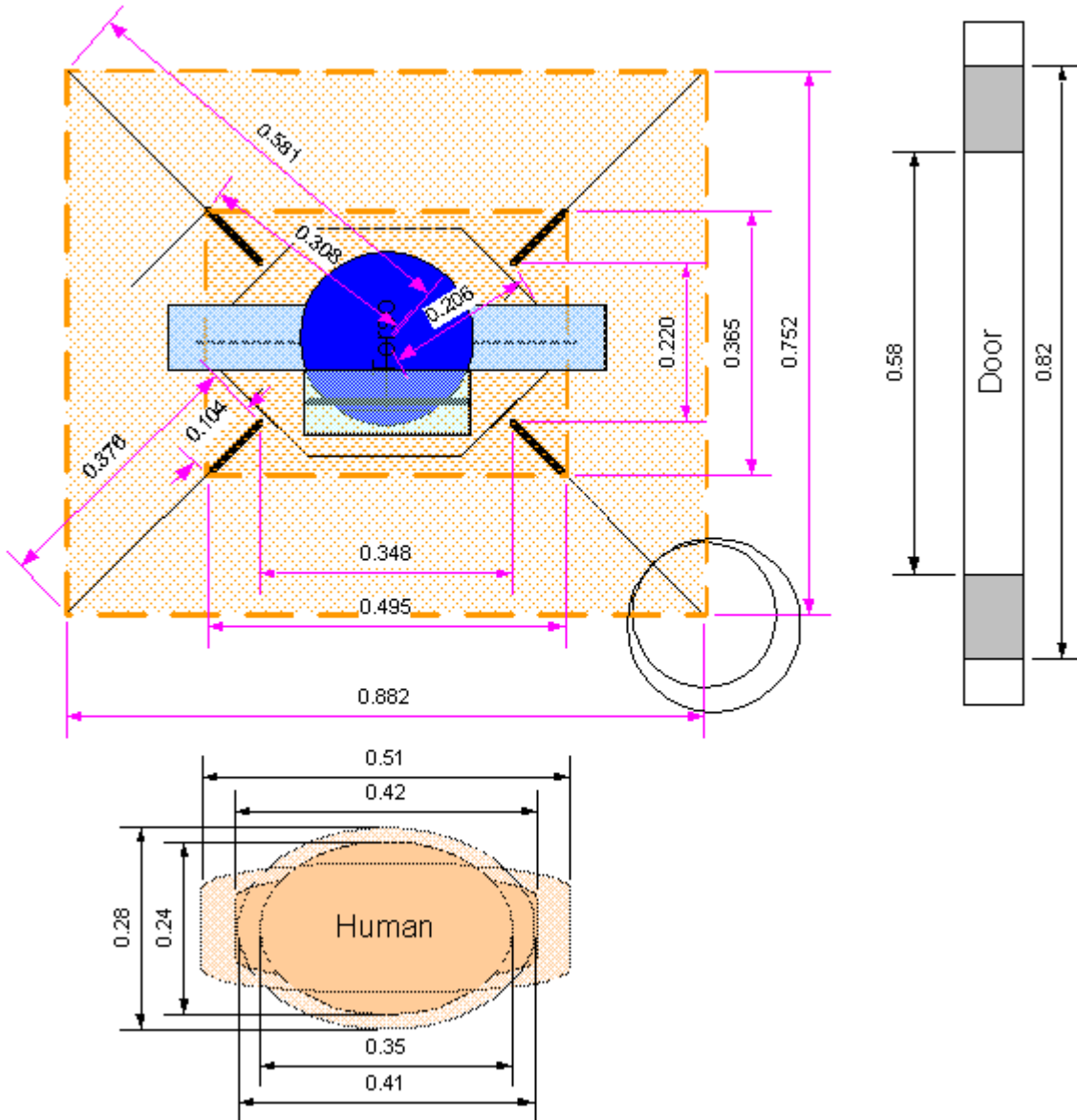


Figure 9.4: Chosen base shape and footprint in retracted as well as extended configuration compared to a human cross section and standard door sizes.

9.7.3 Ground Clearance

In order to pass over a bump that is shorter than the wheelbase, the ground clearance must be at least as high as the bump. Some allowance must be made for the motion of the suspension, which has a maximum travel of 2 cm. Also of concern is the top edge of a ramp, as shown in Figure 9.5. An 8 cm ground clearance plus a 2 cm allowance for suspension travel is sufficient to clear a 15° ramp with a 2 cm sill at the top. This represents a generous clearance that should prevent the system from ever getting stuck on the ground in its environment.

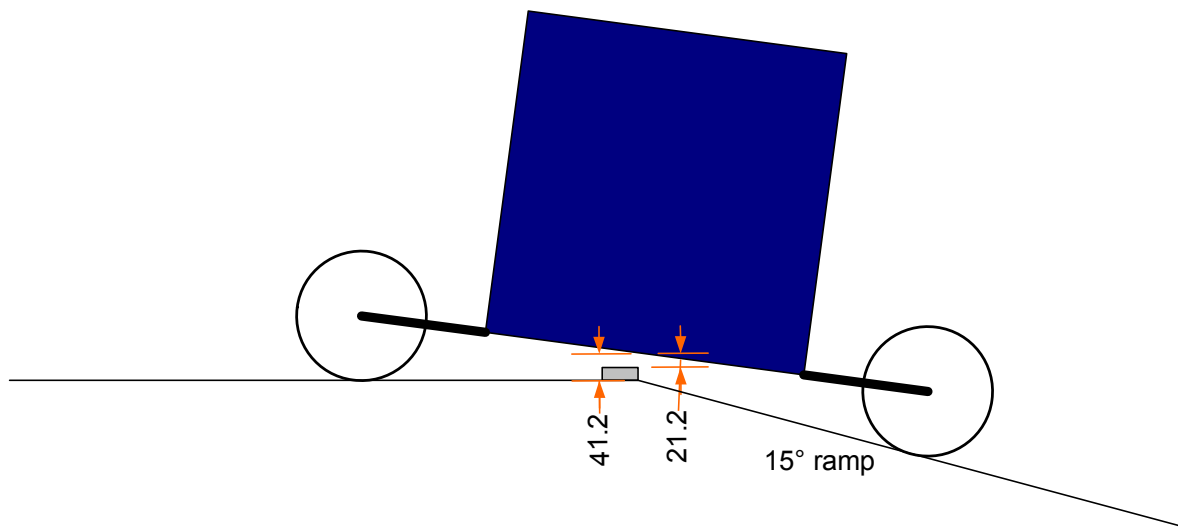


Figure 9.5: clearance (mm) when travelling over the edge of a 15° ramp with a 2 cm sill.

Chapter 10

Proposed Design

The proposed design addresses all the goals for the mobile platform described in 1.3 successfully. The system specifications are given in Table 10.1. The design is completed to a point where the configuration has been chosen and general parameters for the geometry, the locomotion system and the reconfigurable footprint have been set. Accompanying investigations of the power and energy needs and the processing and sensing components ensure that the detailed design will be feasible.

The challenge of the conflicting goals of high mobility and stability is met with the VFM, whereby the trade-off between mobility and stability is a fluid continuum. Although the VFM helps span a good portion of the continuum, it can only cover a certain range. A decision on what range of stability footprint sizes the VFM covers was made based on the expected use, which ranks mobility ahead of stability. The system is significantly more mobile than an equally stable platform without a variable footprint, and significantly more stable than a platform as small as the minimum platform size. This high stability was also achieved without an unduly heavy platform, allowing for better acceleration performance and a longer runtime. Based on estimated duty cycles, the robot can operate for over three hours.

High mobility is also provided by the holonomic omnidirectional powered caster drive system, for which the kinetics are analyzed and an optimum caster length is determined. Powered casters with a 10 cm wheel radius are chosen after extensive review and investigation show these to provide the best trade-off between mobility, volume, terrain handling, step-passing and torque requirements.

The target total unloaded system mass of 115 kg, consisting of 65 kg for the platform and the existing 50 kg for Justin, while certainly heavier than the average human, is not unheard of. In particular, when one considers the size and performance of the system, which is quite a bit larger and stronger than the average human, the mass seems appropriate and should agree with people's preconceptions, helping them handle and interact with the system appropriately.

Figure 10.1 to Figure 10.7 show a CAD mock-up of the proposed design in different configurations. Figure 10.1 shows the torso upright facing the narrow side with the legs retracted, demonstrating how the system can move through narrow spaces. Figure 10.2 is a similar configuration with the torso facing the wide side; the base is approximately as wide as Justin's shoulder width. Figure 10.3 is a top view of the same system with the legs retracted. Figure 10.4 shows two of the legs in the extended position and the torso oriented over the narrow side for maximum reach, for instance for reaching to the back of a counter-space. Figure 10.5 shows the legs extended with the torso bent down over the wide side for maximum workspace. This would be the preferred position for picking a large object off the ground. Figure 10.6 is a top view of this position. Finally, Figure 10.7 shows a close-up of the base with the side cover removed, where the green rectangular prisms represent batteries and the brown rectangular prisms represent computer units. This illustrates that there is sufficient space for all the components.

Table 10.1: Specifications of system as proposed.

	Capability	Specifications
Configuration	4-wheeled mobile platform with variable footprint	
Mass		115 kg total without payload; 65 kg base 50 kg upper body
Geometry	torso shoulder height equal to 95% male Minimum footprint not much larger than human a 10° ramp with 2 cm sill can be cleared	shoulder height: 161 cm top of base: 65 cm ground clearance: 8 cm footprint from 0.495 × 0.365 m to 0.882 × 0.752 m
Payload/Stability	3 kg fully extended with torso and arm horizontal 15 kg with torso vertical, arms horizontal	15 kg can be accelerated at 2 m/s ² . Maximum design payload of 26.4 kg.
Locomotion	holonomic omnidirectional	4 powered casters caster length: 2 cm wheel radius: 10 cm
Propulsion	maximum acceleration: 2 m/s ² 0.5 m/s ² on 4.8° slope 3 cm steps from standing start	actuator with 15.5 Nm peak and 4.0 Nm continuous torque output at wheel
Steering	sufficient to sustain linear holonomic motion at maximum acceleration	actuator with 5.4 Nm peak torque output at wheel
Suspension	Passive Spring-Damper	Spring constant: 40 kN/m Damping Constant: 2344 Ns/m bicycle-style with lockout 2 cm travel
Power use		837W average, 6.5 kW peak
Energy Storage	3 h runtime	lithium-ion batteries, 22 kg, 14 L

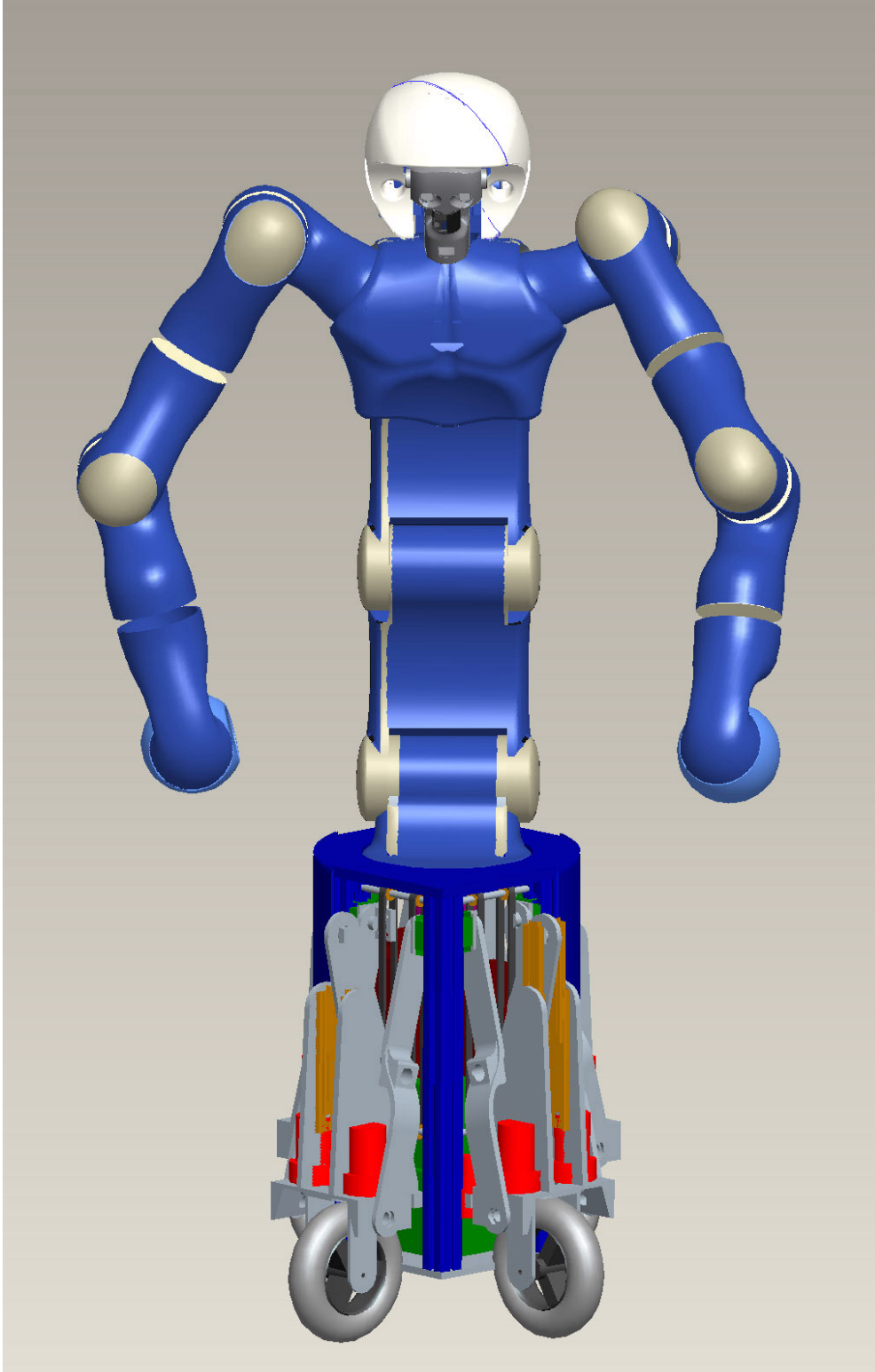


Figure 10.1: Torso upright and facing the narrow side with the legs retracted for best manoeuvrability through narrow spaces.

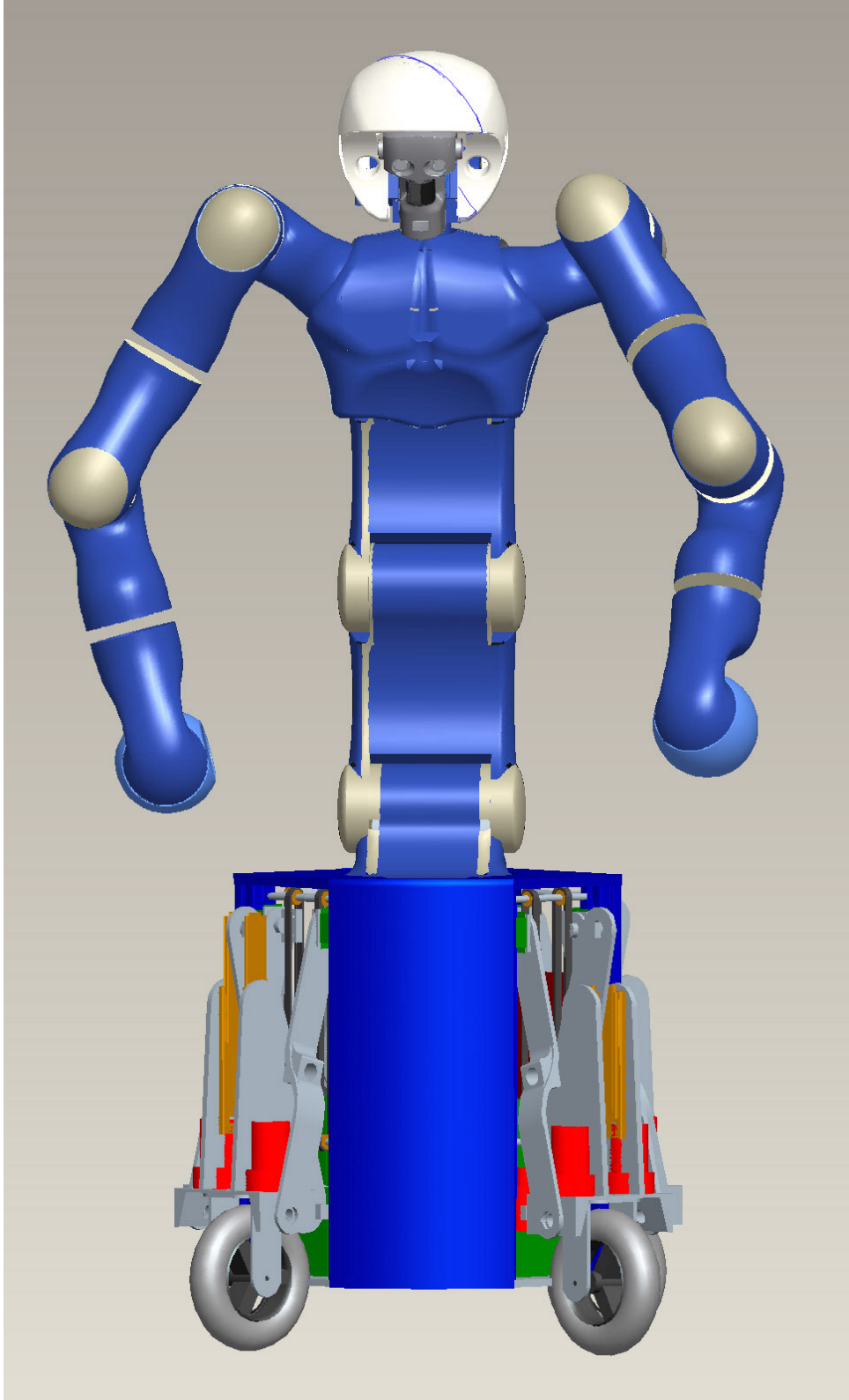


Figure 10.2: Torso upright and facing the wide side with the legs retracted.

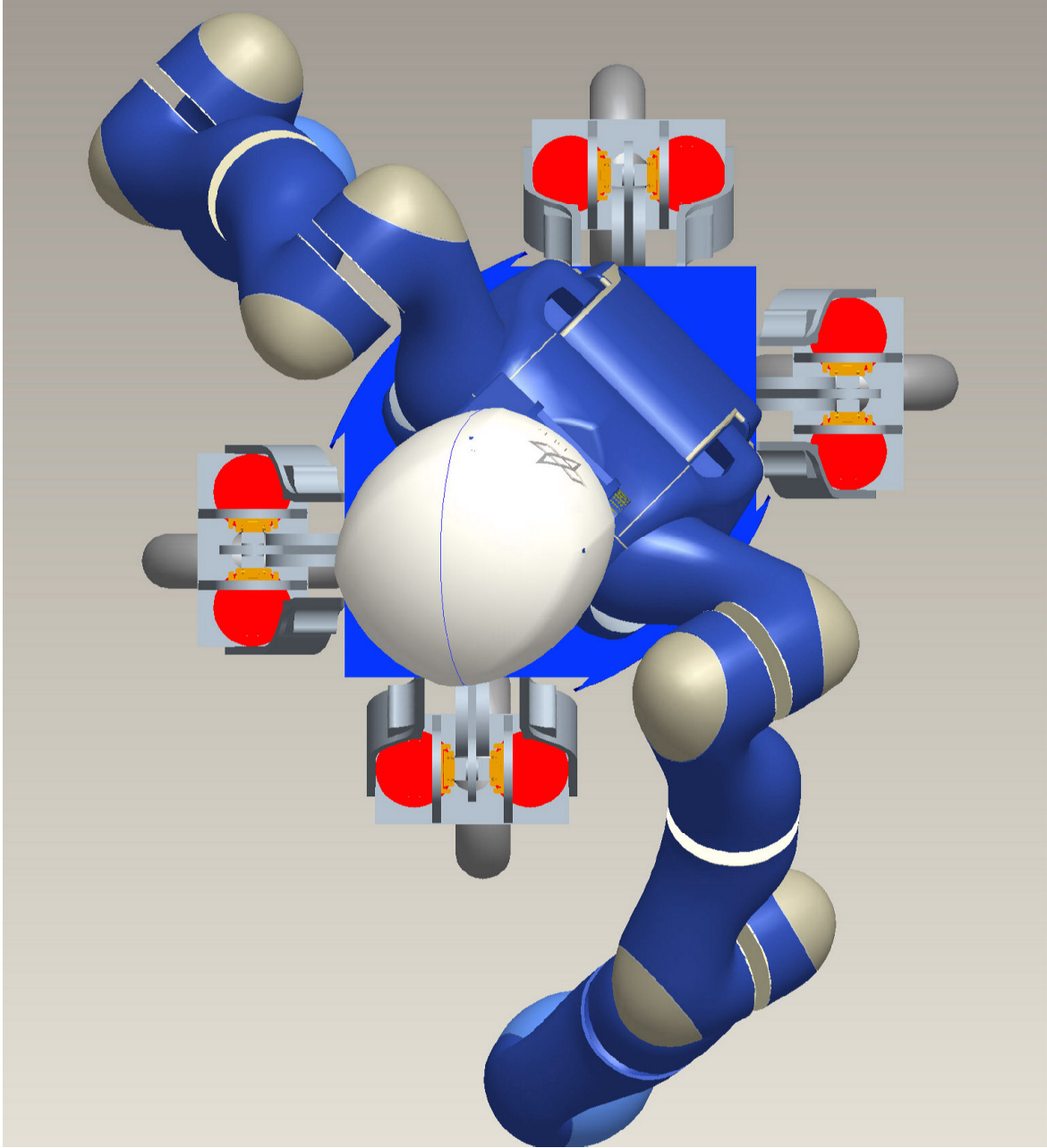


Figure 10.3: Top view of system with legs retracted.

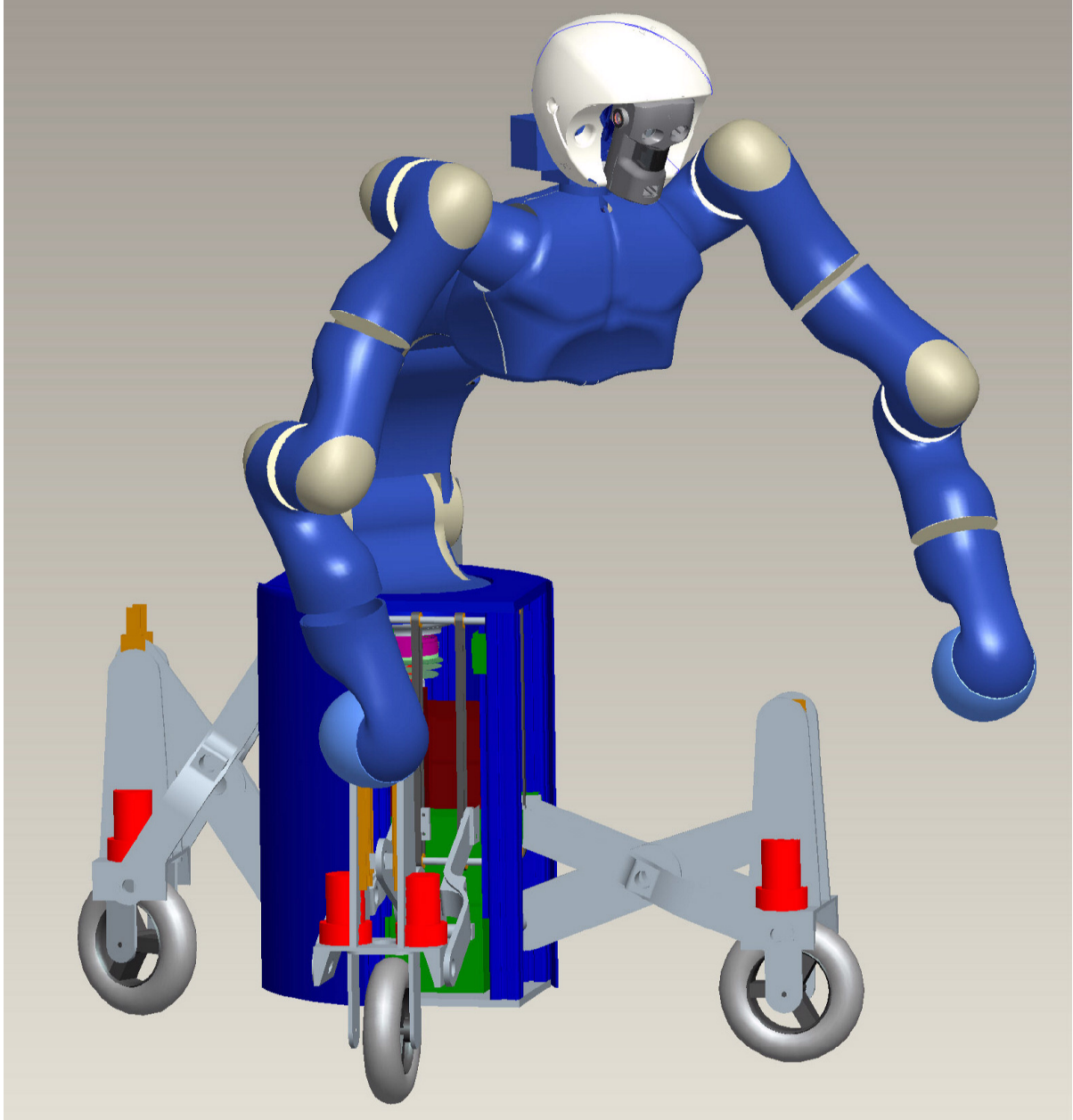


Figure 10.4: Two legs extended with torso over narrow side; configuration for best reach.

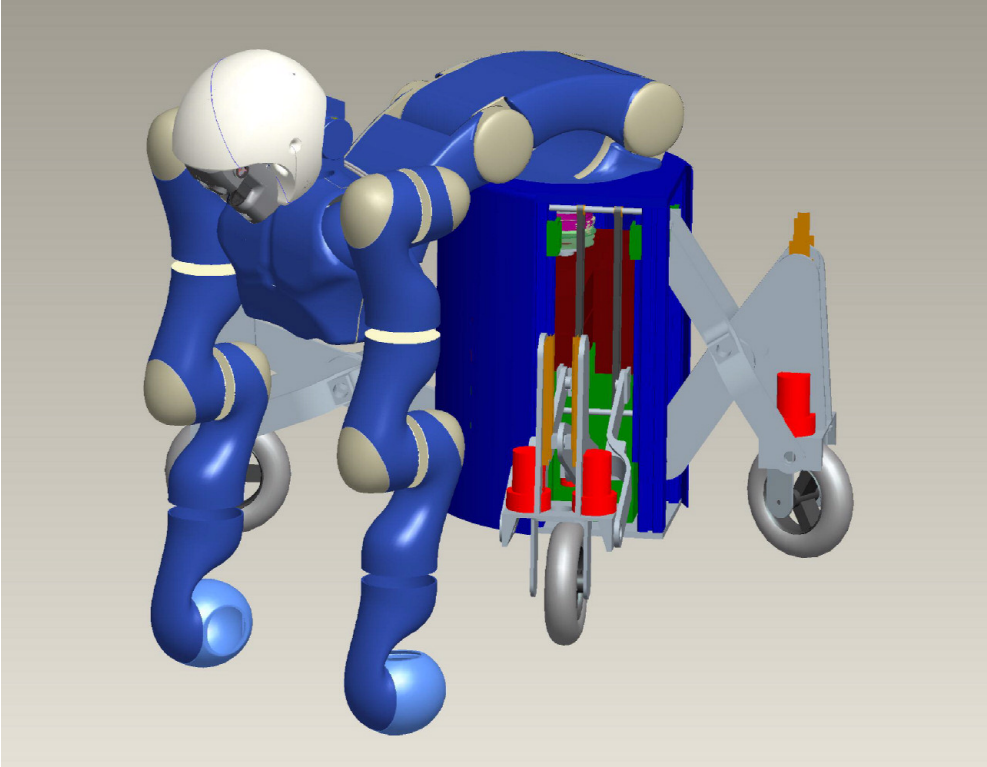


Figure 10.5: Two legs extended and torso over wide side reaching down to the ground.

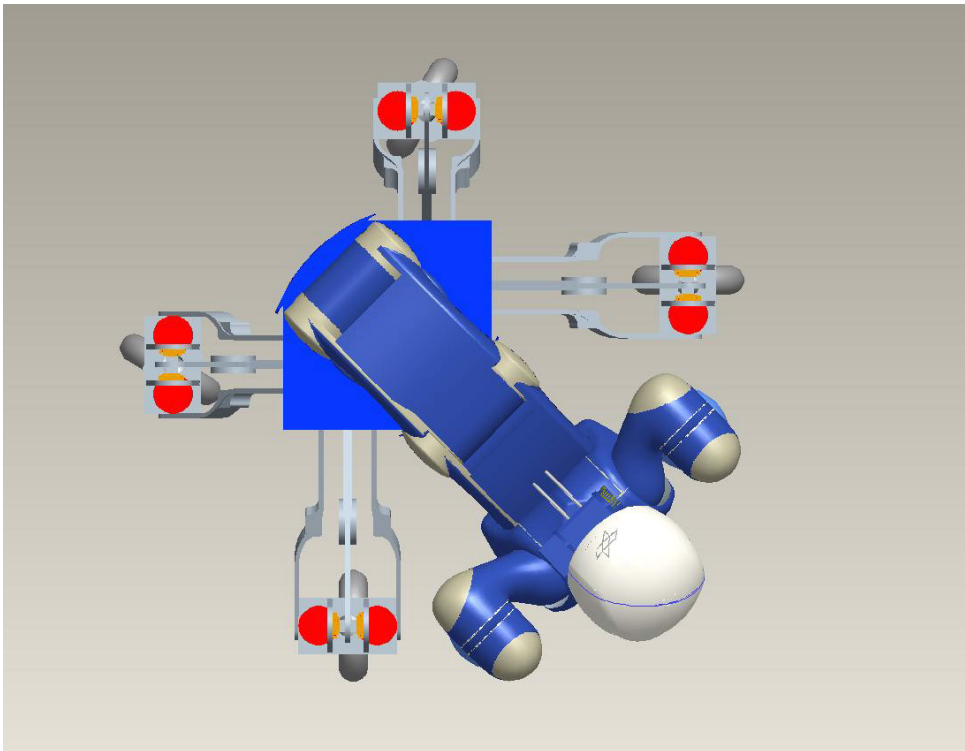


Figure 10.6: Top view of two legs extended and torso over wide side.

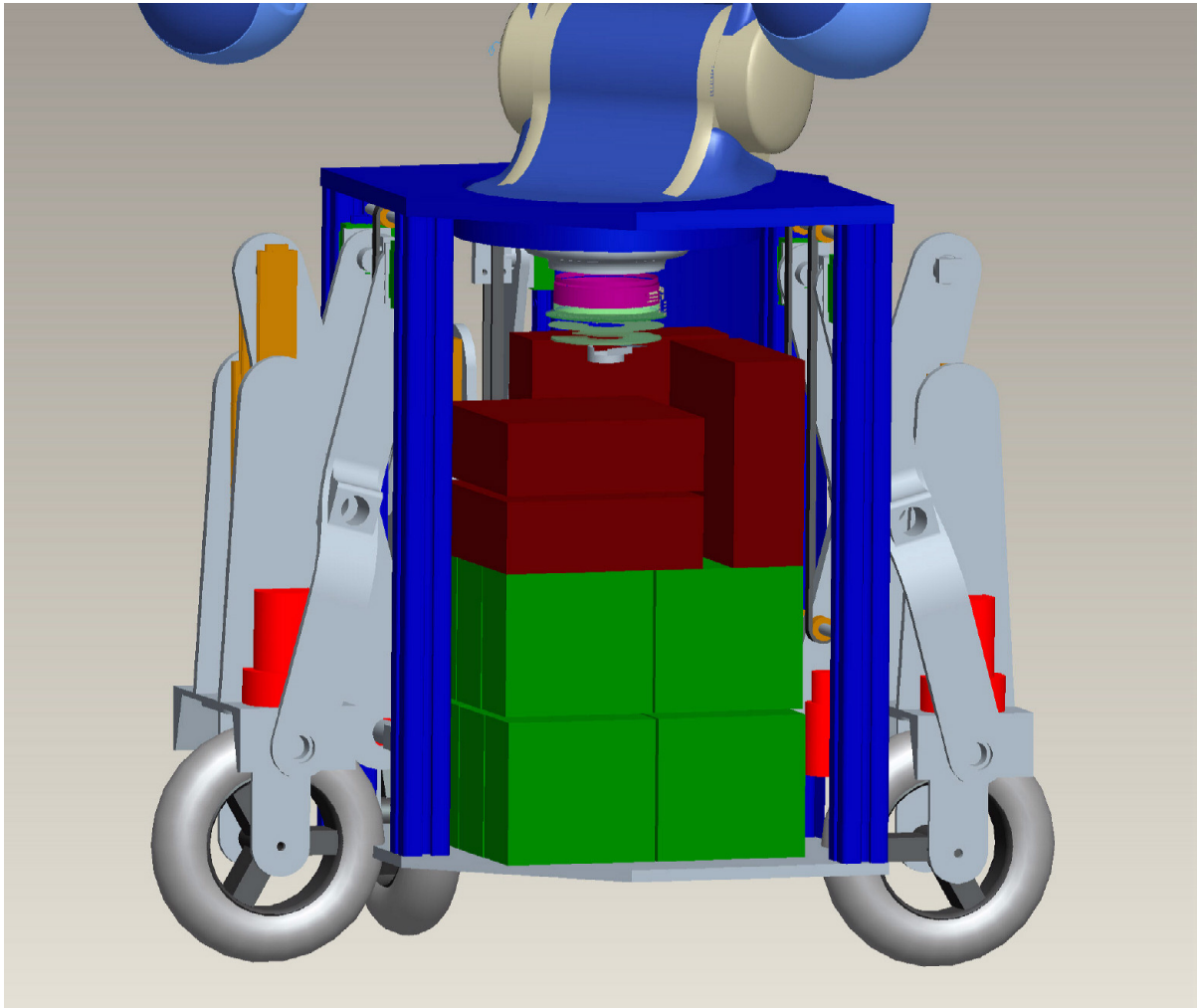


Figure 10.7: Side view of base with cover removed; battery place-holders in green, computer place-holders in brown.

Appendix A

Existing Mobile Robots and Manipulators

In Table A.1, different types of robots that are mobile and either have a manipulator or could support one are compared. Both commercial and research platforms are included.

Table A.1: Comparison of different mobile robots, mobile manipulators and humanoid robots.

Manufacturer	Model	Type	Locomotion Type	Dimensions			Weight (kg)	Payload Capacity (kg)	Speed	Energy/Battery Life	Comments
				Height (cm)	Width (cm)	Depth (cm)					
Toyota	Walking	humanoid	biped	120			35				
	Rolling	humanoid	2-wheel dynamic	100			35				
Kawada Industries	HRP-2P	humanoid	biped	154	62	35.5	58	6kg /2kgf hand	2.5km/h	48V 18Ah	Can perform controlled fall and get up again
AIST	HRP-3	humanoid	biped	160	66.4	36.3	65				
Honda	Asimo	humanoid	biped	130			54	1kg/arm	6km/h	40 min. at 2.7km/h	
Hitachi	EMIEW	humanoid	2-wheel dynamic with sideways tilt	130			~70		6km/h, 4m/s^2		6DoF arm with 1DoF hand
Bundeswehr Universität München	Hermes	humanoid	2-wheel driven & steered with 2 castors	250	170	70	70	2kg/arm	2m/s, 1m/s^2		
Helsinki University of Technology	Hybtor	platform	hybrid wheel-leg				200	40	7km/h rolling		3DoFs in each wheel-leg plus rotation, one in vehicle center
	Workpartner	centuar	hybrid wheel-leg					10kg			2 3DoF arms, 2 body jnts
Carnegie Mellon University	Nomad	platform, all-terrain	4-wheeled static				750				Four-bar linkage to change footprint from 1.8 to 2.4 m2 area
Activmedia	PeopleBot	platform	2-wheel differential plus castor	112			12	10	.8m/s	12-18hrs on 252Whrs	
Activmedia	PatrolBot	platform	2-wheel differential plus castor	38			46	22	1.7m/s	3.5hrs on 375Whrs	
Activmedia	PowerBot	platform	2-wheel differential plus 2 castors	85			120	100		2.5hrs on 2160Whrs	
Activmedia	Seekur	platform	4-wheel steered and driven	110	130	140	350	70	2.2m/s	7hrs	
Robosoft	Robulab80	platform	2-wheel differential plus castor	46.5	48	60	70	80	0.8m/s		
Robosoft	Robulab150			44	68	102.5	150	120	1.25m/s		
Robodynamics	Milo	platform with sensors	2-wheel differential drive with 2 castors	107	52	52	~25			12v, 26Ah, 12hrs	
Gecko Systems		platform with sensors	2-wheel differential drive with castors	~4ft	~20"		~55	~45	2.1m/s		1.5" vertical bump traverse
Segway	RMP 200	platform	2-wheel dynamic	75	64	61	64	91	4.4m/s, 180deg/s1 .96m/s2	400whrs, up to 24kms	\$18000

Manufacturer	Model	Type	Locomotion Type	Dimensions			Weight (kg)	Payload Capacity (kg)	Speed	Energy/Battery Life	Comments
				Height (cm)	Width (cm)	Depth (cm)					
MIT	Cardera	mobile manipulator	Segway RMP	165			70				
IHI	IMR-Type 1	platform	4-wheel static/dynamic	115-172	78	40	60	60	2.5km/h, 4.0s/step	75 min	13 DoF; 3 in leg, 2 in hip, 4 in ankle, 4 in wheels
Robomotio	Azimut 2	platform	omnidirectional 4 steered wheels with elastic steering and vertical suspension	35	29	60	52	34	5.3km/h		
Nomad	XR4000	platform	holonomic 4 steered and driven wheels	150incl.	85	62	150	100	1.5m/s, 5m/s^2	300W when active, 1575Wh, 8h battery life	
CMU	Ballbot	platform	1-wheel dynamic	150	40	40	45				
Independence Now	iBot 4000	balancing wheelchair	2-wheel dynamic/4 wheel		65	109	131	person	10.9km/h	20.4km	\$29,000
Neobotics	MP-L655	platform with sensors	2-wheel differential drive with suspension, 3 castors	56	65.5	65.5	150	100	1m/s	8hrs, 48V, 84Ah	
			2-wheel differential drive, one castor	56	65.5	65.5	150	100	1m/s	8hrs, 48V, 84Ah	
Neobotics	MP-M470	platform with sensors		75.6	47	47	150	60	1m/s	12hrs	
	MP-M470			55.6	47	47	100	110	1m/s	6hrs	
Fraunhofer IPA	Opel Museums robots	platform with sensors	2-wheel differential drive, three castors						0.4m/s	8 12V batteries, 10hrs	
Metralabs	Scitos G5		2-wheel differential drive	57	73.5	61	58	50	1.4m/s, 360deg/s	24V 912Wh, 12hrs	1.5cm steps, 15cm ground clearance
IDMind	3WD Holonomic Robot	holonomic platform	holonomic 3-wheel swedish	30	45	45	15		3m/s	2 x 12V 9Ah NiMH	
	Helios-VI	platform	two crawlers with two passive wheels in front	40	70	105.5	85	120	0.867m/s	36V 5Ah	can climb stairs
BlueBotics	MB835	platform with sensors	2-wheel differential drive, 2 castors (1 sprung)	70	70	70	100	50	1m/s, 360deg/s	10-12hrs	
DLR	old platform	platform	4 steered wheels		56	63					
Cybermotion	K3A-Nav	platform with sensors	6-wheel syncro drive	80	69		255	207	0.762m/s 0.55m/s ² 120deg/s	12hr with 50lbs load, 85 Ah@24V	
ROMAN	Tu Munich	mobile manipulator		185	63	64	260		2m/s		6DoF arm

Appendix B

Multi-body Dynamic Modelling in Modelica/Dymola

Several parts of the mobile platform design were simulated using Dymola software [116], a front end for the open-source Modelica multi-engineering simulation language. Modelica is developed in part by the DLR, and is designed to become the standard for the modeling of any engineering system. It allows acausal formulations, meaning there do not need to be explicit inputs and outputs; constitutive equations such as Ohm's law are combined with conservation equations by the software to determine the system to solve. The system can handle differential algebraic equations, so less work is needed from the user to formulate ordinary differential equations [117]. While it is possible to build block-diagram style models with Modelica as in Simulink, it is not necessary to formulate one's system this way. Models can be built with hierarchical structures that are linked with connectors, and parts from different libraries can interact if connected properly.

The Modelica language comes with a standard library of components from various disciplines, and additional ones are available. These allow simulation of complex systems much faster than if the model were to be based on equations built from first principles. The most important model used in this work is the Multi-Body Library [118], which allows simulation of 3D mechanical systems that adhere to Newtonian physics with rigid parts and various joints. In addition, a proprietary tire model called WheelDynamics is used (Appendix D).

Limitations of Model

As with any model, there are simplifications and restrictions that limit the accuracy of the simulation. The hierarchical structure of the Modelica language makes it easy to add many levels of detail in a model, but in this study the following limitations are present:

Rigid Links – All bodies are considered to be rigid, however it is expected that lightweight design will allow for some deflection under load in various components. Flexible bodies cannot yet be simulated with the Multi-Body Systems library in Modelica [119].

Tire Model Simplifications – Level 4 of the WheelDynamics tire model does not consider lateral and longitudinal tire deformation.

Uniform Ground Surface – The ground is perfectly flat with a uniform friction coefficient; a varied surface with bumps would be more realistic.

Ideal Joints – Both the drive joints and the manipulator joints are frictionless.

Solver Precision – as with any numerical method, there is a finite precision in all values.

Appendix C

Disturbance Forces due to Upper Body Dynamics

The force values in Table C.1 were found using 3D multibody simulation in Dymola with inertial properties for the head, torso and arms specified as built as well as simplified close-to point-masses for the hands and the load (both 10cm from the end of each hand). The simulation uses a simplification of the joint drivetrain with 60% efficiency. The listed forces were recorded when the joint was at maximum velocity.

Table C.1: Forces at upper-body base for various motions, base fixed.

Configuration	Trajectory	Payload	Acceleration	Forces at base
Torso vertical, Arms down	Torso R2 peak torque (4.5 Nm) to accelerate up to 100 deg/s	3 kg	28 rad/s ²	Fx: 740 N Fz: 525 N Torque: 368 Nm
Torso horizontal, Arms Down,	Torso R2 peak torque (-4.2 Nm) to decelerate from 100 to 0 deg/s.	3 kg	-55 rad/s ²	Fx: -145 N Fz: 1994 Nm Torque: -1071 Nm
	Static	3 kg	0	Fx: 0 N Fz: 525 N Torque: 248Nm
Starting at Torso vertical, arms horizontal and moving to torso horizontal, arms horizontal	Torso R2 peak torque (4.5 Nm) to accelerate up to 100 deg/s	3 kg	28 rad/s ²	Fx: 740 N Fz: 525 N Torque: 479 Nm
	Torso R2 peak torque (-4.0 Nm) to decelerate from -100 to 0 deg/s	3 kg	71 rad/s ²	Fx: 1890 N Fz: 154 N Torque: 1560 Nm
Starting at Torso horizontal, arms horizontal and moving to torso vertical, arms horizontal	Torso R2 peak torque (4.6 Nm) to accelerate up to -100 deg/s	3 kg	-12 rad/s ²	Fx: 0 N Fz: 834 N Torque: 698 Nm
	Torso R2 peak torque (-4.2 Nm) to decelerate from 100 to 0 deg/s	3 kg	-55 rad/s ²	Fx: -153 N Fz: 1994 N Torque: -1818 Nm
	Static	3 kg	0	Fx: 0 N Fz: 525 N Torque: -411 Nm

Appendix D

Tire Model

The wheel model used (developed at the DLR RM [84]) allows for a fairly detailed representation of the tire and tire-ground interaction. Different levels of analysis can be chosen representing different degrees of realism; the more realistic levels require greater knowledge about the wheel. In this study, level 4, ‘tread-tired wheel with slip dependent velocities and torques’ is used, as this models the important traction behaviour of the tire without requiring detailed tire specifications. A complete list of model settings is shown in Table D.1. The ground is modelled as a rigid plane.

Table D.1: Tire model parameters (unlisted model parameters remain at their default).

Parameter	Variable	Value
Mass	m	0.5 kg
Inertia	I_11	0.000948 kg·m ²
	I_22	0.00177 kg·m ²
Radius	r	0.1 m
Width	width	0.05 m
Radius of curvature	rCurvature	0.04 m
Minimum slip velocity for total slip	vSlide	0.1 m/s
Friction coefficient for rolling resistance	muRoll	0.045
Spring constant (normal direction)	cN	varied
Damping constant (normal direction)	dN	varied
Standard normal load	fN1	280 N
minimum longitudinal friction coeff. at fN = fN1	muMinLong1	0.65
minimum longitudinal friction coeff. at fN = 2·fN1	muMinLong2	0.40
coeff. of turning friction at fN = fN1	muTurn1	0.8
coeff. of turning friction at fN =2·fN1	muTurn2	0.73

The rolling coefficient of friction (0.045) is chosen to match value for industrial carpet (see Appendix E).

Turning friction in the model is calculated based on a representative particle located at $\frac{1}{4}$ of the length and width of the contact patch from the contact patch centre which creates a friction torque dependent on the normal force, the turning friction factor, and the turning velocity. Special provisions are made for small velocities to transition to zero turning torque. The turning friction factor was set at 0.8, a value for rubber on concrete from [120].

Appendix E

Propulsion System Calculations

Tire Properties affecting Propulsion

As the primary contact between the drive system and the environment, the tire material and geometry can greatly affect the performance of the propulsion system. In addition to its suspension characteristics, the proposed tire (Table 6.7) was chosen based on the following properties.

Geometry

The most significant geometric parameter of a tire in terms of its propulsion is its radius. Larger wheels have better traction and travel over bumps more easily, but require more space, have a higher mass and inertia, and require more torque at the wheel. Given the proven performance of the tires on the old platform, a similar type is proposed for use in this design with an increase in radius from 7.4 cm to 10 cm, or 35%, to improve step-passing capabilities and reduce rolling resistance.

The wider the tire, the better the ground adhesion due to the increased contact area; this increases traction but also causes higher scrubbing torque during steering. A 5 cm width is chosen.

Material

Tire material affects the rolling friction. In a study of wheelchair tires, properly inflated pneumatic tires have the lowest rolling resistance compared to polyurethane foam (15% more) and molded polyisoprene (40% more) [121], although it should be noted that the profile shapes of the tires was not the same. Pneumatic tires inflated only 75% have approximately 10% more rolling resistance than when fully inflated [105]. In the study, foam tires have greater wear resistance and lower mass, and a tapered foam tire profile was found to be more resistant to compression set, which is the failure of the tire to return to its unloaded shape in a short time period after prolonged compression. A foam-filled tire is chosen because it has low mass and the second-best suspension characteristics, as discussed in section 6.6, without the need to monitor tire pressure as with a pneumatic tire.

Requirements at the Wheel

High demand from the propulsion system is expected to occur during peak acceleration up to maximum velocity, accelerating up a grade, and when passing over steps. Simulation of the test trajectory (section 8.5.1.2) also shows a high torque requirement for both steering and drive actuators during caster reversal. The goal is to size actuators to be able to meet these peak demands (which in some cases have been limited by design to allow smaller actuators) while operating efficiently during typical conditions, considered to be constant peak velocity on level ground.

Constant Velocity

At constant velocity, the only resistance force, assuming air drag can be neglected at these low speeds, is friction. To determine the torque required to overcome friction, the coefficient of rolling friction must first be chosen. This constant depends on the type of tire and the surface it is rolling on, and must be empirically determined. Unfortunately, few reliable sources for this coefficient exist. Al-Eisawi et al. determine the coefficient for hard-rubber wheels on smooth concrete, tile, asphalt, and industrial carpet floors to be 0.0022, 0.0024, 0.0033, 0.0045 m respectively, and find that the harder the surface and the wheel, the lower the force of rolling friction [122]. Van der Woude et al. test a wheelchair with a pneumatic tire of the same radius at 400 kPa and a width of 0.05 m and find the normal force coefficient to overcome rolling friction to be 0.0105 for tarpaulin and 0.0292 for high pile carpet [123], which is equivalent to a rolling friction value of 0.00105 m and 0.00292 m respectively. In the face of these somewhat contradictory results, the maximum value (0.0045 m) is used as a conservative upper bound. The rolling resistance force $F_{friction}$ is defined as

$$F_{friction} = \frac{\mu_{roll} F_{normal}}{r} \quad (E.1)$$

where μ_{roll} is the rolling friction coefficient, F_{normal} is the normal force acting on the tire and r is its radius. The torque at the wheels, $\tau_{friction}$, to overcome the rolling resistance force is simply

$$\tau_{friction} = F_{friction} r \cdot \quad (E.2)$$

Substituting (E.1) into (E.2) and $m_{sys}g$ for the normal force, the torque simplifies to

$$\tau_{friction} = \mu_{roll} m_{sys} g \quad (E.3)$$

where m_{sys} is the system mass and g is the acceleration of gravity. On average, each wheel is expected to carry one quarter of the system mass, so the torque for each wheel, $\tau_{friction/wheel}$, is

$$\tau_{friction/wheel} = \mu_{roll} \frac{m_{sys}}{4} g \cdot \quad (E.4)$$

The steady-state wheel drive velocity for a maximum linear velocity of 1.67 m/s with a wheel radius, r , of 0.1 m, is found to be 16.67 rad/s (159 rpm) in 8.2.3.2. At a system mass of 130 kg (65 kg base, 50 kg for the upper-body and a 15 kg load) and the maximum velocity, the torque and power required at the wheels for all four wheels combined to overcome rolling friction on industrial carpet is 5.74 Nm and 96 W respectively.

Acceleration

The steady-state wheel drive acceleration, $\ddot{\omega}_{wheel_max}$, for the desired maximum linear acceleration, a_{max} , of 2 m/s², is found to be 20 rad/s² with the equation

$$\dot{\omega}_{wheel_max} = a_{max} / r \cdot \quad (E.5)$$

Using Newton's 2nd law and the maximum desired acceleration, the net force that needs to be applied to the system can be determined:

$$\sum F = m_{sys} a_{max} \quad (E.6)$$

On a level surface, the net force is the applied force F_{app} minus the rolling resistance friction force. Air drag is again negligible.

$$F_{app} - F_{friction} = m_{sys} \dot{\omega}_{wheel_max} r . \quad (E.7)$$

The forces are converted to moments at the wheel axis by multiplying by the wheel radius:

$$\tau_{accel} - \tau_{friction} = (F_{app} - F_{friction}) r . \quad (E.8)$$

Thus, by substituting (E.7) into (E.8), the torque required for maximum acceleration, τ_{accel} , becomes

$$\tau_{accel} = m_{sys} \dot{\omega}_{wheel_max} r^2 + \tau_{friction} \quad (E.9)$$

which is 31.9 Nm for all the wheels together. At maximum velocity, this results in a peak acceleration power requirement of 531 W. Per wheel, the torque and power for maximum acceleration is thus 8.0 Nm and 133 W respectively.

Slope

On an inclined surface, the system must also overcome a component of the gravitational force such that the net force with the desired acceleration up a slope, a_{slope} , of 0.5 m/s², is

$$F_{app} - F_{friction} = m_{sys} (a_{slope} - g \sin \theta) \quad (E.10)$$

where θ is the slope angle. By substituting

$$F_{friction} = \mu_{roll} mg \cos \theta \quad (E.11)$$

for the friction force and multiplying (E.10) by the radius, the applied torque τ_{app} can be expressed as

$$\tau_{app} = m_{sys} (\mu_{roll} g \cos \theta + a_{slope} - g \sin \theta) r . \quad (E.12)$$

The maximum slope for a wheelchair ramp is 4.8°, which results in a torque of 17.74 Nm or 4.4 Nm per wheel.

Step

As determined in Chapter 5, the torque requirements depend on step height and tire radius as well as the tire elasticity. For the system as designed, the maximum torque was found to be 17.1 Nm for a set of two wheels, or 8.6 Nm per wheel.

Caster Reversal

As determined by the test trajectory simulation, drive torque during caster reversal, which occurs when the direction of motion changes, can reach up to 15.7 Nm per wheel with the maximum payload.

Requirements for the Drivetrain

Peak Requirements

In order to choose an appropriate motor/geartrain combination, the momentary peak torque and velocity at the geartrain and motor need to be known, as well as the maximum continuous or rated torque. These will be higher than the respective quantities at the wheel due to mechanical losses in the motor and geartrain. Furthermore, the peak and average motor electrical power is of interest for selecting power and energy system components (see section 9.3); these will be higher than the mechanical power output at the motor due to electrical losses in the motor and its controller.

Figure E.1 describes the selection process and make-up of the peak torque, rated torque and the constant velocity torque values. Of the wheel torque requirements described above for acceleration, slopes, steps and caster reversal, the latter is found to be the maximum and is set as the peak torque, with a value of 15.7 Nm at the wheel, per wheel.

The continuous torque that must be supplied to the wheel is set to be half the torque required for maximum acceleration at maximum speed, or 4.0 Nm. Situations that exceed this torque, such as step climbing or maximum acceleration, are expected to be of short duration such that the motor can supply the necessary power without overheating.

The torque and power flow from electrical input at the motor controller to mechanical output at the wheel is shown for acceleration in Figure E.2 and for constant velocity in Figure E.3. The calculations for each of the steps are detailed below.

The torque at the input end of the gearbox, τ_{gear} , depends on the gear ratio, n_{ratio} , and the geartrain efficiency, η_{gear} ,

$$\tau_{gear} = \frac{\tau_{wheel}}{\eta_{gear} n_{ratio}}. \quad (E.13)$$

Geartrain efficiency depends on the type of gearing. If harmonic drive gears are used, efficiency values depend on gear ratio, input speed, load torque, temperature and lubricant, ranging up to about 85% but generally around 70% for high speed operation at rated torque. Planetary geartrain efficiency on the other hand does not depend on speed. It can reach efficiencies of up to 95% for a single stage, with two-stage efficiencies around 85% and three-stage efficiencies around 75%.

The output torque required from the drive motors, $\tau_{motmech}$, is the gearbox input torque plus inertial loads from the geartrain and motor,

$$\tau_{motmech} = \tau_{gear} + \dot{\omega}_{max} (J_{gear} + J_{motor}) \quad (E.14)$$

Where J_{gear} and J_{motor} are the geartrain inertia reflected to the input axis and motor rotor inertia respectively. The geartrain and motor inertia naturally only play a role during acceleration. Since these inertias are fixed for a given geartrain and motor, the losses will become proportionally smaller at higher loads. The smaller the motor inertia, the less torque needs to be expended to accelerate it and the more is available for performing the task. A large difference between motor inertia and system inertia reflected to the motor can cause problems for control, although it is less of an issue

when no position control is required. The value of the reflected inertia changes depending on the gear ratio.

The motor electrical power P_{elec} is a combination of the mechanical power, P_{mech} , and the power losses, P_{losses} ,

$$P_{elec} = P_{losses} + P_{mech} \quad (E.15)$$

The losses can be assumed to consist only of resistance losses in the motor winding and are defined as

$$P_{losses} = \left(I_{noload} + \frac{\tau_{motmech}}{k_i} \right) R \quad (E.16)$$

where I_{noload} is the motor no load current, k_i is the motor torque constant, and R is the motor winding resistance. The size of these parameters will depend on the motor. The resistance losses will get proportionally smaller as load increases because the no load current stays constant.

Finally, to determine the power demand on the energy system, motor controller efficiency, η_{ctrl} , needs to be considered as well to find the power input to the controller, P_{ctrl} ,

$$P_{ctrl} = \frac{P_{elec}}{\eta_{ctrl}}.$$

Controller efficiency is typically around 95%; the Copley controller used on the experimental cart reaches 97% at maximum continuous load [124].

Average Requirements

Determining the average torque and power requirements of the drive system is difficult, since it depends on the trajectory style and the platform loading. A trajectory with many periods of acceleration and the maximum payload will have a higher average power requirement than a trajectory at slow constant speeds. The test trajectory in section 8.5.1.2 represents a fairly demanding trajectory, and it will be used to determine the average power requirement of the drive and steering actuators. For this purpose, the RMS torque and power of each steering and drive actuator is determined for the entire 24 s trajectory and then an average over the four wheels for steering and drive is taken; the results are shown in Table E.1. The simulation only gives the mechanical torque and power at the wheel before any losses internal to the system; to determine the electrical power needed at the motor, it is estimated that average efficiency of electrical input to mechanical output is 50%, consisting of 80% geartrain efficiency, 66% motor efficiency and 95% controller efficiency.

Table E.1: RMS torque and power for drive and steering actuators during test trajectory.

Actuator	Torque at Wheel (Nm)	Power at Wheel (W)	Estimated Electrical Power (W)
Drive	3.07	31.7	64
Steer	0.79	6.68	14

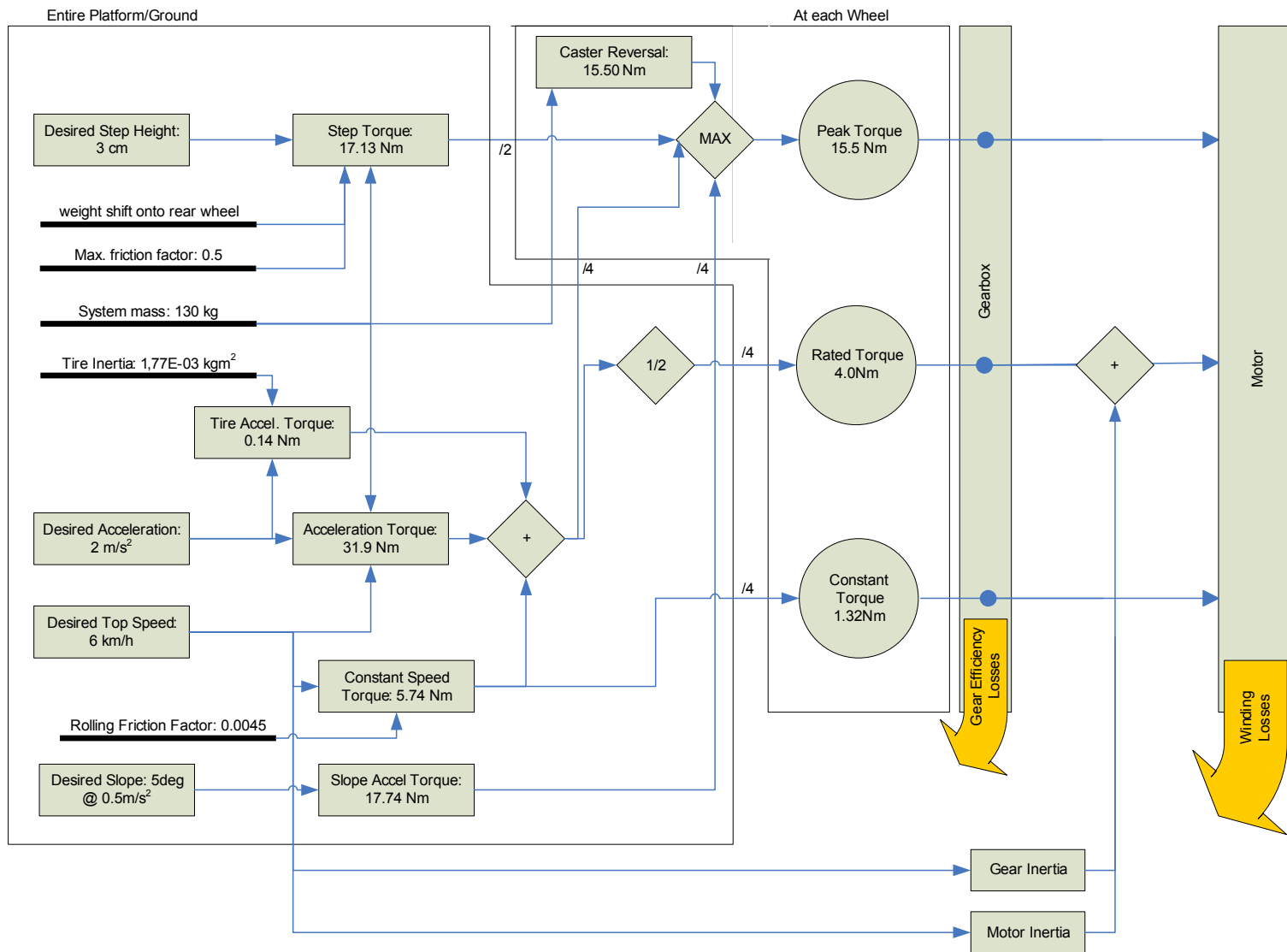


Figure E.1: Process for determining motor torque requirements.

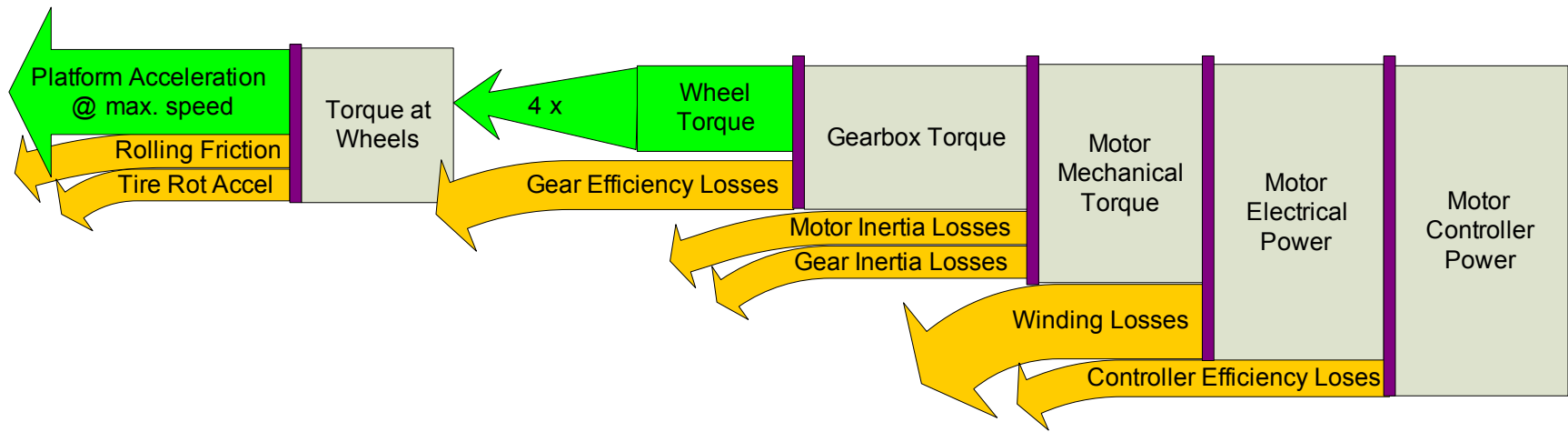


Figure E.2: Steady-state drive actuator power flow for platform acceleration.

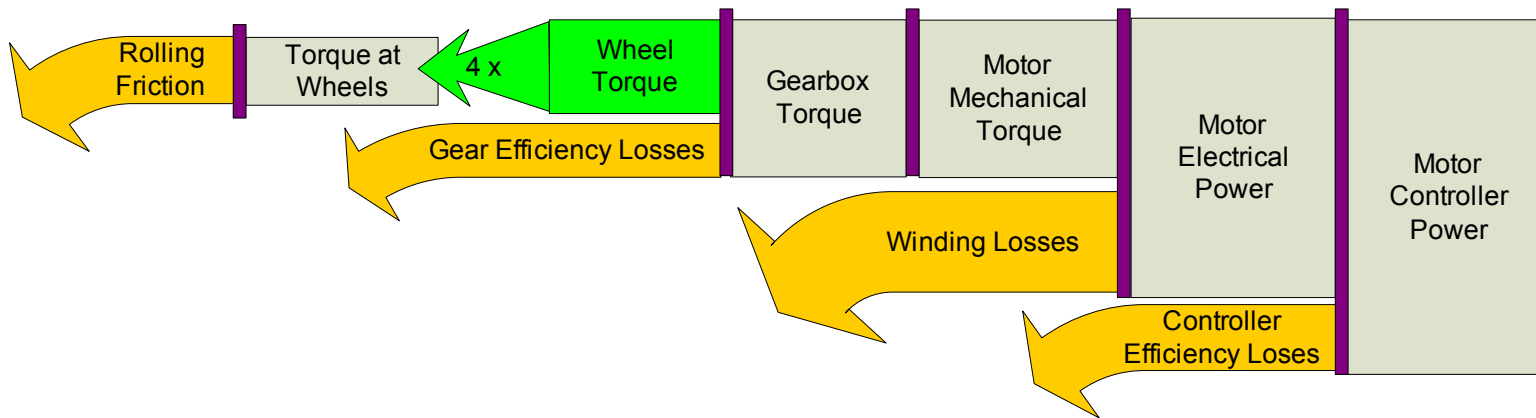


Figure E.3: Steady-state drive actuator power flow for platform moving at constant velocity.

Appendix F

Configuration Evaluation Matrix

In Table F.1, the evaluation matrix used to choose the overall platform configuration is shown.. Each contains a configuration that is evaluated for different criteria listed at the top, with a score summary on the last page of the table.

Table F.1: Configuration evaluation matrix (continues onto next 3 pages).

Configuration									
Configuration Number	# of ground contact points	ground contact type	Propulsion DoFs	Steering DoFs	Additional DoFs	Additional DoF type	Total number of actuators	Comments	
1.2a	1	ball	3		0		3		
1.2b	1	ball	3		0		3		
2.4	2	standard wheels	2	0	0		2	segway type	
2.5	2.5	standard wheels	2	0	1	rotary	3	support leg on rotational joint	
2.6	2.5	standard wheels	2	0	2	rotary, prismatic	4	support leg with rot and prism joint	
2.7	2.5	standard wheels	2	0	3	rotary hip, rotary & prismatic leg	5	hip joint, support leg with rot and prism joint	
3.1a	3	standard wheels, steered	3	3	0		6	static stable with three steered wheels, same footprint as dynamic	
3.1b	3	standard wheels, steered	3	3	0		6	static stable with three steered wheels, same mass as dynamic	
3.2	3	standard wheels, steered	3	3	1	prismatic	7	variable footprint with one actuator; leg length is height -0.1, max. 70deg extended	
3.3	3	standard wheels, steered	3	3	4	1 prismatic for extension, 3 for leg length	10	variable footprint with one actuator for extension, prismatic for leg length	
4.1	4	standard wheels, steered	4	4	0		8	static stable with four steered wheels, same footprint as two-wheel dynamic	
4.1	4	standard wheels, steered	4	4	0		8	static stable with four steered wheels	
4.1	4	standard wheels, steered	4	4	0		8	static stable with four steered wheels, optimized	
4.2a	4	standard wheels, steered	4	4	1	prism	9	variable footprint with one actuator; leg length is height -0.1, max. 70deg extended	
4.2b	4	standard wheels, steered	4	4	1	prism	9	variable footprint with one actuator; leg length is height -0.1, max. 70deg extended, optimized	
4.3	4	standard wheels, steered	4	4	6	2 prism for extension, 4 for leg length	14	variable footprint with one actuator for extension, prismatic for leg length	

Configuration Number	Geometry														Mobility									
															Category weight →									
	height		width		breadth		CM height	wheel radius	actuator mass	actuator volume estimate	fixed mass	total mass	support distance req'd to balance 15kg horizontally extended	can platform statically handle 3kg fully extended?	sub category weight	min footprint area (ankle height)	turning footprint (largest min. dimension as diameter)	Holonomic/Omni/Steered	reach at 3kg load (over shortest nesc distance from	Category				
min (m)	max (m)	min (m)	max (m)	min (m)	max (m)	(m)	(m)	(kg)	L	(kg)	(kg)	m		(m^2)	rank	m^2	rank	1-3	rank	rank	rank			
															4		1		3		1	9		
															13%		3%		10%		3%			
1.2a	0.6	0.6	0.3	0.3	0.3	0.3	0.4	0.15	6	6.0	50	56	0.392	FALSE	0.071	0.88	0.071	0.91	3	1.00	1.14	0.05	0.73	
1.2b	0.6	0.6	0.2	0.2	0.2	0.2	0.4	0.1	6	6.0	50	56	0.392	FALSE	0.031	1.00	0.031	1.00	3	1.00	1.14	0.05	0.78	
2.4	0.6	0.6	0.4	0.4	0.2	0.2	0.4	0.1	4	4.0	50	54	0.400	FALSE	0.080	0.86	0.126	0.79	2	0.33	1.13	0.00	0.49	
2.5	0.45	0.6	0.4	0.4	0.2	0.7	0.4	0.1	6	6.0	50	56	0.392	FALSE	0.080	0.86	0.126	0.79	1.5	0.00	1.16	0.13	0.39	
2.6	0.6	0.6	0.4	0.4	0.2	0.8	0.4	0.1	8	8.0	50	58	0.385	TRUE	0.080	0.86	0.126	0.79	2	0.33	1.16	0.16	0.51	
2.7	0.6	0.6	0.4	0.7	0.2	0.8	0.4	0.1	10	10.1	50	60	0.378	TRUE	0.080	0.86	0.126	0.79	2	0.33	1.17	0.19	0.51	
3.1a	0.4	0.4	0.4	0.4	0.2	0.2	0.3	0.1	12	12.1	146	158	0.200	TRUE	0.120	0.74	0.126	0.79	2.5	0.67	1.35	1.00	0.66	
3.1b	0.4	0.4	0.4	0.4	0.78	0.78	0.3	0.1	12	12.1	45	57	0.389	TRUE	0.236	0.39	0.478	0.00	2.5	0.67	1.16	0.14	0.41	
3.2	0.6	0.6	0.34	1.04	0.29	0.9	0.4	0.1	14	14.1	50	64	0.365	TRUE	0.118	0.74	0.091	0.87	2.5	0.67	1.19	0.25	0.58	
3.3	0.5	0.6	0.34	1.04	0.29	0.9	0.35	0.1	20	20.1	50	70	0.347	TRUE	0.118	0.74	0.091	0.87	2.5	0.67	1.20	0.33	0.59	
4.1	0.4	0.4	0.4	0.4	0.2	0.2	0.3	0.1	16	16.1	142	158	0.200	TRUE	0.160	0.62	0.126	0.79	2.5	0.67	1.35	1.00	0.61	
4.1	0.4	0.4	0.4	0.4	0.72	0.72	0.3	0.1	16	16.1	50	66	0.359	TRUE	0.368	0.00	0.407	0.16	2.5	0.67	1.19	0.28	0.25	
4.1	0.4	0.4	0.5	0.5	0.24	0.24	0.3	0.1	16	16.1	101	117	0.250	TRUE	0.220	0.44	0.196	0.63	2.5	0.67	1.30	0.77	0.50	
4.2	0.6	0.6	0.3	0.82	0.3	0.82	0.4	0.1	18	18.1	50	68	0.353	TRUE	0.150	0.65	0.071	0.91	2.5	0.67	1.20	0.31	0.54	
4.2	0.6	0.6	0.24	0.78	0.37	0.88	0.4	0.1	18	18.1	50	68	0.353	TRUE	0.138	0.68	0.110	0.82	2.5	0.67	1.20	0.31	0.56	
4.3	0.6	0.6	0.3	0.82	0.3	0.82	0.4	0.1	28	28.1	50	78	0.325	TRUE	0.150	0.65	0.071	0.91	2.5	0.67	1.23	0.43	0.56	

Configuration Number	Stability											Complexity											
	10 36%											6 21%											
	min distance from CM to tip edge in most stable config (supports out, torso vert)		max distance from CM to tip edge in most stable config (supports out, torso vert)		max footprint area		min. horizontal tipover force at 60cm from ground		max. tipover force		Category	# of actuators plus # of DOFS	Control system (1=low, 2=medium, 3=high)	Mechanical Design (1=low, 2=medium, 3=high)	Emergency Stop Design (1=low, 2=medium, 3=high)	Approx. Volume	Approx. Available Volume 30% - drives & drive energy	Category					
(m)	rank	(m)	rank	rank	N	rank	N	rank	rank	rank	rank	rank	rank	rank	L	L	rank	rank					
	3		2	1		3		2	11		2		3		2		1		9				
	10%		6%	3%		10%		6%			5%		7%		5%		2%						
1.2a	0.000	0.00	0.000	0.00	0.071	0.06	173.3	0.07	173.3	0.05	0.03	3	0.92	3	0.00	1.5	0.75	3.00	0.00	42.4	2.3	0.07	0.37
1.2b	0.000	0.00	0.000	0.00	0.031	0.00	104.0	0.00	104.0	0.00	0.00	3	0.92	3	0.00	1.5	0.75	3.00	0.00	18.8	-4.7	0.00	0.37
2.4	0.000	0.00	0.200	0.33	0.080	0.07	102.0	0.00	340.1	0.17	0.10	2	1.00	2	0.50	1.0	1.00	2.00	0.50	48.0	39.7	0.45	0.67
2.5	0.128	0.29	0.467	0.77	0.140	0.17	222.2	0.11	808.8	0.49	0.36	3	0.92	2.5	0.25	1.5	0.75	2.00	0.50	36.3	25.9	0.31	0.51
2.6	0.129	0.30	0.533	0.88	0.160	0.20	228.4	0.12	941.8	0.59	0.40	4	0.83	2.5	0.25	2.0	0.50	2.00	0.50	48.0	35.5	0.41	0.44
2.7	0.214	0.49	0.533	0.88	0.280	0.38	384.5	0.26	959.2	0.60	0.51	5	0.75	2.5	0.25	3.0	0.00	2.50	0.25	48.0	33.5	0.39	0.28
3.1a	0.094	0.22	0.100	0.17	0.120	0.14	321.1	0.20	340.6	0.17	0.19	6	0.67	1	1.00	1.0	1.00	1.00	1.00	16.0	-3.7	0.01	0.81
3.1b	0.129	0.29	0.390	0.65	0.236	0.31	226.0	0.12	682.3	0.40	0.33	6	0.67	1	1.00	1.0	1.00	1.00	1.00	62.4	46.0	0.51	0.81
3.2	0.302	0.69	0.603	1.00	0.472	0.67	562.0	0.43	1124.0	0.71	0.68	7	0.58	2	0.50	2.5	0.25	1.50	0.75	30.0	11.4	0.16	0.44
3.3	0.302	0.69	0.603	1.00	0.472	0.67	885.9	0.73	1477.4	0.96	0.80	10	0.33	2.5	0.25	3.0	0.00	1.50	0.75	25.0	0.1	0.05	0.24
4.1	0.200	0.46	0.224	0.37	0.160	0.20	681.1	0.54	761.5	0.46	0.44	8	0.50	1	1.00	1.0	1.00	1.00	1.00	32.0	8.3	0.13	0.78
4.1	0.200	0.46	0.412	0.68	0.368	0.51	379.3	0.26	781.1	0.47	0.45	8	0.50	1	1.00	1.0	1.00	1.00	1.00	115.2	94.4	1.00	0.78
4.1	0.250	0.57	0.277	0.46	0.220	0.29	680.6	0.54	754.9	0.46	0.49	8	0.50	1	1.00	1.0	1.00	1.00	1.00	48.0	25.6	0.31	0.78
4.2a	0.412	0.94	0.583	0.97	0.680	0.99	795.4	0.65	1124.8	0.71	0.83	9	0.42	2	0.50	2.5	0.25	1.50	0.75	54.0	31.2	0.36	0.40
4.2b	0.438	1.00	0.587	0.97	0.686	1.00	845.7	0.69	1133.3	0.72	0.86	9	0.42	2	0.50	2.5	0.25	1.50	0.75	53.8	31.0	0.36	0.40
4.3	0.412	0.94	0.583	0.97	0.680	0.99	1176.7	1.00	1534.0	1.00	0.98	14	0.00	2.5	0.25	3.0	0.00	1.50	0.75	54.0	20.8	0.26	0.17

Configuration Number	Power & Energy							SUMMARY						
	3 11%							28						
	W	J	rank	L	1-3	rank	rank	weight	Mobility	Stability	Complexity	Power and Energy	TOTAL SCORE	Rank
			4			1	5	points/cat	9	11	9	4		
			9%			2%								
1.2a	218	174	0.98	4.35	3	0.00	0.78		6.58	0.32	2.22	2.35	11.48	16
1.2b	218	174	0.98	4.35	3	0.00	0.78		7.05	0.00	2.22	2.35	11.63	15
2.4	214	172	1.00	4.29	2.5	0.25	0.85		4.42	0.97	4.00	2.55	11.94	14
2.5	218	174	0.98	4.35	2	0.50	0.88		3.55	3.56	3.06	2.65	12.81	13
2.6	221	177	0.96	4.42	2	0.50	0.87		4.58	3.98	2.61	2.61	13.78	11
2.7	224	179	0.94	4.48	2	0.50	0.85		4.61	5.09	1.67	2.56	13.93	10
3.1a	381	305	0.00	7.63	1	1.00	0.20		5.95	1.87	4.89	0.60	13.30	12
3.1b	219	175	0.97	4.38	1	1.00	0.98		3.71	3.31	4.89	2.93	14.84	8
3.2	230	184	0.90	4.61	1	1.00	0.92		5.22	6.77	2.61	2.77	17.37	4
3.3	240	192	0.85	4.80	1.5	0.75	0.83		5.30	8.04	1.44	2.48	17.27	5
4.1	381	305	0.00	7.63	1	1.00	0.20		5.47	4.40	4.67	0.60	15.14	7
4.1	234	187	0.88	4.67	1	1.00	0.91		2.28	4.52	4.67	2.72	14.19	9
4.1	314	252	0.40	6.29	1	1.00	0.52		4.53	4.95	4.67	1.56	15.71	6
4.2a	237	189	0.87	4.74	1	1.00	0.89		4.90	8.28	2.39	2.68	18.24	2
4.2b	237	189	0.87	4.74	1	1.00	0.89		5.04	8.60	2.39	2.68	18.71	1
4.3	253	202	0.77	5.06	1.5	0.75	0.77		5.02	9.77	1.00	2.30	18.09	3

Bibliography

- [1] Arai, T., 1996, “Robots with Integrated Locomotion and Manipulation and Their Future,” *Proc. Int. Conf. Intelligent Robots and Systems*, **2**, pp. 541—545.
- [2] Ott, Ch., Eiberger, O., Friedl, W., Bäuml, B., Hillenbrand, U., Borst, Ch., Albu-Schäffer, A., Brunner, B., Hirschmüller, H., Kielhöfer, S., Konietzschke, R., Suppa, M., Wimböck, T., Zacharias, F., Hirzinger, G., 2006, “A Humanoid Two-Arm System for Dexterous Manipulation,” *Proc. IEEE-RAS Int. Conf. Humanoid Robots*, pp. 276—283.
- [3] Hirzinger, G., Sporer, N., Albu-Schäffer, A., Hähle, M., Krenn, R., Pascucci, A., Schedl, M., 2002, “DLR’s torque-controlled light weight robot III - are we reaching the technological limits now?,” *Proc. IEEE Int. Conf. Robotics and Automation*, **2**, pp. 1710—1716.
- [4] “Data sheet of DLR Hand II,” DLR Robotics and Mechatronics Institute. Online: http://www.dlr.de/rm/desktopdefault.aspx/tabid-398/535_read-970/ (May 2007)
- [5] Friedl, W., conversation, July 2006, DLR Robotic and Mechatronics Institute, Oberpfaffenhofen, Germany.
- [6] Hillenbrand, U., Ott, C., Brunner, B., Borst, C., Hirzinger, G., 2004 “Towards Service Robots for the Human Environment: the Robutler” *Mechatronics & Robotics*, pp. 1497—1502.
- [7] Hanebeck, U. D., Fischer, C., Schmidt, G., 1997, “ROMAN: A Mobile Robotic Assistant for Indoor Service Applications,” *Proc. Int. Conf. Intelligent Robots and Systems*, **2**, pp. 518—525.
- [8] Siegwart, R., Nourbakhsh, I., 2004, *Autonomous Mobile Robots*, “Locomotion,” MIT Press, Cambridge, Massachusetts. pp.13—46, Chap. 2.
- [9] Siegwart, R., Nourbakhsh, I., 2004, *Autonomous Mobile Robots*, “Mobile Robot Kinematics,” MIT Press, Cambridge, Massachusetts. pp.47—88, Chap. 3.
- [10] Angeles, J., López-Cajún, C.S., 1992, “Kinematic Isotropy and the Conditioning Index of Serial Robotic Manipulators,” *Int. J. Robotics Research*, **11**(5), pp. 560—571.
- [11] Bétourné, A. and Campion, G., 1996, “Kinematic Modelling of a Class of Omnidirectional Mobile Robots”, *Proc. Int. Conf. Robotics and Automation*, pp. 3631—3636.
- [12] Bétourné, A. and Campion, G., 1996, “Dynamic Modelling and Control Design of a Class of Omnidirectional Mobile Robots,” *Proc. Int. Conf. Robotics and Automation*, pp. 2810—2815.

- [13] Alexander, J.C., Maddocks, J.H., 1989, "On the Kinematics of Wheeled Mobile Robots," *Int. J. Robotics Research*, **8** (5), pp. 15—27.
- [14] Betourne, A., Fournier, A., 1993, "Kinematics, dynamics and control of a conventional wheeled omnidirectional mobile robot", *Proc. Int. Conf. Systems, Man and Cybernetics*, **2**, pp. 276—281.
- [15] Borenstein, J., 1995, "Control and Kinematic Design of Multi-degree-of-freedom Mobile Robots with Compliant Linkage," *IEEE Trans. Robotics and Automation*, **11**(1), pp. 21—35.
- [16] Holmberg, R., Khatib, O., 2000, "Development and Control of a Holonomic Mobile Robot for Mobile Manipulation Tasks," *Int. J. of Robotics Research*, **19**(11), pp. 1066—1074.
- [17] Reister, D., 1993, "Position and Constraint Force Control of a Vehicle with Two or More Steerable Drive Wheels," *IEEE Trans. Robotics and Automation*, **9**(6), pp. 723—731.
- [18] Spenko, M., Yu, H., Dubowsky, S., 2002, "Analysis and Design of an Omnidirectional Platform for Operation on Non-Ideal Floors," *Conf. Robotics and Automation*, **1** pp. 726—731.
- [19] Mori, Y., Nakano, E., Takahashi, T., Takayama, K., 1996, "A Study of the Mechanism and Control of Omni-Directional Vehicle," *Proc. Int. Conf. Intelligent Robots and Systems*, **1**, pp. 52—59.
- [20] Mori, Y., Nakano, E., Takahashi, T., 2002, "Mechanism, Control and Design Methodology of the Nonholonomic Quasi- mnidirectional Vehicle 'ODV9'," *Int. J. Robotics Research*, **21**(5—6), pp. 511—525.
- [21] Lee, J. H., Yuta, S., Koyanagi, E., Yi, B.-J., 2005, "Command System and Motion Control for Caster-type Omni-directional Mobile Robot," *Proc. Int. Conf. Intelligent Robots and Systems*, pp. 1862—1868.
- [22] Yu, H., Dubowsky, S., Skwersky, A., 2004, "Omni-directional mobility using active split offset castors," *ASME J. Mechanical Design*, **126** (5) pp. 822—829.
- [23] Jung, M.-J., Kim, J.-H., 2002, "Mobility Augmentation of Conventional Wheeled Bases for Omnidirectional Motion," *IEEE Trans. Robotics and Automation*, **18**(1), pp. 81—87.
- [24] Wada, M., Takagi, A., Mori, S., 2000, "Caster Drive Mechanisms for Holonomic and Omnidirectional Mobile Platforms with no Over Constraint," *Proc. IEEE Int. Conf. Robotics & Automation*, **2**, pp. 1531—1538.

- [25] Han, F., Yamada, T., Watanabe, K., Kiguchi, K., 2000, "Construction of an Omnidirectional Mobile Robot Platform Based on Active Dual-Wheel Caster Mechanisms and Development of a Control Simulator," *J. Intelligent and Robotic Systems*, **29**, 257—275.
- [26] Yamada, T., Watanabe, K., Kiguchi, K., 2001, "Dynamic Model and Control for a Holonomic Omnidirectional Mobile Robot," *Autonomous Robots*, **11**, pp. 173—189.
- [27] "Omni Wheel," Kornylak Corp. Online: <http://www.omniwheel.com/omniwheel/omniwheel-lightweight.htm> (July 2007).
- [28] Ferrière, L., Raucent, B., Campion, B., 1996, "Design of Omnimobile Robot Wheels," *Proc. IEEE Int. Conf. Robotics and Automation*, **4**, pp. 3664—3670.
- [29] Asama, H., Sato, H., Bogoni, L., Kaetsu, H., Matsumoto, A., Endo, I., 1995, "Development of an Omni-Directional Mobile Robot with 3 DoF Decoupling Drive Mechanism," *IEEE Int. Conf. Robotics and Automation*, **2**, pp. 1925—1930.
- [30] Ferriere, L., Raucent, B., Samin, J.-C., 1997, "Rollmobs, A New Omnimobile Robot," *Proc. Int. Conf. Intelligent Robots and Systems*, **2**, pp. 913—918.
- [31] Ferrière, L., Raucent, B., 1998, "ROLLMOBS, a new Universal Wheel Concept," *Proc. IEEE Int. Conf. Robotics and Automation*, **3**, pp. 1877—1882.
- [32] Ferrière, L., Campion, G., Raucent, B., 2001, "ROLLMOBS, a New Drive System for Omnimobile Robots," *Robotica*, **19**, pp. 1—9.
- [33] West, M., Asada, H., 1995, "Design and Control of Ball Wheel Omnidirectional Vehicles," *Proc. Int. Conf. Robotics and Automation*, **2**, pp. 1931—1939.
- [34] Lee, Y.C., Lee, D., Chung, J., Velinsky, S., 2007, "Control of a Redundant, Reconfigurable Ball Wheel Drive Mechanism for an Omnidirectional Mobile Platform," *Robotica*, **25**, pp. 385—395.
- [35] Pin, F., Killough, S., 1994, "A New Family of Omnidirectional and Holonomic Wheeled Platforms for Mobile Robots," *IEEE Trans. Robotics and Automation*, **10** (4), pp. 480—490.
- [36] Diegel, O., Badve, A., Bright, G., Potgieter, J., Tlale, S., 2002, "Improved Mecanum Wheel Design for Omni-directional Robots," *Australasian Conf. Robotics and Automation*, W. Friedrich & P. Lim, eds., pp. 117—121.

- [37] Byun, K.S., Kim, S.J., Song, J.B., 2001, "Design of Continuous Alternate Wheels for Omnidirectional Mobile Robots," *Proc. IEEE Int. Conf. Robotics and Automation*, **1**, pp. 767–772.
- [38] Halme, A., Leppänen, I., Salmi, S., 1999, "Development of WorkPartner-robot – design of actuating and motion control system," *Proc. 2nd Int. Conf. Climbing and Walking Robots*, G.S. Virk et al., eds., Wiley.
- [39] Halme, A., Leppänen, I., Montonen, M., Ylönen, S., 2001, "Robot motion by simultaneous wheel and leg propulsion," *Proc. 4th Int. Conf. Climbing and Walking Robots*, pp. 1013–1020.
- [40] Wood, C., Riche, S., Frandsen, M., Davidson, M., Maxfield, R., Keller, J., Day, B., Mecham, M., Moore, K., 2000, "Mechatronic Design and Integration for a Novel Omni-directional Robotic Vehicle," *Proc. 7th Mechatronics Forum and Int. Conf.*, Atlanta, USA.
- [41] Takita, Y., Shimoi, N., Date, H., 2004, "Development of a wheeled mobile robot 'octal wheel' realized climbing up and down stairs," *Proc. IEEE Int. Conf. Intelligent Robots and Systems*, **3**, 2440–2445.
- [42] Adachi, H., Koyachi, N., 2001, "Development of a Leg-Wheel Hybrid Mobile Robot and its Step-Passing Algorithm," *Proc. IEEE Int. Conf. Intelligent Robots and Systems*, **2**, pp. 728–733.
- [43] Chugo, D., Kawabata, K., Kaetsu, H., Asama, H., Mishima, T., 2003, "Development Of Omni-Directional Vehicle With Step-Climbing Ability," *IEEE Int. Conf. Robotics and Automation*, **3**, pp. 3849–3854.
- [44] Rehnmark, F., Ambrose, R., Michael Goza, S., Junkin, L., Neuhaus, P., Pratt, J., 2005, "Centaur: a mobile dexterous humanoid for surface operations," *Proc. SPIE, Unmanned Ground Vehicle Technology VII*, Gerhart, et al., eds., pp. 315–323.
- [45] Wada, M., Asada, H., 1999, "Design and Control of a Variable Footprint Mechanism for Holonomic Omnidirectional Vehicles and its Application to Wheelchairs," *IEEE Trans. Robotics And Automation*, **15**(6), pp. 978–989.
- [46] Song, J.-B., Byun, K.-S., 2004, "Design and Control of a Four-Wheeled Omnidirectional Mobile Robot with Steerable Omnidirectional Wheels," *J. Robotic Systems*, **21**(4), pp. 193–208.

- [47] Rollins, E., Luntz, J., Foessel, A. Shamah, B., and Whittaker, W., 1998, “Nomad: A Demonstration of the Transforming Chassis,” *Proc. IEEE Int. Conf. Robotics and Automation*, **1**, pp. 611–617.
- [48] Apostolopoulos, D., 2001, “Analytical Configuration of Wheeled Robotic Locomotion,” Ph.D. thesis, CMU-RI-TR-01–08, Carnegie Mellon Univ., Pittsburgh, PA.
- [49] Hirose, S., Fukushima, E., Damoto, R., and Nakamoto, H., “Design of Terrain Adaptive Versatile Crawler Vehicle HELIOS-VI,” *Proc. IEEE Int. Conf. Intelligent Robots and Systems*, **3**, pp. 1540–1545.
- [50] Michaud, F., Létourneau, D., Arsenault, M., Bergeron, Y., Cadrin, R., Gagnon, F., Legault, M., Millette, M., Paré, J., Tremblay, M., Lepage, P., Morin, Y., Bisson, J., Caron, S., 2005, “Multi-Modal Locomotion Robotic Platform Using Leg-Track-Wheel Articulations,” *Autonomous Robots*, **18**, pp. 137–156.
- [51] Bischoff, R., 1997, “HERMES – A Humanoid Mobile Manipulator for Service Tasks,” *Proc. Int. Conf. Field and Service Robots*, Canberra, Australia.
- [52] “About the Robotic Mobility Platform,” Segway Inc., available online: <http://www.segway.com/products/rmp/> (July 2007).
- [53] Nguyen, H., Morrell, K., Mullens, K., Burmeister, A., Miles, S., Farrington, N., Thomas, K., Gage, D., 2004, “Segway Robotic Mobility Platform,” *Proc SPIE, Mobile Robots XVII*, Gage, D., ed., **5609**, pp. 207–220.
- [54] Brooks, R., Aryananda, L, Edsinger, A., Fitzpatrick, P., Kemp, C., O’Reilly, U.-M., Torres-Jara, E., Varshavskaya, P., and Weber, J., 2004, “Sensing And Manipulating Built-For-Human Environments,” *Int. J. Humanoid Robotics*, **1**(1), pp. 1–28.
- [55] Goza, S., Ambrose, R., Diftler, M., Spain, I., 2004, “Telepresence Control of the NASA/DARPA Robonaut on a Mobility Platform,” *Proc. SIGCHI Conf. on Human Factors in Computing Systems*, **6**(1), pp. 623–629.
- [56] Benjamin, B., “A Report on the Segway’s Performance as a Robotic Mobility Platform,” Technical Report, GRASP Lab, University of Pennsylvania, <http://www.cis.upenn.edu/marsteams/Segway/Segway%20Report.doc> (July 2006).

- [57] , Grasser, F., D'Arrigo, A., Colombi, S., and Rufer, A., 2002, "JOE: A Mobile, Inverted Pendulum," *Ieee Trans.on Industrial Electronics*, **49**(1), pp. 107–114.
- [58] "Overview of Partner Robots," Toyota Motor Corporation, <http://www.toyota.co.jp/en/special/robot/> (July 2007).
- [59] Thibodeau, B., Deegan, P., Grupen, R., 2006, "Static Analysis of Contact Forces With a Mobile Manipulator," *Proc. IEEE Int. Conf. Robotics and Automation*, Orlando, FL, pp. 4007–4012.
- [60] "Hitachi's Robot 'EMIEW'," Hitachi Ltd., online: <http://www.hqrd.hitachi.co.jp/merle/emiew.cfm> (July 2007).
- [61] Lauwers, T., Kantor, G., Hollis, R., 2005, "One is Enough!," *Proc. 12th Intl. Symp. Robotics Research*, San Fransisco, USA.
- [62] Nakajima, R., Tsubouchi, T., Yuta, S., Koyanagi, E., 1997, "A Development of a New Mechanism of an Autonomous Unicycyle," *Proc. IEEE Int. Conf. Intelligent Robots and Systems*, pp. 906–912.
- [63] "Asimo," Honda Motor Co. Ltd., online: <http://asimo.honda.com/> (July 2006).
- [64] "Humanoid Robot HRP-2 'Promet'," Kawada Industries Inc., online: http://www.kawada.co.jp/global/ams/hrp_2.html (July 2006).
- [65] Ota, Y., Tamaki, T., Yoneda, K., Hirose, S., 2003, "Development of Walking Manipulator with Versatile Locomotion," *Proc. IEEE Int. Conf. on Robotics and Automation*, **1**, pp. 477–483.
- [66] McNeill Alexander, R., 2005, "Walking Made Simple," *Science*, **308**, pp. 58–59.
- [67] Murakami, H., Sonehara, M., Oikawa, T., Banno, H., Tateishi, J., 2007, "Development of Leg-Wheeled Type Mobile Robot Prototype," *IHI Engineering Review*, **40**(1), online: http://www.ihl.co.jp/ihl/file/technologygihou2/10012_2.pdf (July 2007).
- [68] Matsumoto, O., Kajita, S., Saigo, M., and Tani, K., 1998, "Dynamic trajectory control of passing over stairs by a biped type leg-wheeled robot with nominal reference of static gait," *Proc. IEEE Intl. Conf.on Intelligent Robots and Systems*, **1**, pp. 406–412.
- [69] Matsumoto, O., Kajita, S., Komirya, K., 2002, "Flexible Locomotion Control of a Self-contained Biped Leg-wheeled System," *Proc. IEEE Intl. Conf. Intelligent Robots and Systems*, **3**, pp. 2599–2604.

- [70] Steeves, C., Buehler, M., Penzes, S.G., 2002, “Dynamic behaviours for a hybrid leg-wheel mobile platform,” *Proc. SPIE, Unmanned Ground Vehicle Technology IV*, G. Gerhard et al., eds., **4715**, pp. 75–86.
- [71] Abo-Shanab, R. F., Sepehri, N., 2001, “On Dynamic Stability of Manipulators on Moveable Platforms,” *Proc. IEEE Int. Symposium on Computational Intelligence in Robotics and Automation*, pp. 479–485.
- [72] Abo-Shanab, R. F., Sepehri, N., 2005, “Tip-Over Stability of Manipulator-Like Mobile Hydraulic Machines,” *J. of Dynamic Systems, Measurement, and Control*, **127**(2), pp. 295–301.
- [73] Garcia, E., Gonzalez de Santos, P., 2005, “An improved energy stability margin for walking machines subject to dynamic effects,” *Robotica*, **23**, pp. 13–20.
- [74] Korayem, M. H., Ghariblu, H., 2004, “The effect of base replacement on the dynamic load carrying capacity of robotic manipulators,” *Int. J. Advanced Manufacturing Technology* **23**, pp. 28–38.
- [75] Sugano, S., Huang, Q., Kato, I. (1993) “Stability Criteria in Controlling Mobile Robotic Systems” *Proc. Int. Conf. Intelligent Robots and Systems*, **2**, pp. 832–838.
- [76] Papadopoulos, E. G., 1996 “A new measure of tipover stability margin for mobile manipulators,” *Proc. IEEE Int. Conf. on Robotics and Automation*, **4**, pp. 3111–3116.
- [77] Rey, D. A., Papadopoulos, E. G. (1997) “On-line Automatic Tipover Prevention for Mobile Manipulators” *Proc. Int. Conf. Intelligent Robots and Systems*, pp. 1273–1278.
- [78] “Manual Material Handling”, MECH495 Course Notes, Queen’s University, Kingston, Canada. Online: <http://me.queensu.ca/courses/MECH495/> (Dec. 2005)
- [79] “Quality Function Deployment”, *QFD Institute*. Online: <http://www.qfdi.org/> (July 2007)
- [80] “Anthropometrics”, MECH495 Course Notes, Queen’s University, Kingston, Canada. Online: <http://me.queensu.ca/courses/MECH495/> (Dec. 2005)
- [81] Park, T. B., Lee, J. H., Yi, B.-J., Kim, W. K., You, B. J., Oh, S.-R., 2002, “Optimal design and Actuator sizing of redundantly actuated omni-directional mobile Robots,” *Proc. IEEE Int. Conf. Robotics & Automation*, **1**, pp. 732–737.
- [82] Gipser, M., “ADAMS/FTire - A Tire Model for Ride & Durability Simulations.” Online: http://www.ftire.com/download/ftire_eng_2.pdf (May 2007).

- [83] Zegelaar, P.W.A., Pacejka, H.B., 1996, “The In-plane Dynamics of Tyres on Uneven Roads” *Vehicle System Dynamics*, **25** (Suppl.), pp. 714–730.
- [84] Zimmer, D., 2005, “Real-Time Models for Wheels and Tyres,” Internal Report 515–05–04, German Aerospace Center (DLR), Institute of Robotics and Mechatronics, Oberpfaffenhofen, Germany.
- [85] J.-L. Ha, R.-F. Fung, K.-Y. Chen, and S.-C. Hsien, 2006, “Dynamic Modeling and Identification of a Slider-Crank Mechanism,” *J. Sound a. Vibration*, vol. 289, pp. 1019–1044.
- [86] Hanebeck, U., Saldic, N., Schmidt, G., 1999, “A Modular Wheel System for Mobile Robot Applications,” *Proc. Int. Conf. Intelligent Robots and Systems*, **1**, pp. 17–22.
- [87] Pope, E., 1996, *Rules of Thumb for Mechanical Engineers*, Elsevier Gulf, Houston, TX, pp. 234–235.
- [88] Peer, A., Bajcinca, N., Schweiger, C., 2003, “Physical-based Friction Identification of an Electro-Mechanical Actuator with Dymola/Modelica and MOPS,” *Proc. 3rd Int. Modelica Conference*, P. Fritzson ed., pp. 241–248.
- [89] Gordon, J., Kauzlarich, J., Thacker, J., “Tests of two new polyurethane foam wheelchair tires,” *J. of Rehabilitation Research*, **26** (1), pp. 33–46.
- [90] Jones, E., Childers, R., 1992, *Contemporary College Physics*, Addison-Wesley, Chap. 4.8, cited in “Friction and Automobile Tires” Online: <http://hyperphysics.phy-astr.gsu.edu/hbase/mechanics/frictire.html> (Aug. 2007).
- [91] Ellis, R. E. and Ricker, S. L., 1994, “Two numerical Issues in simulating constrained Robot Dynamics,” *IEEE Trans. Systems, Man, a. Cybernetics*, **24**(1), pp. 19–27.
- [92] “dsolve/numeric/rkf45” *Maple Online Help*, Ver. 10, Waterloo Maple Inc., Waterloo, Canada, 2005.
- [93] Blundell, M., Harty, D., 2004, *Multibody Systems Approach to Vehicle Dynamics*, Elsevier Butterworth Heinemann, Oxford, pp. 149–152, Chap. 4.2.
- [94] Hrovat, D., 1997, “Survey of Advanced Suspension Developments and Related Optimal Control Applications,” *Automatica*, **33**(10), pp. 1781–1817.
- [95] Jalili, N., 2002, “A Comparative Study and Analysis of Semi-Active Vibration Control Systems,” *J. of Vibration and Acoustics*, **124**, pp. 593–605.

- [96] Sharp, R. S., 1998, "Variable Geometry Active Suspension for Cars," *Computing & Control Engineering J.*, **9**(5), pp. 217–222.
- [97] Schenker, P. S., Pirjanian, P., Balram, B., Ali, K. S., Trebi-Ollenu, A., Huntsberger, T. L., Aghazarian, H., Kennedy, B. A., Baumgartner, E. T., Iagnemma, K., Rzepniewski, A., Dubowsky, S., Leger, P. C., Apostolopoulos, D., McKee, G. T., 2000, "Reconfigurable robots for all terrain exploration," *Proc. SPIE, Conf. Sensor Fusion and Decentralized Control in Robotic Systems*, **4196**, pp. 454–469.
- [98] Yamashita, A., Asama, H., Kaetsu, H., Endo, I. Arai, T., 2001m "Development of a Step-climbing Omnidirectional Mobile Robot," *Proc. Int. Conf. Field and Service Robotics*, Helsinki, pp. 327–332.
- [99] Waechter, M., Riess F., Zacharias, N., 2002, "A Multibody Model for the Simulation of Bicycle Suspension Systems," *Vehicle System Dynamics*, **37** (1), pp. 3–28.
- [100] "Example: Modeling a Bus Suspension System," Carnegie Mellon University. Online: <http://www.engin.umich.edu/group/ctm/examples/susp/susp.html> (Aug. 2007).
- [101] Online: <http://www.engr.panam.edu/~kypuros/SystemDynamics/QuarterCarSuspension.m>
- [102] Kader, A., Dobos, A., Cullinan, M., "Speed Bump and Automotive Suspension Analysis," Online: <http://www.sccs.swarthmore.edu/users/06/adem/engin/e12/lab4/> (Aug. 2007)
- [103] Peng, H., Stathearn, R., Ulsoy, A.G., 1997, "A Novel Active Suspension Design Technique – Simulation and Experimental Results," *Proc. American Control Conference*, **1**, pp. 709–713.
- [104] Dixon, J., 1996, *Tires, Suspension and Handling*, Society of Automotive Engineers, Warrendale, PA., Chap. 2.
- [105] Sawatzky, B., Kim, W., Denison, I., 2004, "The Ergonomics of different Tyres and Tyre Pressure During Wheelchair Propulsion," *Ergonomics*, **46**(14), pp. 1475–1483.
- [106] Kim, W., Yi, B-J., Lim, D. J., 2004, "Kinematic Modeling of Mobile Robots by Transfer Method of Augmented Generalized Coordinates," *J. Robotic Systems*, (**21**)6, pp. 301–322.
- [107] Oetomo, D., Li. Y. P., Ang Jr., M., Lim, C. W., 2005, "Omnidirectional Mobile Robots with Powered Caster Wheels: Design Guidelines from Kinematic Isotropy Analysis," *Proc. Int. Conf. Intelligent Robots and Systems*, pp. 3034–3039.

- [108] Schilling, Robert, 1990, *Fundamentals of Robotics: Analysis and control*, Prentice-Hall, Englewood Cliffs, NJ, pp.194–233, Chap. 6.
- [109] Jarvis, R., 2004, “A ‘Do-it-Yourself’ Segway Mobile Robot Platform,” *Proc. Australasian Conf. Robotics & Automation*, N. Barnes, D. Austin, eds.
- [110] “Scanning range finder – URG series,” Hokuyo Automatic Co. Online: <http://www.hokuyo-aut.jp/02sensor/07scanner/urg.html> (Aug. 2007).
- [111] “S3000 Professional Laser Scanner,” Sick AG. Online: <http://ecatalog.sick.com/Products/ProductFinder/product.aspx?finder=Produktfinder&pid=22718&lang=en> (Aug. 2007).
- [112] Borst, C., conversation, Aug. 2006, DLR Robotic and Mechatronics Institute, Oberpfaffenhofen, Germany.
- [113] UBI-02590 Specifications, Ultralife Batteries Inc., online: <http://www.ultralifebatteries.com/datasheet.php?ID=UBBL02> (Aug. 2007).
- [114] “Innentüren” (in German) Online: <http://www.maxbahr.de/selbermachen/tueren/index.html> (May 2007).
- [115] “Maße für gefälzte Türblätter und Türzargen” (in German) from DIN 18101 1985–01 Online: <http://www.khries.de/tueren.htm> (May 2007).
- [116] “Dymola Dynamic Modeling Laboratory,” Ver. 6, Dynasim AB, 2006. Online: <http://www.dynasim.com/dymola.htm> (Aug. 2007).
- [117] Tiller, M., 2001, *Introduction to physical modeling with Modelica*, Kluwer Academic Publishers, Boston.
- [118] Otter, M., Elmqvist H., Mattsson, S. E., 2003, “The New Modelica MultiBody Library” *Proc. 3rd Int. Modelica Conf.*, pp.311—330.
- [119] Fritzon, P., 2004, “Multibody Systems”, *Principles of Object-Oriented Modeling and Simulation with Modelica 2.1* John Wiley & Sons.
- [120] “Friction Coefficient Database,” Center for Advanced Friction Studies, Southern Illinois University. Online: <http://frictioncenter.siu.edu/databaseSearch.html> (Aug. 2007).
- [121] Kauzlarich, J., Thacker, J., 1985, “Wheelchair Tire Rolling Resistance and Fatigue,” *J. Rehabilitation Research*, **22**(3), pp. 25–41.

- [122] Al-Eisawi K.W.1; Kerk C.J.; Congleton J.J.; Amendola A.A.; Jenkins O.C.; Gaines W., 1999, “Factors affecting minimum push and pull forces of manual carts,” *Applied Ergonomics*, **30** (3), pp. 235—245.
- [123] van der Woude, L.H.V, Geurts, C., Winkelman, H., Veeger, H.E.J., 2003, “Measurement of wheelchair rolling resistance with a handle bar push technique,” *J. Medical Engineering & Technology*, **27** (6), pp. 249–258.
- “[124] 4122CE, 4212CE DC Brush Servo Amplifiers,” Specifications, Copley Controls Corp., online: <http://www.copleycontrols.com/motion/downloads/pdf/4122ce.pdf> (Aug. 2007).